Evaluation of Motor Vehicle Fire Initiation and Propagation Part 12: Propagation of an Underbody Gasoline Pool Fire in a 1998 Front-Wheel Drive Passenger Vehicle

Jeffrey Santrock
General Motors Corporation

ABSTRACT

This report describes a vehicle fire propagation test conducted pursuant to an agreement between GM and the United States Department of Transportation. This fire test was conducted on February 25, 1999. The test vehicle was a crash-tested 1998 Honda Accord. In the crash test, this vehicle was stationary and was struck in the left rear (driver's side) by a moving barrier. The fuel tank in the test vehicle was compromised during this crash test and fluid was observed leaking from the fuel tank after the crash test. No fire was observed during this crash test, nor was evidence of fire present in the test vehicle detected during an inspection of the test vehicle after the crash test. An artificial method of creating an underbody gasoline pool was used in the test described in this report. Gasoline was pumped continuously from an external reservoir onto the top of the fuel tank. The outlet of the artificial gasoline supply tube was in the area of the fuel pump assembly and the tear in the fuel tank. Liquid gasoline flowed from several points on the rear cross-member of the rear suspension sub-frame onto the floor under the rear of the test vehicle. The gasoline was ignited with a propane torch. Flames entered the passenger compartment through crash-induced seam openings around the left and right wheelhouses. The test was stopped when flames were observed on the headlining panel in the test vehicle. Fire suppression began at approximately 155 seconds after the gasoline was ignited.

Table of Contents

Appendicies

List of Figures

Report

List of Figures

Appendicies

List of Tables

Report

List of Tables

Appendicies

1 Introduction and Test Summary

The work described in this report was conducted by General Motors (GM) pursuant to an agreement between GM and the United States Department of Transportation. According to this agreement, GM and the National Highway Traffic Safety Administration (NHTSA) jointly developed fifteen separate vehicle fire safety research projects. One of these projects, entitled "Fire Initiation and Propagation Tests", involves conducting 1) vehicle crash tests to investigate potential ignition events that occur in vehicle crashes, and 2) subsequent vehicle fire tests to characterize fire propagation in these crash-tested vehicles. The vehicle models to be tested, and the crash- and fire-test methods to be used for Project B.3 are described in another report [1]. The objectives of the fire tests are:

- To determine the principal fire paths and time-lines for flame propagation into the passenger compartment under the test conditions;
- To identify which components burn and to measure the thermal environments around those components associated with their ignition under the test conditions; and
- To measure air temperatures, heat fluxes, and combustion gas concentrations in the passenger compartment under the test conditions.

These tests were conducted under carefully designed experimental conditions noted throughout this and other reports. They cannot be relied upon to predict the specific nature and characteristics of actual post-collision fires in the field.

The test vehicle was a 1999 Honda Accord (VIN: 1HGCG5646WA018992). The test vehicle was crash tested on May 13, 1998 at the General Motors Proving Ground in Milford, Michigan [2]. In the crash test, this vehicle was stationary and was struck in the left rear (driver's side) by a moving barrier. The barrier had a deformable aluminum honeycomb face similar to that described in FMVSS214 [3]. The test vehicle was parked with the brakes on. The test vehicle was positioned so that the longitudinal center-line of the test vehicle was parallel to the direction of motion (velocity vector) of the barrier and offset to the right so that approximately 70% of the barrier face overlapped the rear of the test vehicle. The barrier speed at impact was 84.7 km/h (52.6 mph). The mass of the test vehicle, including Anthropomorphic Test Devices and test instrumentation, was 1,649 kg (4,415lbs.). The mass of the barrier was 1371 kg (3022 lbs.). The maximum change in velocity of the test vehicle was 41.9 km/h (26.0 mph). The fuel system of the test vehicle leaked during this crash. Inspection of the test after this crash test revealed a crack in the fuel pump assembly and a tear in the fuel tank. A detailed description of this test can be found in another report [2].

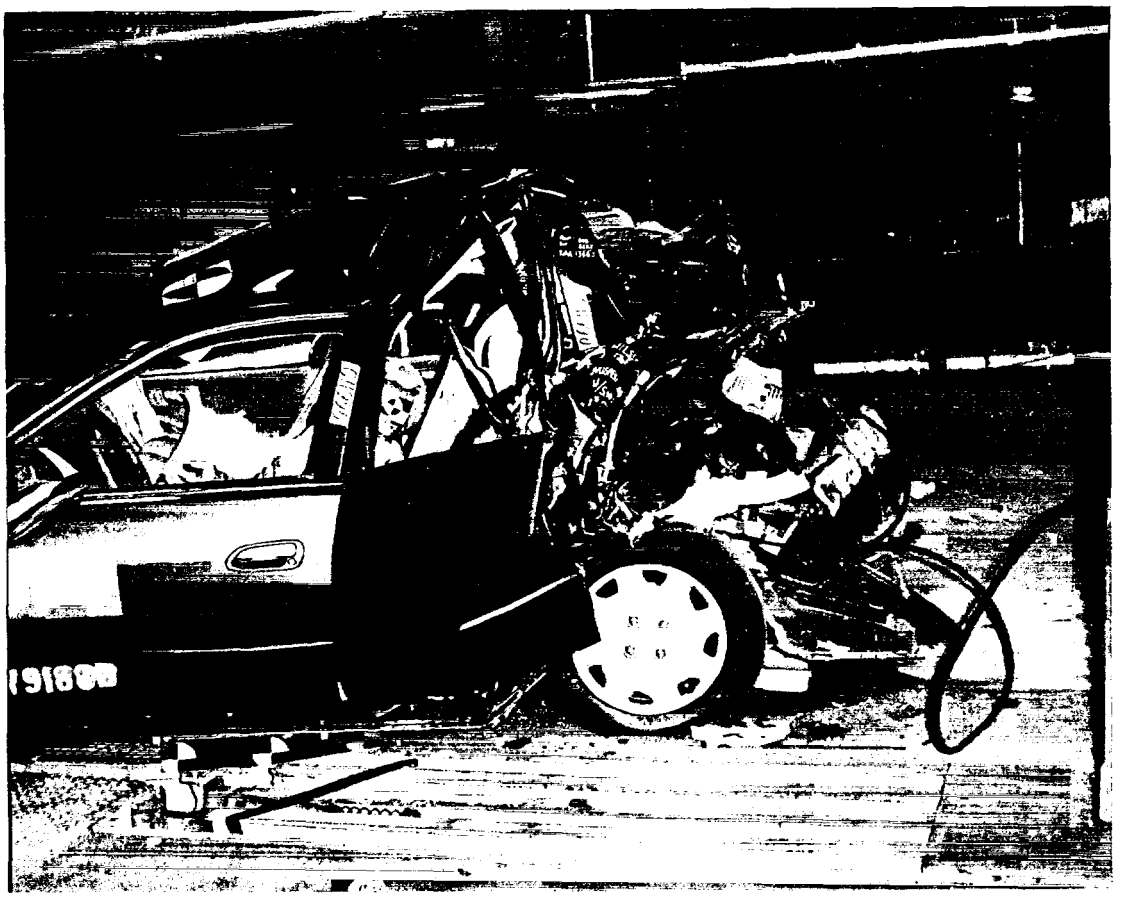

Figure 1. Fire Test F99030A. Photograph of the test vehicle after the crash test.

Figure 1 is a photograph of the test vehicle after the crash test. Numerical analysis of high speed film of this crash test indicated that the longitudinal displacement on the right side of the test vehicle relative to a target on the moving barrier was approximately 1299 mm [2]. Longitudinal displacement on the left side of the test vehicle was not measured because the target on the left side of the test vehicle became obscured during this crash test [2]. The rear window glass, and the glass in the right and left rear doors was broken in the crash test (Fig. 1). The left rear door bent and was displaced outward from the door frame, creating gaps between the rear and lower edges of the door and the door frame (Fig. 1). The left rear door remained latched during this crash test. The roof was displaced upward in this crash test (Fig. 1).

Figure 2 is a photograph of the rear interior of the test vehicle after the crash test. The rear seat back had been folded down and the left seat wing had been removed when this photograph was taken. The trim on the rear package shelf was dislodged in the crash test and was laying on top of the folded down seat back in this photograph. The arrows in Figure 2 indicate the approximate

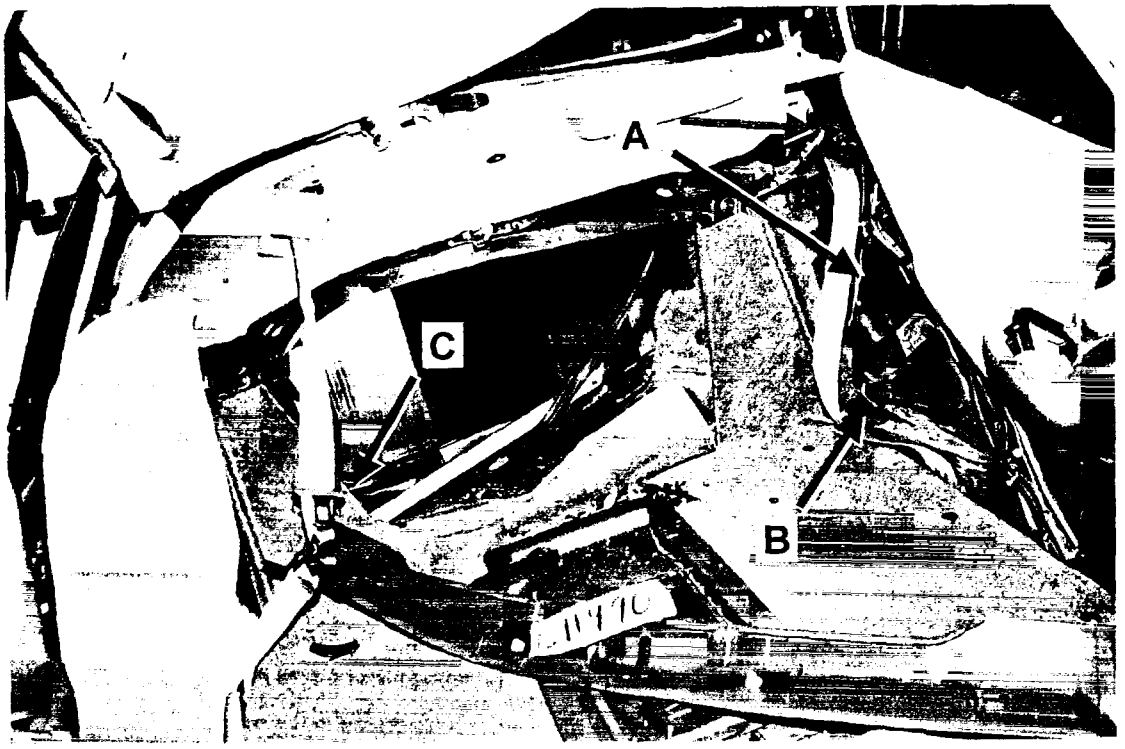

Figure 2. Fire Test F99030A. Photograph of the rear interior of the test vehicle after the crash test. The arrows indicate the approximate locations of crash-induced seam openings observed in the test vehicle after the crash test.

locations of crash-induced seam openings observed in the test vehicle after the crash test. Arrow A indicates a crash-induced seam opening between the left wheelhouse panel and inner quarter panel. Arrow B indicates a crash-induced seam opening between the left wheelhouse panel and floor panel. Arrow C indicates a crash-induced seam opening between the right wheelhouse panel and inner quarter panel which is not visible in this photograph.

Figure 3 is a photograph of the lower rear section of the left rocker panel and the left rear door of the test vehicle after the crash test. The outer panel partially detached from the door during the crash test (Fig. 3). The door remained latched during the crash test and was not unlatched during preparation of the test vehicle for the fire test described in this report. Crash-induced deformation of the quarter panel, rocker panel, and door resulted in a gap between the lower and rear edges of the door and door sill and latch pillar (Fig. 3).

The fire test described in this report was conducted on February 25, 1999 at the Factory Mutual Test Center in West Glocester, Rhode Island. The fire test was designed to study propagation of an under-body gasoline pool fire into the passenger compartment. Potential fire paths into the

Figure 3. Fire Test F99030A. Photograph of the left rear door and left rear wheel of the test vehicle after the crash test. The test vehicle was on a vehicle hoist for this photograph.

occupant compartment observed during inspection of the test vehicle after the crash test included the rear window opening (Fig. 1), the window-openings in the left and right rear doors (Fig. 1), seam openings between the floor panel and the left and right wheel house panels (Fig. 2), and gaps around the left rear door and door frame that were the result of deformation to the structure of the test vehicle during the crash test (Fig. 3). The test vehicle was instrumented with thermocouples and heat flux transducers to measure flame spread from the under-body gasoline pool fire into the passenger compartment.

Table 1 summarizes the timing of flame-spread into the passenger compartment along these pathways. An artificial method of creating an underbody gasoline pool was used in this test. Gasoline was pumped continuously from an external reservoir onto the top of the fuel tank during the fire test. The outlet of the artificial gasoline supply tube was in the area of the fuel pump assembly and the tear in the fuel tank. Liquid gasoline flowed from several points on the rear cross-member of the rear suspension sub-frame onto the cement board surface under the rear of the test vehicle. The gasoline was ignited with a propane torch. Flames entered the passenger compartment through crash-induced seam openings around the left and right wheelhouses. The

test was stopped when flames were observed on the headlining panel in the test vehicle. Fire suppression began at approximately 155 seconds after the gasoline was ignited.

Table 1

Summary of Fire Development during Fire Test F99030A

Time[1] (sec)	Event
-35	Start of gasoline flow
0	Gasoline under the test vehicle was ignited using a propane torch
15	Flames in the area between the left side of the floor panel in the trunk and the left rear tire
75	Flames started to vent from the right rear wheelhouse
75 - 90	Flames began to contact the rear surface of the left side of the rear seat back and ignite the foam pads in the rear seat back and rear seat bolsters
120	Flames were observed on the lower surface of the roof trim panel in the rear left quadrant of the passenger compartment
155	Fire suppression began

[1]Time after ignition of the gasoline pool.

2 Vehicle Condition and Test Protocol

The crash-tested vehicle was prepared for the fire test at the General Motors Research and Development Center (GM R&D Center) in Warren, Michigan, and shipped to the Factory Mutual Test Center in West Glocester, Rhode Island where this test was conducted. The test vehicle was returned to the GM R&D Center after the fire test, where it was systematically disassembled to permit closer inspection of the fire damage and identification of fire spread paths that were not obvious during the tests.

A description of the video cameras used during this test is in **APPENDIX A**. A description of the infrared cameras used in this test is in **APPENDIX B**. A description of the thermocouples installed in the test vehicle and data from these thermocouples are in **APPENDIX C**. A description of the aspirated thermocouples used in this test appears in **APPENDIX D**. Data was not collected from the aspirated thermocouples during this test because of an equipment malfunction. A description of the heat flux transducer/radiometer assemblies installed in the test vehicle and data from these devices are in **APPENDIX E**. Description of the pressure and airflow measurement equipment and analysis procedures, and data from these measurements are in **APPENDIX F**. Description of the Fire Products Collector (FPC) at the Factory Mutual Global Test Center and analysis procedures, and data from this device are in **APPENDIX G**. A description of the Fourier Transform Infrared Gas Analysis System used during this test and results from this device are in **APPENDIX H**. Descriptions of the Gas Chromatography/Mass Spectrometry equipment and analysis procedures, and the results of these analyses are in **APPENDIX I**. Descriptions of the particulate sampling equipment and analysis procedures, and the results of these analyses are in **APPENDIX J**.

The vehicle was placed in a rectangular steel pan (length = 25 ft., width = 15 ft., height = 4 in.) to prevent spilled and leaking automotive fluids from spreading in the test facility. This fluid containment pan was fabricated from two sheets of carbon steel. Angle-braces were welded to the under-side of the pan to keep it from flexing under the weight of the vehicle. The corners of the support frame rested on load cells. Mass loss was determined from data acquired from the load cells during the test.

A layer of fiberglass-reinforced cement construction board (DuraRock, USG Corporation) was placed on the bottom of the fluid containment pan. A thin layer of sand was used to level the concrete board so that the grade of the surface measured from the center to the edges along the major and minor axes was no greater than 1%. The joints between the boards were sealed with latex caulking.

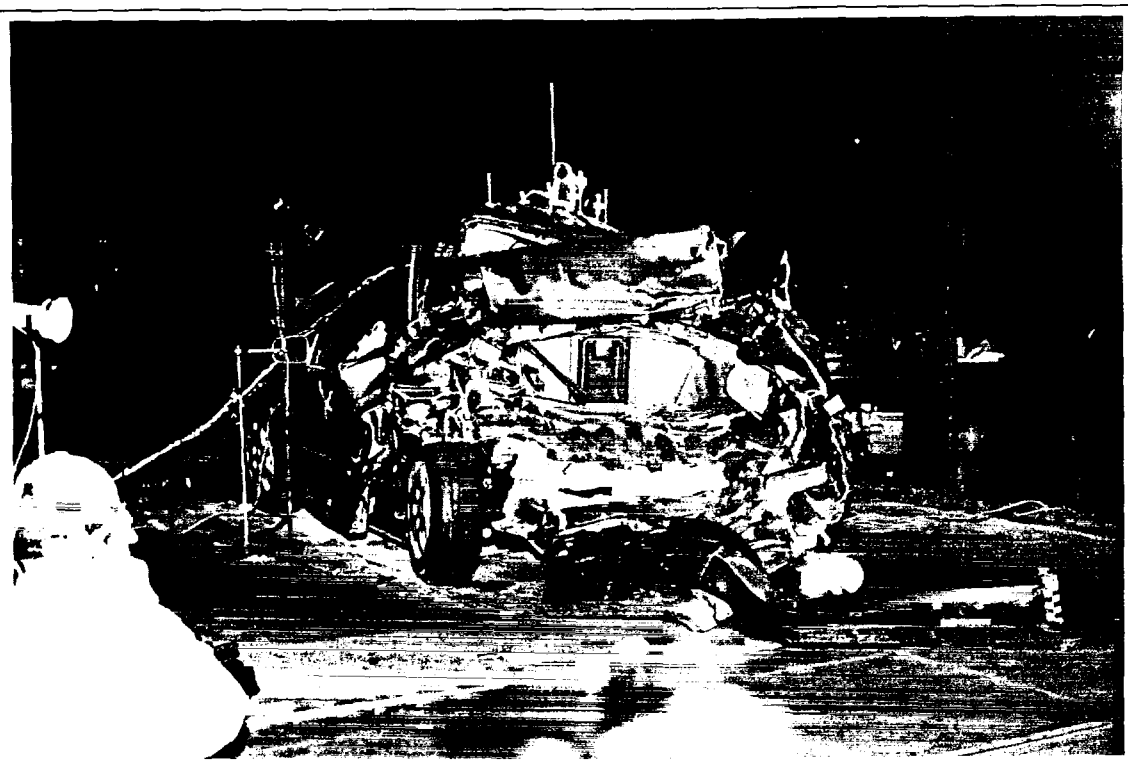

Figure 4. Fire Test F99030A. Photograph of the test vehicle in the fluid containment pan before the fire test.

The test vehicle was placed in the center of the pan (Fig. 4). All doors were closed, and the window glasses in both front doors were raised to their fully closed position. The glass in the rear window, and the left and right rear doors, which were broken in the crash test, were not replaced for the fire test.

An air horn was sounded to signal three events during the test: (1) the start of gasoline flow, (2) ignition of the gasoline pool by a propane torch, and (3) the end of the test and start of fire suppression. The air horn was used to synchronize the data acquisition systems used in this test. The air horn was audible on the videotapes and infrared imaging systems. One channel of the data acquisition system for vehicle instrumentation monitored a normally open switch, which was depressed at each sounding. The real-time clock in the FTIR data system was synchronized to the real-time clock in the vehicle instrumentation data system.

Gasoline was delivered from a pressurized external receiver at a constant flow rate during this test. Technical personnel from the Building and Fire Research Laboratory of the National Institutes of Standards and Technologies designed, built, and operated the gasoline delivery

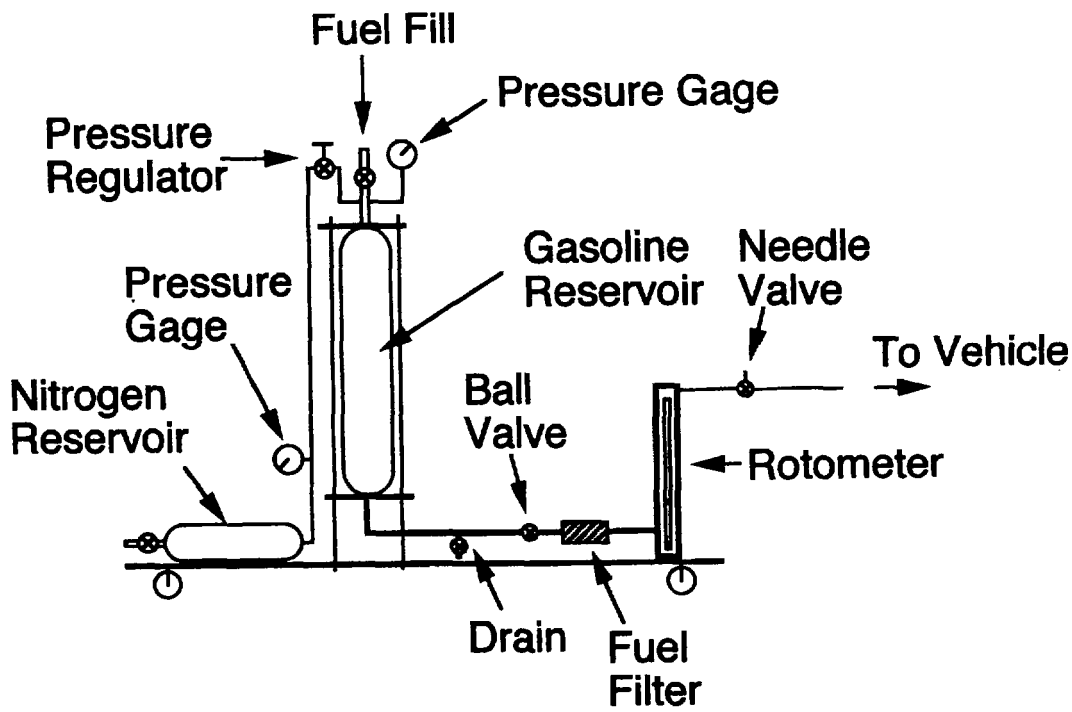

Figure 5. Fire Test F980609. Schematic diagram of the external gasoline reservoir and delivery system used to artificially supply gasoline to the test vehicle during this test.

system used in this test. Figure 5 shows a schematic diagram of the gasoline delivery system used in this test. This system consisted of two stainless steel cylinders. One cylinder functioned as a fluid reservoir and had a capacity of 4 L, while the other cylinder functioned as a gas reservoir and had a capacity of 2 L. A pressure regulator in the line connecting the gas reservoir to the fluid reservoir controlled the head pressure in the fluid reservoir. The outlet line of the fluid reservoir contained a ball valve that was used to turn on and off the flow of gasoline during the test, a rotometer to indicate the flow of gasoline during the test, and a needle valve to control the flow of gasoline.

The outlet of the tube was located near the rear inboard corner of the fuel tank in the test vehicle. The outlet of the tube was fitted with a flow restrictor (i.d. = 0.125") to reduce vaporization of gasoline by maintaining some back-pressure in the delivery tube.

Gasoline (4 L) was added to a steel fluid reservoir (4 L). The gas reservoir was filled with dry nitrogen gas. The pressure regulator was adjusted to maintain a head pressure of 275 kPa (25.0 psi) in the fluid reservoir. Before the test, the delivery tube was purged with gasoline before the start of the test to eliminate air. The needle valve was adjusted to give a flow rate of approximately 400 ± 20 cm^3/min of gasoline. A valve approximately 3 feet from the outlet of the gasoline delivery tube was mounted to the right rocker panel just rearward of the front wheel and opened to start the flow of gasoline during this test. The flow rate of gasoline through the delivery tube was determined from readings taken from the rotometer. The head pressure in the fluid reservoir and ball position in the rotometer was checked at 30 second intervals during the test to determine if the initial flow rate of gasoline had changed. The pressure regulator and needle valve were adjusted as necessary to maintain a constant flow rate of gasoline during the test.

The test was ended approximately 145 seconds after the gasoline pool under the test vehicle was ignited. A water mist was used to extinguish the flames after the flow of gasoline was stopped.

3 Ignition

To start this test, gasoline flow was started by opening the valve on the right rocker-panel fo the test vehicle. The flow rate of liquid gasoline was maintained at 400 ± 20 cm^3/min throughout this test by manually adjusting the needle valve to maintain a constant rotometer reading. Liquid gasoline started to flow from several points on the rear cross-member of the rear suspension sub-frame onto the cement board surface under the test vehicle within 5 seconds after starting gasoline flow (Fig. 6).

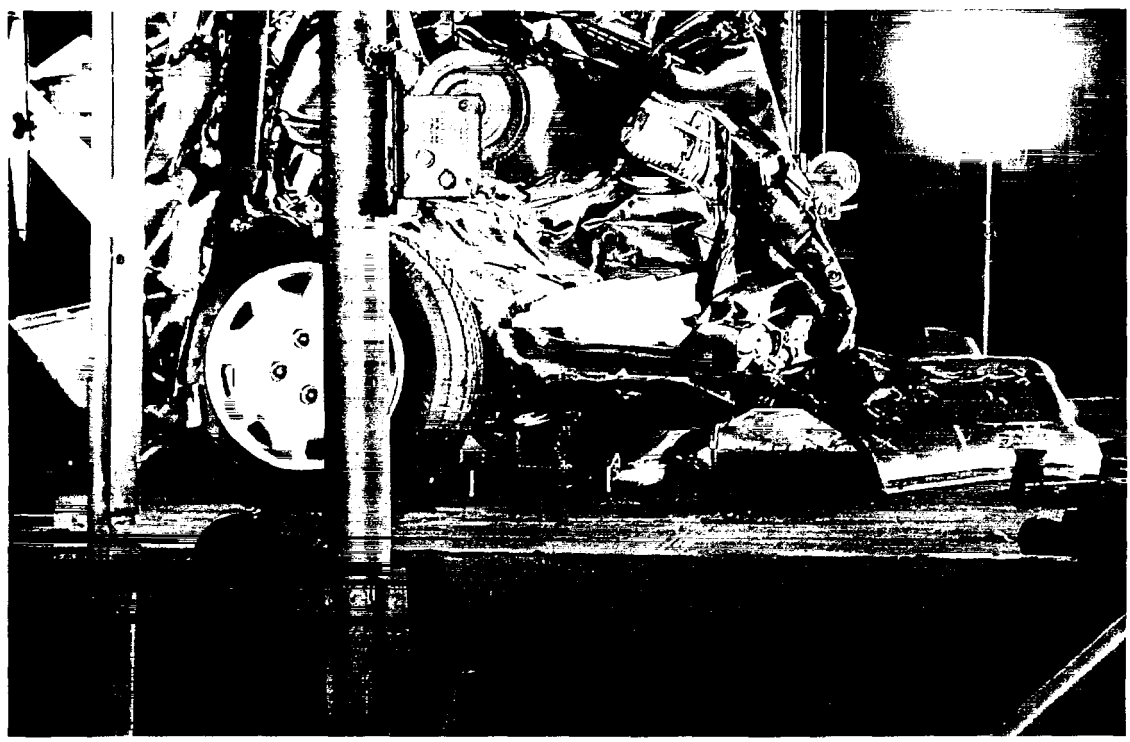

Figure 6. Fire Test F99030A. Photograph of the rear of the test vehicle and fluid containment pan approximately 30 seconds after the start of gasoline flow.

Gasoline was allowed to flow onto the cement board surface under the test vehicle for approximately 30 seconds before igniting the gasoline vapor above the liquid gasoline with a propane torch.

Figures 7 through 11 show a series of video stills from Cameras 1 through 5 at 5 seconds before ignition and about ½ second after ignition.

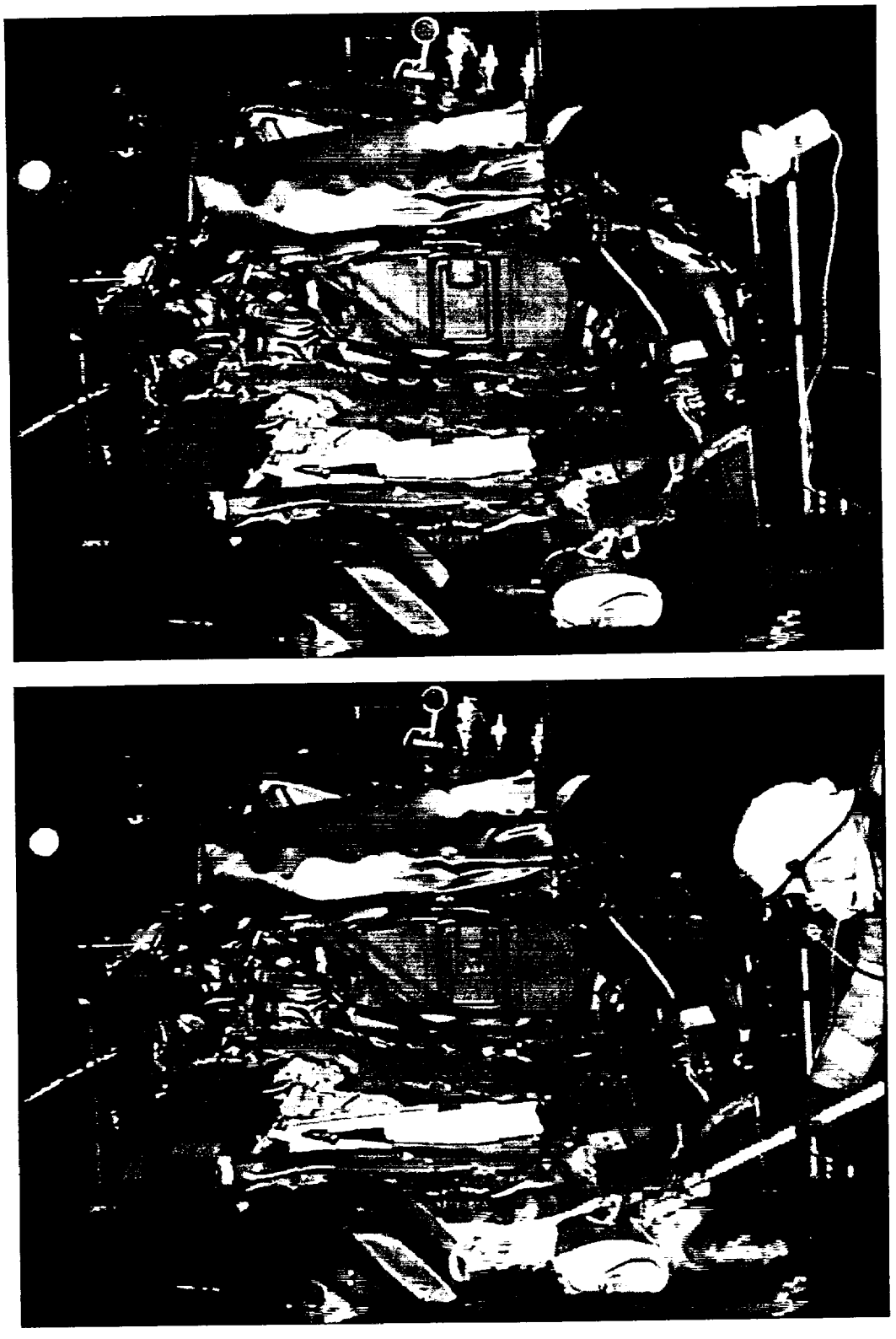

Figure 7. Fire Test F99030A. Video stills from Camera 1 at 5 seconds before ignition (upper) and approximately ½ second after ignition (lower).

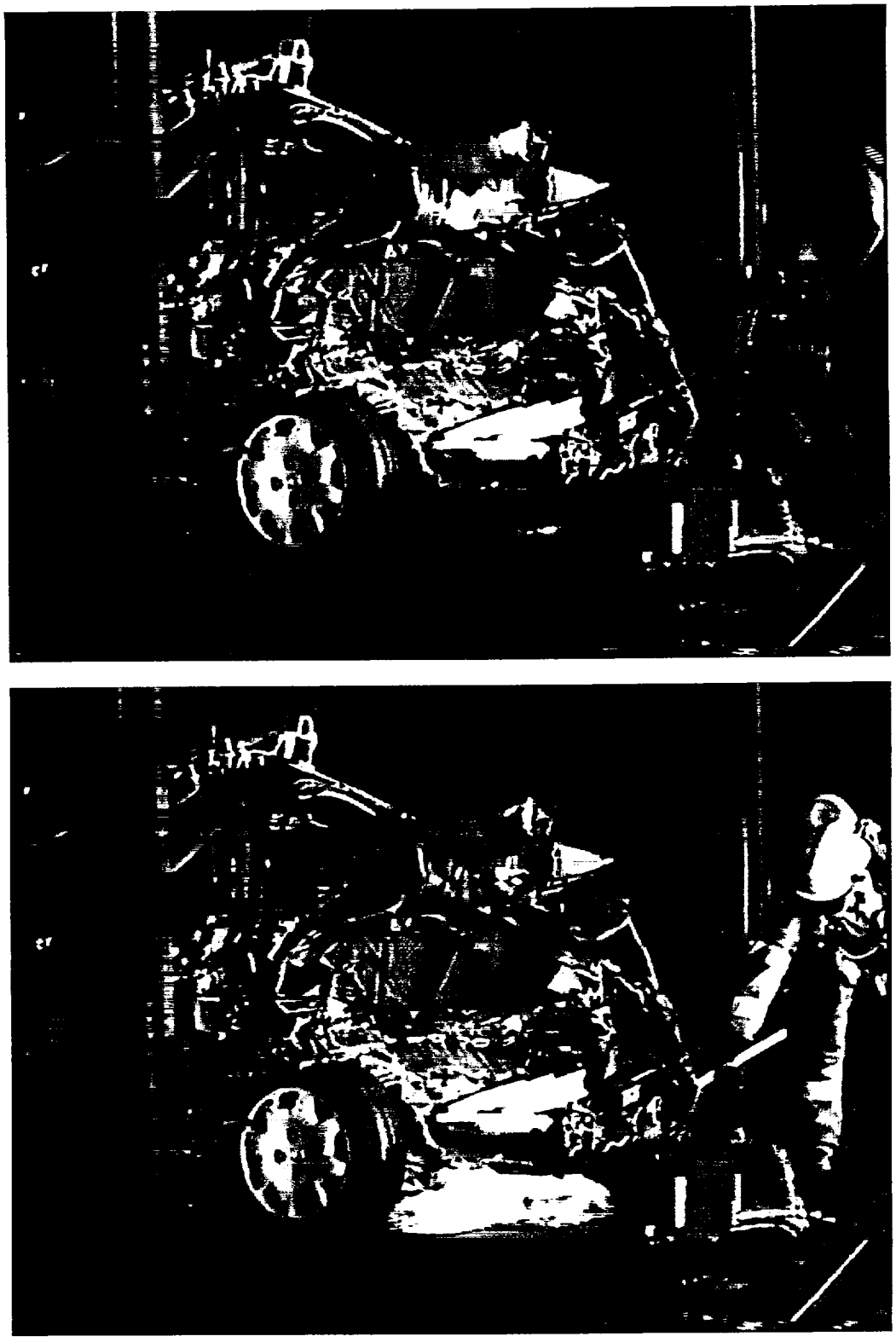

Figure 8. Fire Test F99030A. Video stills from Camera 2 at 5 seconds before ignition (upper) and approximately ½ second after ignition (lower).

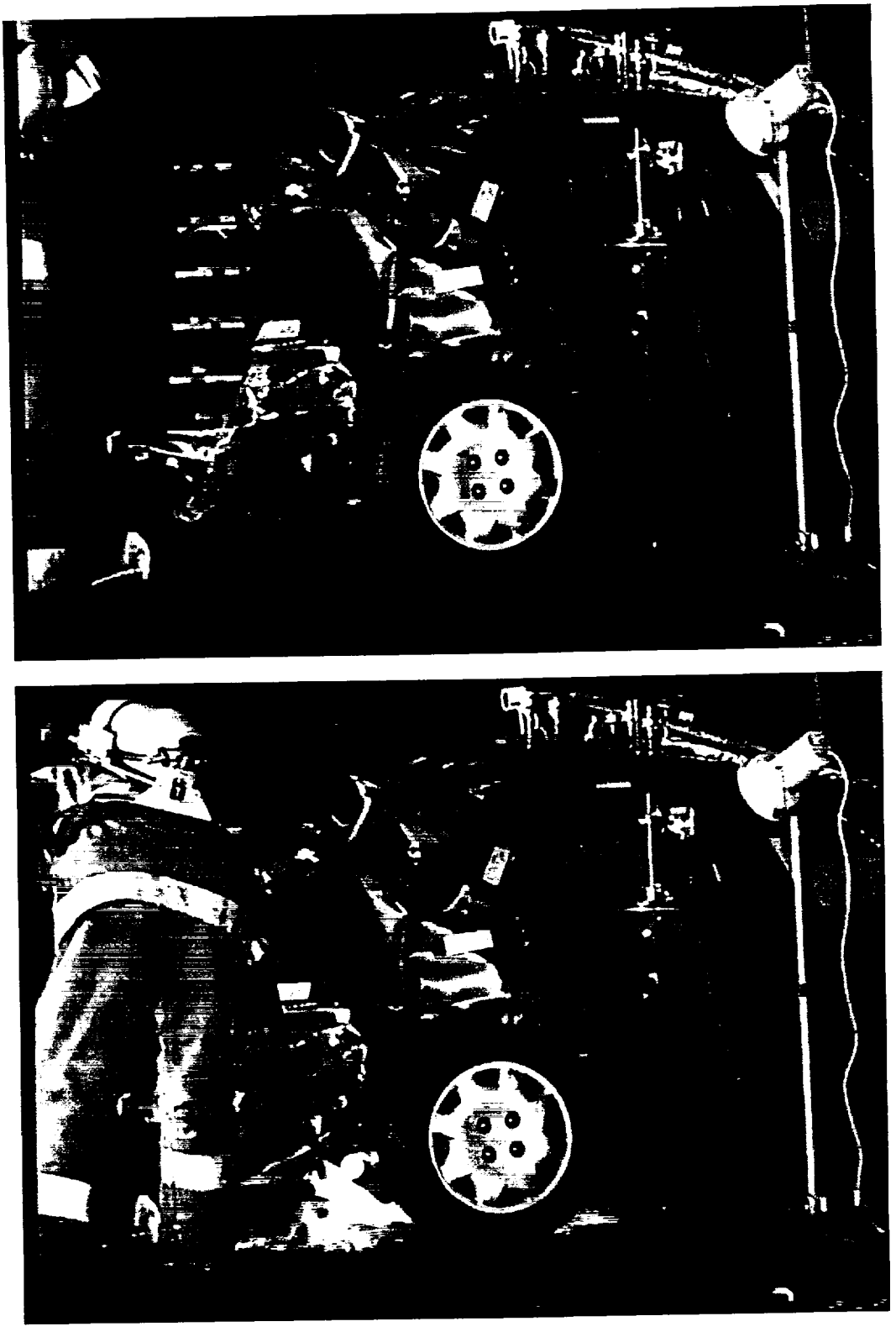

Figure 9. Fire Test F99030A. Video stills from Camera 3 at 5 seconds before ignition (upper) and approximately ½ second after ignition (lower).

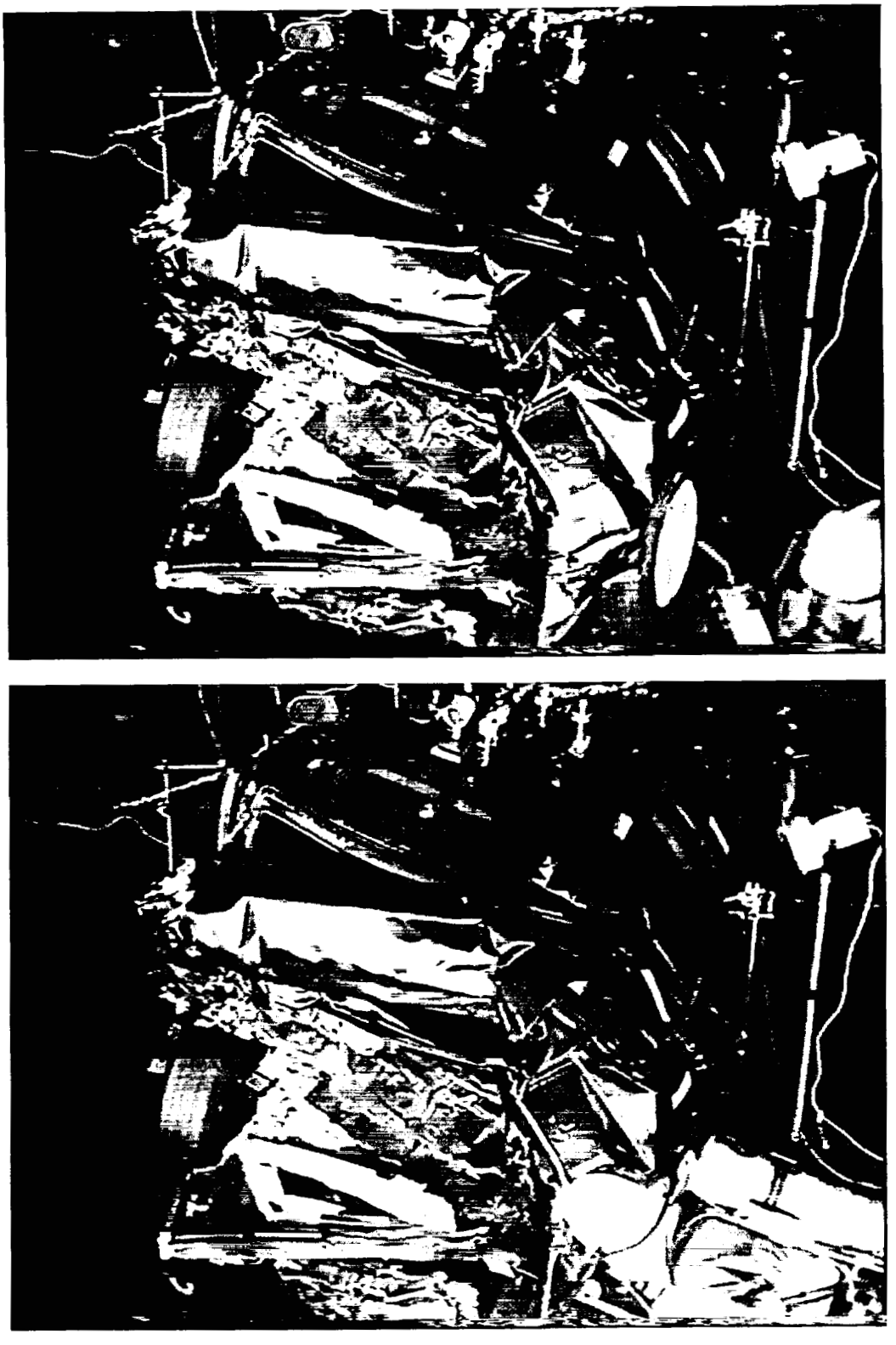

Figure 10. Fire Test F99030A. Video stills from Camera 4 at 5 seconds before ignition (upper) and approximately ½ second after ignition (lower).

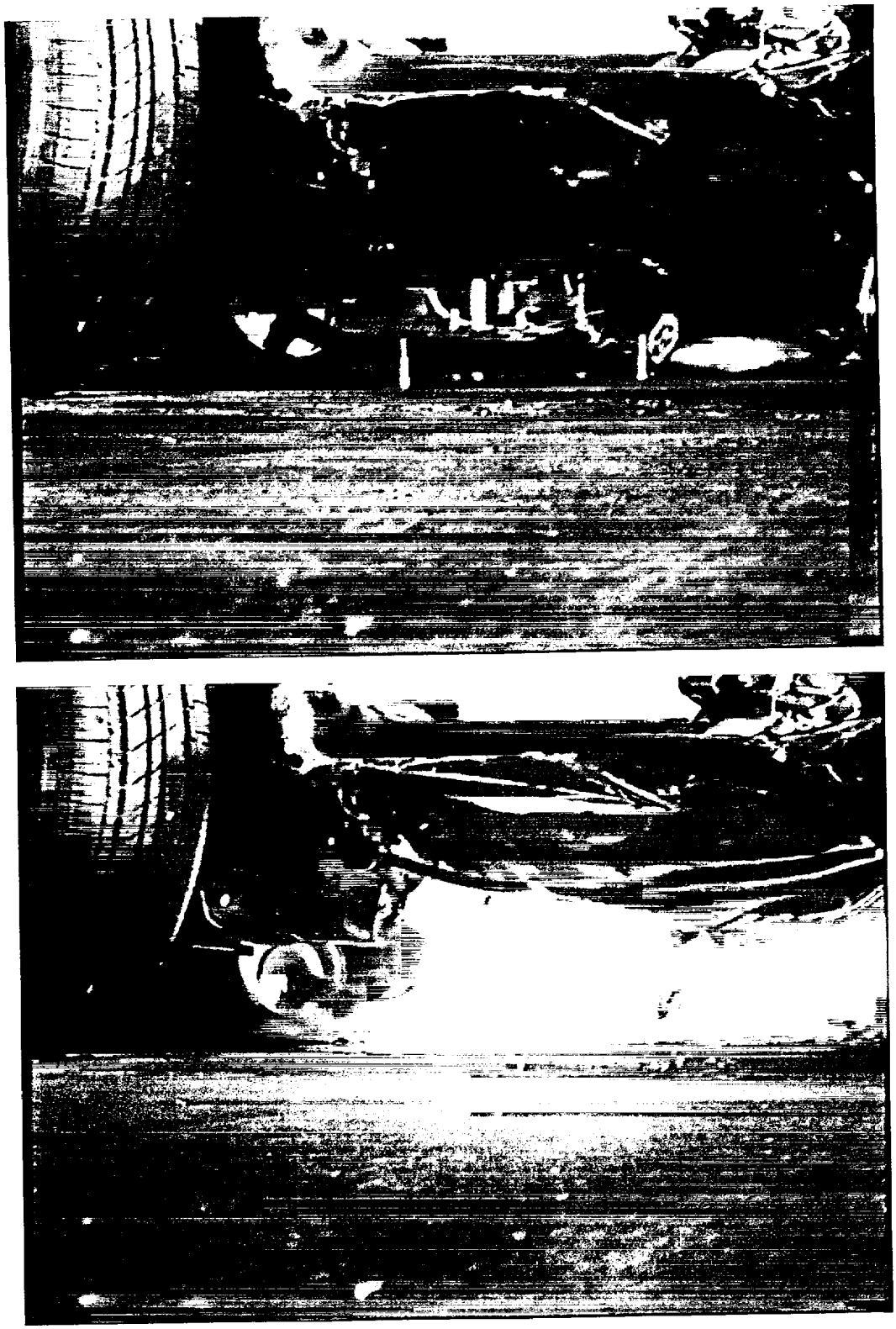

Figure 11. Fire Test F99030A. Video stills from Camera 5 at 5 seconds before ignition (upper) and approximately ½ second after ignition (lower).

Ignition occurred under the rear suspension sub-frame. Blue flames spread from the point of ignition at the edge of the flame front (lower video still, Fig. 11).

As liquid gasoline flowed from several places along the rear cross-member of the rear suspension sub-frame, it flowed onto the surface of the cement boards under the floor panel in the trunk of the test vehicle. The wetted area on the cement boards appeared to be approximately circular (lower video stills, Fig.'s 6 and 11).

4 Behavior of the Underbody Gasoline Pool Fire in this Test

The flow rate of gasoline was maintained at approximately at 400 cm^3/min throughout the test. After ignition, the diameter of the burning gasoline pool was estimated from the video from Camera 5. Two bolts placed on the cement-board surface under the rear of the test vehicle were used to determine distances. These bolts are visible in Figure 6. The distance between these bolts measured perpendicular to the line-of-sight of Camera 5 was approximately 30 cm. The resonator, muffler, and the section of exhaust pipe between the resonator and muffler partially obscured the right hand edge of the flames, making a precise measurement of pool diameter difficult. The uncertainty in the estimated pool size was ± 10 cm.

Figure 12 shows a plot of the estimated diameter of flames at the cement board surface under the test vehicle at five-second intervals from the time of ignition to 150 seconds post-ignition. The flow of gasoline was stopped between 140 and 145 seconds post-ignition.

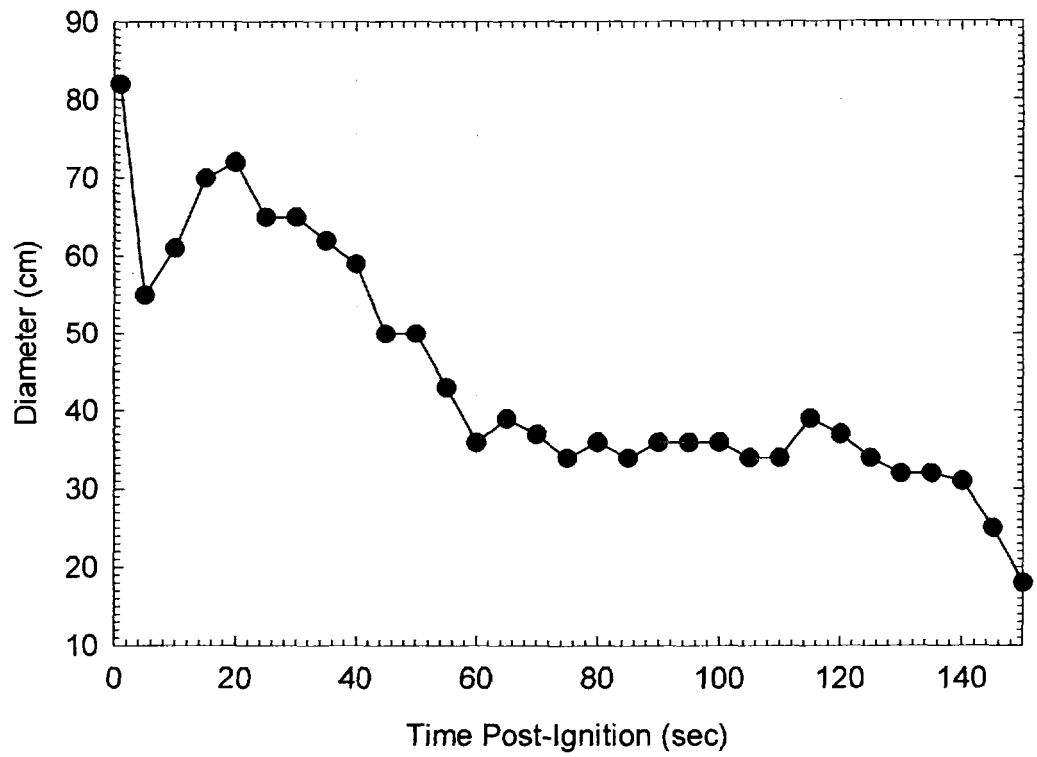

Figure 12. Fire Test F99030A. Estimated diameter of flames at the cement board surface under the test vehicle at five-second intervals from 0 through 150 seconds post-ignition obtained by analysis of the video from Camera 5.

The estimated diameter of flames at the cement board surface was estimated at approximately 82 cm at 1 seconds post-ignition and decreased to about 35 cm by 60 seconds post-ignition (Fig. 12). The estimated flame diameter was between 30 and 40 cm from 60 to 140 seconds post-ignition, and decreased after about 138 seconds post-ignition when the flow of gasoline was stopped (Fig. 12).

The distribution of flames on the underbody of the test vehicle was affected by the location of the gasoline pool on the cement board relative to the test vehicle, the distance from the cement board to the vehicle underbody, and the shape of the test vehicle underbody. Figures 13 through 22 show a series of video stills from Cameras 4 and 5 at ½, 10 15, 30, 45, 60, 75, 90, 120, and 153 seconds post-ignition. At the time of ignition, flames extended laterally from about the center of the test vehicle to the right rear wheel and longitudinally from about the rear cross-member of the rear suspension sub-frame rearward to the spare tire well in trunk (Fig. 13). Gasoline vapor that accumulated under the rear of the test vehicle was consumed within a few seconds after ignition.

The shape and distance between the vehicle underbody and the cement-board surface affected the distribution of flames on the test vehicle. Liquid gasoline flowing off of the rear cross-member pooled under the rear section of the rear suspension sub-frame and the spare tire well in the trunk. Before ignition, the gasoline pool appeared to be radially symmetrical with a diameter of 18 – 22 cm, and the gasoline pool appeared to be was centered on the longitudinal centerline of the test vehicle (Fig. 13). Approximate vertical distances between the cement-board surface to the underbody were as follows: 9 – 13 cm at the rear cross-member of the rear suspension sub-frame and 10 – 12 cm at the spare tire well in the trunk.

By 10 seconds post-ignition, the diameter of flames just above the cement board surface was approximately 60 cm and was defined by the diameter of the gasoline pool (Fig. 14). Flames spread laterally outward as they encountered objects on the underbody of the test vehicle (Fig. 14). Flames did not contact either wheel at this time (Fig. 14). By 15 seconds post-ignition, flames on the underbody of the test vehicle had started to extend beyond the perimeter of the gasoline pool (Fig. 15). Flames started to emerge sporadically from crash-induced seam openings around the left rear wheelhouse between 10 and 15 seconds post-ignition just inboard of the top of the left rear tire (Fig. 15). The volume of flames in this area increased throughout this test. Flames had emerged from the right rear wheelhouse by 75 seconds post-ignition (Fig. 19) and from the left rear wheelhouse by 90 seconds post-ignition (Fig. 20). The volume of flames extending rearward along the spare tire well increased from the time of ignition through about 138 seconds post-ignition (Fig.'s 13 through 21).

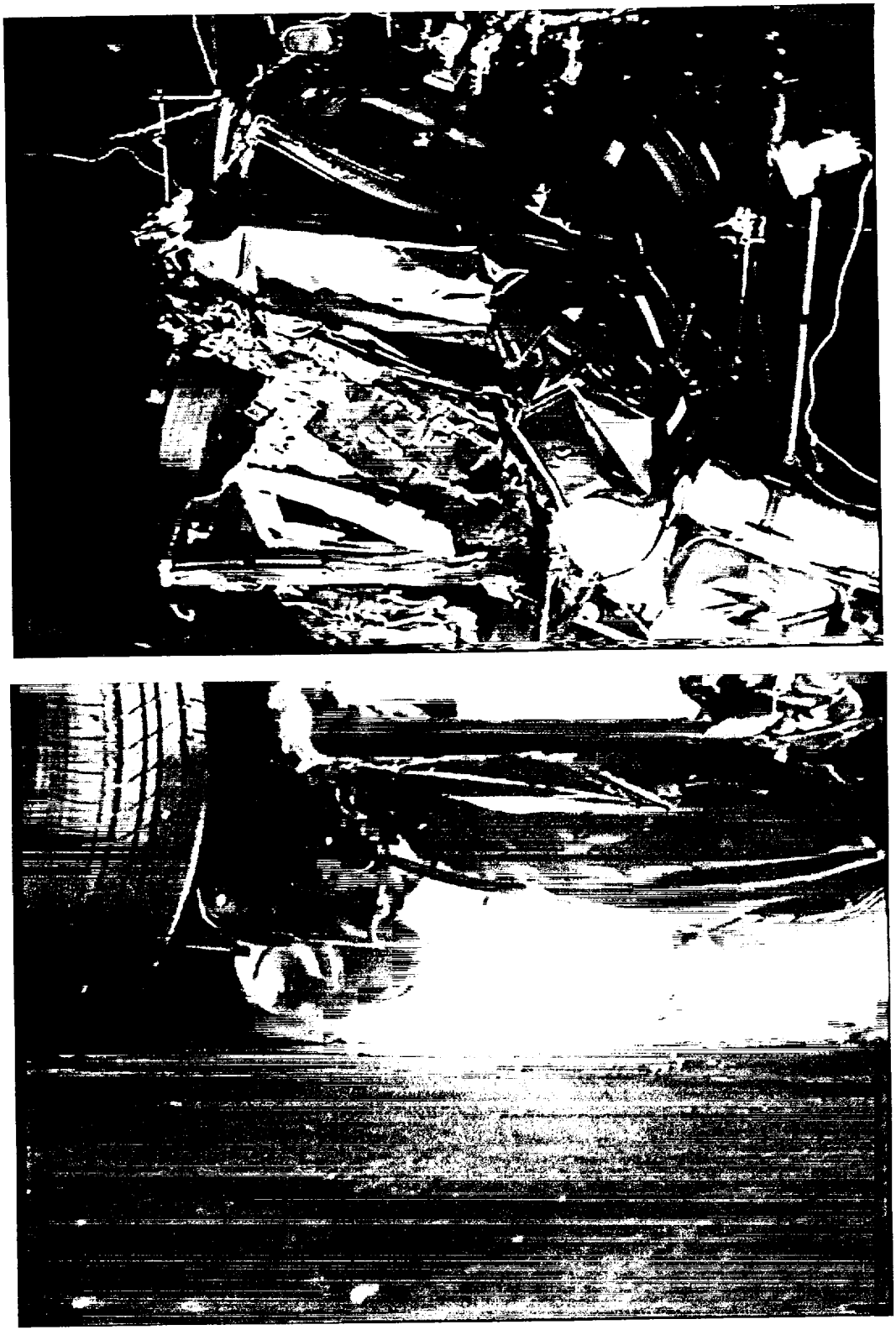

Figure 13. Fire Test F99030A. Video stills from Camera 4 (upper) and 5 (lower) at approximately ½ second after ignition.

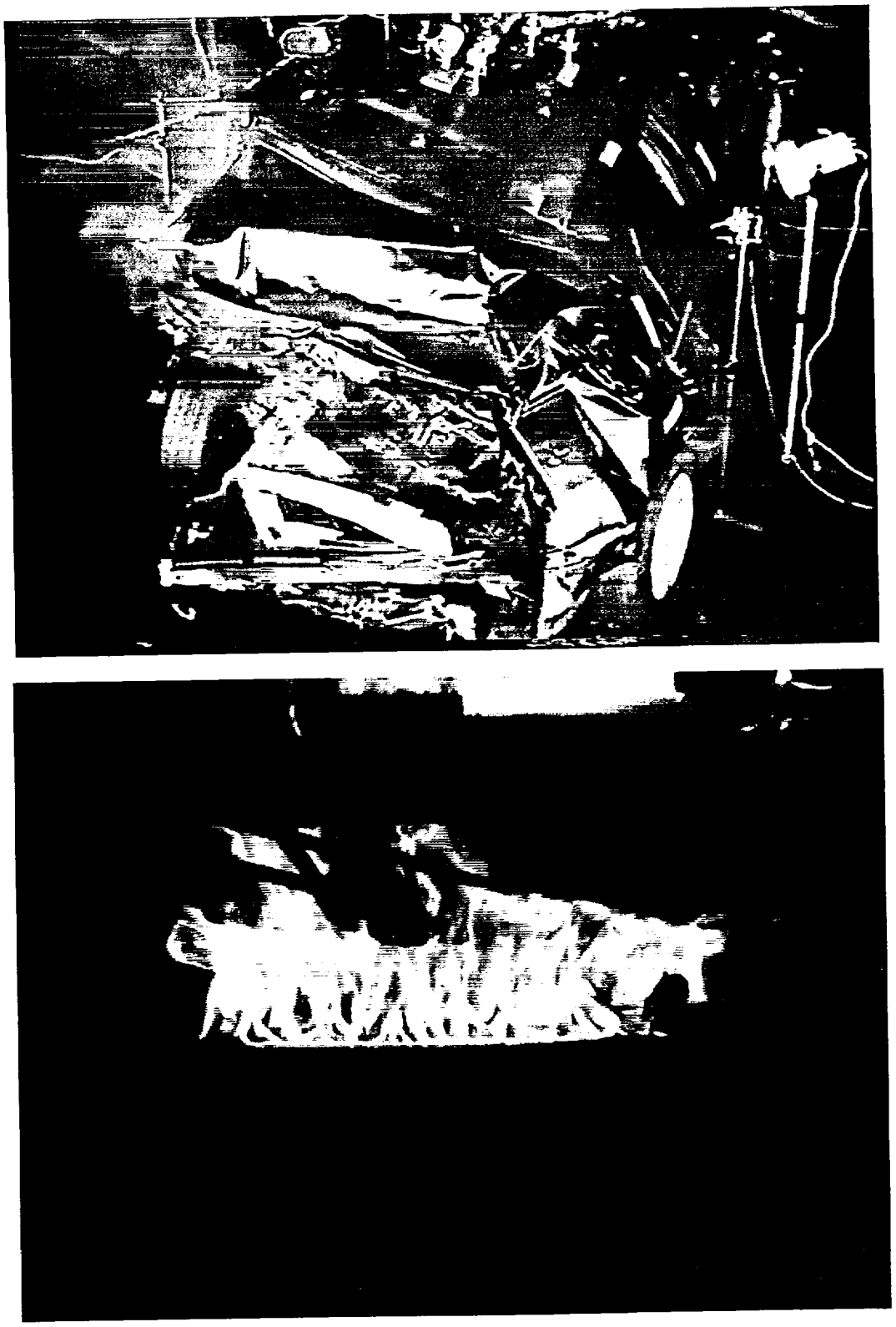

Figure 14. Fire Test F99030A. Video stills from Video Cameras 4 (upper) and 5 (lower) at 10 seconds post-ignition.

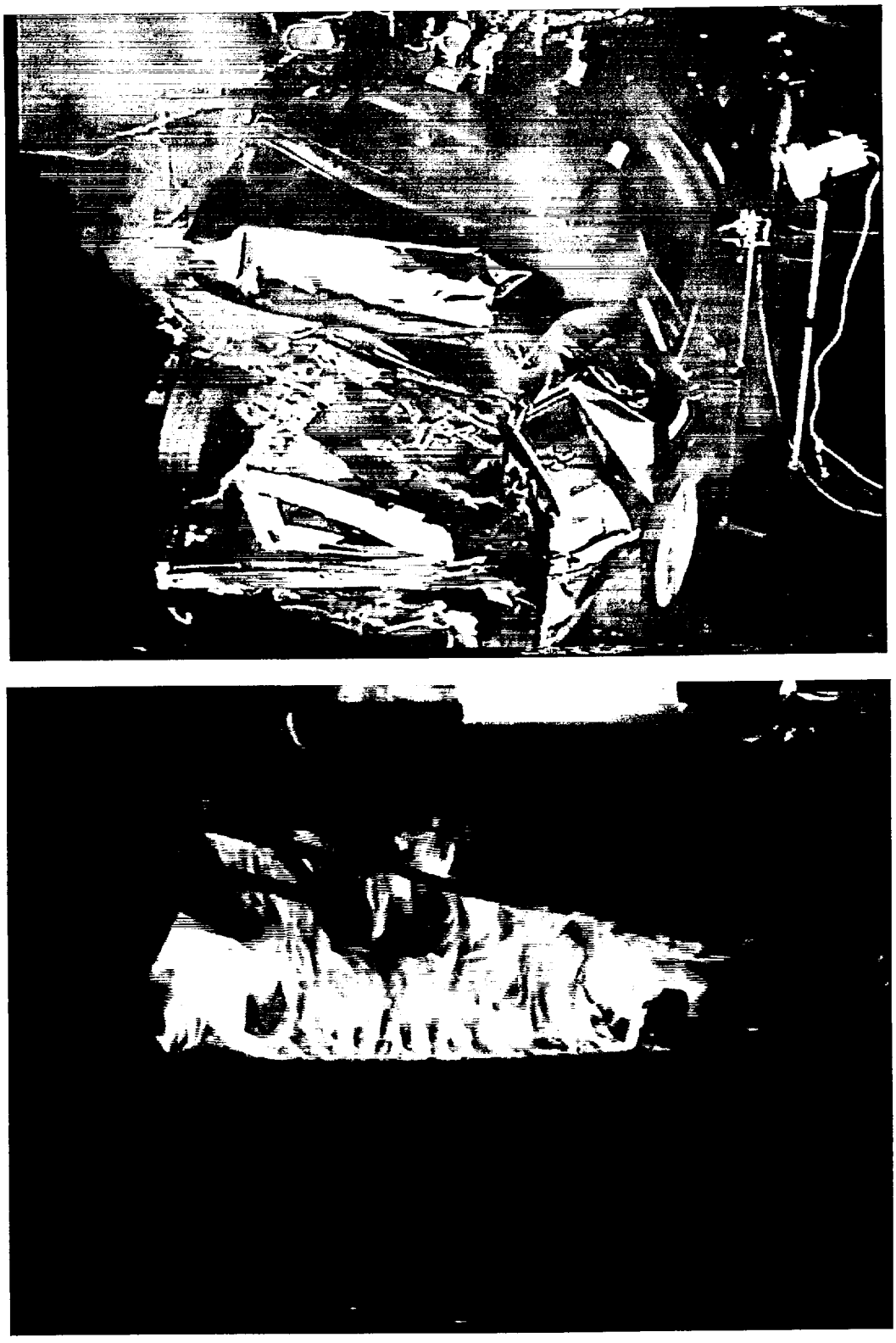

Figure 15. Fire Test F99030A. Video stills from Video Cameras 4 (upper) and 5 (lower) at 15 seconds post-ignition.

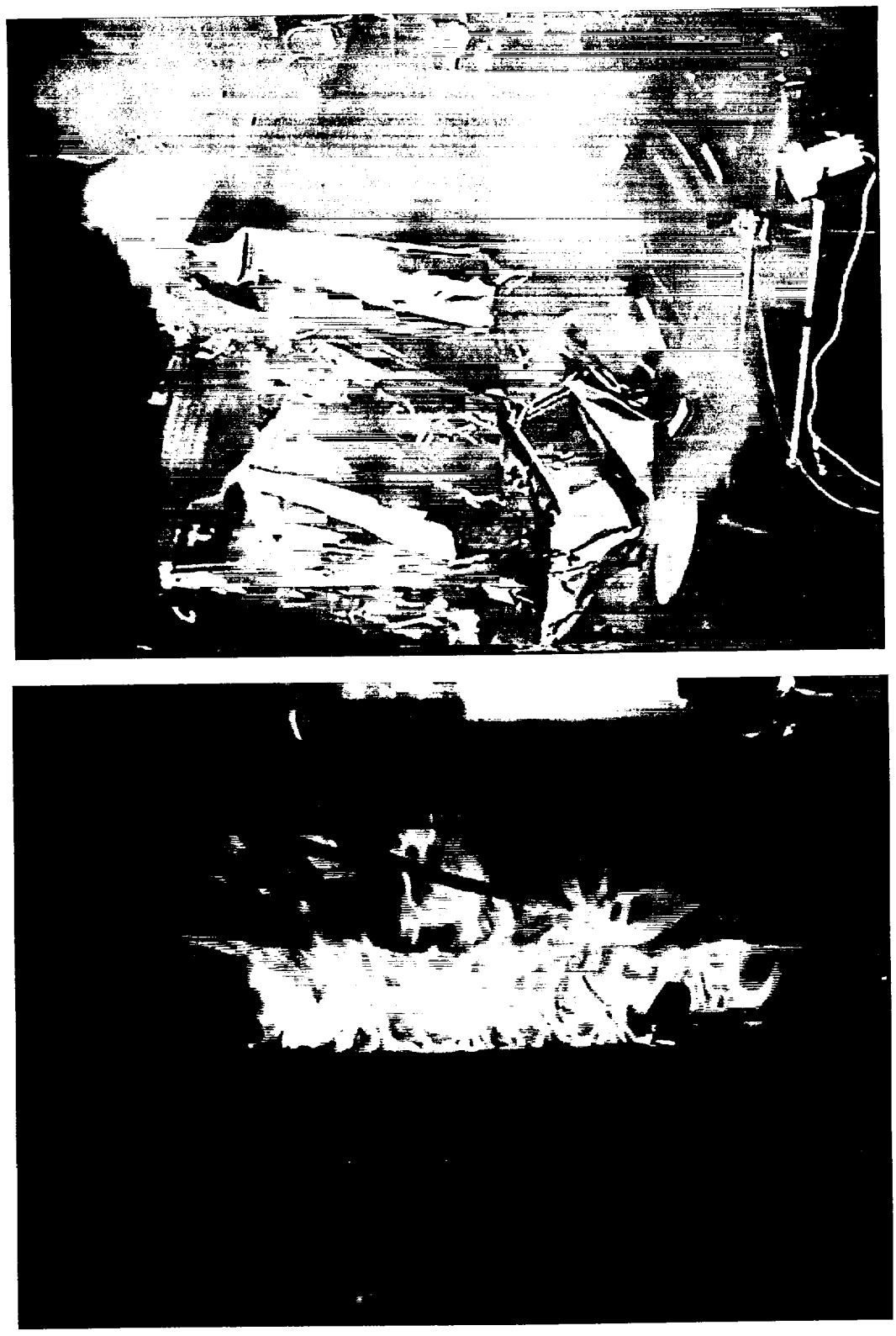

Figure 16. Fire Test F99030A. Video stills from Video Cameras 4 (upper) and 5 (lower) at 30 seconds post-ignition.

Figure 16. Fire Test F99030A. Video stills from Video Cameras 4 (upper) and 5 (lower) at 30 seconds post-ignition.

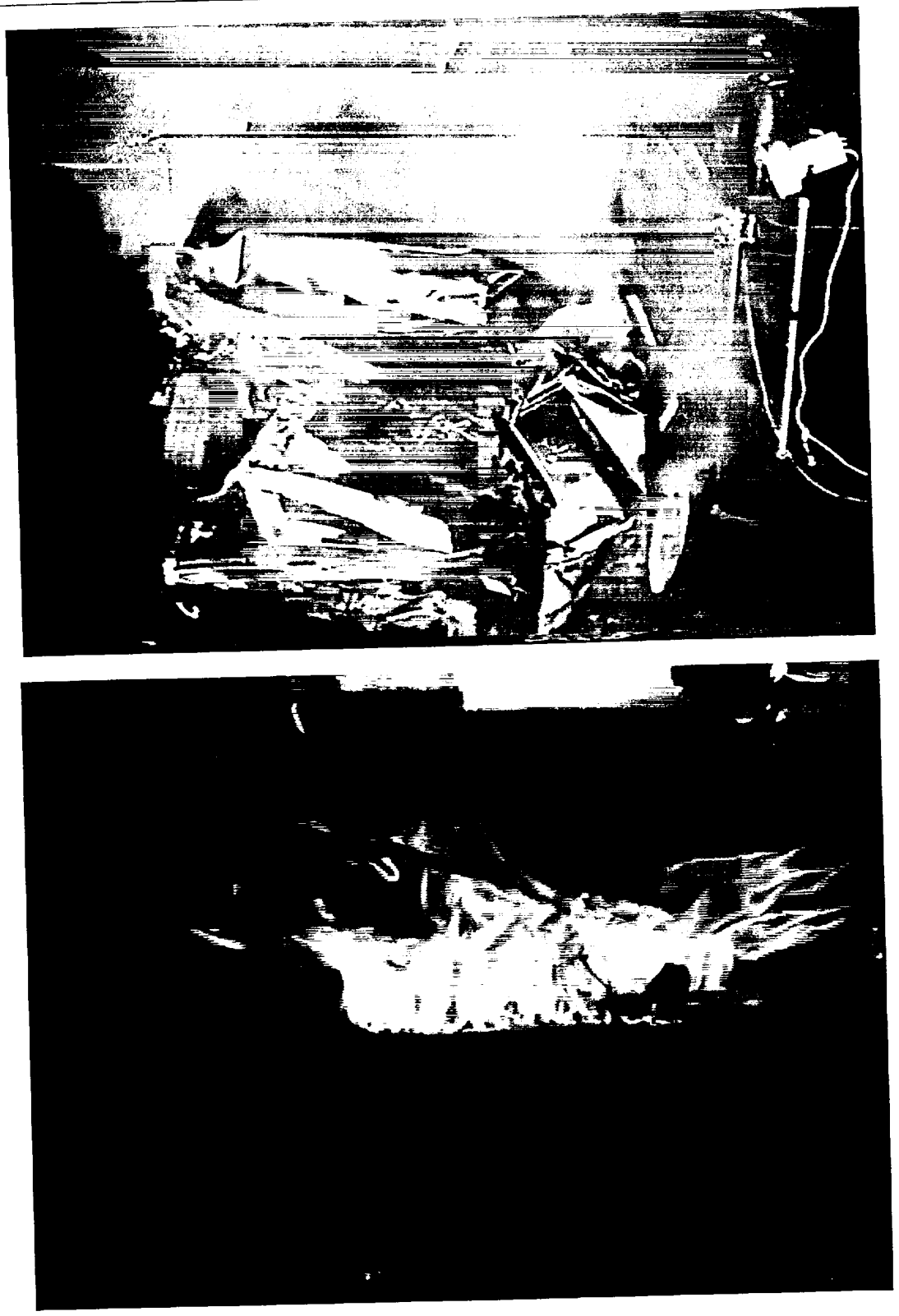

Figure 17. Fire Test F99030A. Video stills from Video Cameras 4 (upper) and 5 (lower) at 45 seconds post-ignition.

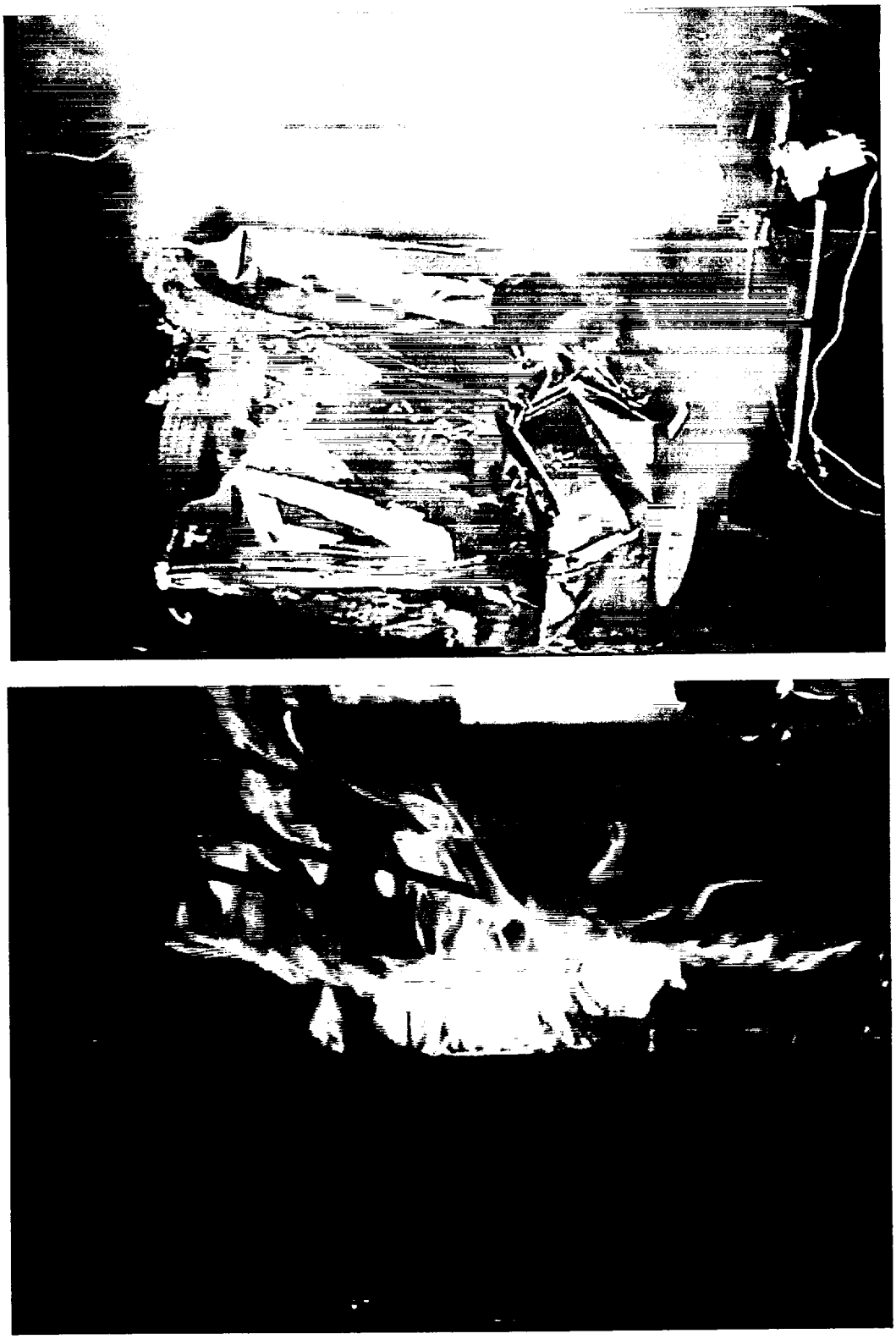

Figure 19. Fire Test F99030A. Video stills from Video Cameras 4 (upper) and 5 (lower) at 75 seconds post-ignition.

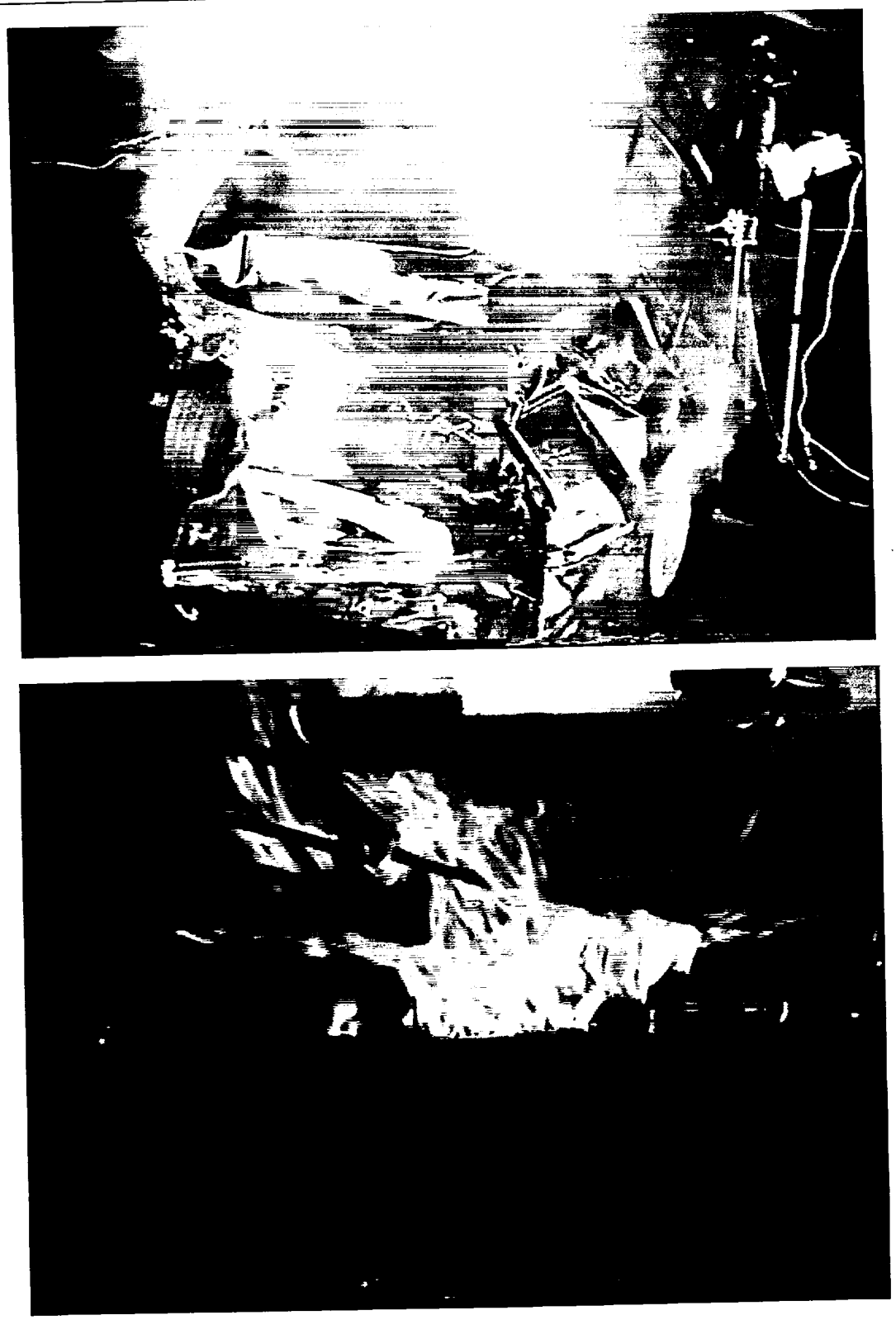

Figure 20. Fire Test F99030A. Video stills from Video Cameras 4 (upper) and 5 (lower) at 90 seconds post-ignition.

Figure 21. Fire Test F99030A. Video stills from Video Cameras 4 (upper) and 5 (lower) at 120 seconds post-ignition.

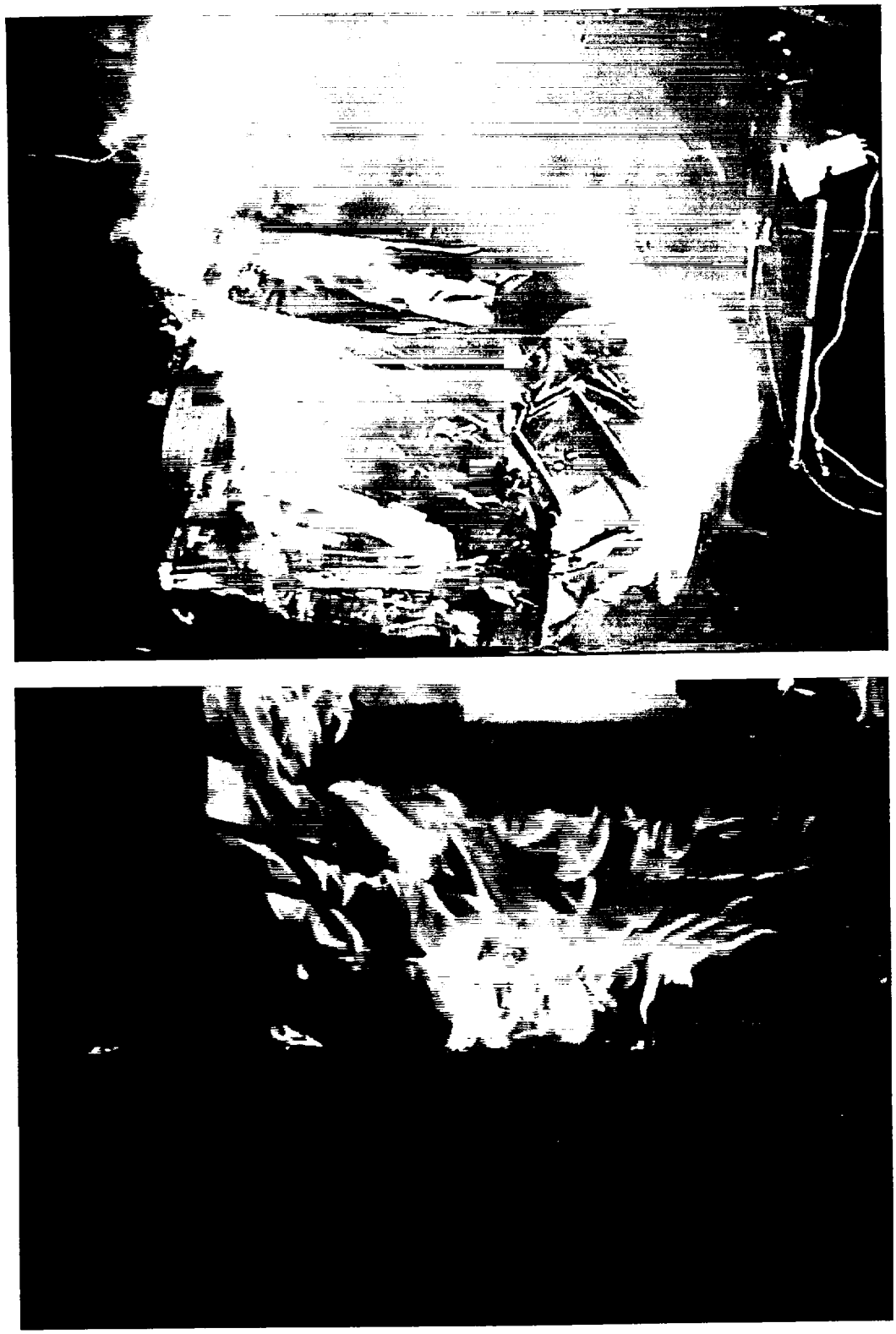

Figure 22. Fire Test F99030A. Video stills from Video Cameras 4 (upper) and 5 (lower) at 138 seconds post-ignition.

The diameter of flames at the cement board surface and the volume of flames impinging on the underbody of the test vehicle decreased after the flow of gasoline from the tubing at the top of the fuel tank was discontinued.

The decrease in the estimated flame diameter at the surface of the cement board from approximately 82 to 36 cm between the time of ignition and 60 seconds post-ignition was attributed to an increase in the burning rate of liquid gasoline flowing downward on underbody components in the test vehicle. After ignition, liquid gasoline in contact with the fuel tank and rear suspension sub-frame would have been heated by the fire, increasing the vaporization rate from liquid gasoline on underbody components in the test vehicle. An increased vaporization rate would have resulted in a decrease in the volume flow rate of liquid gasoline onto the cement board surface and, consistent with the decrease in the diameter of flames on the cement board surface observed in Figure 12, a decrease in the size of the gasoline pool under the test vehicle as this test progressed. An increased vaporization rate from liquid gasoline in contact with underbody components also would have resulted in an increase in the volume of flames in spaces along the test vehicle underbody as this test progressed, which is evident in the video stills from Camera 5 in Figures 13 through 22.

From 60 to 140 seconds post-ignition, the flame diameter at the cement board surface decreased from approximately 36 to 31 cm (Fig. 12). The distribution of flames on the test vehicle underbody did not appear to increase appreciably during this time (Fig.'s 18 through 22). These observations suggest that the vaporization rate from liquid gasoline in contact with components on the vehicle underbody and flow rate of liquid gasoline onto the cement board surface were approximately constant during this time interval.

5 Flame-Spread into the Passenger Compartment

Flames spread into the passenger compartment through the crash-induced seam openings around the left and right wheelhouses simultaneously. Flames entering the passenger compartment through a crash-induced seam opening between the left rear wheelhouse panel and left rear inner quarter panel ignited the left side of the rear seat back, the left rear seat belt, and the left side of the rear shelf trim panel. Flames entering the trunk through a crash-induced seam opening between the left rear wheelhouse and floor panel ignited the trunk floor panel, the interior trim panel on the left side of the trunk, the left speaker in the rear shelf, and the grille over the speaker. Flames entering the passenger compartment through crash-induced seam openings between the right wheelhouse and the right inner quarter panel ignited the right rear seat back bolster and the interior trim panel on the right rear pillar.

Figures 23 through 32 show a series of video stills from Camera 1 and Infrared thermograms from IR8 at 0, 10, 15, 30, 45, 60, 75, 90, 120, and 153 seconds post-ignition. This sequence of video stills shows the approximate timing of flame-spread to the area around the rear wheelhouses and into the passenger compartment. Although a temperature scale for these thermograms from IR8 is not available, the Infrared thermograms in Figures 23 through 32 show the areas in the test vehicle that were exposed to heated gases and flames. For example, smoke (video still, Fig. 24) and heated gases (Infrared thermogram, Fig. 24) had started to vent from both wheelhouses by 10 seconds post-ignition. Smoke and heated gases were also observed behind the rear surface of the rear seat back at this time (Fig. 24). Flames were visible in the area between the left side of the floor panel in the trunk and the inboard side of the left rear tire by 15 seconds post-ignition (Fig. 25). The height of this fire plume increased between 15 and 60 seconds post-ignition (Fig.'s 25 through 28). The Infrared thermograms in Figures 25 through 28 show that, although this fire plume did not contact the trunk lid directly during this time, it did heat the left rear area of the deformed trunk lid. Flames had begun to vent from the right rear wheelhouse by 75 seconds post-ignition (Fig. 29) and from the left rear wheelhouse by 90 seconds post-ignition (Fig. 30). The height of the fire plumes venting from the rear wheelhouses increased until the fire was extinguished starting at about 155 seconds post-ignition (Fig.'s 29 through 32).

Flames also began to contact the rear surface of the left side of the rear seat back between 75 and 90 seconds post-ignition (Fig.'s 29 and 30). Flames were visible on the lower surface of the roof trim panel through the upper left corner of the rear window opening by 120 seconds post-ignition (Fig. 31) and venting from the passenger compartment along the rear edge of the roof by 153 seconds post-ignition (Fig. 32).

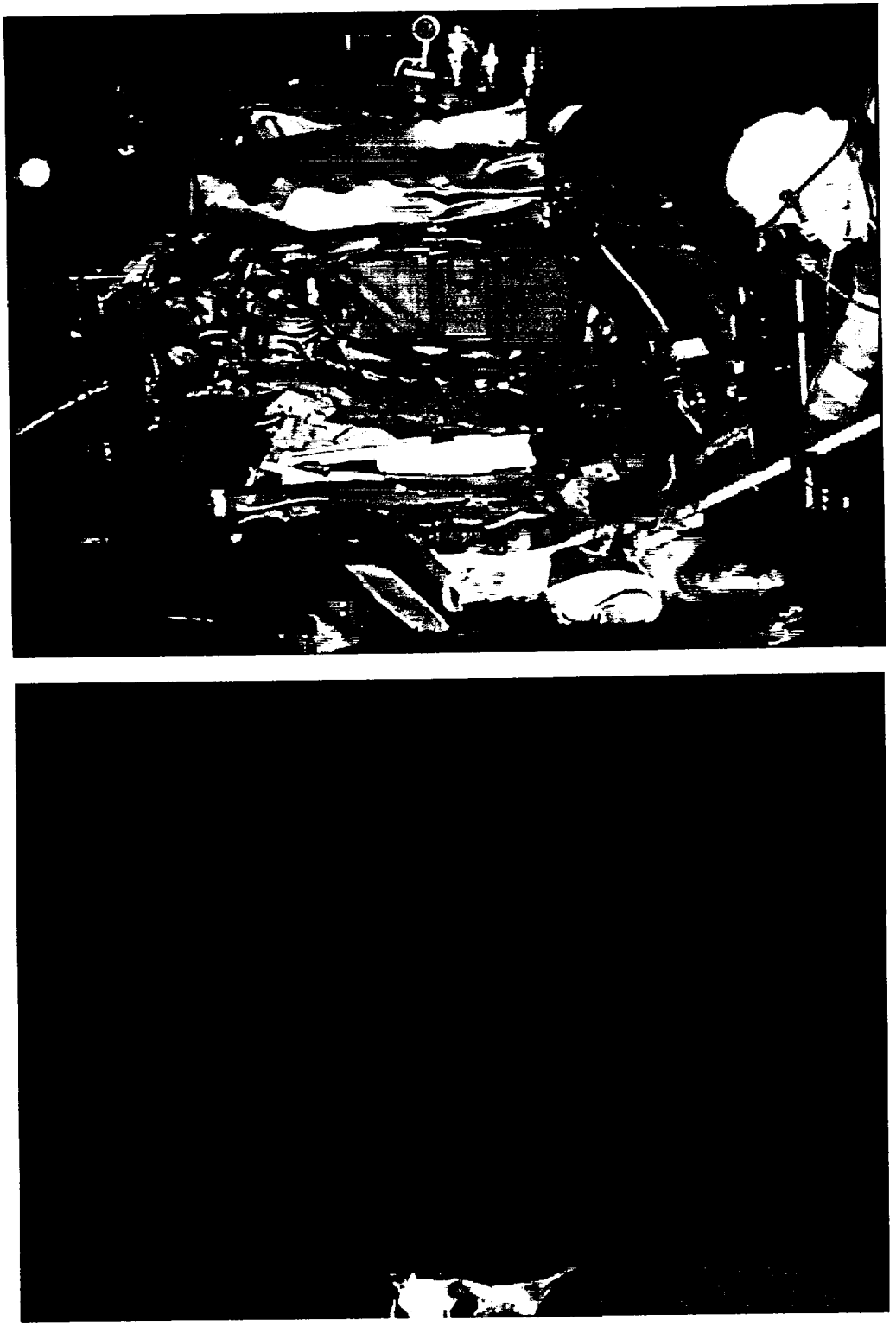

Figure 23. Fire Test F99030A. Video still from Video Camera 1 (upper) and Infrared thermogram from IR8 (lower) at the time of ignition (0 seconds post-ignition).

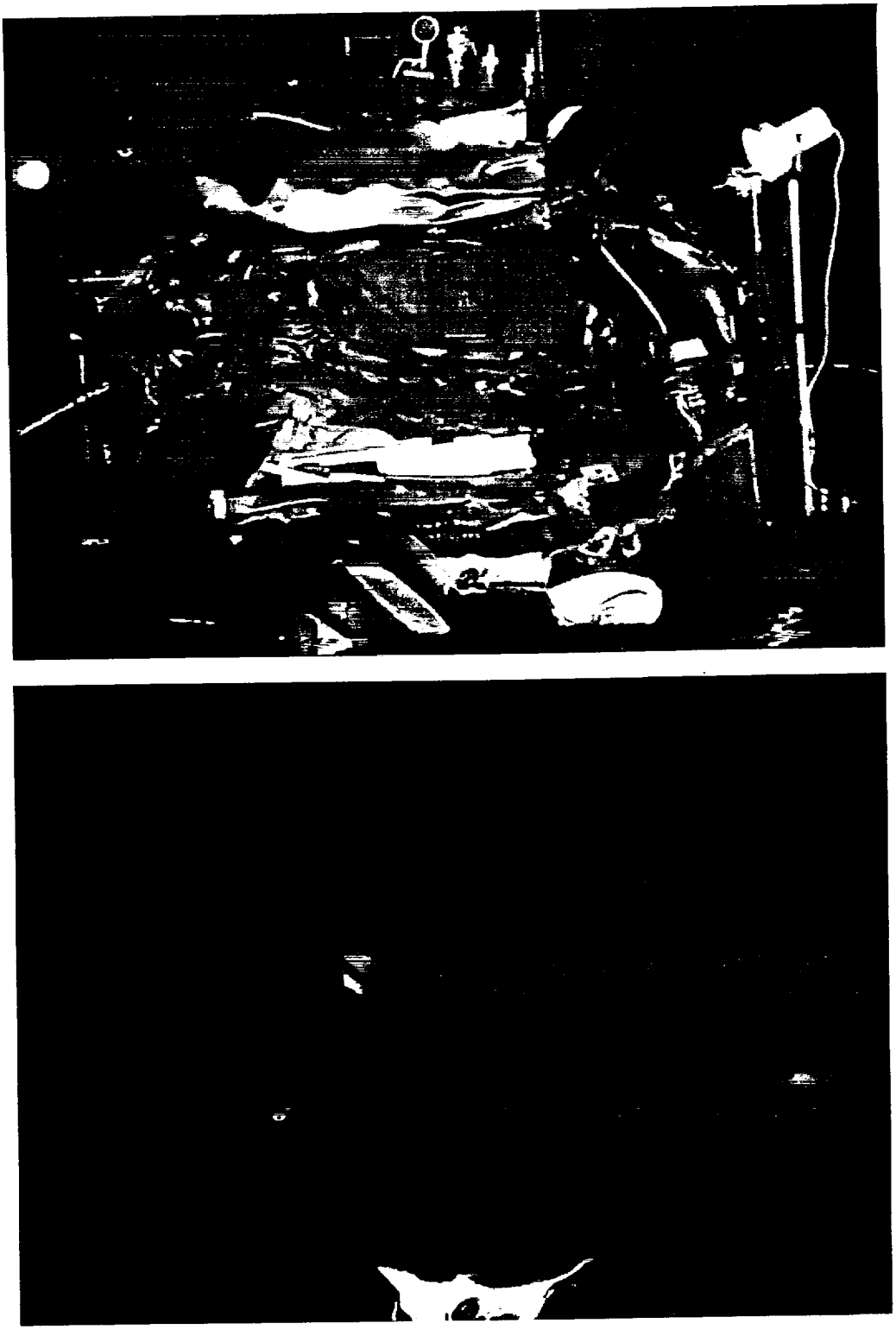

Figure 24. Fire Test F99030A. Video still from Video Camera 1 (upper) and Infrared thermogram from IR8 (lower) at 10 seconds post-ignition.

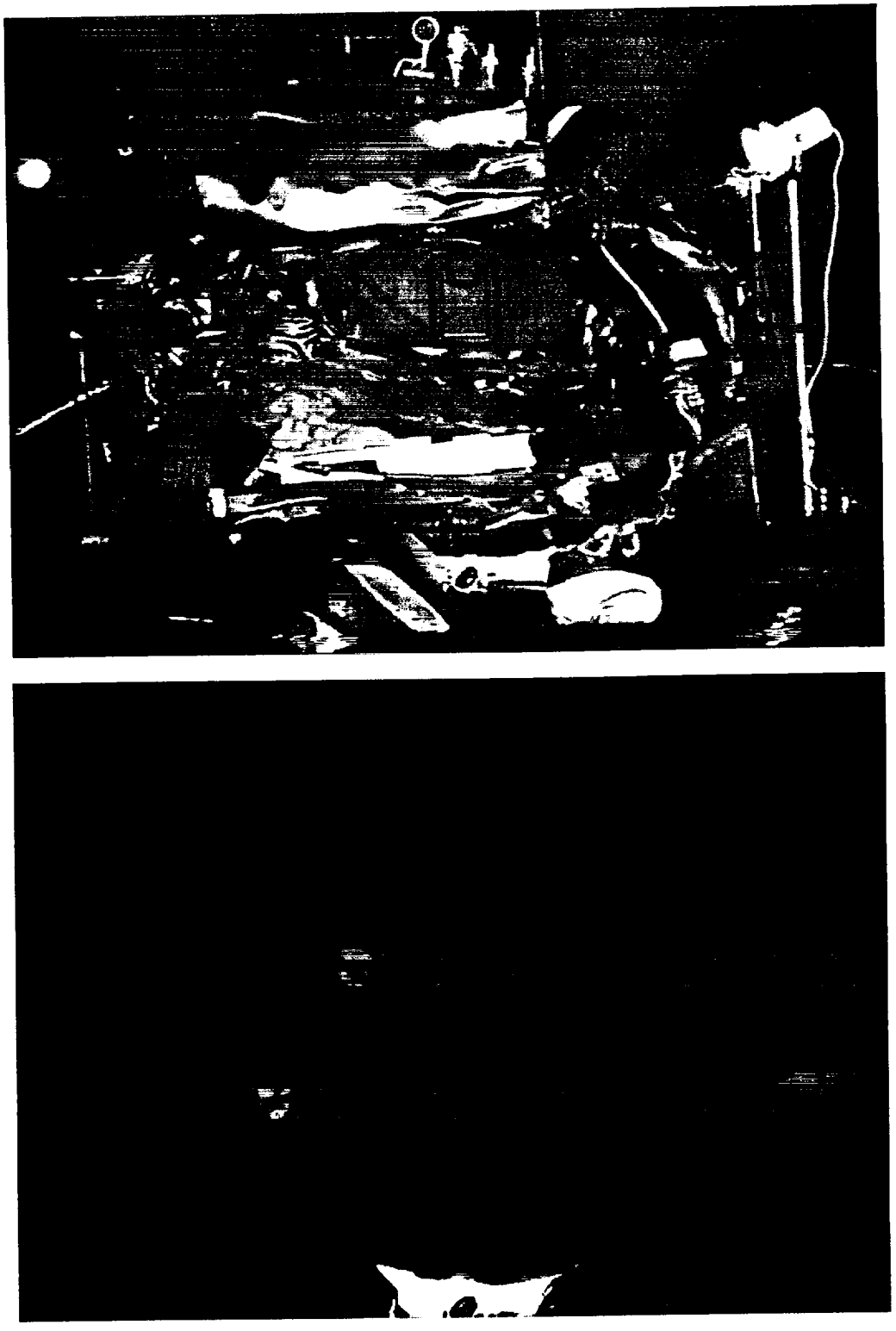

Figure 25. Fire Test F99030A. Video still from Video Camera 1 (upper) and Infrared thermogram from IR8 (lower) at 15 seconds post-ignition.

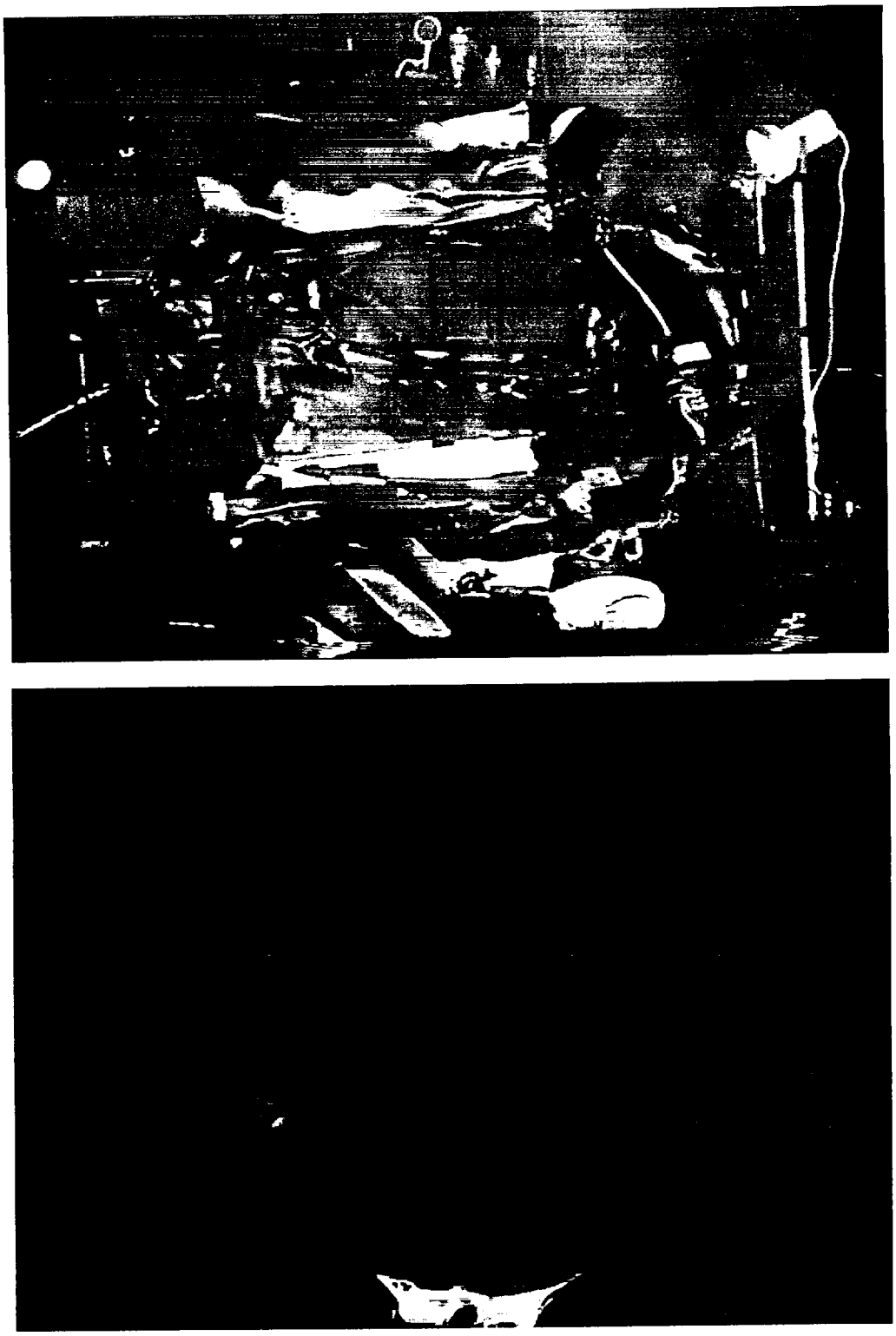

Figure 26. Fire Test F99030A. Video still from Video Camera 1 (upper) and Infrared thermogram from IR8 (lower) at 30 seconds post-ignition.

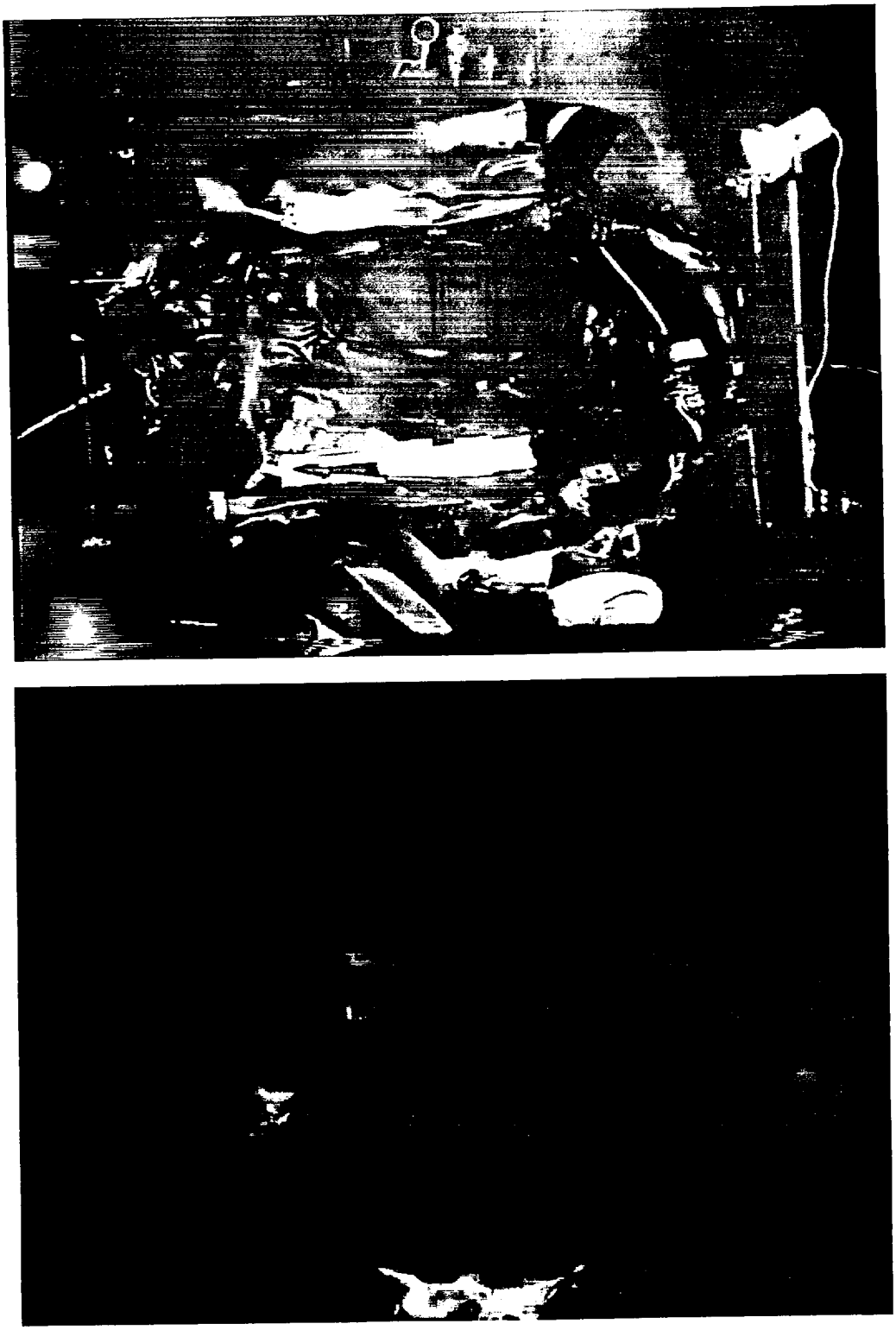

Figure 27. Fire Test F99030A. Video still from Video Camera 1 (upper) and Infrared thermogram from IR8 (lower) at 45 seconds post-ignition.

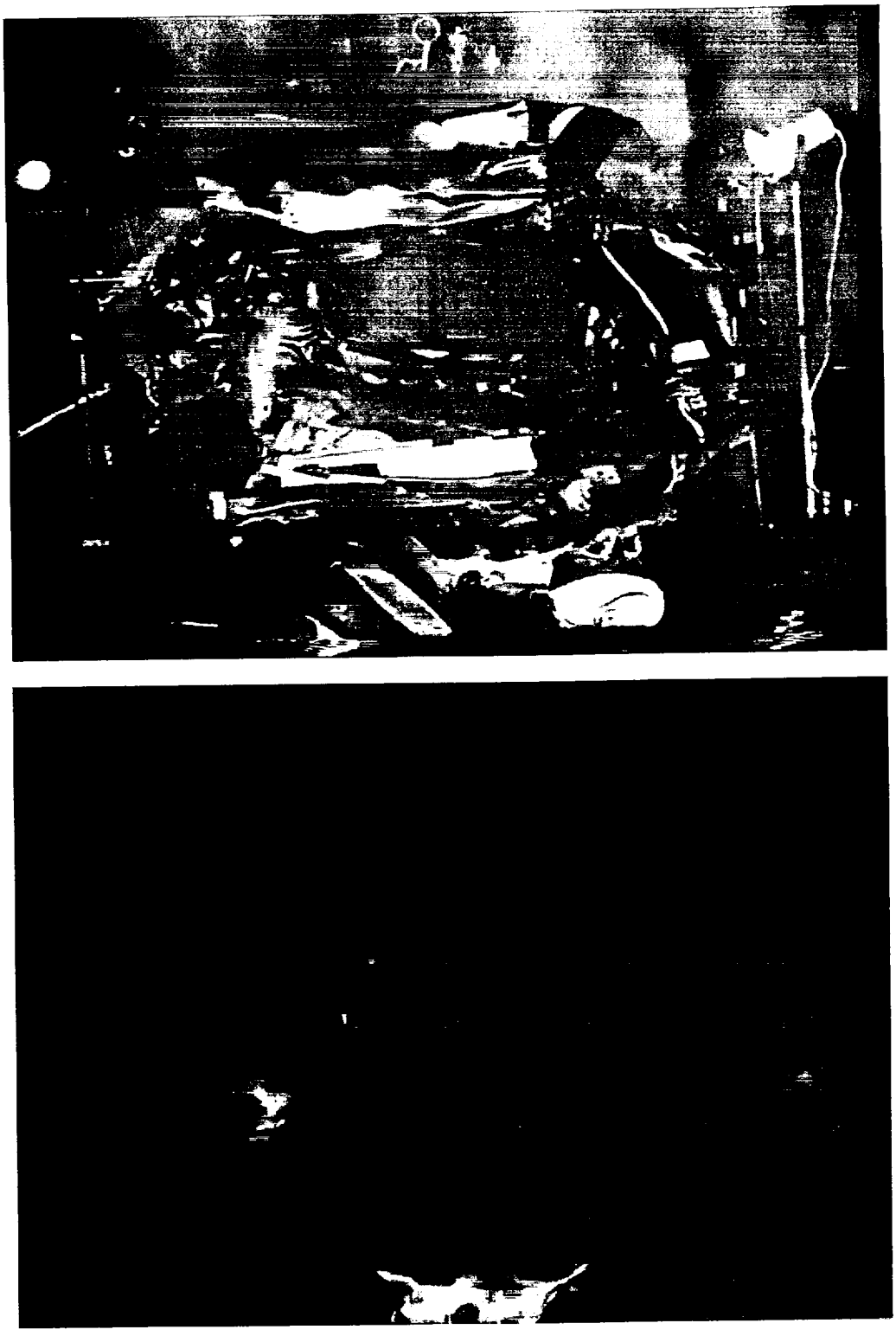

Figure 28. Fire Test F99030A. Video still from Video Camera 1 (upper) and Infrared thermogram from IR8 (lower) at 60 seconds post-ignition.

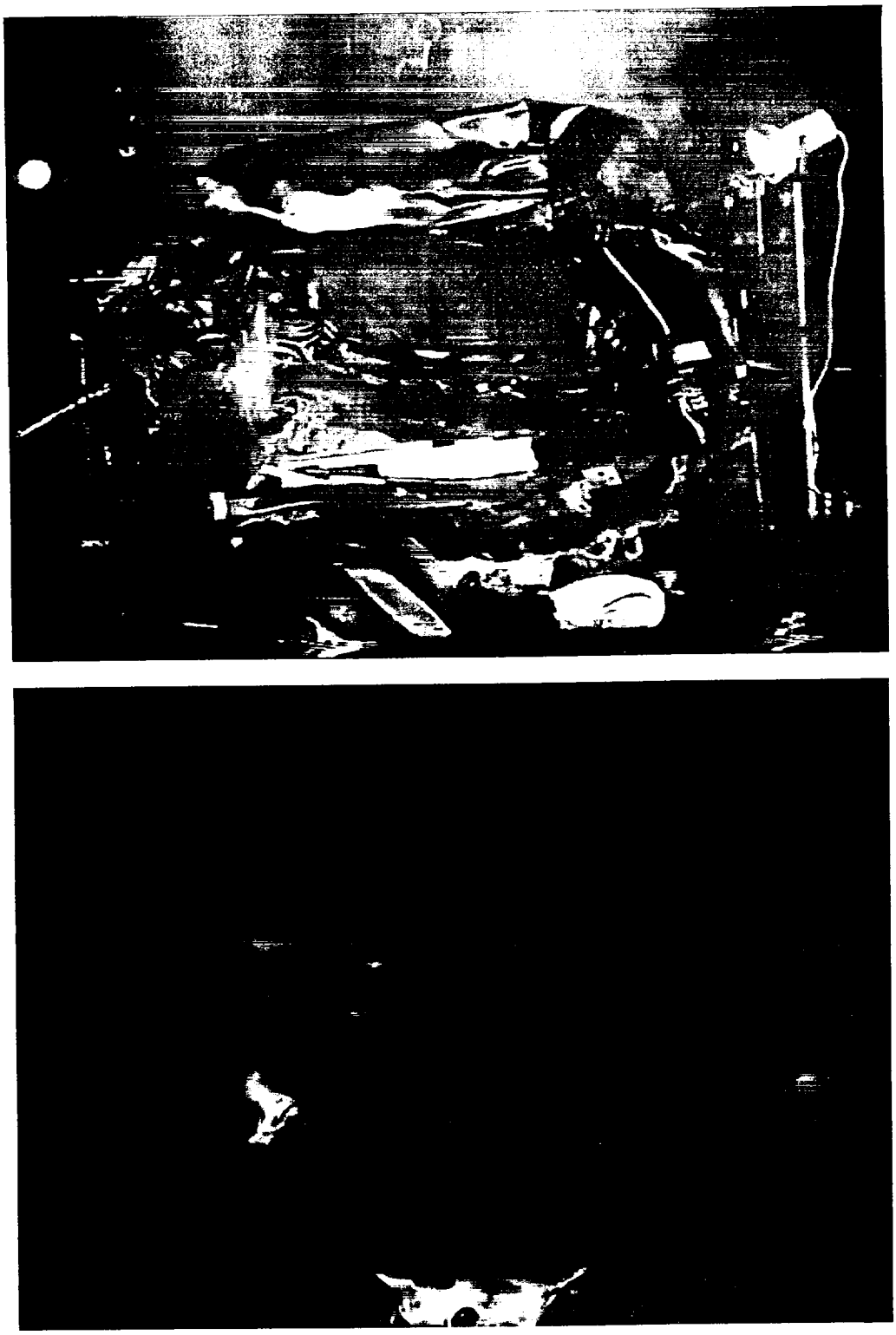

Figure 29. Fire Test F99030A. Video still from Video Camera 1 (upper) and Infrared thermogram from IR1 (lower) at 75 seconds post-ignition.

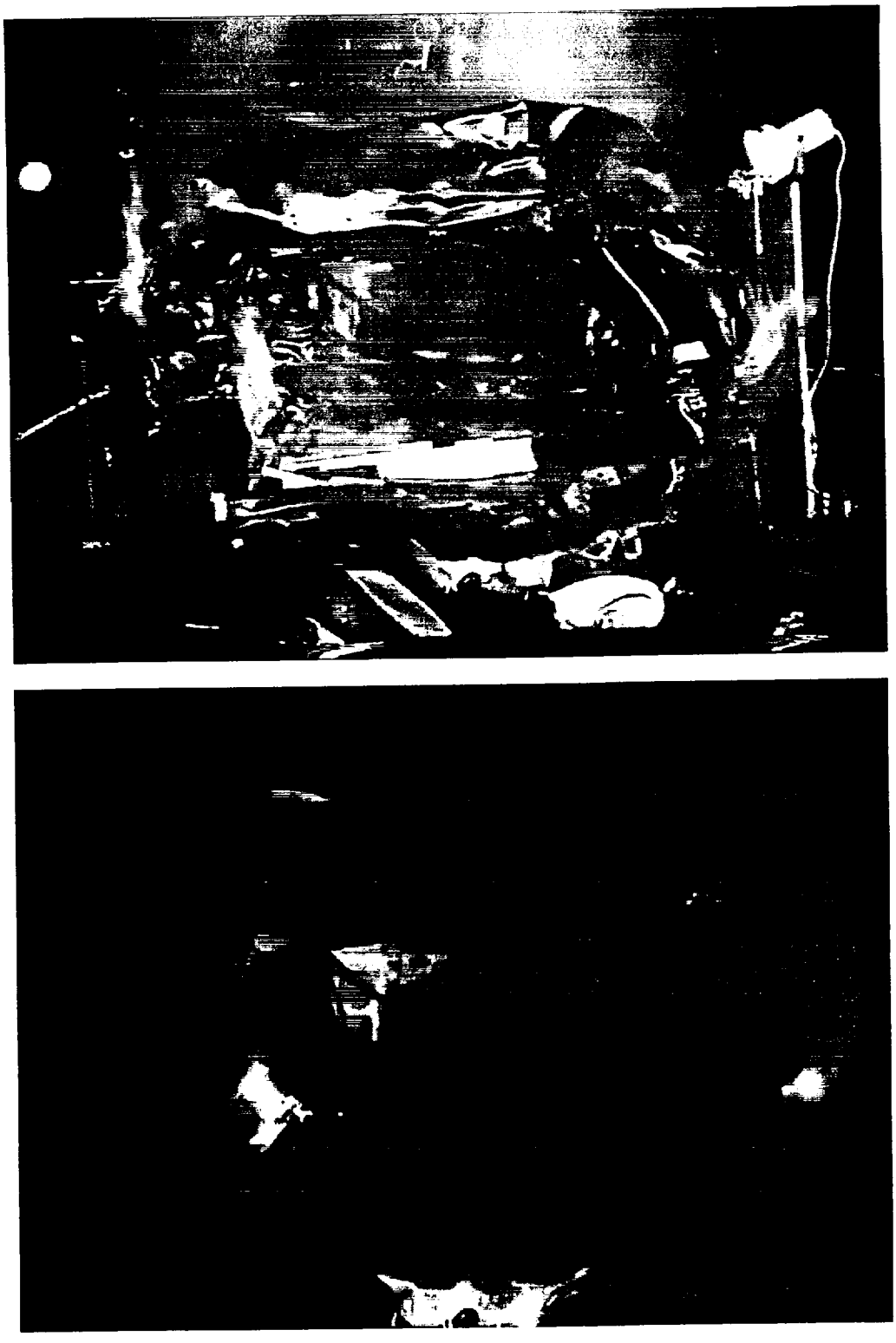

Figure 30. Fire Test F99030A. Video still from Video Camera 1 (upper) and Infrared thermogram from IR8 (lower) at 90 seconds post-ignition.

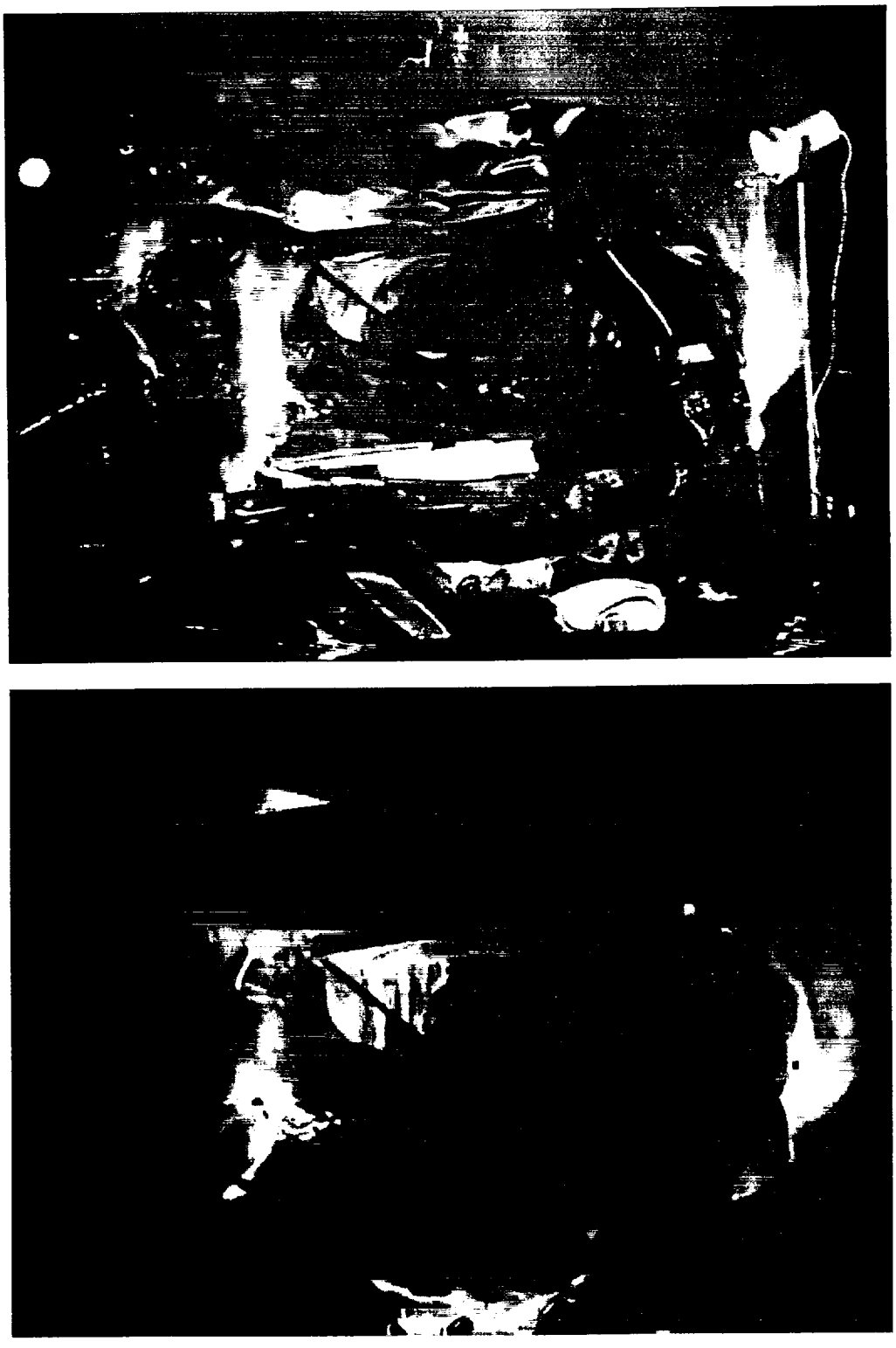

Figure 31. Fire Test F99030A. Video still from Video Camera 1 (upper) and Infrared thermogram from IR8 (lower) at 120 seconds post-ignition.

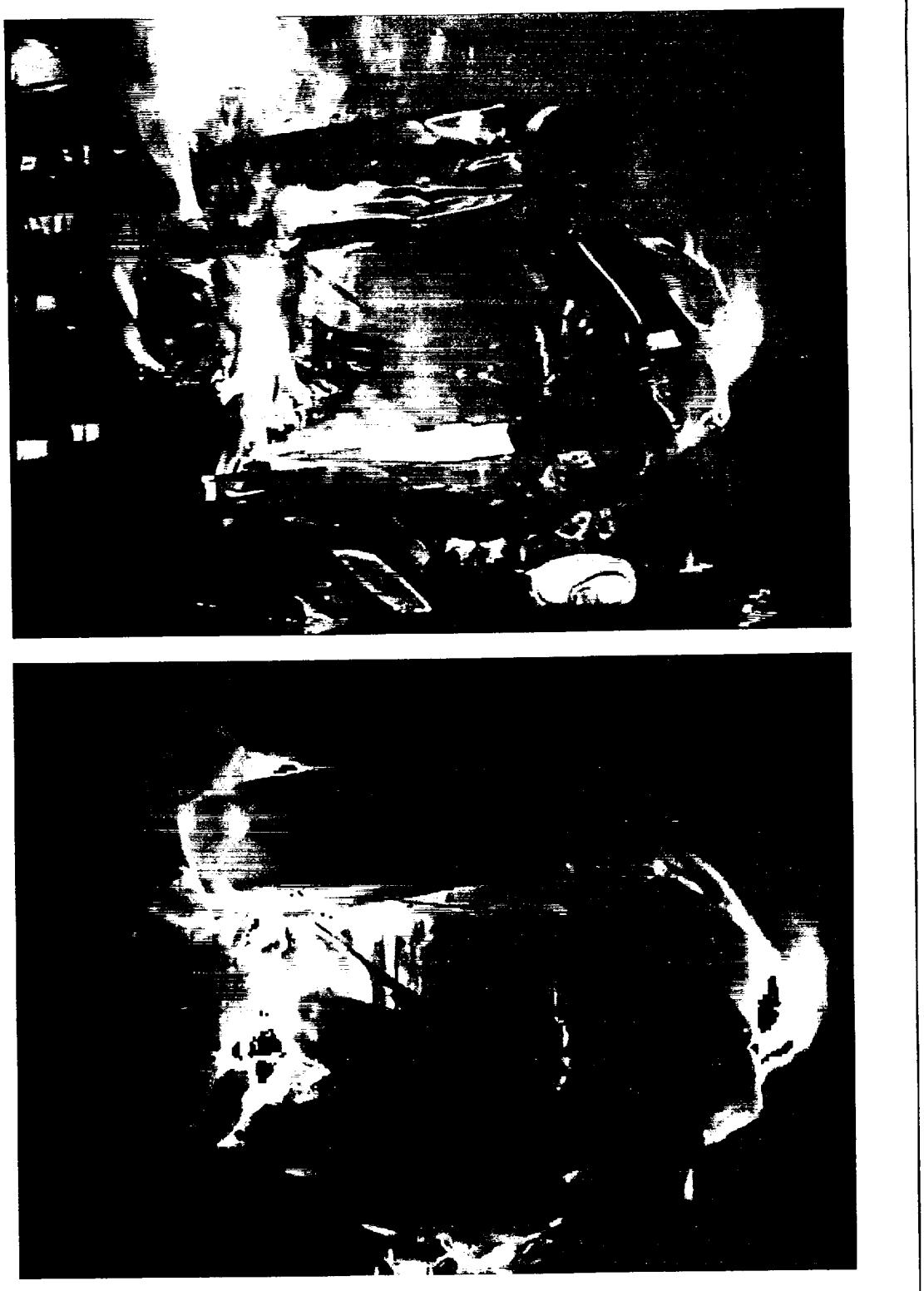

Figure 32. Fire Test F99030A. Video still from Video Camera 1 (upper) and Infrared thermogram from IR8 (lower) at 153 seconds post-ignition.

5.1 Flame-Spread Through Crash-Induced Seam Openings Around the Left Rear Wheelhouse

Data recorded from heat flux transducers and thermocouples in the test vehicle indicate that flames started to spread into the passenger compartment through a crash-induced seam opening between the left rear wheelhouse panel and the left inner quarter panel between 20 and 30 seconds post-ignition. Figure 33 shows the approximate locations of thermocouples in this seam opening and of a heat flux transducer in the left rear wheelhouse panel.

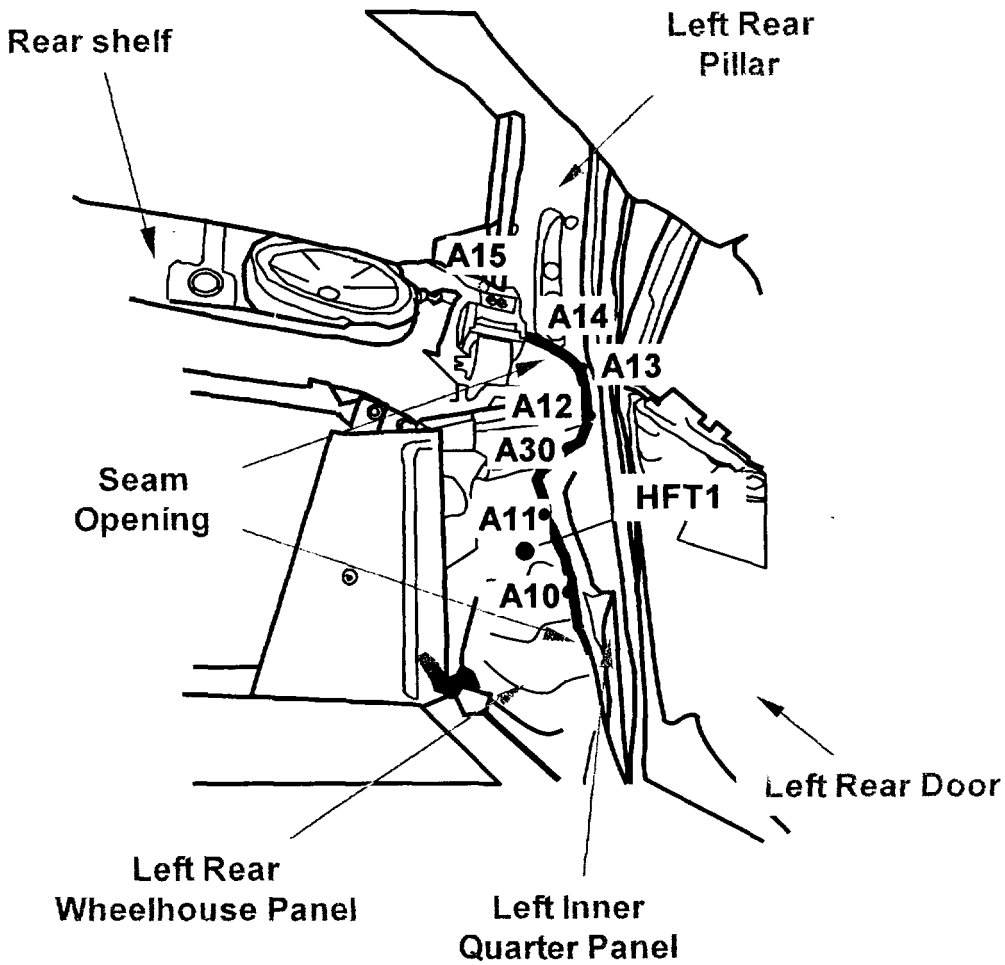

Figure 33. Diagram showing the approximate locations of thermocouples in a crash-induced seam opening between the left rear wheelhouse panel and the left inner quarter panel and a heat flux transducer in the left rear wheelhouse panel.

Thermocouples A10, A11, A12, A13, A14, A15, and A30 were located in the crash-induced seam opening between the left rear wheelhouse panel and the left inner quarter panel (see Appendix C). Heat Flux Transducer HFT1 was mounted to the front of the left rear wheelhouse panel of the test vehicle (see Appendix E). The body of this transducer was inserted through a clearance hole drilled in the wheelhouse panel and mounted on stand-offs. The transducer face was flush with the exterior surface of the wheelhouse panel and facing the left rear tire.

Figure 34 shows plots of temperature data recorded from Thermocouples A10 and A11, and heat flux data recorded from Heat Flux Transducer HFT1.

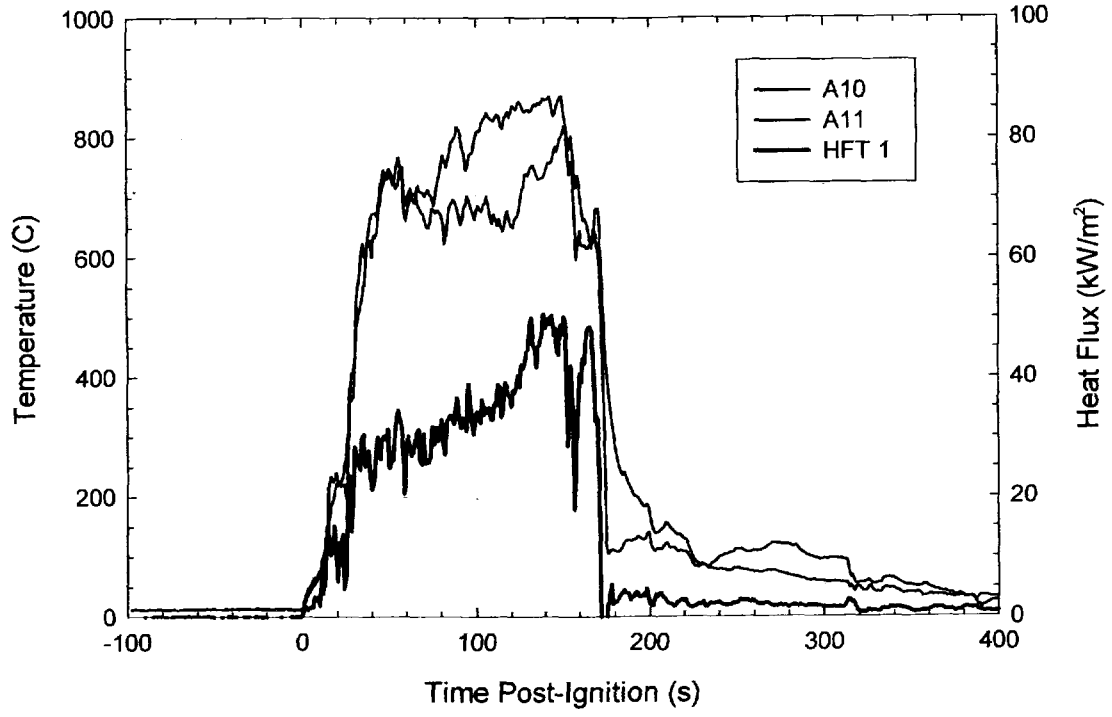

Figure 34. Fire Test F99030A. Plots of data recorded from Thermocouples A10 and A11, and from Heat Flux Transducer HFT1.

The heat flux to the section of the wheelhouse panel adjacent to the crash-induced seam opening between the left rear wheelhouse panel and the left inner quarter panel increased from 0 kW/m^2 at the time of ignition to 25 - 30 kW/m^2 by 30 seconds post-ignition (Fig. 34), indicating flames had spread into this area of the wheelhouse during the first ½ minute after ignition. The heat flux recorded from Heat Flux Transducer HFT1 increased to approximately 50 kW/m^2 by the time the fire in the test vehicle was extinguished (Fig. 34), indicating that flames were present in this area of the left rear wheelhouse continuously from about 30 seconds post-ignition until the end of this test.

Temperature data recorded from Thermocouples A10 and A11 indicate that heated gases started to enter the lower section of this seam opening within a few seconds after ignition. For example, temperatures recorded from these thermocouples increased from the ambient temperature before ignition to 79 and 73°C, respectively, by 10 seconds post-ignition and 223 and 162°C, respectively, by 15 seconds post-ignition (Fig. 34). Temperatures recorded from these thermocouples exceeded 600°C between 30 and 40 seconds post-ignition and remained greater than 600°C until about 175 seconds post-ignition (Fig. 34), indicating flames were present in the lower section of this seam-opening continuously from about 15 seconds post-ignition to the end of this test.[1]

Figure 35 shows plots of temperature data recorded from Thermocouples A12, A13, A14, A15, and A30.

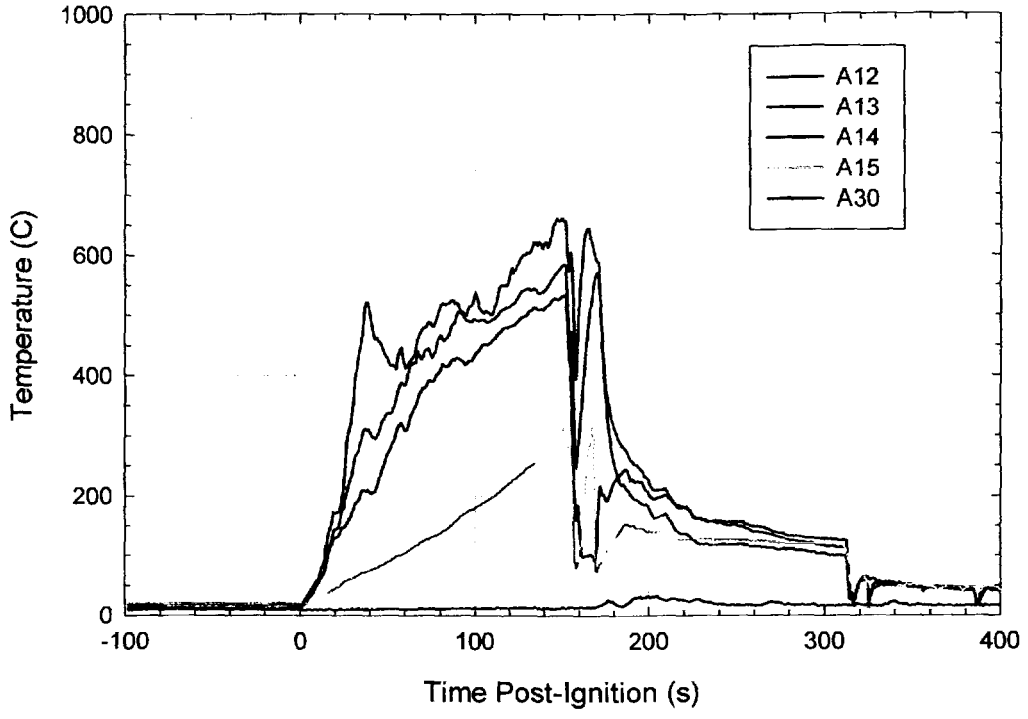

Figure 35. Fire Test F99030A. Plots of data recorded from Thermocouples A10 and A11, and from Heat Flux Transducer HFT1.

The timing of flame-spread into the passenger compartment through the upper section of the crash-induced seam opening between the left rear wheelhouse panel and the left inner quarter panel is more difficult to assess from the temperature data recorded from Thermocouples A12,

[1] As in previous reports, a value of 600°C was used in this report as the threshold to indicate the presence of flame.

A13, A14, and A30. The temperatures recorded from these thermocouples were 56, 47, 47, 25, and 9°C, respectively, at 10 seconds post-ignition and were 120, 91, 86, 34, and 9°C, respectively, at 15 seconds post-ignition (Fig. 35). These temperatures were less than the temperatures recorded from Thermocouples A10 and A11 at 10 and 15 seconds post-ignition, indicating that the flow of heated gases through the upper sections of this seam opening during the first 15 seconds of this test was less than the flow of heated gases through the lower section. Temperature data recorded from Thermocouple A12 was > 600°C between 128 and 153 seconds post-ignition (Fig. 35). Temperature data recorded from Thermocouples A13, A14, A15, and A30 did not exceed the 600°C threshold used here to indicate flames at any time during this test (Fig. 35), indicating that flames did not spread into the passenger compartment through the upper section of the crash-induced seam opening between the left rear wheelhouse panel and the left inner quarter panel.

This assessment of where flames-spread from the left rear wheelhouse into the passenger compartment through the crash-induced seam opening between the wheel house panel and the quarter panel is consistent with the pattern of heat and fire damage observed in the test vehicle after this test. Figure 36 is a photograph of the left rear wheelhouse in the test vehicle after this test.

Figure 36. Fire Test F99030A. Photograph of the left rear wheelhouse in the test vehicle after this fire test.

The pattern of fire damage is consistent with the greatest flame exposure on the forward lower section of the exterior surface of the wheelhouse panel (Fig. 36). This is the area where Thermocouples A10 and A11 were located in the crash-induced seam opening.

Figure 37 shows the approximate locations of thermocouples in a crash-induced seam opening between the left rear wheelhouse and the floor panel, above the rear edge of the rear shelf, and above the left speaker in the rear shelf.

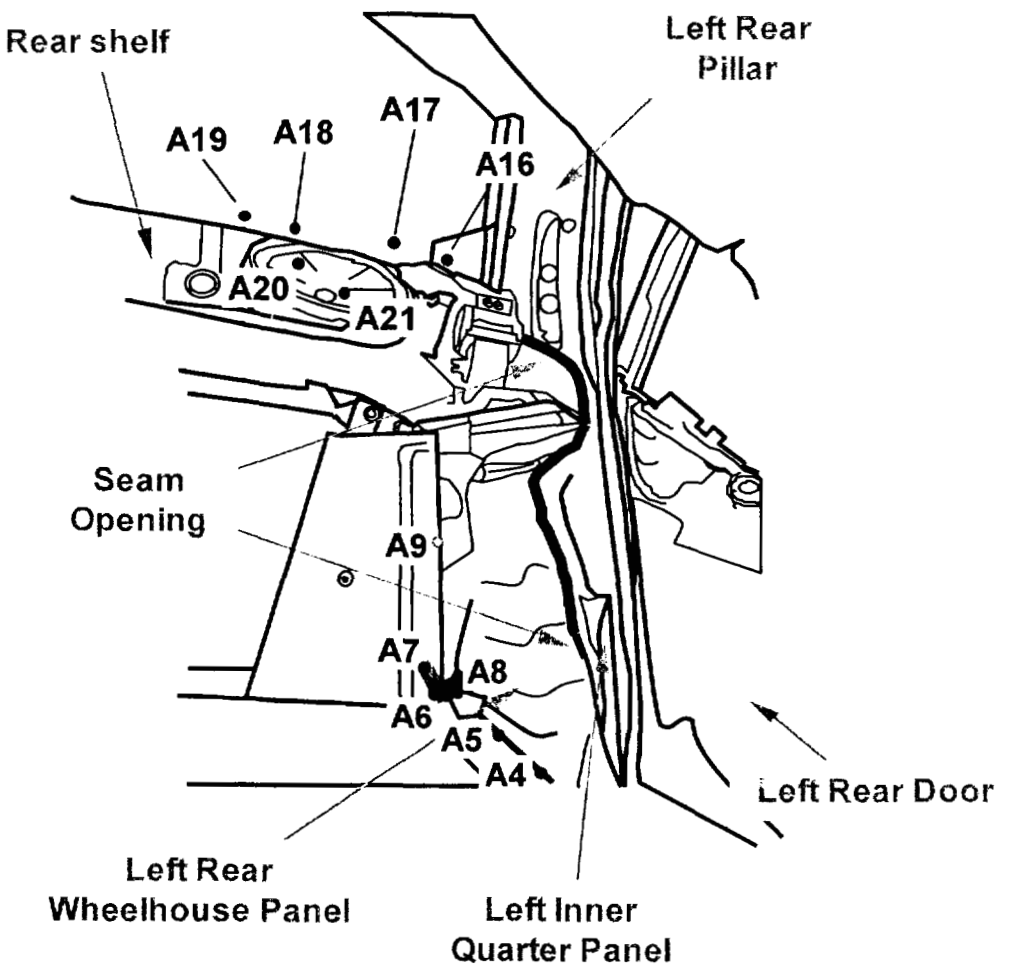

Figure 37. Fire Test F99030A. Diagram showing the approximate locations of thermocouples in a crash-induced seam opening between the left rear wheelhouse panel, the floor panel, above the rear edge of the rear shelf, and, above the left speaker in the rear shelf.

Thermocouples A4, A5, A6, A7, and A8 were located in the crash-induced seam opening between the left rear wheelhouse panel and the floor panel (see Appendix C). Thermocouples

A4, A5, and A8 were in the passenger compartment. Thermocouples A1 and A7 and A9 were in the trunk. Thermocouple A9 was located in a cavity formed by the deformed left quarter panel and the left rear seat back support. Thermocouples A16, A17, A18, and A19 were located above the rear edge of the left side of the rear shelf (see Appendix C). Thermocouples A20 and A21 were located above the cone in the left speaker in the rear shelf (see Appendix C).

Figure 38 shows plots of temperature data recorded from Thermocouples A4, A5, A6, A7, A8, and A9. Figure 39 shows plots of data recorded from Thermocouples A16, A17, A18, and A19. Figure 39 shows plots of data recorded from Thermocouples A20 and A21.

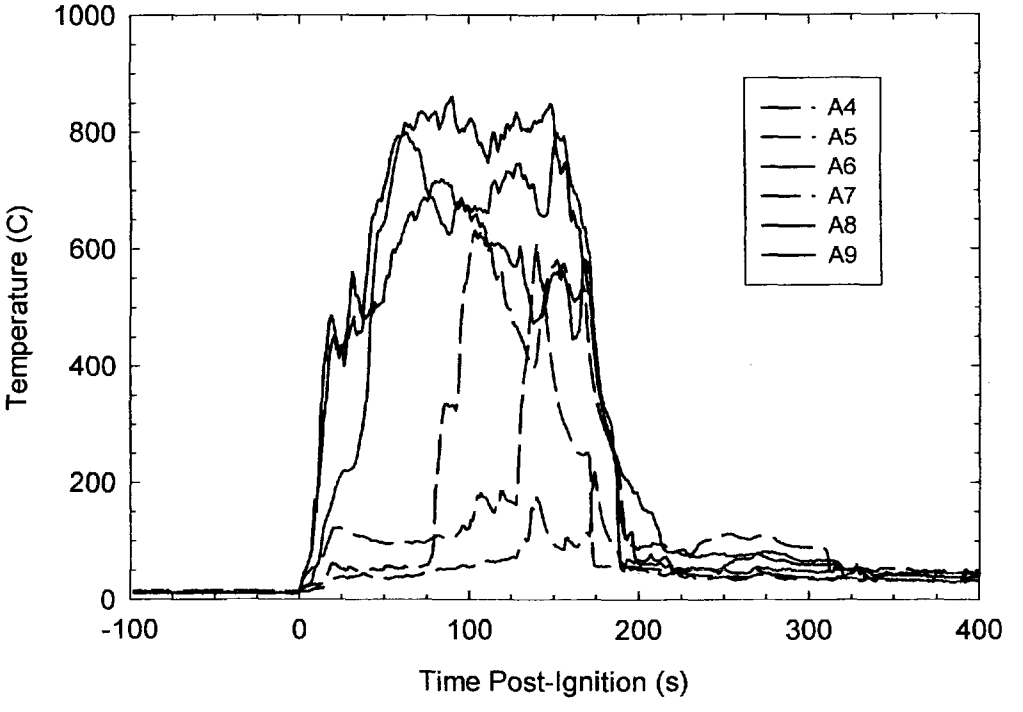

Figure 38. Fire Test F99030A. Plots of temperature data recorded from Thermocouples A4, A5, A6, A7, A8, and A9.

Temperature data recorded from Thermocouples A4 through A8 started to increase from ambient temperatures by 5 seconds post-ignition (Fig. 38). Temperature data recorded from Thermocouples A6 and A8 exceeded 600°C at 57 and 41 seconds post-ignition, respectively (Fig. 38). Temperature data recorded from Thermocouple A9 exceeded 600°C at 45 seconds post-ignition (Fig. 38). Temperature data recorded from Thermocouple A7 exceeded 600°C approximately 100 seconds post-ignition and temperature data recorded from Thermocouples A4 and A5 did not exceed 600°C at any time during this test (Fig. 38).

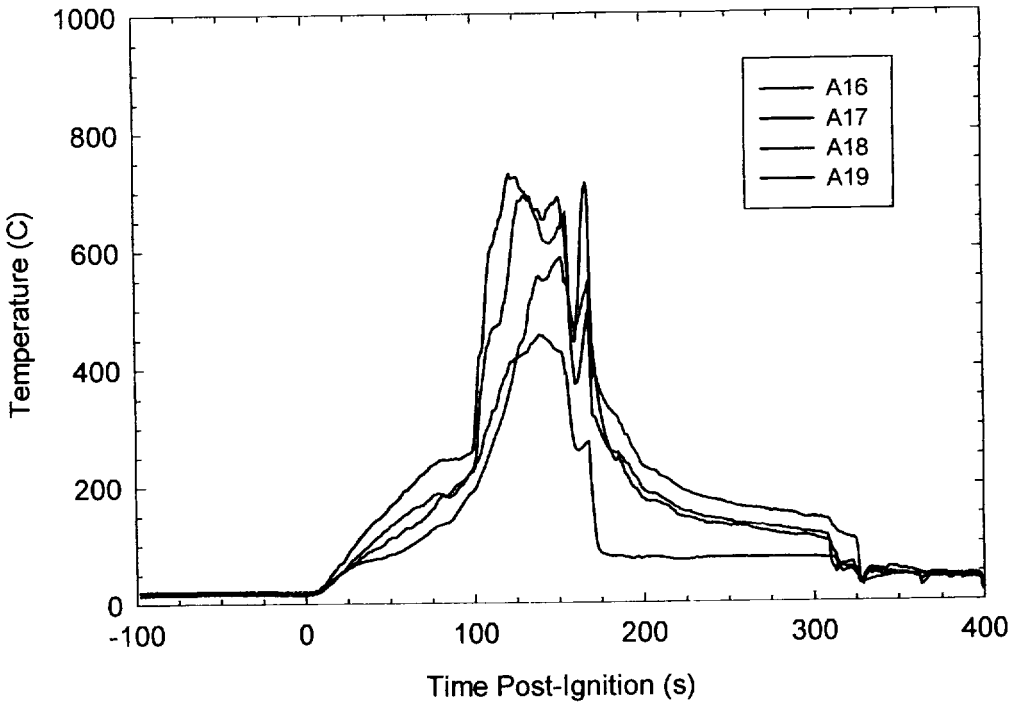

Figure 39. Fire Test F99030A. Plots of temperature data recorded from Thermocouples A16, A17, A18, and A19.

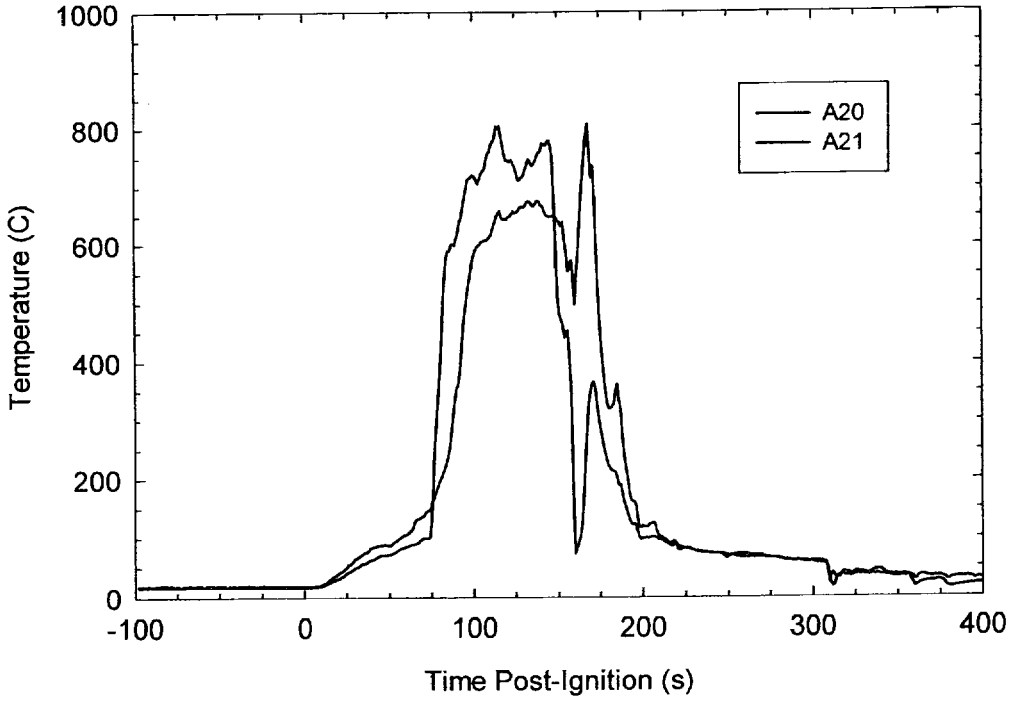

Figure 40. Fire Test F99030A. Plots of temperature data recorded from Thermocouples A16, A17, A18, and A19.

Temperature data recorded from Thermocouples A17 and A18 exceeded 600°C at about 111 and 123 seconds post-ignition, respectively (Fig. 39). Temperature data recorded from Thermocouples A16 and A19 did not exceeded 600°C at any time during this test (Fig. 39). Temperature data recorded from Thermocouples A20 and A21 exceeded 600°C at 87 and 108 seconds post-ignition, respectively (Fig. 40).

This temperature data indicates that heated gases started to enter the passenger compartment and trunk of the test vehicle through the crash-induced seam opening between the left rear wheelhouse panel and floor panel by 5 seconds post-ignition. Flames spread into the passenger compartment through this seam opening between 35 and 45 seconds post-ignition and into the trunk between 50 and 60 seconds post-ignition. Flame temperatures were recorded by the thermocouple in the cavity formed by the deformed left quarter panel and the left rear seat back support between 40 and 50 seconds post-ignition. Flames burned through the speaker cone in the speaker in the left side of the rear shelf between 80 and 110 seconds post-ignition. Flames were present along the left side of the rear edge of the rear shelf starting at about 110 seconds post-ignition.

This assessment of flame-spread in the left rear area of the passenger compartment and left front area of the trunk is consistent with the video and infrared camera record and the pattern of heat and fire damage observed on the right quarter trim panel after this test. For example, smoke and heated gases were in an area behind the left side of the rear seat back by 10 seconds post-ignition (Fig. 24) and flames were in this area by 90 seconds post-ignition (Fig. 30).

Figures 41 through 46 show a series of video stills from Camera 9 and infrared thermograms from IR2 at 0, 30, 60, 90, 120, and 138 seconds post-ignition. Both Camera 9 and IR2 show views of the interior of the test vehicle through the rear left window. These video stills and infrared thermograms show smoke and heated gases venting from the space behind the left rear seat bolster by 30 seconds post-ignition (Fig. 42), and flames in this area on the tops of the left side of the rear seat back and left rear seat bolster at 90 seconds post-ignition (Fig. 44). These figures also show flames burning through the left speaker grille in the rear shelf trim panel between 90 and 120 seconds post-ignition (Fig.'s 44 and 45). Flames had emerged between the left side of the rear seat back and the left rear seat bolster by 138 seconds post-ignition (Fig. 46).

Figure 46 is a photograph of the interior of the test vehicle through the rear left window after this test. Sections of the fabric cover on the tops of the left side of the rear seat back and left rear seat bolster are discolored and burned (Fig. 47). The left speaker grille in the rear shelf trim panel was consumed by fire (Fig. 47).

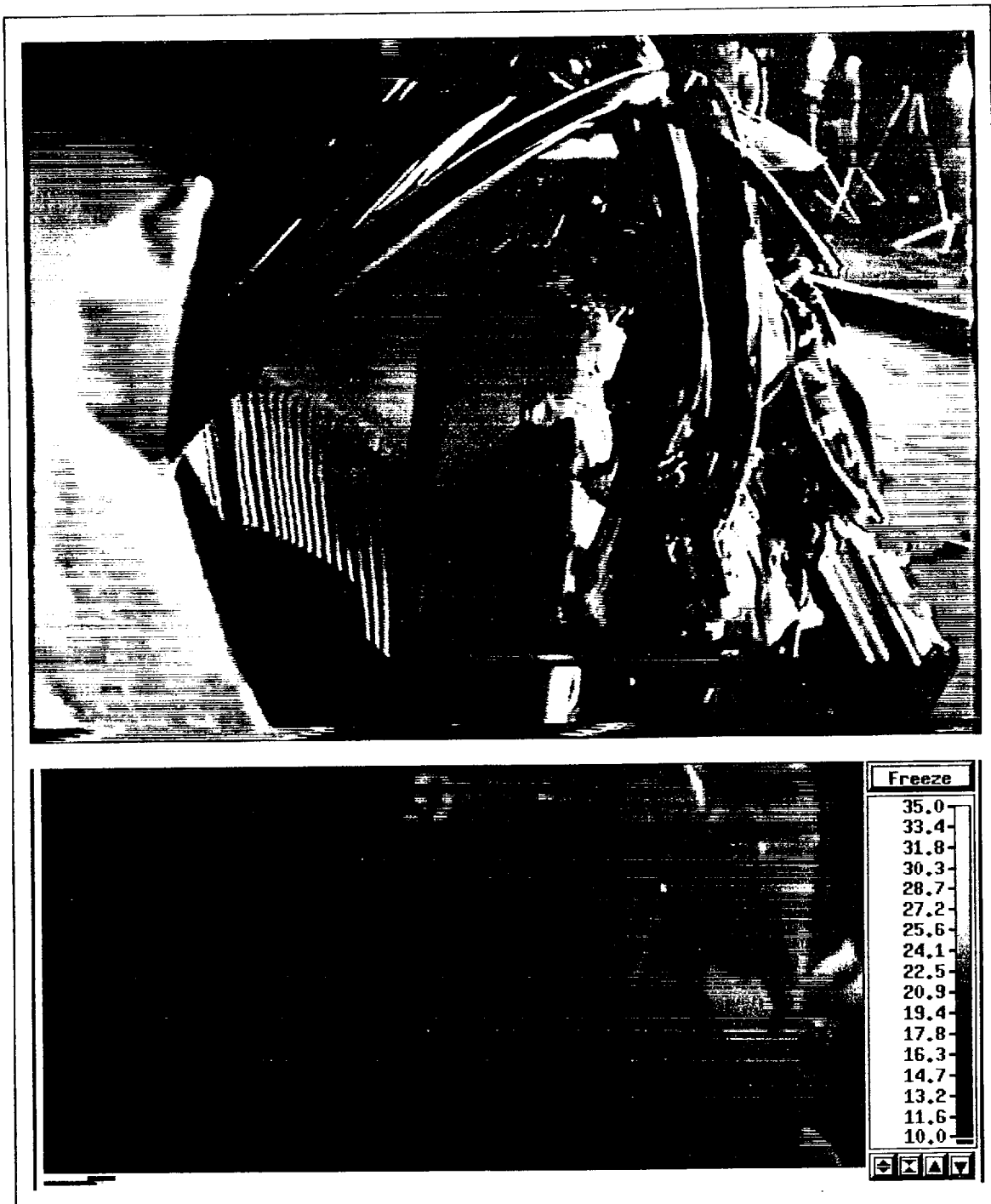

Figure 41. Fire Test F99030A. Video still from Video Camera 9 (upper) and Infrared thermogram from IR2 (lower) at the time of ignition (0 seconds post-ignition).

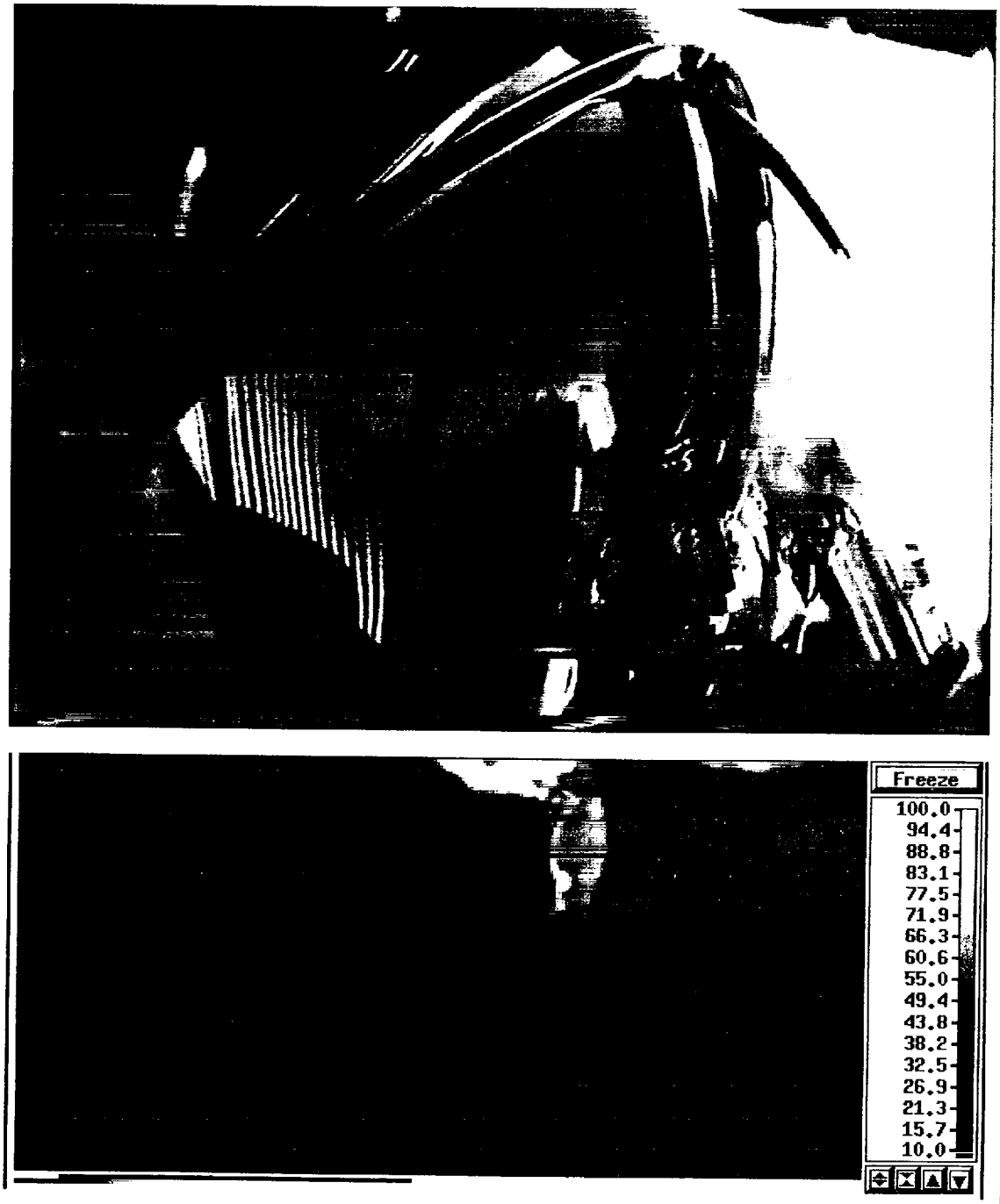

Figure 42. Fire Test F99030A. Video still from Video Camera 9 (upper) and Infrared thermogram from IR2 (lower) at 30 seconds post-ignition.

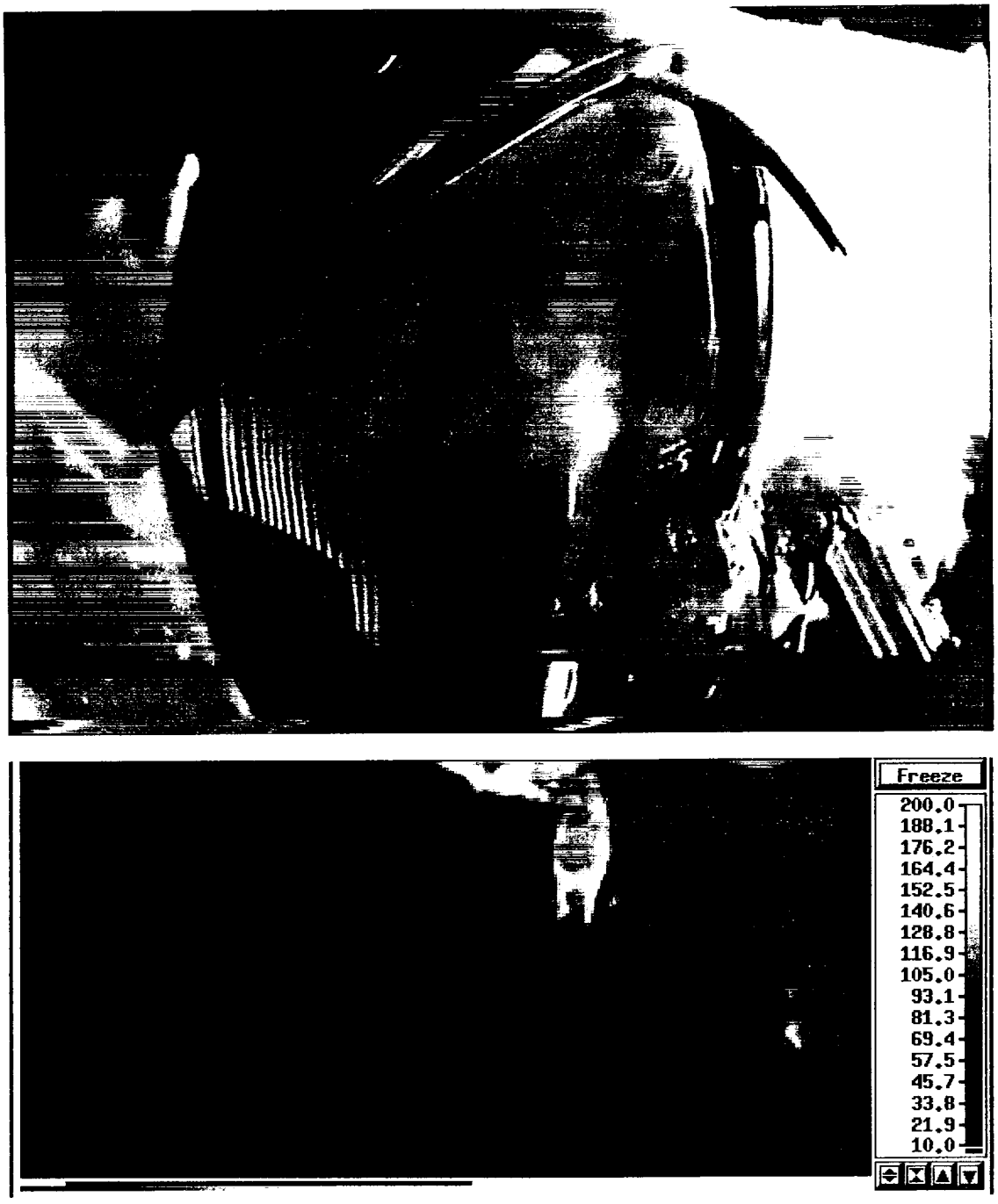

Figure 43. Fire Test F99030A. Video still from Video Camera 9 (upper) and Infrared thermogram from IR2 (lower) at 60 seconds post-ignition.

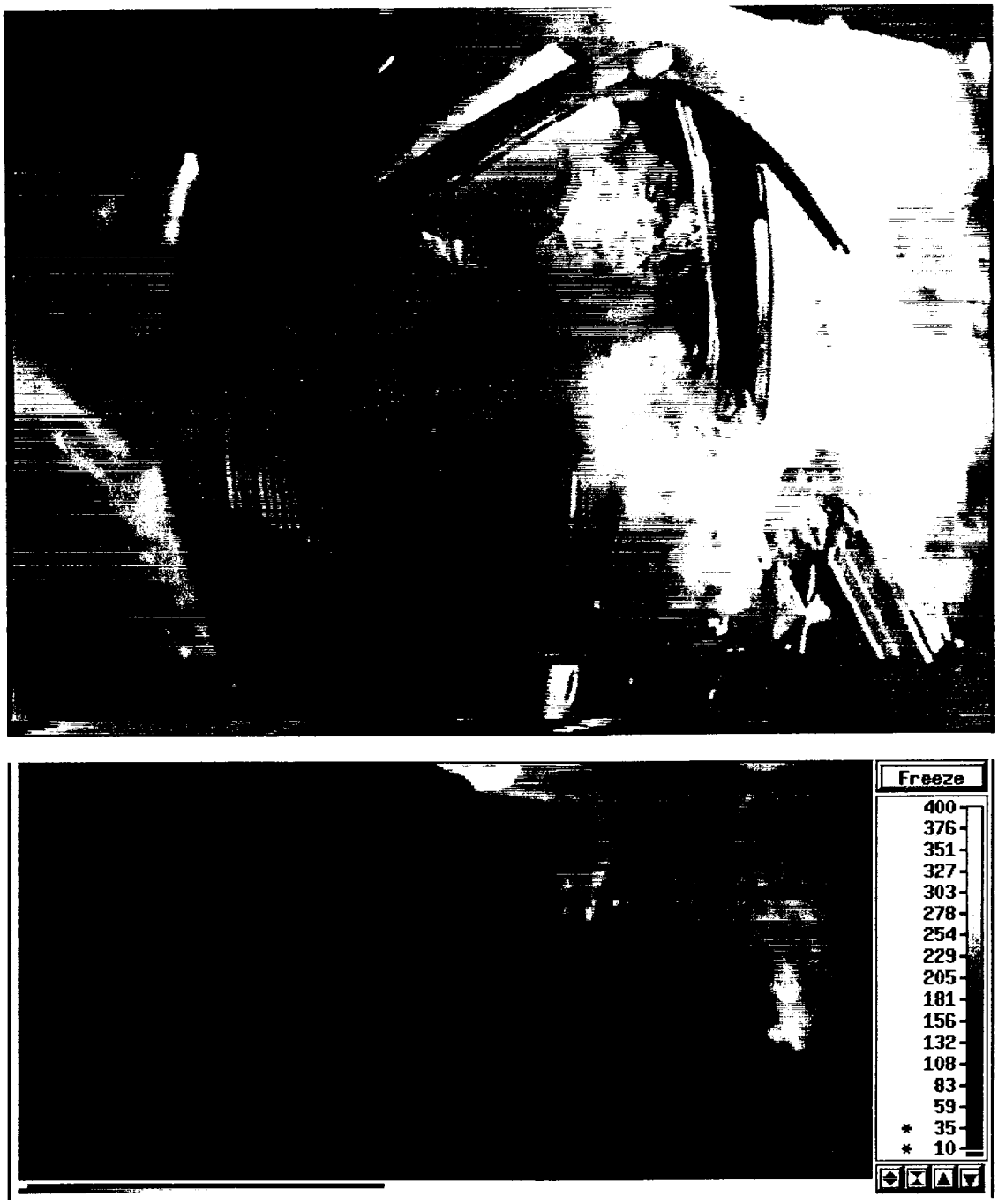

Figure 44. Fire Test F99030A. Video still from Video Camera 9 (upper) and Infrared thermogram from IR2 (lower) at 90 seconds post-ignition.

Figure 45. Fire Test F99030A. Video still from Video Camera 9 (upper) and Infrared thermogram from IR2 (lower) at 120 seconds post-ignition.

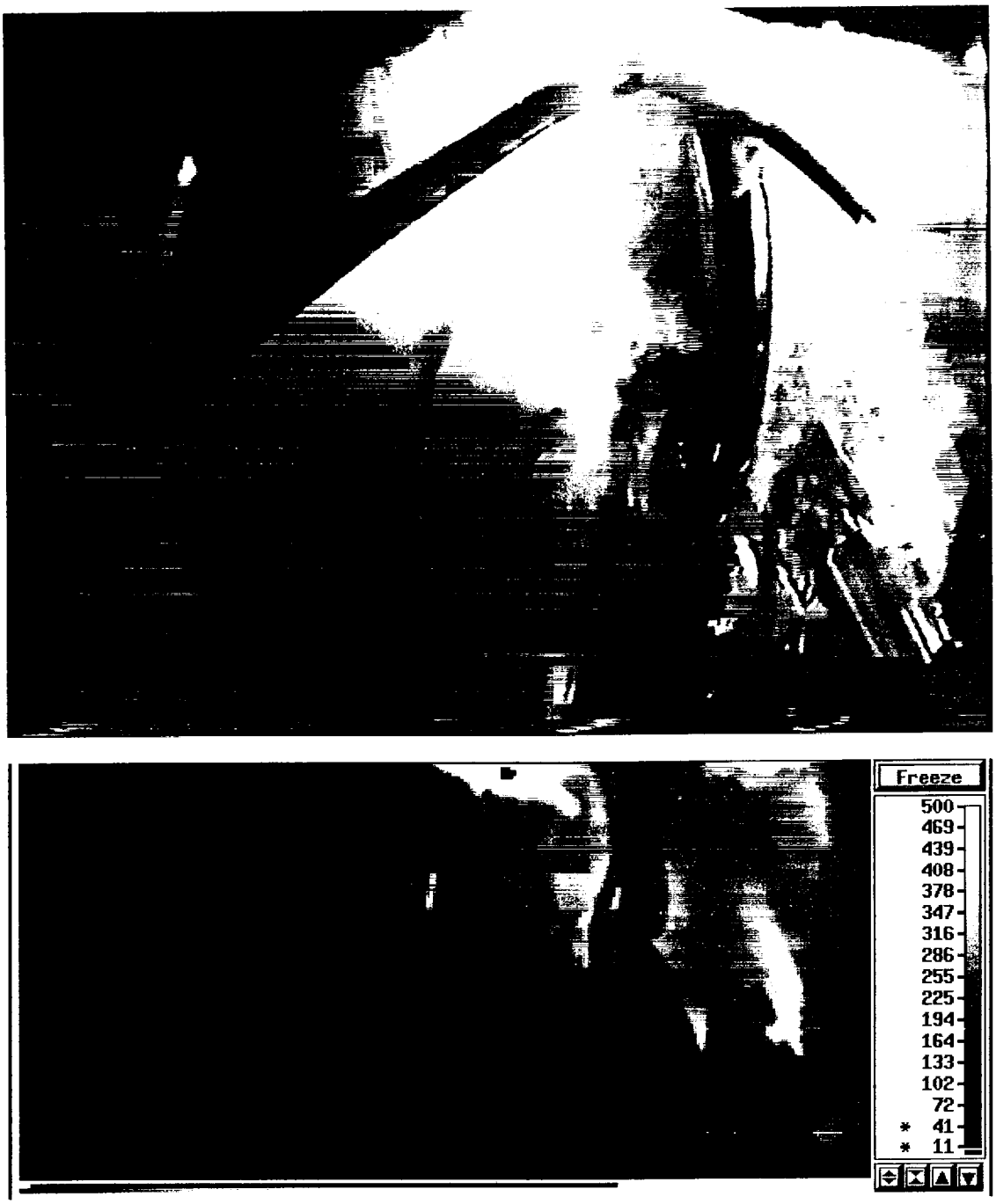

Figure 46. Fire Test F99030A. Video still from Video Camera 9 (upper) and Infrared thermogram from IR2 (lower) at 138 seconds post-ignition.

Plastic on the perimeter of this opening for the left speaker in the rear shelf trim panel was melted and charred (Fig. 47). The insulation attached to the bottom of the rear shelf trim panel was charred around the opening for the left speaker (insert, Fig. 47).

Figure 47. Fire Test F99030A. Photograph of the interior of the test vehicle through the left rear window after this fire test. The insert is a photograph of the insulation attached to the lower surface of the rear shelf trim panel removed from the test vehicle after this test.

Figure 48 is a photograph of the interior of the test vehicle through the rear left window. The rear seat cushion and left rear seat bolster have been removed. This photograph shows that the speaker cone in the left speaker in the rear shelf was consumed by fire (Fig. 48). Fabric on the left edge of the rear seat back is burned and charred (Fig. 48). Interior surfaces of the left rear wheelhouse panel and rear shelf panel are coated with soot (Fig. 48).

Figure 48. Fire Test F99030A. Photograph of the interior of the test vehicle through the left rear window after this fire test. The rear seat cushion and left rear seat bolster have been removed.

5.2 Flame-Spread Through Crash-Induced Seam Openings Around the Right Rear Wheelhouse

Figure 49 shows the approximate locations of thermocouples in this seam opening and of a heat flux transducer in the left rear wheelhouse panel.

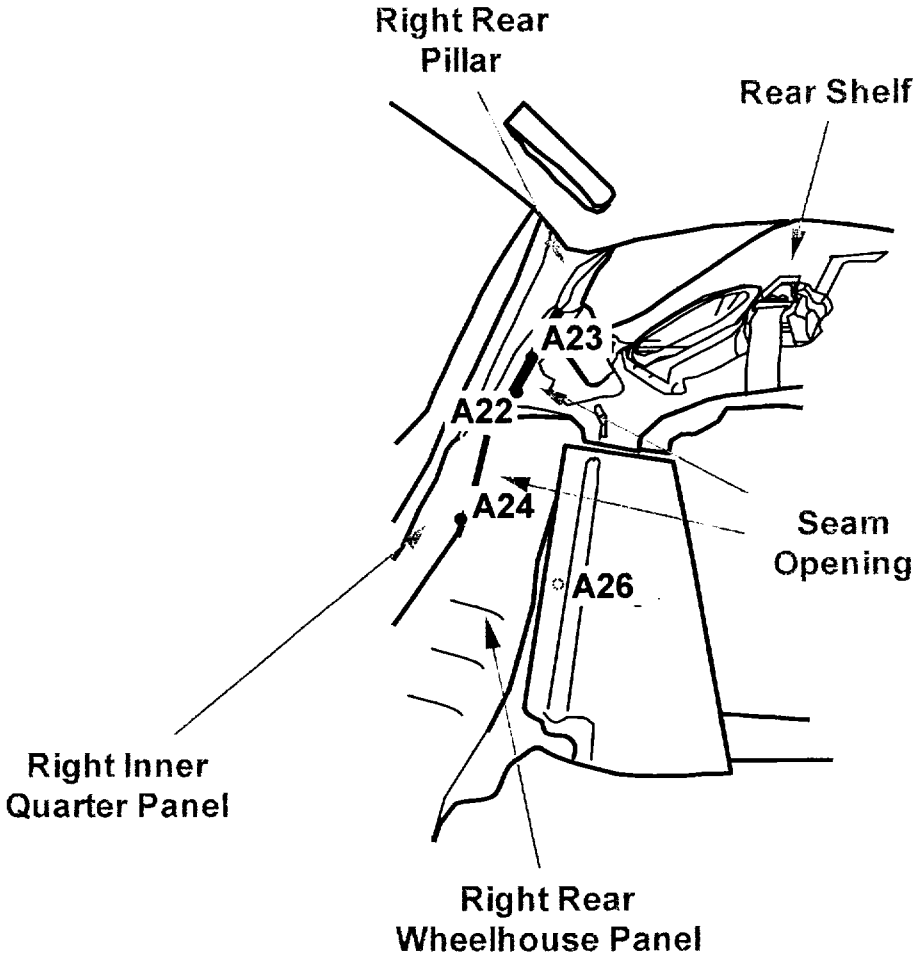

Figure 49. Diagram showing the approximate locations of thermocouples in a crash-induced seam opening between the left rear wheelhouse panel and the left inner quarter panel and a heat flux transducer in the left rear wheelhouse panel.

Thermocouples A22, A23, and A24 were located in the crash-induced seam opening between the right rear wheelhouse panel and the right inner quarter panel (see Appendix C). Thermocouple A26 was located behind the support panel for the rear seat back on the right side of the test vehicle.

Figure 50 shows plots of temperature data recorded from Thermocouples A4, A5, A6, A7, A8, and A9.

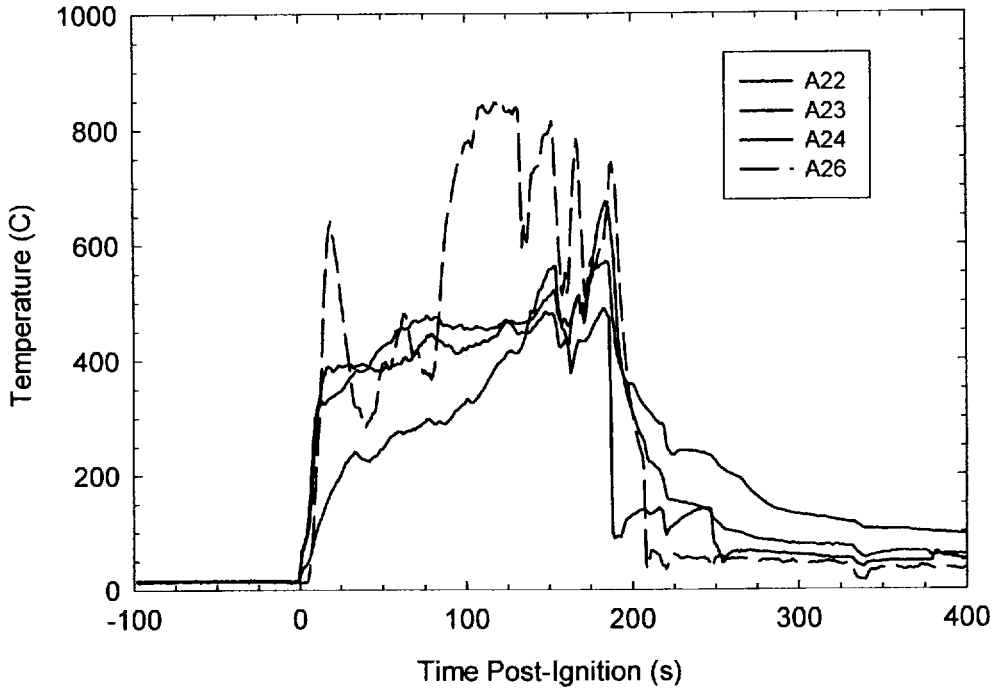

Figure 50. Fire Test F99030A. Plots of temperature data recorded from Thermocouples A4, A5, A6, A7, A8, and A9.

Temperature data recorded from Thermocouples A22, A23, and A24 did not exceed 600°C at any time before the start of fire suppression at approximately 155 seconds post-ignition (Fig. 50). Temperature data recorded from Thermocouple A26 exceeded 600°C between 17 and 21 seconds post-ignition and from 87 seconds post-ignition through the end of this test (Fig. 50). This data indicates that flames were present behind the right side of the rear seat back sporadically starting at 15 – 20 seconds post-ignition. Flames did not enter the passenger compartment through the seam opening between the right wheelhouse panel and the right inner quarter panel during this test, indicating another pathway for flame-spread into the passenger compartment on the right side of the test vehicle.

The series of video stills and infrared thermograms in Figures 22 through 31 show smoke and heated gases rising from inside the right side of the trunk and out of the right rear window during this test. The temperature of the instrumented section of the right outer quarter panel also appeared to be greater than the temperature of the surrounding metal by 10 seconds post-ignition (Fig. 24). The temperature of the right of the rear seat back increased starting at about

15 seconds post-ignition (Fig. 25), with flames visible on the upper right corner of the rear seat back by 120 seconds post-ignition (Fig. 31).

Inspection of the test vehicle after this test showed that the interior trim panel on the right side of the trunk was melted and charred in the area of the right shock tower (Fig. 51). A section of the fabric covering on the back of the right side of the rear seat back was burned (Fig. 51). Further inspection revealed that flames entered the right side of the trunk through a crash-induced seam opening between the right wheelhouse panel and floor panel in the area of the shock tower. This seam opening was not detected during the preparation of the test vehicle for this fire propagation test; thus, no thermocouples were installed in this seam opening and the exact timing for flame-spread at this location could not be determined.

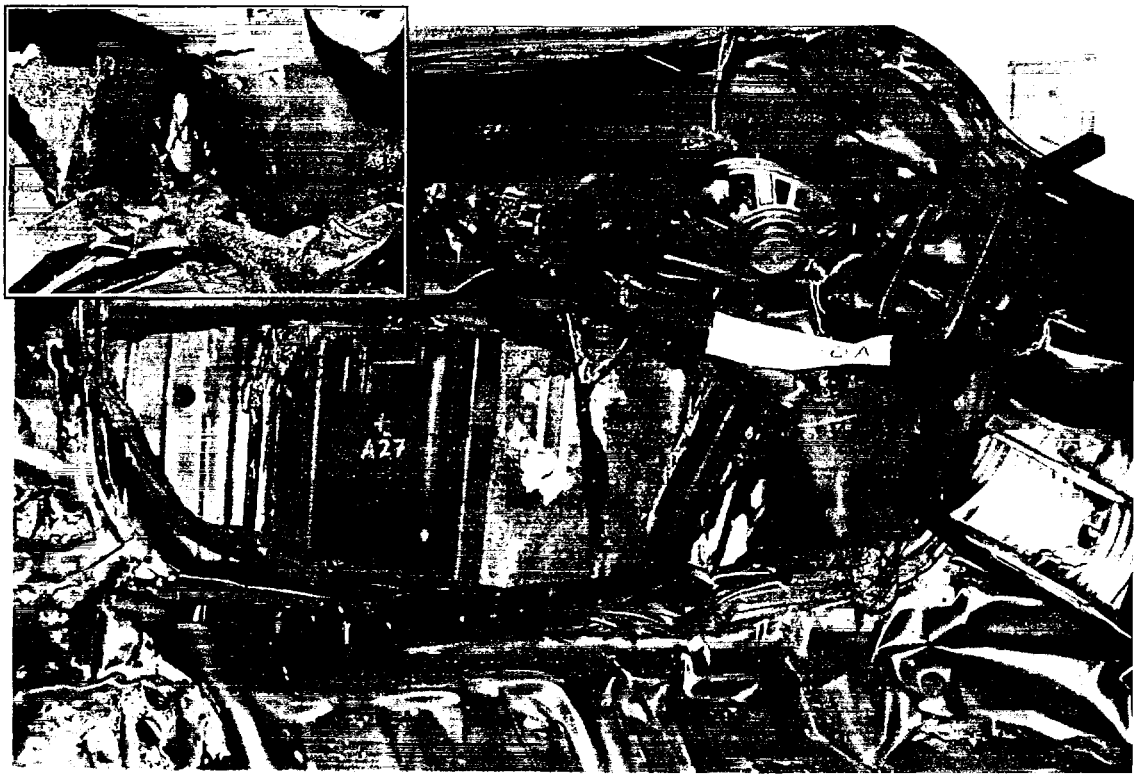

Figure 51. Fire Test F99030A. Photograph of the right side of the trunk of the test vehicle after this test. The insert is a close-up photograph of the area around the right rear shock tower.

Fire damage to the rear seat back and rear seat bolsters observed during inspection of the test vehicle after this test is consistent with flame-spread through crash-induced seam openings around the left and right wheelhouses. Figure 52 is a photograph of the rear-facing surfaces of

the rear seat back and the left and right rear seat bolsters removed from the test vehicle after this test (Fig. 52). The rear-facing surface of the foam pad in the left seat bolster was discolored and charred. The polymeric support structure in the upper section of the left seat bolster was melted and charred (Fig. 52). The fabric cover on the rear-facing surface of the left side of the rear seat back had been consumed by fire and the underlying metal panel was coated with soot (Fig. 52). The upper section of the rear-facing surface of the foam pad in the right seat bolster was discolored and charred (Fig. 52). A section of the fabric cover on the rear-facing surface of the right side of the rear seat back was melted exposing the underlying metal panel (Fig. 52).

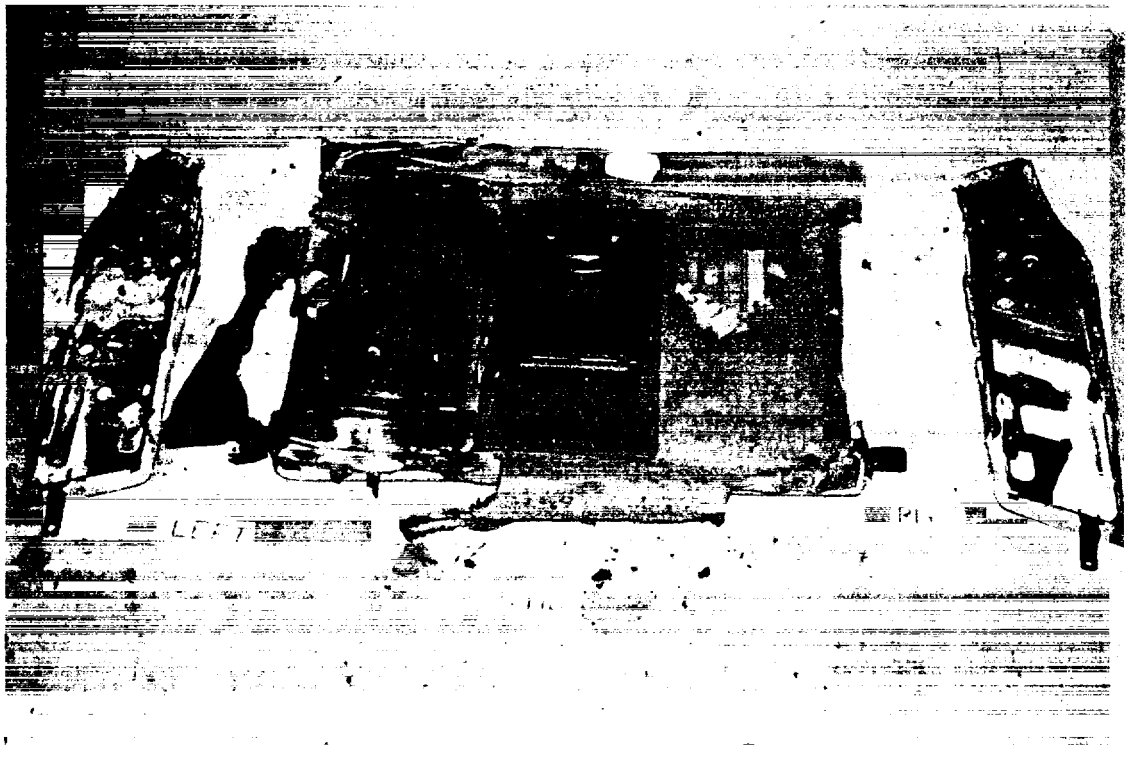

Figure 52. Fire Test F99030A. Photograph of the backs of the rear seat back and rear seat bolsters removed from the test vehicle after this test.

5.3 Flame-Spread on the Roof Trim Panel

Temperatures recorded from thermocouples located just below the lower surface of the roof trim panel indicated that heated gases started to accumulate in a upwardly concave cavity in the deformed roof within the first few seconds after ignition and flames were present in this area by 90 seconds post-ignition. Figure 53 shows a series of diagrams of the test vehicle with estimated isothermal contour plots of temperature profiles below the headlining panel at 0, 10, 15, 30, 45, 60, 75, 90, 120, 153 seconds post-ignition.[2]

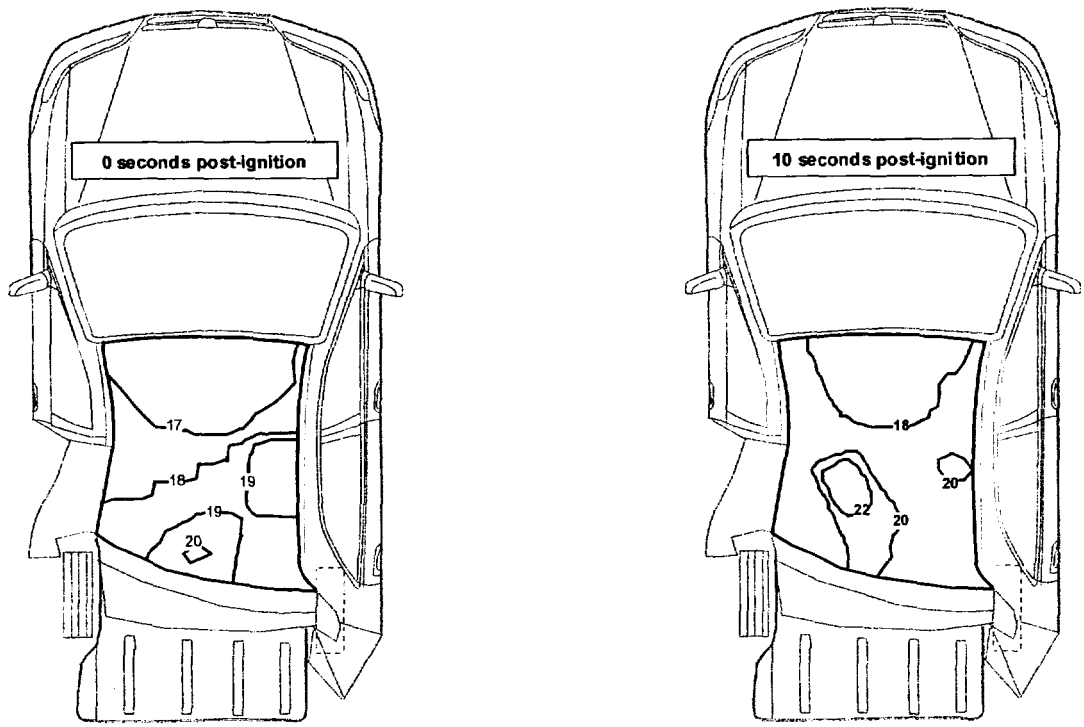

Figure 53. Fire Test F99030A. Diagrams showing isothermal contour plots of estimated temperature along the lower surface of the roof trim panel at 0, 10, 15, 30, 45, 60, 75, 90, 120, 153 seconds post-ignition.

[2] Isothermal contours of the temperature below the lower surface of the headlining panel were estimated from the temperature data recorded from Thermocouples R1, R2, R3, R4, R5, R6, R7, R8, R9, and R10 using a three-dimensional interpolation algorithm available in SigmaPlot for Windows Version 4.00 [4]. This algorithm used an inverse distance method to interpolate temperature values for points on a uniformly spaced Cartesian grid from the [x,y,t] triple data from these thermocouples. Refer to **APPENDIX C** for the approximate locations of these thermocouples.

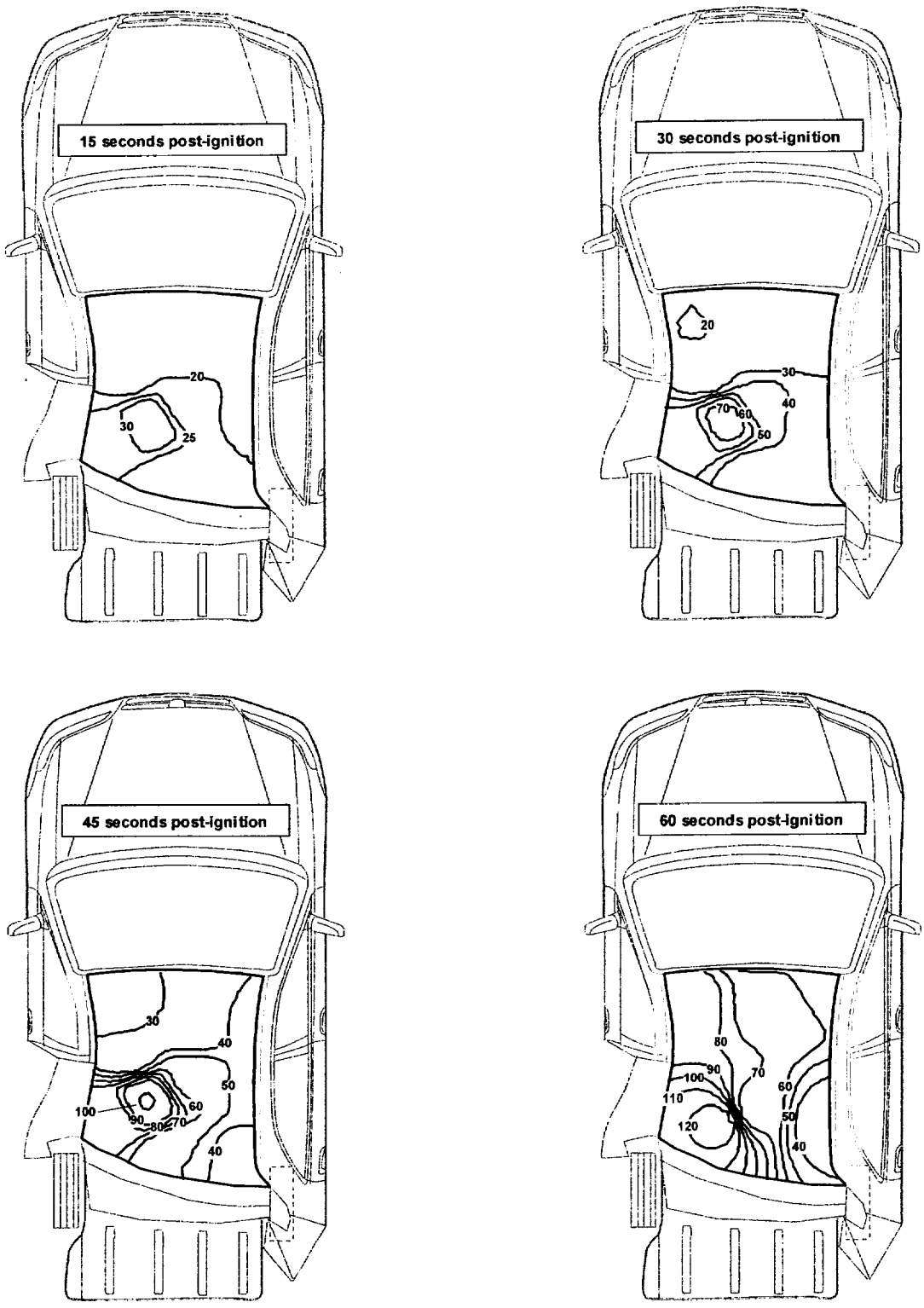

Figure 53, continued. Fire Test F99030A. Diagrams showing isothermal contour plots of estimated temperature along the lower surface of the roof trim panel at 0, 10, 15, 30, 45, 60, 75, 90, 120, 153 seconds post-ignition.

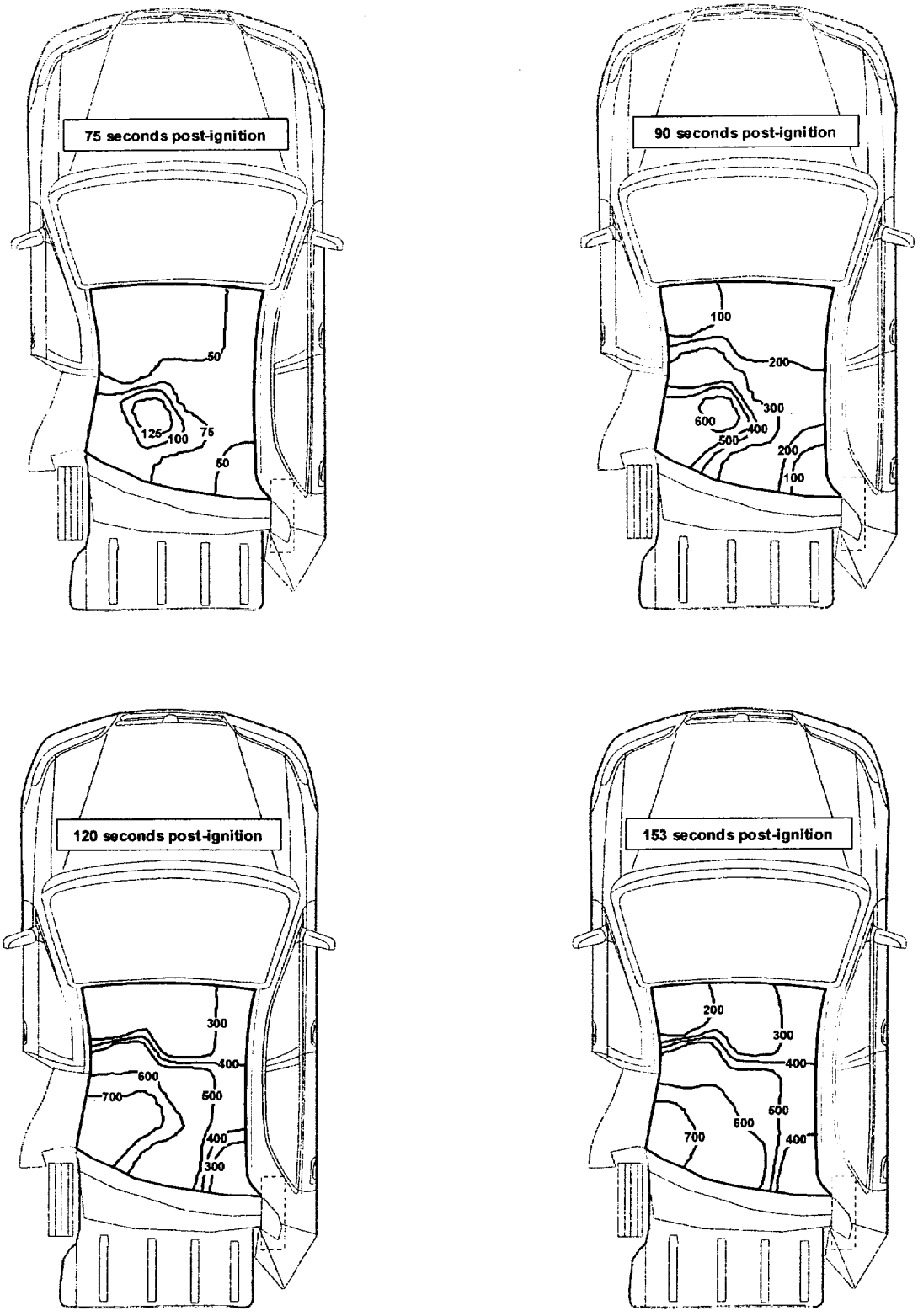

Figure 53, continued. Fire Test F99030A. Diagrams showing isothermal contour plots of estimated temperature along the lower surface of the roof trim panel at 0, 10, 15, 30, 45, 60, 75, 90, 120, 153 seconds post-ignition.

The timing and approximate distribution of flames along the roof trim panel is indicated by isothermal contours with $t \geq 600°C$. This analysis indicates that estimated temperatures below the left rear section of the roof trim panel started to increase by 10 seconds post-ignition (Fig. 53), indicating that heated gases had started to flow into this area shortly after ignition. The isothermal contour plots in Figure 53 show that temperatures > 600°C were recorded from thermocouples below the left rear section of the roof trim panel by 90 seconds post-ignition, indicating flames in contact with this area of the roof trim panel at this time. This interpretation of the isothermal contours in Figure 53 is consistent with the video stills and infrared thermograms in Figures 22 through 31, which show that the temperature of the left rear corner of the roof trim panel started to increase by about 15 seconds post-ignition (Fig. 25) and that flames were present in this area by 90 seconds post-ignition (Fig. 30). Maximum temperatures recorded below the roof trim panel during this test were between 700 and 800°C (Fig. 53). The pattern of fire damage to the roof trim panel observed after this test indicates that the area where the fabric on the lower surface of the roof trim panel was charred (Fig. 54) corresponds to the area where estimated temperatures below the roof trim panel exceeded about 500°C (Fig. 53).

Figure 54. Fire Test F99030A. Photograph of the interior of test vehicle after this test showing fire damage to the rear seat back, rear seat bolsters, and roof trim panel.

6 Combustion Conditions

The output of combustion products from a fire depends on the material burning and on the supply of air to the flame. A well-ventilated fire is one in which the air supplied to the flames is sufficient for complete combustion. In partially enclosed spaces, such as an engine compartment or passenger compartment, airflow to the flames may be inadequate for complete combustion. In this case, called a ventilation-controlled or under-ventilated fire, the supply of air limits both the heat released by the fire and oxidation (combustion) of the gaseous fuel in the fire zone. As ventilation decreases, the output of carbon monoxide, hydrocarbons, smoke, and other products of incomplete combustion increase. The chemical composition of these gases depends on the chemical compositions of the materials burning and on the burning conditions, primarily ventilation. For fires in an enclosed space, heated buoyant gases can accumulate below the ceiling or roof of the enclosed space, forming what is called the upper layer. The upper layer can be ignited by flames from burning objects (piloted ignition) or can ignite spontaneously (autoignition) when the temperature of the gases exceeds a minimum threshold temperature (autoignition temperature), which depends on the chemical composition and the fuel/oxygen ratio of the gaseous upper layer. Once ignited, radiation from the burning upper layer transfers heat downward, and may ignite combustible materials below the burning upper layer. Ventilation of the flames affects the chemical composition of the gases produced in a fire.

The equivalence ratio is a quantitative measure of the amount of oxygen consumed during combustion, and is defined as follows:

$$\Phi = \frac{\left[fuel/O_2\right]_{fire}}{\left[fuel/O_2\right]_{stoichiometric}},$$

where Φ is the equivalence ratio, $[fuel/O_2]_{fire}$ is the fuel-to-oxygen ratio in the fire, and $[fuel/O_2]_{stoichiometric}$ is the fuel-to-oxygen ratio required for complete (stoichiometric) combustion. Combustion product concentration data, oxygen concentration data, gas temperature data, and airflow data are typically used to calculate a value of the equivalence ratio in laboratory tests [5]. In most instances, the equivalence ratio is not determined for large-scale tests where objects made of different materials may burn in different physical environments. Ventilation and thus the equivalency ratio may be different in each environment. Since it was not possible to isolate and measure the fire products produced by each of the materials burning or to measure airflow into each of the unique environments that existed during this test, the equivalence ratio was not determined here.

Air temperature and gas concentration data collected during this test were used to estimate derived parameters that are related to ventilation. Air temperature and gas concentration data from the Fire Products Collector at the test facility were used to estimate the ratios $[G_{CO}]/[G_{CO2}]$ and $[G_{HC}]/[G_{CO2}]$. Air temperature data from the aspirated thermocouples in the passenger compartment and gas concentration data from the FTIR gas analysis of air in the passenger compartment were used to estimate the ratios $[C_{CO} \times d_{CO}]/[C_{CO2} \times d_{CO2}]$, $[C_{HC} \times d_{HC}]/[C_{CO2} \times d_{CO2}]$, $[C_{CO2} \times d_{CO2}]/[t_{air} \times Cp]$, $[C_{CO} \times d_{CO}]/[t_{air} \times Cp]$, and $[C_{CO2} \times d_{CO2}]/[t_{air} \times Cp]$. Ventilation was assessed by comparing the values of these derived parameters estimated from the test data to reference values obtained during the testing of individual materials in small-scale flammability tests,[3] where the equivalence ratio was measured precisely [7]. The reference parameters used in this comparison include $Y(CO)/Y(CO_2)$, $Y(HC)/Y(CO_2)$, $Y(CO_2)/\Delta H_{CON}$, $Y(CO)/\Delta H_{CON}$, $Y(HC)/\Delta H_{CON}$ (Table 1).

Table 2

Fire Products for Well-ventilated Fires[1,2]

material	$Y(CO)/Y(CO_2)$ (g/g)	$Y(HC)/Y(CO_2)$ (g/g)	$Y(CO_2)/\Delta H_{CON}$ (g/kJ)	$Y(CO)/\Delta H_{CON}$ (g/kJ)	$Y(HC)/\Delta H_{CON}$ (g/kJ)
gasoline[3]	0.011 – 0.014	0.0032 – 0.0039	0.14 – 0.16	0.0021 – 0.0026	0.00058 – 0.00073
poly(ethylene)	0.0087	0.0025	0.13	0.0011	0.00032
poly(propylene)	0.0086	0.0022	0.12	0.0011	0.00027
poly(styrene)	0.026	0.0060	0.21	0.0054	0.00127
polyester	0.05	0.019	0.15	0.0065	0.00185
Nylon	0.018	0.0078	0.13	0.0035	0.00098
Flexible urethane foams	0.006 - 0.027	0.0013 - 0.0033	0.15 - 0.21	0.0012 - 0.0055	0.00023 - 0.00069
Rigid urethane foams	0.015 - 0.046	0.006 - 0.036	0.17 - 0.23	0.0028 - 0.0081	0.00011 - 0.00070

[1]Values reported in Table 2 were calculated from data reported in Table 3-4.11 in reference 5.

[2]Y(CO) is the mass-yield of carbon monoxide (g). $Y(CO_2)$ is the mass-yield of carbon dioxide (g). Y(HC) is the mass-yield of gaseous hydrocarbons (g). $Y(CO_2)/\Delta H_{con} = (C_{CO_2}/c_p\Delta T)(\rho_{CO_2}/\rho_{air})$, $Y(CO)/\Delta H_{con} = (C_{CO}/c_p\Delta T)(\rho_{CO}/\rho_{air})$, and $Y(HC)/\Delta H_{con} = (C_{HC}/c_p\Delta T)(\rho_{HC}/\rho_{air})$. ΔH_{CON} is the convective heat of combustion per unit fuel vaporized (kJ/g). The C_j are the gas-phase concentrations (volume fraction) of carbon dioxide, carbon monoxide, and total hydrocarbons. The ρ_j are the gas-phase densities (g/m^3) of carbon dioxide, carbon monoxide, total hydrocarbons, and air. c_p is the heat capacity of air (kJ/g-K). ΔT is the difference between the gas temperature and the temperature of the ambient air (K).

[3]Values for gasoline were estimated from the data in Table 3-4.11 in reference 7 assuming an aliphatic hydrocarbon content of 60 to 70 % and an aromatic hydrocarbon content of 30 to 40%.

[3] Small-scale flammability tests to determine combustion properties of materials were conducted in the Factory Mutual Research Corporation Flammability Apparatus is a small-scale test apparatus (see reference 5).

The values of these parameters in Table 2 were determined for the well-ventilated combustion of poly(ethylene), poly(propylene), poly(styrene), polyester, Nylon, a group of flexible urethane foams, and a group of rigid urethane foams in controlled small-scale laboratory tests.[4]

An analysis of combustion conditions based on data from the Fire Products Collector was not done because the carbon monoxide release rate data collected during this test was unreliable (see **Appendix H**).

An analysis of combustion conditions based on air temperature and gas concentration data from the passenger compartment is shown in Figures 55 through 59. Air temperature and gas concentration data from the passenger compartment were used to determine $[C_{CO} \times d_{CO}]/[C_{CO2} \times d_{CO2}]$, $[C_{HC} \times d_{HC}]/[C_{CO2} \times d_{CO2}]$, $[C_{CO2} \times d_{CO2}]/[t_{air} \times Cp]$, $[C_{CO} \times d_{CO}]/[t_{air} \times Cp]$, and $[C_{HC} \times d_{HC}]/[t_{air} \times Cp]$. In these formulas, C_j is the gas-phase concentration of species j, d_j is the density of species j, t_{air} is the air temperature, and C_p is the heat capacity of air. The product $[C_j \times d_j]$ equals the mass-concentration of species j in passenger compartment. The concentrations of the gaseous combustion products (C_j) were determined by Fourier Transform Infrared Spectrometry (**APPENDIX I**). Air temperature data from the aspirated thermocouple assemblies in the passenger compartment (**APPENDIX D**) was used to determine t_{air}. The ratios $[C_{CO} \times d_{CO}]/[C_{CO2} \times d_{CO2}]$, $[C_{HC} \times d_{HC}]/[C_{CO2} \times d_{CO2}]$, $[C_{CO2} \times d_{CO2}]/[t_{air} \times Cp]$, $[C_{CO} \times d_{CO}]/[t_{air} \times Cp]$, and $[C_{HC} \times d_{HC}]/[t_{air} \times Cp]$ are equivalent to $Y(CO)]/[Y(CO_2)$, $Y(HC)]/[Y(CO_2)$, $Y(CO_2)/\Delta H_{CON}$, $Y(CO)/\Delta H_{CON}$, and $Y(HC)/\Delta H_{CON}$, respectively, in Table 2.

Trends in $[C_{CO} \times d_{CO}]/[C_{CO2} \times d_{CO2}]$, $[C_{HC} \times d_{HC}]/[C_{CO2} \times d_{CO2}]$, $[C_{CO2} \times d_{CO2}]/[t_{air} \times Cp]$, $[C_{CO} \times d_{CO}]/[t_{air} \times Cp]$, and $[C_{HC} \times d_{HC}]/[t_{air} \times Cp]$ appear to have been related to transition from pyrolysis to flaming combustion as flames spread to combustible materials in the passenger compartment. Before combustible materials in the passenger compartment ignited, gases detected in the passenger compartment were produced either by combustion of gasoline vapor in the space under the test vehicle or by thermal decomposition (pyrolysis) of materials in the test vehicle. Restricted airflow into the space under the rear of the test vehicle would be expected to have resulted in under-ventilated combustion of gasoline vapor in these spaces. Thermal decomposition of materials in the test vehicle generally yields organic gaseous hydrocarbons and does not yield appreciable amounts of carbon dioxide and heat.

[4] The compositions and physical properties such as density, thermal conductivity, and heat capacity of these materials were not specified.

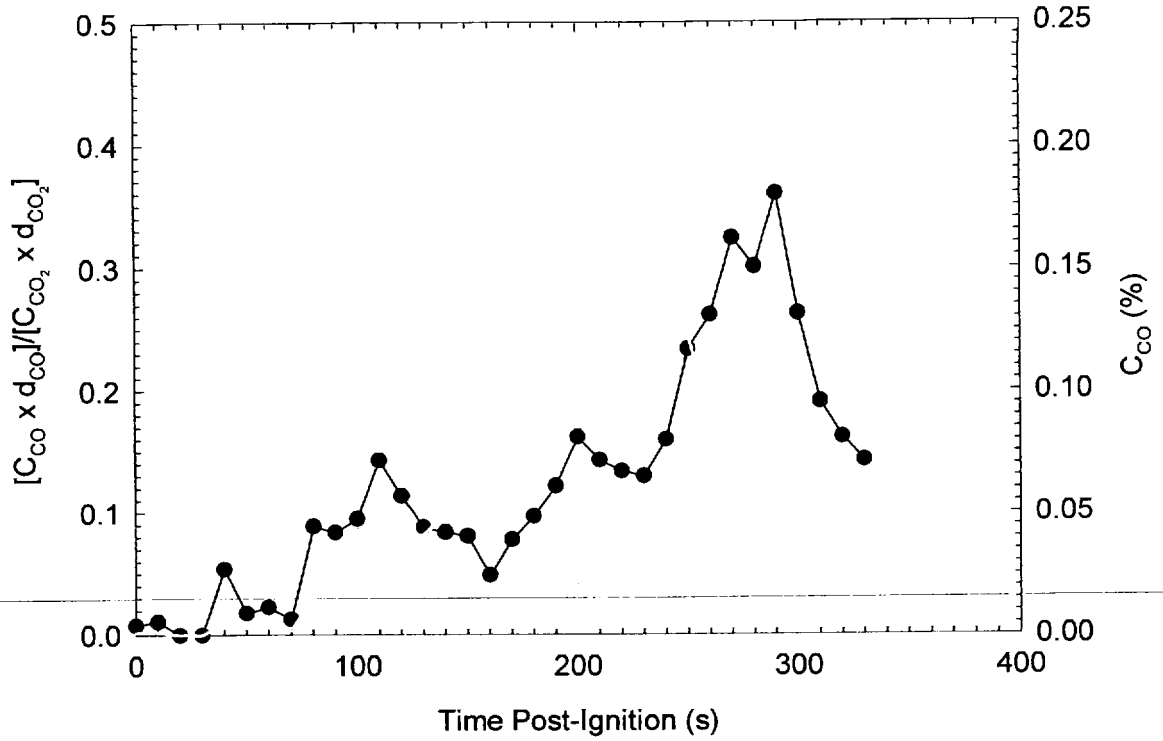

Figure 55. Fire Test F99030A. Plots of $[C_{CO} \times d_{CO}]/[C_{CO2} \times d_{CO2}]$ (—●—, left axis) and the concentration of carbon monoxide (—, right axis) in the passenger compartment.

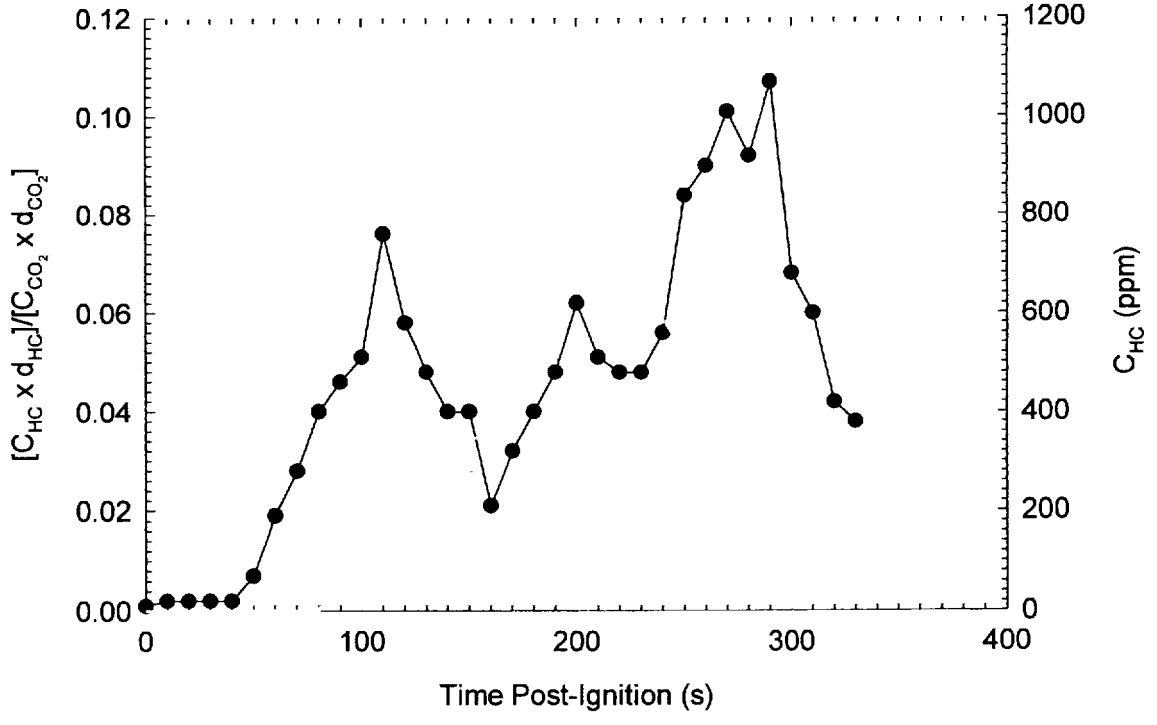

Figure 56. Fire Test F99030A. Plots of $[C_{HC} \times d_{HC}]/[C_{CO2} \times d_{CO2}]$ (—●—, left axis) and the concentration of total hydrocarbons (—, right axis) in the passenger compartment.

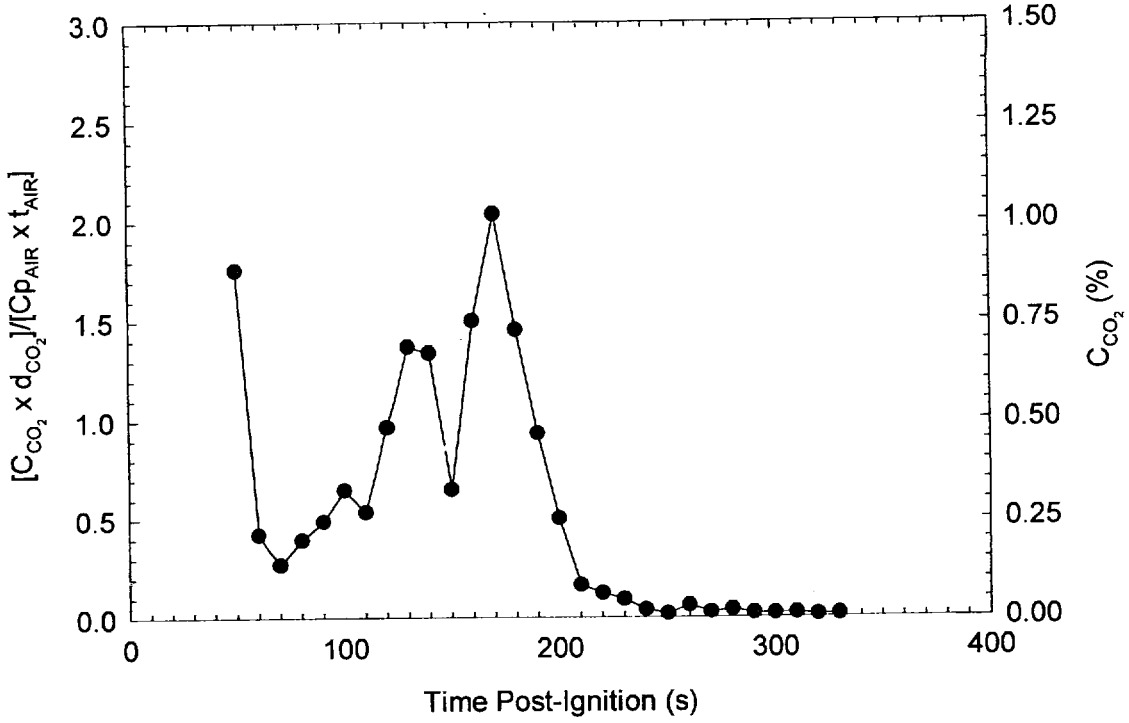

Figure 57. Fire Test F99030A. Plots of $[C_{CO2} \times d_{CO2}]/[t_{air} \times Cp]$ (—●—, left axis) and the concentration of carbon dioxide (—, right axis) in the passenger compartment.

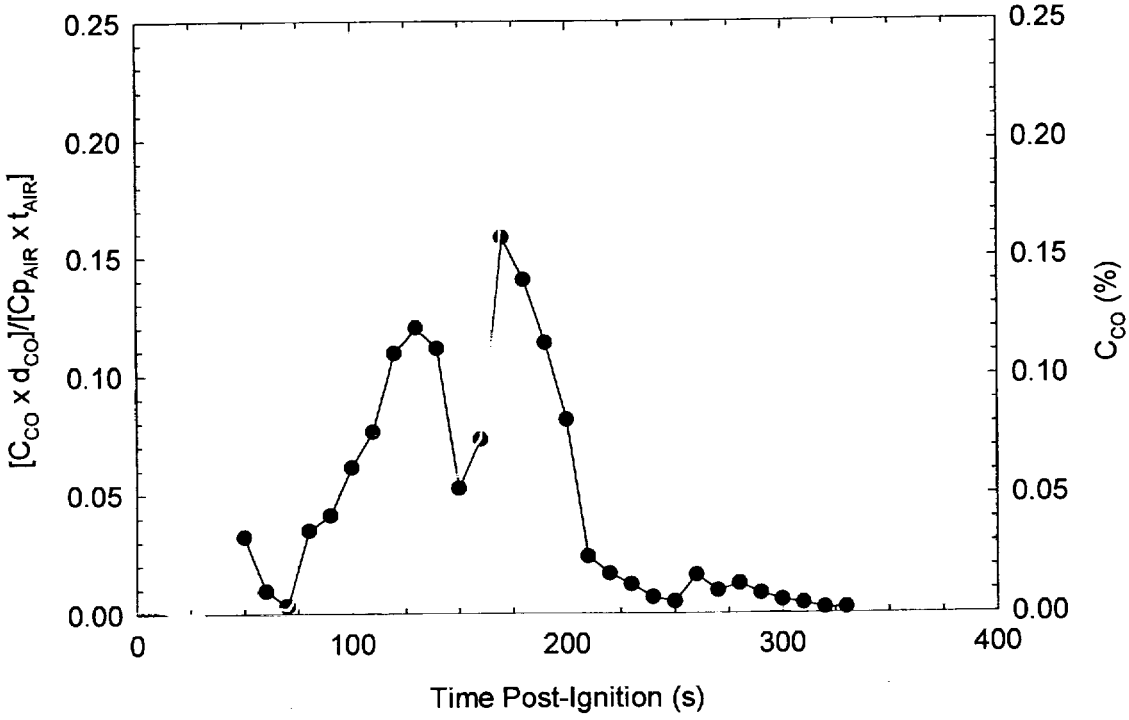

Figure 58. Fire Test F99030A. Plots of $[C_{CO} \times d_{CO}]/[t_{air} \times Cp]$ (—●—, left axis) and the concentration of carbon monoxide (—, right axis) in the passenger compartment.

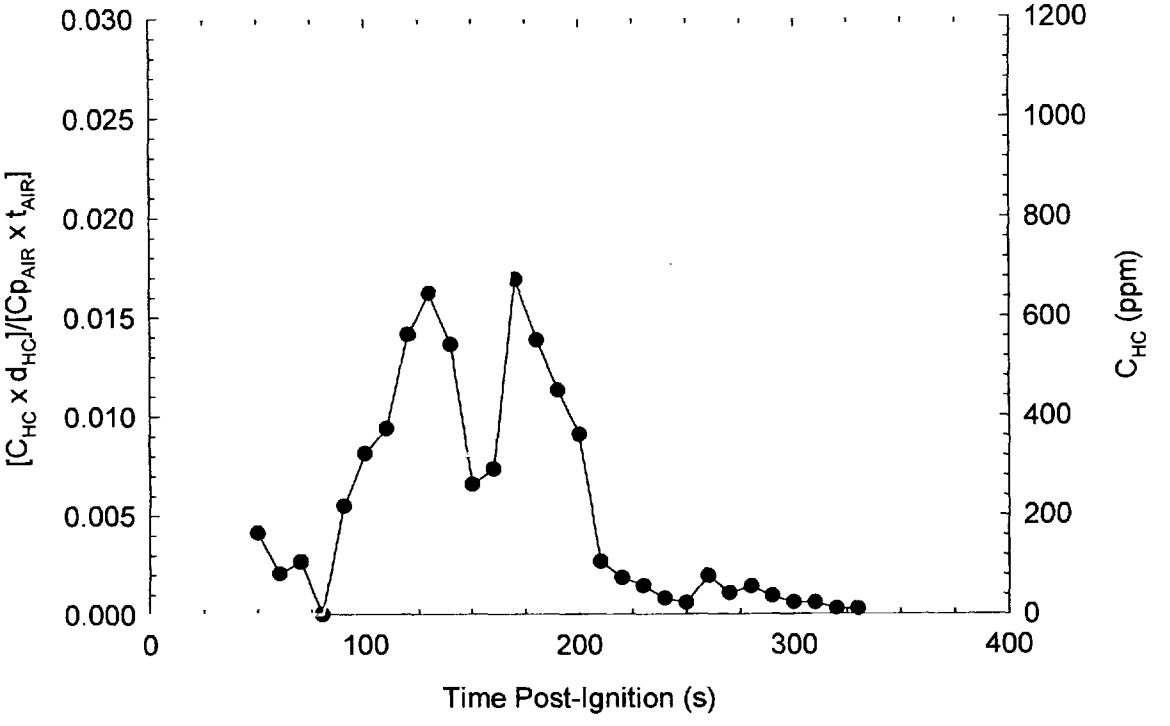

Figure 59. Fire Test F99030A. Plots of $[C_{HC} \times d_{HC}]/[t_{air} \times Cp]$ (—●—, left axis) and the concentration of hydrocarbons (—, right axis) in the passenger compartment.

Based on these considerations, values of $[C_{CO} \times d_{CO}]/[C_{CO2} \times d_{CO2}]$, $[C_{HC} \times d_{HC}]/[C_{CO2} \times d_{CO2}]$, $[C_{CO2} \times d_{CO2}]/[t_{air} \times Cp]$, $[C_{CO} \times d_{CO}]/[t_{air} \times Cp]$, and $[C_{HC} \times d_{HC}]/[t_{air} \times Cp]$ would be expected to be greater than the respective reference values for well-ventilated combustion of shown in Table 2 as flames spread to combustible materials in the test vehicle and decrease as these materials ignited. The plots of $[C_{CO} \times d_{CO}]/[C_{CO2} \times d_{CO2}]$ and $[C_{HC} \times d_{HC}]/[C_{CO2} \times d_{CO2}]$ indicate a period between about 40 and 110 seconds post-ignition where the values of these parameters increased and were greater than the respective reference values for well-ventilated combustion of shown in Table 2 (Fig.'s 55 and 56). These results are consistent with the influx into the passenger compartment of combustion products from under-ventilated combustion of gasoline vapor under the test vehicle and of products from thermal decomposition of combustible materials in the test vehicle, such as the trim panels in the trunk, and the foam pads rear seat backs and rear seat bolsters in the passenger compartment[5], at this time. Values of $[C_{CO} \times d_{CO}]/[C_{CO2} \times d_{CO2}]$ and $[C_{HC} \times d_{HC}]/[C_{CO2} \times d_{CO2}]$ decreased between 110 and about 170 seconds post-ignition, approaching values in the respective ranges for well-ventilated combustion of these materials. This trend is consistent with ignition of these materials by about 110 seconds post-ignition, with increasing combustion

[5] The trim panels in the trunk were polyester and the foam pads in the rear seat back and rear seat bolsters were a flexible urethane foam.

efficiency following ignition (Fig.'s 55 and 56). The increases in the values of $[C_{CO} \times d_{CO}]/[C_{CO2} \times d_{CO2}]$ and $[C_{HC} \times d_{HC}]/[C_{CO2} \times d_{CO2}]$ between about 170 and 290 seconds post-ignition (*Fig.*'s 55 and 56) occurred when the fire was being extinguished, which is consistent with cessation of flaming combustion with continued thermal decomposition of the extinguished materials that remain at elevated temperatures.

The parameters $[C_{CO2} \times d_{CO2}]/[t_{air} \times Cp]$, $[C_{CO} \times d_{CO}]/[t_{air} \times Cp]$, and $[C_{HC} \times d_{HC}]/[t_{air} \times Cp]$ relate the amount of carbon dioxide, carbon monoxide, and hydrocarbons measured in the gas phase to the rise in air temperature, which is dependent on the heat release of the flame. Trends in the plots of these parameters also indicate an initial period where combustion efficiency apparently decreased, followed by a period where combustion efficiency increased (Fig.'s 57, 58, and 59). Based on the plots of parameters $[C_{CO2} \times d_{CO2}]/[t_{air} \times Cp]$, $[C_{CO} \times d_{CO}]/[t_{air} \times Cp]$, and $[C_{HC} \times d_{HC}]/[t_{air} \times Cp]$, the transition form decreasing combustion efficiency to increasing combustion efficiency occurred at about 140 seconds post-ignition (Fig.'s 57, 58, and 59), approximately 30 seconds after the timing of the transition form decreasing combustion efficiency to increasing combustion efficiency predicted from the plots of $[C_{CO} \times d_{CO}]/[C_{CO2} \times d_{CO2}]$ and $[C_{HC} \times d_{HC}]/[C_{CO2} \times d_{CO2}]$.

7 Estimation of Skin Temperature Profiles from Measured Heat Flux Data, Fractional Equivalent Dose Parameters from Measured Gas Concentration Data, and Thermal Damage to the Respiratory Tract from Measured Air Temperature Data

The mathematical model "BURNSIM: A Burn Hazard Assessment Model" [6] was used to estimate the time and depth of burns to exposed skin. The inputs to this model were heat fluxes derived from the directional flame thermometer measurements and air temperatures measured using the aspirated thermocouple probe.

Two models were used to estimate the potential for toxicity from exposure to the combustion gases measured in the passenger compartment. The Federal Aviation Administration (FAA) Combined Hazard Survival Model [7] was used to estimate the time to incapacitation and the time to lethality. A model described by Purser [8] also was used to estimate the time to incapacitation. Both models estimate the risk from exposure to hot air, reduced oxygen, carbon monoxide, carbon dioxide, hydrogen cyanide, hydrogen chloride, hydrogen fluoride, hydrogen bromide, acrolein, and nitrogen dioxide. Both models also account for the physiological effect of carbon dioxide-induced hyperventilation, which increases the respiratory uptake.

7.1 The BURNSIM Model

The computer model BURNSIM was the analytical tool chosen to estimate skin temperature depth profiles from the heat flux data in **APPENDIX G**. The BURNSIM model divides the skin into a series of ten layers, with a uniform thickness of 0.2 mm per layer. The top layer was divided into 8 layers each with a uniform thickness of 0.025 mm to better account for the non-instantaneous heat transfer from the epidermal surface into the first layer.

Skin Model of BURNSIM

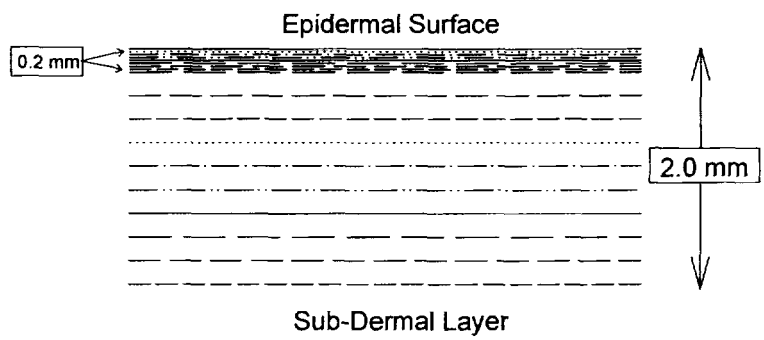

The BURNSIM analysis used here incorporated the following assumptions to estimate skin temperature profiles. The absorbtivity of exposed skin was assumed to be 0.60 (i.e., the skin absorbs 60% of the radiation incident upon the epidermal surface). The absorbtivity of surface

hair was assumed to be 0.05 (i.e., surface hair absorbs 5% of the incident radiation before it reached the skin). Exposed skin was assumed to absorb 100% of the measured convective heat flux to its surface. The temperature of each layer was estimated as a function of the time of exposure to an external heat flux. A portion of the absorbed heat is removed from the skin by the circulatory system. In the BURNSIM model, thermal damage results when the temperature of that layer exceeds 45°C.

In estimating skin temperature, the analysis presented in this paper using BURNSIM did not account for the presence of facial or head hair, or clothing covering the skin, all of which may block direct heat transfer to the skin. This analysis also did not account for variations in skin thickness among individuals, or variations in skin thickness at different parts of the body on the same individual. For example, skin thickness can vary from 1 to 5 mm with body location. This analysis also did not account for the effect of skin pigmentation on absorbtivity. In using the radiative and convective heat flux estimates shown in **APPENDIX G** to estimate skin temperature profiles, this analysis assumed that the location and orientation of the skin was identical to that of the HFT/RAD transducer assemblies used to measure heat flux. Small changes in position or angle of the surface can result in large differences between in the incident heat flux to the surface (see below). Based on the currently available information and data, the accuracy of the estimated skin temperature depth profiles in humans exposed to heat flux levels from fire such as measured in this test obtained using BURNSIM has not been determined.

7.1.1 *Estimation of Skin Temperature Profiles using BURNSIM*

The absorbed heat flux at each of the HFT/RAD assembly locations was estimated from the data recorded from HFT/RAD 10 through HFT/RAD 15. Estimates of absorbed heat flux obtained by analysis of the data recorded from these transducers were input into the BURNSIM model to estimate skin temperature profiles for exposed skin at these locations. The BURNSIM calculations were performed using data recorded between 0 and 153 seconds post-ignition. The resulting estimated temperature profiles are shown in Figures 60 through 65.

This BURNSIM analysis of the HFT/RAD data indicated that estimated skin temperature profiles increased between 80 and 85 seconds post-ignition (Fig. 60 through 65). The timing and magnitude of changes in the estimated skin temperature profiles correlated with the recorded convective and radiative heat flux data used in these calculations, which was dependent on the location and orientation of the HFT/RAD assemblies in the test vehicle. For example, HFT/RAD assemblies 10, 11, and 12 were located above the left front seat back headrest and HFT/RAD assemblies 13, 14, and 15 were located above the left rear seat back headrest (**APPENDIX E**).

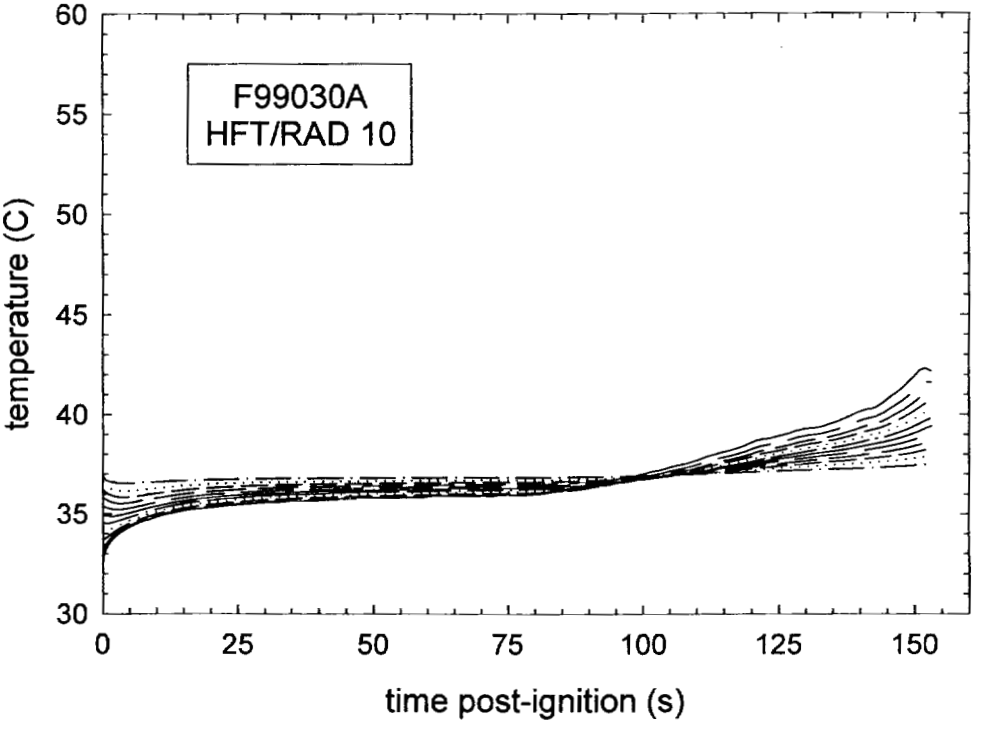

Figure 60. Fire Test F99030A. Skin temperature profiles estimated from heat flux data recorded from HFT/RAD Assembly 10 (**APPENDIX E**, Plots E3 and E4).

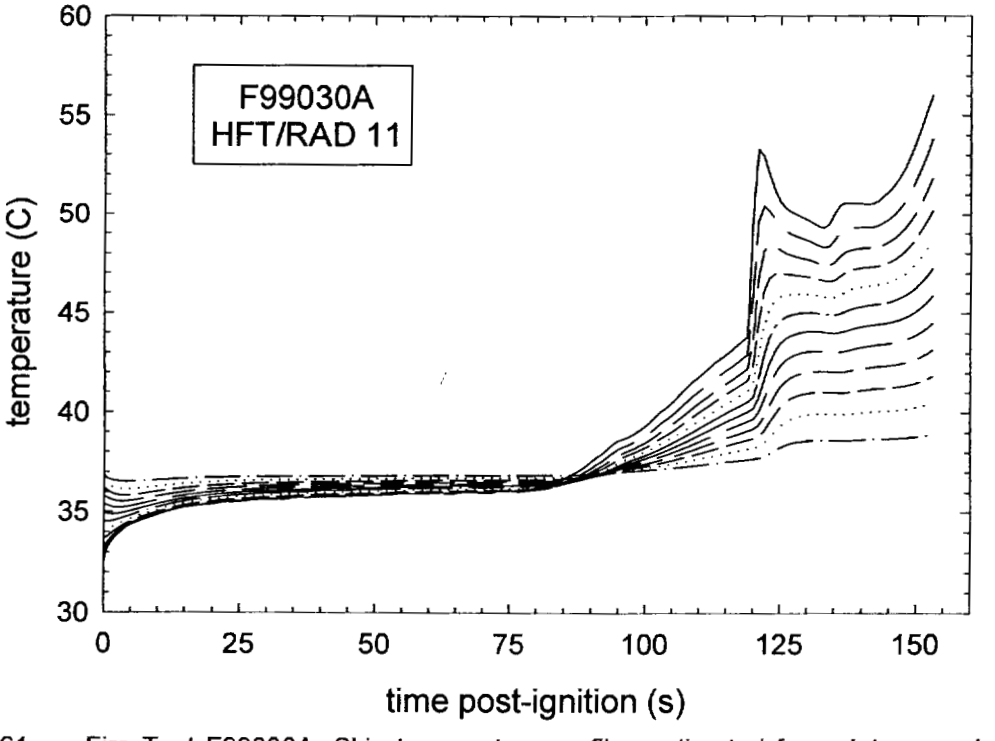

Figure 61. Fire Test F99030A. Skin temperature profiles estimated from data recorded from HFT/RAD Assembly 11 (**APPENDIX E**, Plots E5 and E6).

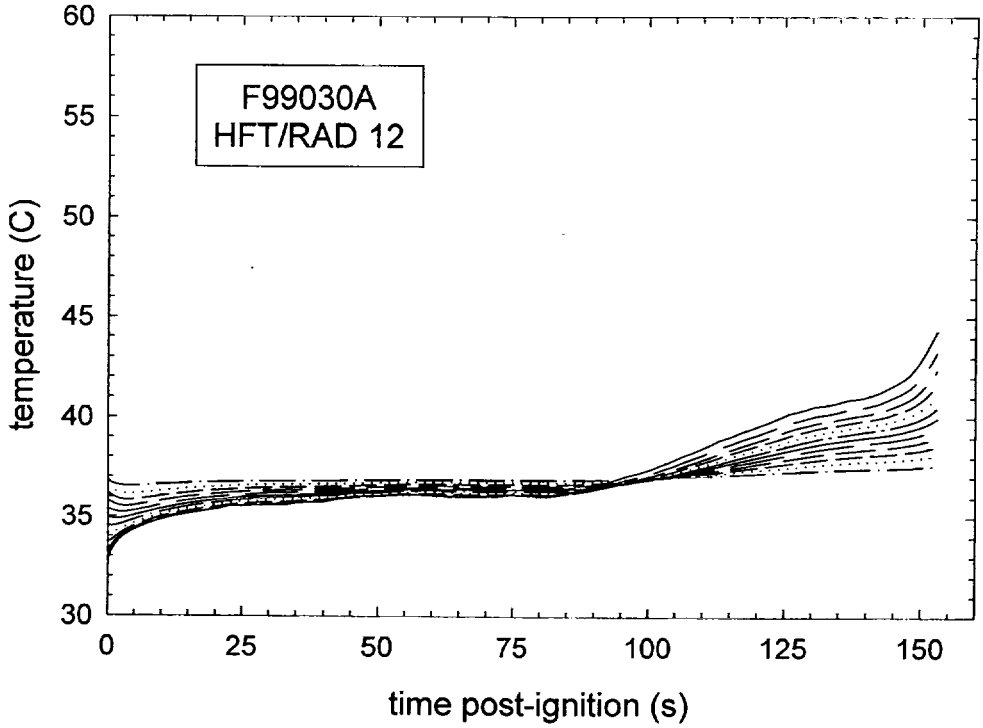

Figure 62. Fire Test F99030A. Skin temperature profiles estimated from data recorded from HFT/RAD Assembly 12 (**APPENDIX E**, Plots E7 and E8).

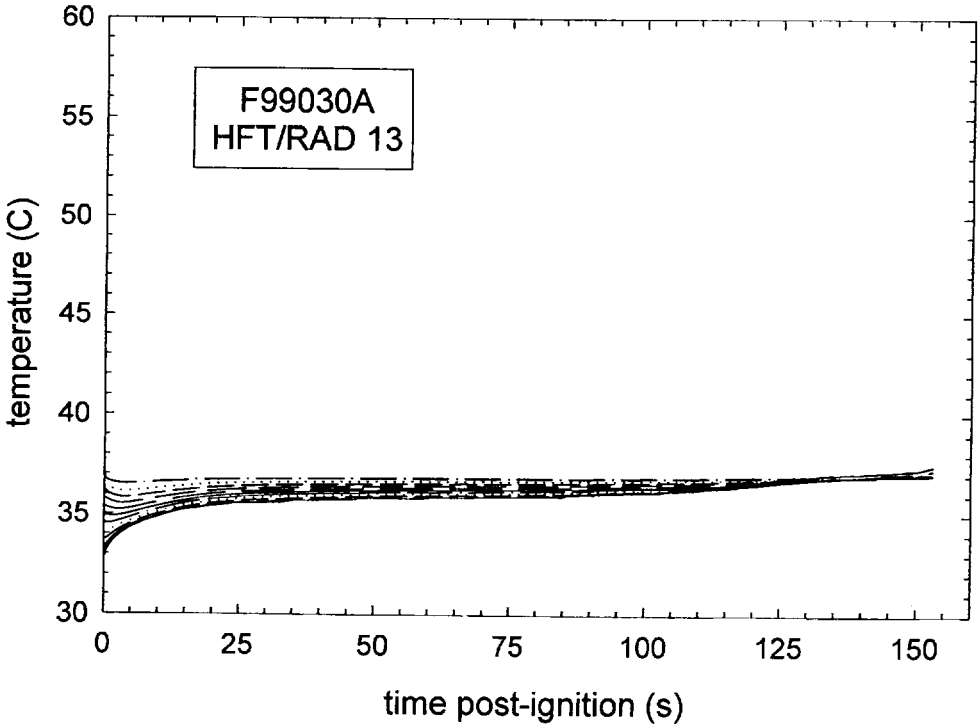

Figure 63. Fire Test F99030A. Skin temperature profiles estimated from data recorded from HFT/RAD Assembly 13 (**APPENDIX E**, Plots E9 and E10).

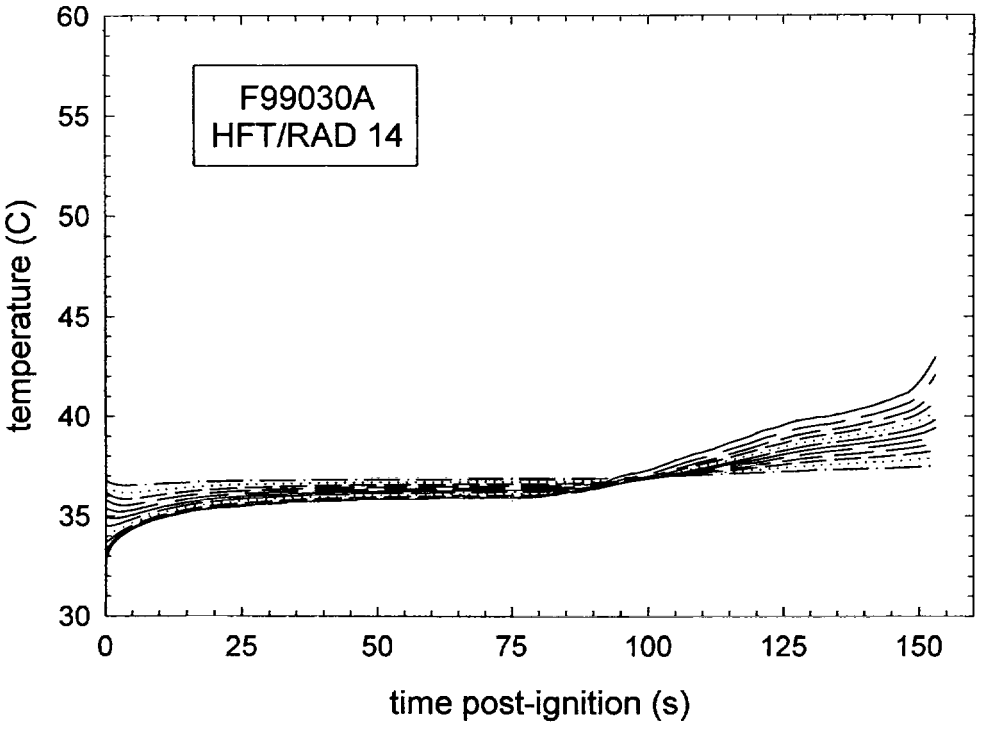

Figure 64. Fire Test F99030A. Skin temperature profiles estimated from data recorded from HFT/RAD Assembly 14 (**APPENDIX E**, Plots E11 and E12).

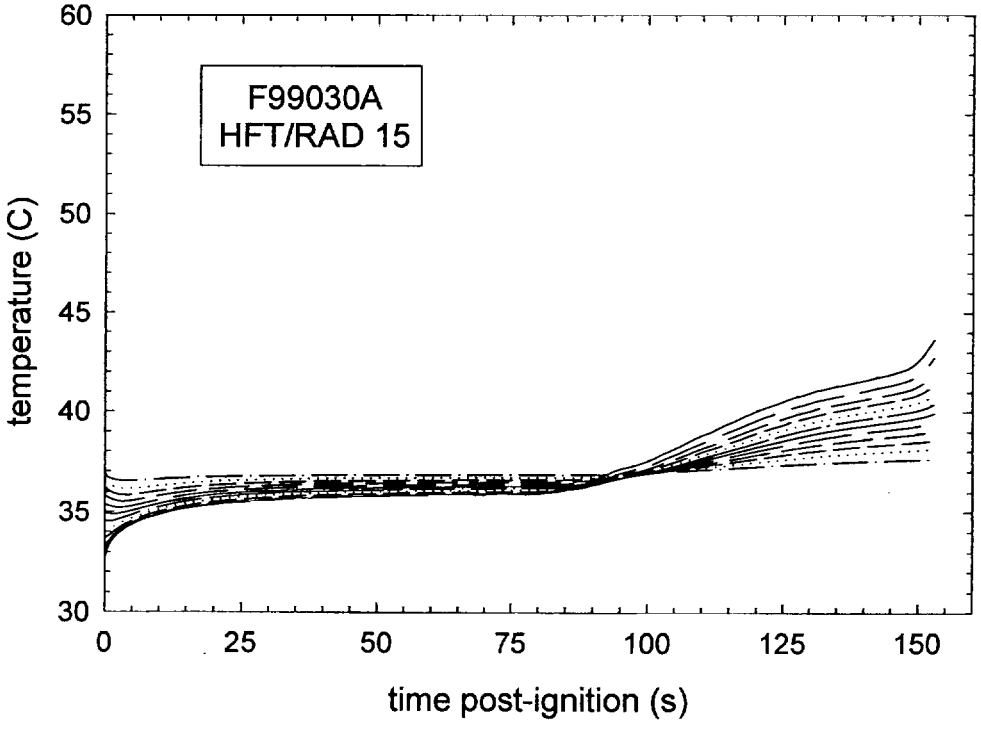

Figure 65. Fire Test F99030A. Skin temperature profiles estimated from data recorded from HFT/RAD Assembly 15 (**APPENDIX E**, Plots E13 and E14).

The transducer surfaces in HTF/RAD10, HTF/RAD11, and HFT/RAD12 were oriented toward the right rear corner of the test vehicle, upward toward the roof trim panel, and toward left rear corner of the test vehicle, respectively (**APPENDIX E**). The transducer surfaces in HTF/RAD13, HFT/RAD14, and HFT/RAD15 were oriented toward the right rear corner of the test vehicle, upward toward the roof trim panel, and toward the left rear corner of the test vehicle, respectively (**APPENDIX E**). Estimated epidermal temperatures at 150 seconds post-ignition were 42°C using data recorded from HFT/RAD10 (Fig. 60), 54°C using data recorded from HFT/RAD11(Fig. 61), and 43°C using data recorded from HFT/RAD12 (Fig. 62). Estimated epidermal temperatures at 150 seconds post-ignition were 37°C using data recorded from HFT/RAD13 (Fig. 63), 42°C using data recorded from HFT/RAD11(Fig. 64), and 43°C using data recorded from HFT/RAD12 (Fig. 65). These results indicate that the major mode of heat transfer to these locations during this test was radiation from flames in the left rear of the test vehicle and along the roof trim panel.

7.2 The FAA Combined Hazard Survival Model and Purser's Model of Combustion Gas Toxicity

The FAA Combined Hazard Survival Model and Purser's model utilize the concept of a Fractional Effective Dose [FED] to estimate the cumulative effects of exposure to a mixture of gases produced by burning materials. For exposure to a single gas with an unchanging concentration in air, the Fractional Effective Dose for Incapacitation [FED(I)] is defined as the product of the gas-phase concentration and the time of exposure ($C \times t$) normalized to the concentration-time product that results in incapacitation of 50% of an exposed population [7,8]. Similarly, the Fractional Effective Dose for lethality [FED(L)] is defined as the product of the gas-phase concentration and the time of exposure normalized to the concentration-time product that results in the death of 50% of an exposed population [see references in 7 and 8]. The estimates of FED(I) and FED(L) obtained using the FAA Combined Hazard Survival Model or Purser's model of combustion gas toxicity and presented in this report cannot be used to predict precisely when the gas concentrations measured in this test would have resulted in incapacitating narcosis or death for a vehicle occupant. Whether exposure to these gases results in toxicity depends on a number of complex physical and physiological variables.

Some of the physical variables include the exact chemical composition of the gaseous mixture, the concentration of each component of the gaseous mixture, and the time of exposure. Exposure to these gases in a burning vehicle can be highly variable, and depend on factors such as elevation in the passenger compartment and airflow through the passenger compartment. As mentioned in the previous section, combustion gases are hotter than the ambient air and form an

upper-layer. As both heat and mass are conserved in a fire, the existence of a steep vertical air-temperature gradient implies the existence of similarly steep vertical concentration gradients for gaseous combustion products accumulating in the passenger compartment. The location of the head and nose in the passenger compartment will effect the exposure concentration. An occupant whose head was located below the level where gases were measured, such as an occupant bent over in the seat, would have been exposed to lower concentrations of combustion gases than those shown in **APPENDIX H**. Airflow through the passenger compartment will dilute or remove these gases.

Uncertainties in the responses of humans exposed to these gases also complicate the determination of when and whether toxicity occurs. The mathematical equations for the calculation of FED(I) and FED(L) were derived by analysis of data from controlled experiments in which different species of laboratory animals were exposed to a range of concentrations of each gas. In using data from these laboratory animal experiments to define FED(I) and FED(L), both models implicitly assume that humans respond the same as laboratory animals to exposure to these gases – an assumption that is largely untested and may not be accurate. For example, except for incapacitation from exposure to carbon dioxide, none of the model predictions using either the FAA Combined Hazard Survival Model or Purser's model have been validated for humans. That is, the accuracy of FED(I) and FED(L) in predicting human responses to exposure to the combustion gases measured in this test has not been determined. Consequently, there is a high degree of uncertainty as to the effect exposure to these levels of combustion gases would actually have on a human vehicle occupant. In addition, neither of these models accounts for variation in individual responses to these gases nor the effect of trauma suffered during the crash on an occupant's response to these gases.

The equations presented in both the FAA Combined Hazard Survival Model and in Purser's model divide the exposure into one-minute intervals when the concentration of the gaseous species changes with time. In this test, Fourier Transform Infrared spectra were obtained at seven-second intervals to characterize the changing gas concentrations observed in the passenger compartment. The equations presented in the FAA Combined Hazard Survival Model and in Purser's model were modified to account for the faster sampling times used in this test. These modified equations are shown below and were used to derive the estimated of FED(I) and FED(L) shown in **SECTION 7.2.1.**

Carbon dioxide-induced hyperventilation can increase the respiratory uptake of airborn combustion products. The FAA Combined Hazard Survival Model uses a multiplication factor to

account for the increased respiratory uptake of gaseous combustion products because of exposure to elevated levels of carbon dioxide [V_{CO2}]:

$$V_{CO_2} = \frac{\exp(1.9086 + 0.2496 \times C_{CO_2})}{6.8} \quad (1)$$

where the units of C_{CO2} are %. This equation was not modified for the analysis presented in **SECTION 7.2.1**.

The Fractional Effective Doses for Incapacitation from exposure to carbon dioxide, carbon monoxide, hydrogen chloride, hydrogen cyanide and decreased oxygen were calculated using the following equations modified to account for sampling intervals of less than 1 minute:

$$FED(I)_{CO_2} = \left(\frac{t}{60}\right) \times \sum \left\{ \frac{1}{2193.8 - (311.6 \times C_{CO_2})} \right\} \quad (2)$$

when $5.5 \leq C_{CO2} \leq 7.0\%$,

$$FED(I)_{CO_2} = \left(\frac{t}{60}\right) \times \sum \left\{ \frac{1}{\exp(6.1623 - (0.5189 \times C_{CO_2}))} \right\} \quad (3)$$

when $C_{CO2} > 7.0\%$,

$$FED(I)_{CO} = \left(\frac{t}{60}\right) \times \left(\frac{1}{3.4250}\right) \times \sum \{V_{CO_2} \times C_{CO}\} \quad (4)$$

when $V_{CO2} \times C_{CO} > 0.01\%$,

$$FED(I)_{HCl} = \left(\frac{t}{60}\right) \times \sum \left\{ \frac{1}{3 + \frac{336{,}000}{(V_{CO_2} \times C_{HCl}) - 300}} \right\} \quad (5)$$

when $V_{CO2} \times C_{HCl} > 300$ ppm;

$$FED(I)_{HCN} = \left(\frac{t}{60}\right) \times \left(\frac{1}{564}\right) \times \sum \{(V_{CO_2} \times C_{HCN}) - 63\} \quad (6)$$

when $V_{CO2} \times C_{HCN} > 63$ ppm; and

$$FED(I)_{O_2} = \left(\frac{t}{60}\right) \times \sum \left\{ \frac{1}{\exp\left(8.55 - \left(0.511 \times \left(20.9 - C_{O_2}\right)\right)\right)} \right\} \qquad (7)$$

when $C_{O2} < 11\%$. The value of t in these equations was the time in seconds between acquisition of FTIR spectra. The overall Fractional Effective Dose for Incapacitation was calculated by summing the terms in equations 2 through 7:

$$FED(I)_{TOTAL} = FED(I)_{CO_2} + FED(I)_{CO} + FED(I)_{HCl} + FED(I)_{HCN} + FED(I)_{O_2} \qquad (8)$$

The Fractional Effective Doses for Lethality from exposure to carbon monoxide and hydrogen cyanide were calculated using the following equations modified to account for sampling intervals of less than 1 minute:

$$FED(L)_{CO} = \left(\frac{t}{60}\right) \times \sum \left\{ \frac{1}{\exp\left(5.85 - \left(0.00037 \times V_{CO_2} \times C_{CO}\right)\right)} \right\} \qquad (9)$$

when $2000 \leq V_{CO2} \times C_{CO} \leq 9000$ ppm,

$$FED(L)_{CO} = \left(\frac{t}{60}\right) \times \sum \left\{ \frac{1}{0.4 + \left(\frac{58{,}000}{V_{CO_2} \times C_{CO}}\right)} \right\} \qquad (10)$$

when $V_{CO2} \times C_{CO} > 9000$ ppm, and

$$FED(L)_{HCN} = \left(\frac{t}{60}\right) \times \left(\frac{1}{2586}\right) \times \sum \left\{ \left(V_{CO_2} \times C_{HCN}\right) - 43.2 \right\} \qquad (11)$$

when $V_{CO2} \times C_{HCN} > 43.2$ ppm;

The overall Fractional Effective Dose for Lethality was calculated by summing the terms in equations 8 through 10:

$$FED(L)_{TOTAL} = FED(L)_{CO} + FED(L)_{HCN} \qquad (12)$$

The model described by Purser also uses a multiplication factor to account for the enhanced respiratory uptake of toxic gases because of exposure to elevated levels of carbon dioxide:

$$V_{CO_2} = \frac{\exp(1.9086 + (0.2496 \times C_{CO_2}))}{6.8} \tag{13}$$

The Fractional Effective Doses for Incapacitation from exposure to carbon monoxide and hydrogen cyanide were calculated using the following equations modified to account for sampling intervals of less than 1 minute:

$$FED(I)_{CO_2} = \left(\frac{t}{60}\right) \times \sum \left\{ \frac{1}{\exp(6.1623 - (0.5189 \times C_{CO_2}))} \right\} \tag{14}$$

when $C_{CO2} > 5\%$,

$$FED(I)_{CO} = \left(\frac{t}{60}\right) \times V_{CO_2} \times \sum \left\{ \frac{0.00082925 \times C_{CO}}{30} \right\} \tag{15}$$

where the units of C_{CO} are ppm,

$$FED(I)_{HCN} = \left(\frac{t}{60}\right) \times V_{CO_2} \times \sum \left\{ \frac{4.4}{185 - C_{HCN}} \right\} \tag{16}$$

when $80 \leq C_{HCN} \leq 180$ ppm,

$$FED(I)_{HCN} = \left(\frac{t}{60}\right) \times V_{CO_2} \times \sum \left\{ \frac{1}{\exp(5.396 - (0.023 \times C_{HCN}))} \right\} \tag{17}$$

when $C_{HCN} > 180$ ppm; and

$$FED(I)_{O_2} = \left(\frac{t}{60}\right) \times \sum \left\{ \frac{1}{\exp(8.13 - (0.54 \times (20.9 - C_{O_2})))} \right\} \tag{18}$$

when $C_{O2} < 11.3\%$.

As in the FAA model, the value of t in these equations was the time in seconds between acquisition of FTIR spectra. The overall Fractional Effective Dose for Incapacitation was calculated by summing the terms in equations 14 through 18:

$$FED(I)_{TOTAL} = FED(I)_{CO_2} + FED(I)_{CO} + FED(I)_{HCN} + FED(I)_{O_2} \quad (19)$$

Both the FAA Combined Hazard Survival model and Purser's model predict that 50% of an exposed population would experience incapacitating narcosis (*i.e.*, an occupant loses consciousness and would be unable to exit a vehicle without assistance) when $FED(I)_{TOTAL} = 1.0$. Similarly, both of these models predict that 50% of an exposed population would die when $FED(L)_{TOTAL} \geq 1.0$.

7.2.1 Estimation of Fractional Equivalent Dose Parameters

Results of analysis of combustion products toxicity following procedures described in the FAA Combined Hazard Survival Model and Purser's model are shown in Figures 66 through 71. These analysis yielded estimates of $FED(I)_{co}$ only. The concentrations of carbon dioxide, hydrogen chloride, and hydrogen cyanide did not exceed the respective threshold concentrations for calculation of FED(I) at any time during this test. Therefore, these models did not yield estimates of $FED(I)_{CO2}$, $FED(I)_{HCN}$, and $FED(I)_{HCL}$. Other gaseous species included in these models, such as O_2, were not measured during this test, and values of FED(I) or FED(L) were not estimated for these gases.

Plots of the $FED(I)_{co}$ parameters estimated using both models are shown in Figure 67. The equations presented in the Purser model for computation of $FED(I)_{co}$ include a term for respiratory minute volume. Minute volumes corresponding to respiration during rest (8.5 L/min) and light activity (25 L/min) were used in these calculations [8]. Purser's model also accounts for the effect of exposure to carbon dioxide on respiratory rate.

The FAA Combined Survival Hazard Model computes only one estimate of $FED(I)_{co}$, which accounts for the effect of exposure to carbon dioxide on respiratory rate [7]. Both models yielded estimates of $FED(I)_{co} > 0$ between 50 and 80 seconds post-ignition. The estimates of $FED(I)_{co}$ derived using the FAA model and Purser's model with a respiratory minute volumes of 8.5 and 25 L/min reached maximum values of about 0.122, 0.112, and 0.149, respectively, at 330 seconds post-ignition, the time when FTIR data acquisition was discontinued.

The concentrations of carbon dioxide, carbon monoxide, hydrogen chloride, and hydrogen cyanide did not exceed the respective threshold concentrations for calculation of FED(L) at any time during this test. Therefore, neither the FAA Combined Survival Hazard Model nor Purser's model yielded estimates of $FED(L)_{CO}$, $FED(L)_{HCN}$, $FED(L)_{HCl}$, $FED(L)_{TOTAL}$ (Fig. 71).

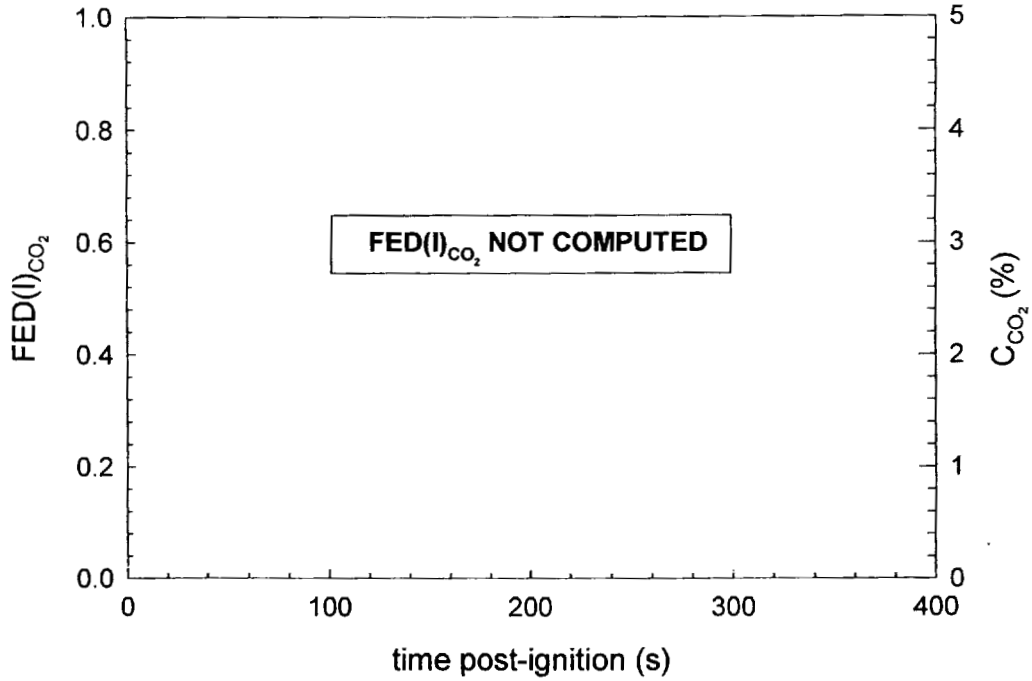

Figure 66. Fire Test F99030A. C_{CO2} did not exceed the threshold concentrations for calculation of FED(I)$_{CO2}$ at any time during this test. A plot of C_{CO2} (——) is shown for reference.

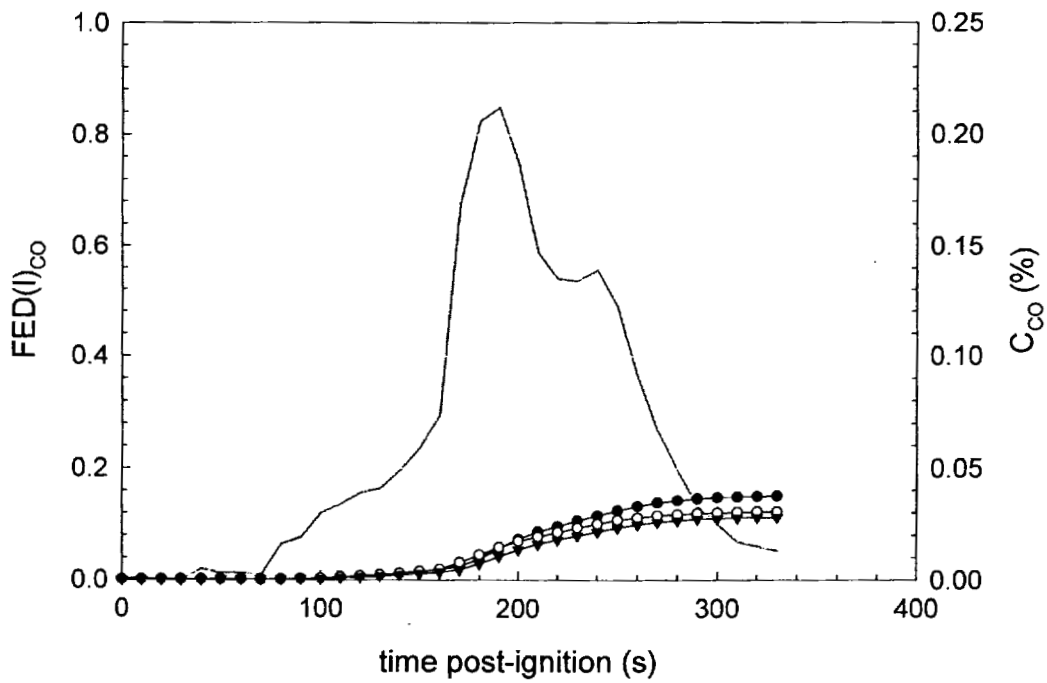

Figure 67. Fire Test F99030A. Plots of estimates of FED(I)$_{CO}$ versus time post-ignition computed using the FAA Combined Hazard Survival Model (—O—), the Purser model with a respiratory minute volume of 8.5 L/min (—▼—), and the Purser model with a respiratory minute volume of 25 L/min (—●—). A plot of C_{CO} (——) is shown for reference.

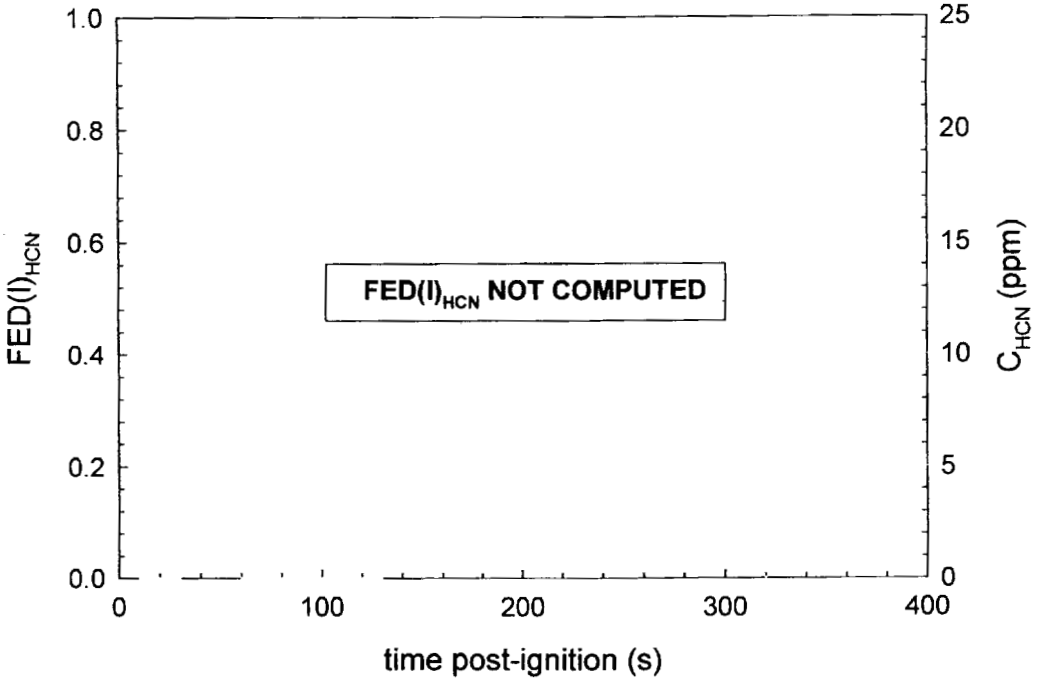

Figure 68. Fire Test F99030A. C_{HCN} did not exceed the threshold concentrations for calculation of $FED(I)_{HCN}$ at any time during this test. A plot of C_{HCN} (——) is shown for reference.

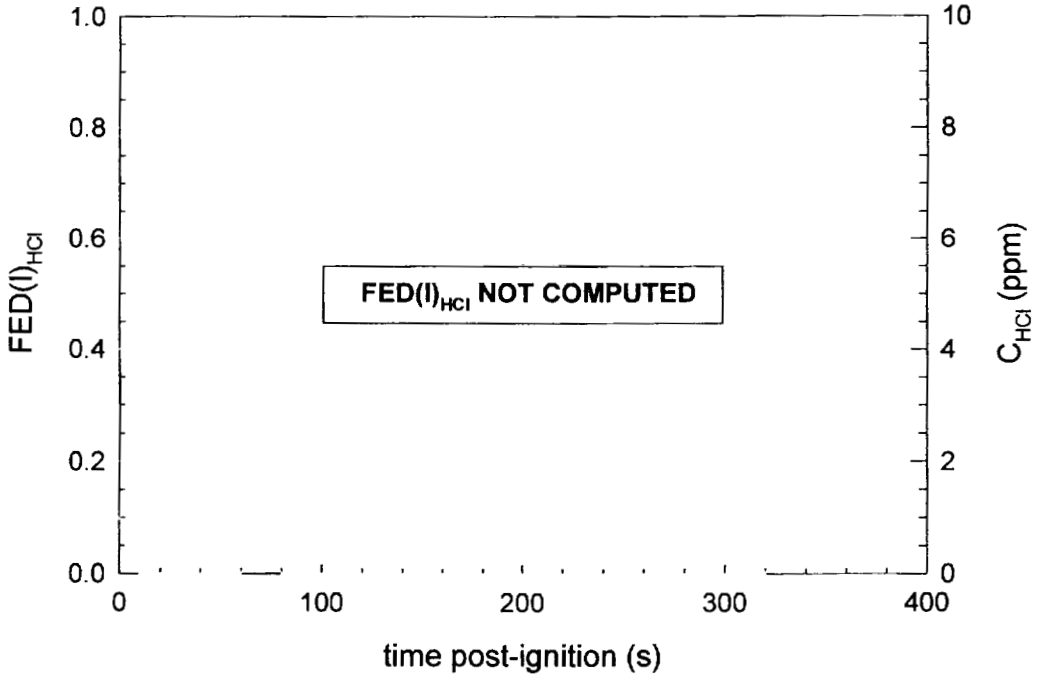

Figure 69. Fire Test F99030A. C_{HCl} did not exceed the threshold concentrations for calculation of $FED(I)_{HCL}$ at any time during this test. A plot of C_{HCl} (——) is shown for reference.

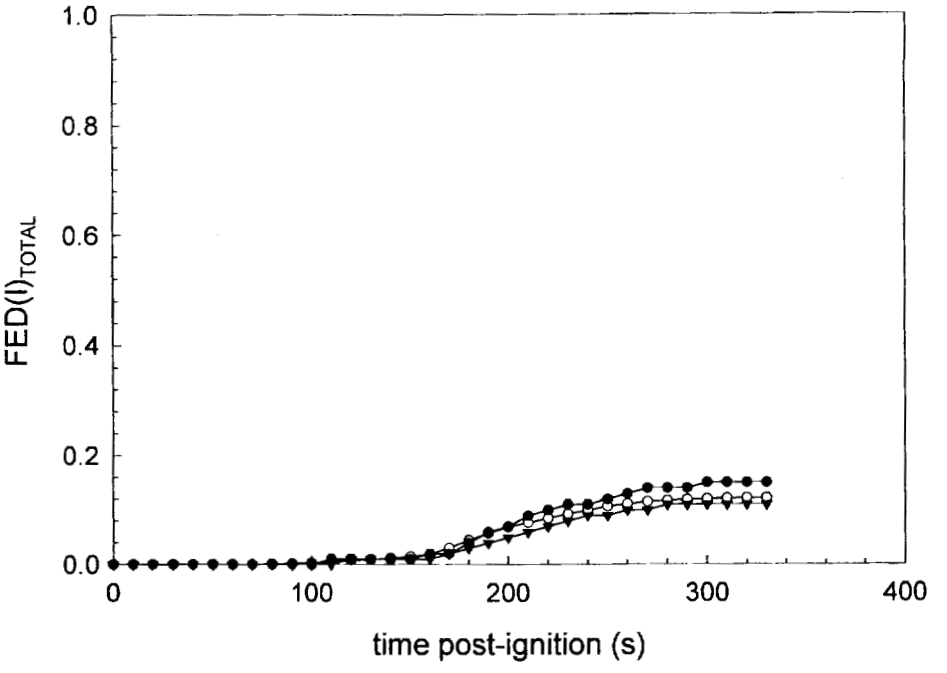

Figure 70. Fire Test F99030A. Plots of $FED(I)_{TOTAL}$ versus time post-ignition: FAA Combined Hazard Survival Model (—O—); Purser's model with RMV = 8.5 L/min (—▼—); and Purser's model with RMV = 25 L/min (—●—).

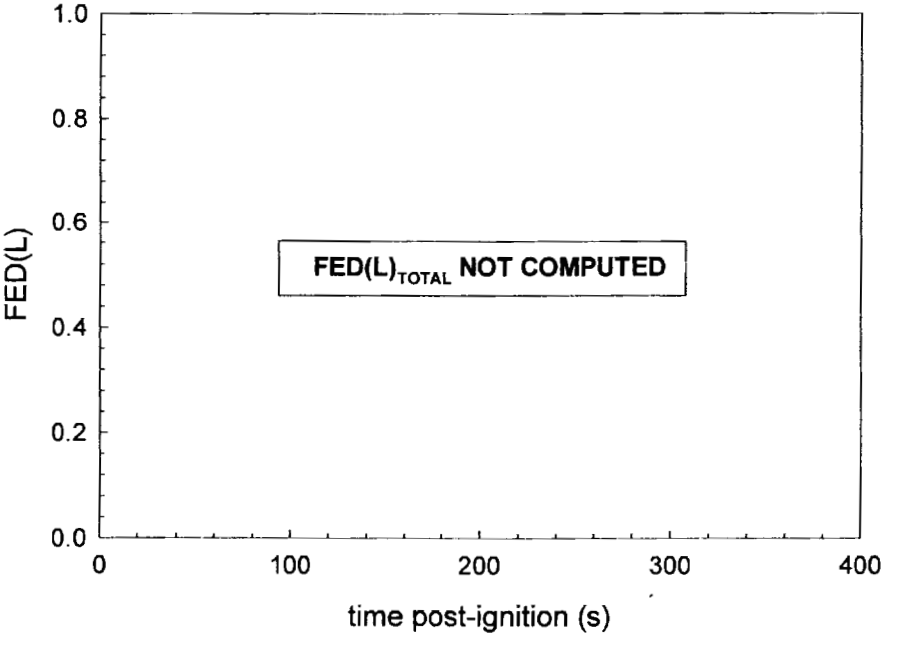

Figure 71. Fire Test F99030A. C_{CO2} , C_{HCN} , and C_{HCl} did not exceed the threshold concentrations for calculation of $FED(L)_{CO}$, $FED(L)_{HCN}$, and $FED(L)_{HCl}$ at any time during this test. Therefore, $FED(L)_{TOTAL}$ was not computed.

The estimates of FED(I) obtained using the FAA Combined Hazard Survival Model and Purser's model of combustion gas toxicity cannot predict precisely when exposure to the gas concentrations measured in this test would have resulted in incapacitating narcosis or death. This is especially true for prediction of lethality, where the mathematical relationships in these models were derived from experiments using laboratory animals or accidental, uncontrolled human exposures [7,8]. Variation in susceptibility to these hazards among the human population also will contribute to the uncertainty in these predictions. In addition, the effect of trauma caused by the crash on an occupant's tolerance to these toxic gases is impossible to quantify.

Another variable that may affect an occupant's susceptibility to the combustion products is the location of the head. The data from the aspirated thermocouples indicated that a steep air-temperature gradient developed in the front of the passenger compartment during this test (see below). As both heat and mass are conserved in a fire, the existence of a steep vertical air-temperature gradient implies the existence of a similarly steep vertical concentration gradient for combustion products accumulating in the passenger compartment. The inlet to the gas sampling tube in the passenger compartment was in the breathing zone of that of a six-foot tall adult male sitting upright in either the driver's or front passenger's seat. An occupant whose head was located below the level where gases were sampled would have been exposed to lower concentrations of combustion gases that those shown in **APPENDIX H**. And, the estimated values of FED(I) and FED(L) for this occupant would have been lower than those shown in Figures 64 through 69.

7.3 Estimation of Burn-Injury to the Respiratory Tract

Figure 70 shows plots of temperature data recorded from the aspirated thermocouples in the passenger compartment of the test vehicle (**APPENDIX D**). The aspirated thermocouple probe was located between the front seat backs and measured air temperature at 6 heights in the passenger compartment.

The data plotted in Figure 72 show the development of a vertical temperature gradient in the rear of the test vehicle during this test. Temperatures recorded from the aspirated thermocouples within the upwardly concave space in the deformed roof started to increase from the ambient air temperature between 10 and 15 seconds post-ignition (Fig. 72) as heated gases from the burning gasoline started to flow into this space. Data recorded from these thermocouples between 55 and 75 seconds post-ignition indicate that the temperature just below the roof trim panel varied randomly between 69 and 73°C (Fig. 72). The vertical temperature gradient in this space was about 1.8°C/cm and did not vary with vertical distance (Fig. 72).

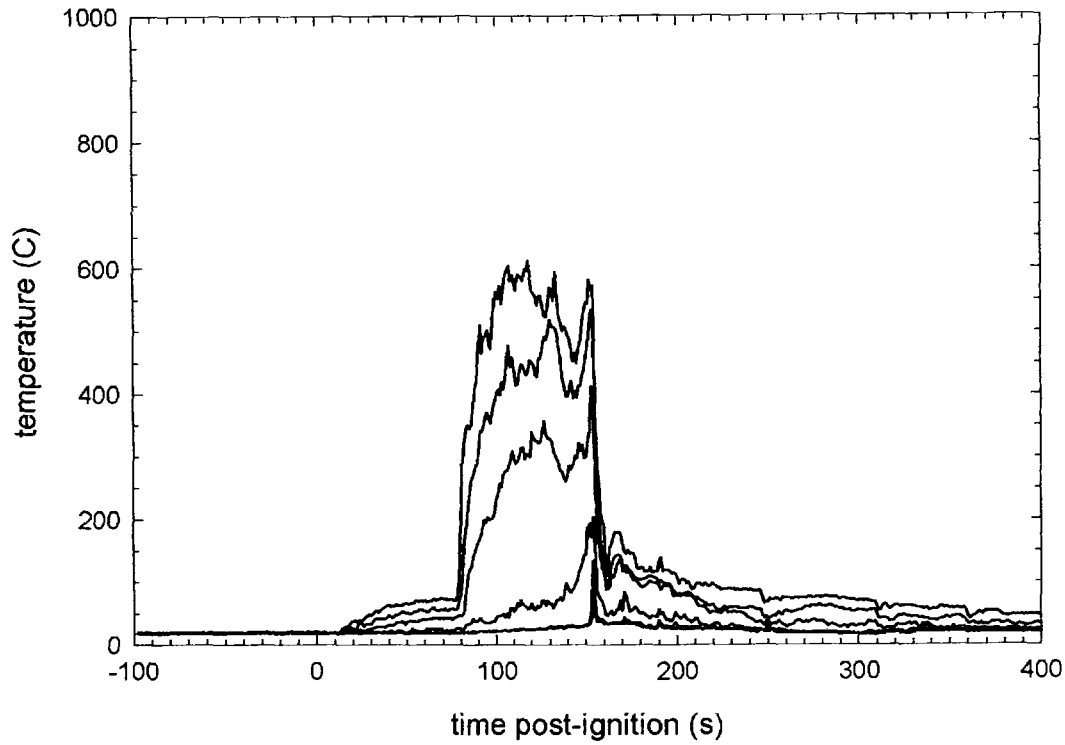

Figure 72. Fire Test F99030A. Plots of temperature data recorded from the aspirated thermocouples in the passenger compartment of the test vehicle.

Temperatures recorded from the aspirated thermocouples located below the concave space in the deformed roof did not increase from pre-ignition levels during this time (Fig. 70).

Temperatures recorded from all of the aspirated thermocouples increased starting at about 80 seconds post-ignition (Fig. 72) as flames started to spread into the passenger compartment and the space in the deformed roof (see **SECTION 5.1**). At 150 seconds post-ignition, the temperature just below the roof trim panel was 546°C (Fig. 72). The vertical temperature gradient in the rear of the passenger compartment varied with vertical distance below the roof trim panel (Fig. 72). This non-uniformity in the vertical temperature gradient reflects different temperature conditions that existed in the burning upper layer and the heated gases below the upper layer. Estimated temperature profiles along the roof trim panel indicate that the burning upper layer did not extend horizontally beyond the left rear quadrant of the passenger compartment during this test (Fig. 53). The temperature data recorded from the aspirated thermocouples indicates that the burning upper layer extended between 8 and 15 cm below the roof trim panel at the location of the aspirated thermocouple probe (Fig. 72). The vertical temperature gradient within the upper layer was about 11°C/cm (Fig. 72). The vertical temperature gradient in the space 15 to 20 cm below the upper layer was about 20C/cm (Fig. 72). The air temperature recorded from

thermocouples located approximate 30 and 38 cm below the roof trim panel was 32°at 150 seconds post-ignition (Fig. 72).

It is not possible to estimate the potential for burn injury to the respiratory tract caused by inhalation of hot air by relying solely on air temperature data. Water and particulate produced by the fire increase the heat capacity of the air. The concentrations of these species in the inhaled air have been shown to affect both the severity and depth of burn injury in the respiratory system [see references in 8]. Neither the water- nor the particulate-concentrations of air in the passenger compartment were measured in this test. Purser states that a robust quantitative relationship between the temperature, water-content, and particulate-content of inhaled air and subsequent burn injury to respiratory airways has not been established [8]. A few controlled animal studies indicate that inhalation of steam at 100°C caused burns to the larynx and trachea similar to those produced by inhalation of dry air at 350°C or flames at 500°C [see references in 8]. In these controlled animal studies, death was not immediate, but resulted from obstructive edema in the burned airways a few to twenty-four hours after the exposure. As the concentration of water vapor in the air sampled from the passenger compartment was not measured during this test, the potential for burn injury to the respiratory airways from inhalation of hot gas cannot be determined accurately from the air temperature data shown. Moreover, as the discussion above shows, the measured air temperature in the passenger compartment was dependent on the height of the thermocouple, specifically the distance below the roof. As small changes in vertical distance resulted in relatively large chances in air temperature, the temperature of inhaled air depends on the height of the breathing zone in the passenger compartment.

ACKNOWLEDGEMENTS

Dr. Thomas Ohlemiller and Thomas Cleary of the Building and Fire Research Laboratory, National Institute of Standards and Technology were responsible for video taping this fire test, and provided an initial analysis of the test data for fire propagation. Dr. Archibald Tewarson of Factory Mutual Research Corporation provided the data from the Fire Products Collector at the test facility that was collected during this test.

REFERENCES

1. Jack L. Jensen and Jeffrey Santrock. Evaluation of Motor Vehicle Fire Initiation and Propagation. Part 1: Vehicle Crash Test and Fire Propagation Test Program. Submitted to the National Highway Transportation Safety Administration pursuant to the Settlement Agreement between General Motors and the Department of Transportation. Submitted July 31, 1997.

2. Jack L. Jensen and Jeffrey Santrock. Evaluation of Motor Vehicle Fire Initiation and Propagation. Part 11: Crash Tests on a Front-Wheel Drive Passenger Vheicle. Submitted to the National Highway Transportation Safety Administration pursuant to the Settlement Agreement between General Motors and the Department of Transportation. Submitted May 7, 2002.

3. Federal Safety Standards. Motor Vehicle Safety Standard No. 214 Side Impact Protection - Passenger Cars, Trucks, Buses & Multipurpose Passenger Vehicles with GVWR of 10,000 Pounds or Less. 60FR57838-39 (November 22, 1995).

4. SigmaPlot® 4.0 for Windows®, SPSS Inc., 444 North Michigan Avenue, Chicago, IL 60611. Copyright © 1997 by SPSS Inc..

5. Archibald Tewarson. "Generation of Heat and Chemical Compounds in Fires" Section 3/Chapter 4, SFPE Handbook of Fire Protection Engineering, 2nd Edition, 1995, pp. 3:53-124.

6. F. S. Knox III, Dena Bonetti, and Chris Perry. User's Manual for BRNSIM/BURNSIM: A Burn Hazard Assessment Model. United States Army Aeromedical Research Laboratory Report No. 93-13. Fort Rucker, Alabama 36362-5292. February 1993.

7. L. C. Speitel. Toxicity Assessment of Combined Gases and Development of a Survival Model. DOT/FAA/AR-95-5. July 1995.

8. David A. Purser. "Toxicity Assessment of Combustion Products" Section 2/Chapter 8, SFPE Handbook of Fire Protection Engineering, 2nd Edition, 1995, pp. 2:85-146.

APPENDIX A
VIDEO CAMERA SET-UP

Scientific and technical personnel from the Building and Fire Research Laboratory, National Institute of Standards and Technology were primarily responsible for obtaining a video record of this test. Seven video cameras were used in this test. Figure A1 shows the approximate locations of the video cameras relative to the test vehicle during this test.

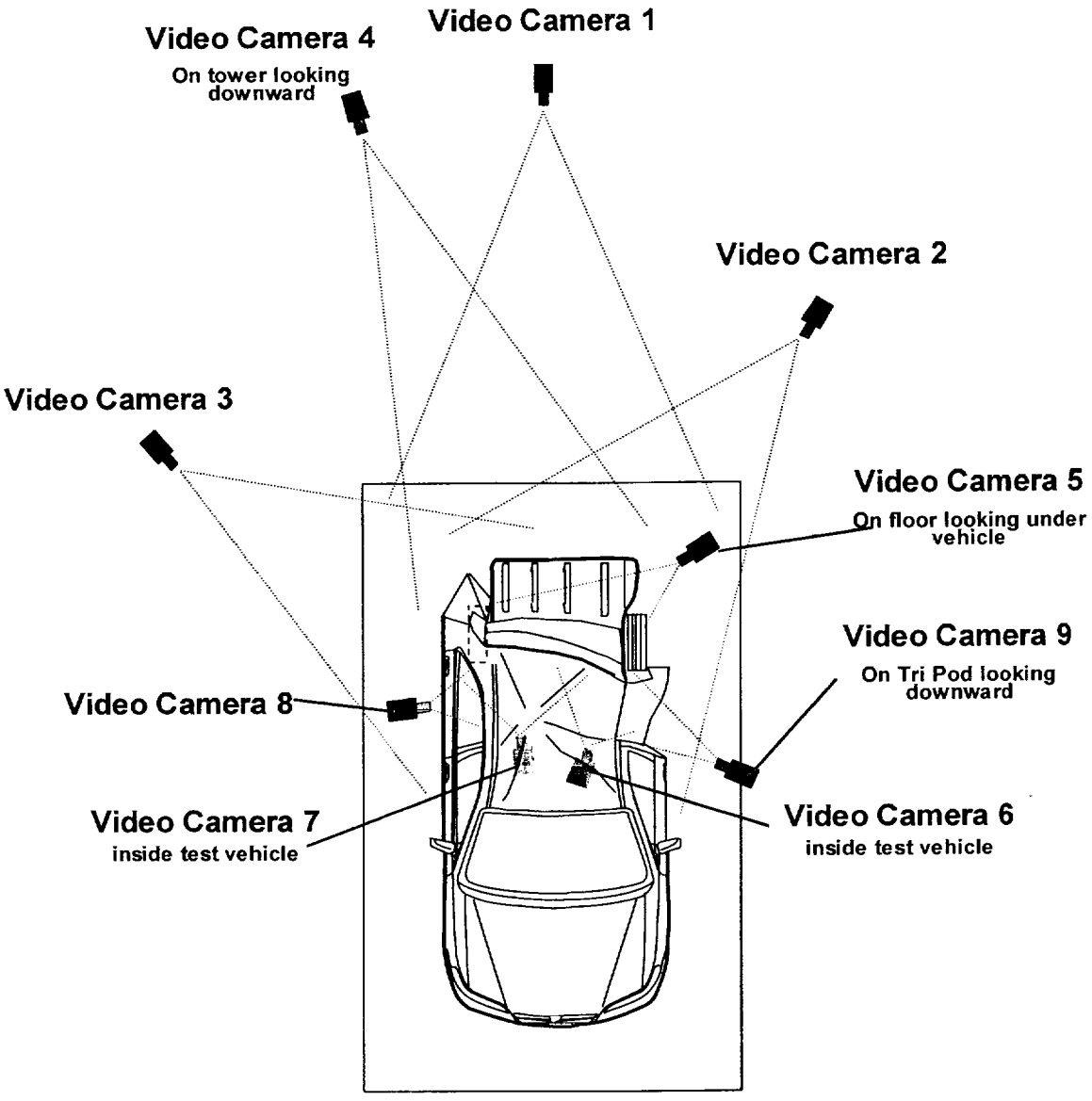

Figure A1. Fire Test F99030A. Diagram showing the approximate locations of the video cameras during this test. Distances in this figure are not to scale in this diagram.

Camera 1 was a Hi-8 camcorder mounted on a tripod. It had a field-of-view that included the full height and width of the rear of the test vehicle. Camera 2 was a Hi-8 camcorder mounted on a tripod. It had a field-of-view that included the left side of the test vehicle from about the rear edge of the front fender to beyond the rear bumper. Camera 3 was a Hi-8 camcorder mounted on a tripod. It had a field-of-view that included the right side of the test vehicle from about the rear edge of the front fender to beyond the rear bumper. Camera 4 was a Hi-8 camcorder mounted on a tower fixture approximately 3m above the test vehicle. Its field-of-view included the rear of the test vehicle. Camera 5 was a Hi-8 camcorder mounted on a stand approximately 10cm above the surface of the fluid containment pan. Its field of view included the area between the vehicle underbody and the test surface between the rear wheels. Camera 6 was a CCD camera installed in the interior of the test vehicle. It had a field of view that included the left rear corner of the rear passenger seat area. Camera 7 was a CCD camera installed in the interior of the test vehicle. It had a field of view that included the right rear corner of the rear passenger seat area. Camera 8 was a CCD camera mounted on a stand at the right rear door of the test vehicle. It had a field of view that included the seat in the rear passenger area. Camera 9 was a CCD camera mounted on a tripod looking down through the left rear door window opening of the test vehicle. It had a field of view that included the left rear corner of the rear passenger seat area.

All video cameras were started before the test. A microphone on each camera recorded an air horn signaling the start of gasoline flow, ignition of the gasoline, and the end of the test.

Quartz-halogen floodlights were used to illuminate the exterior of the vehicle. The level of illumination provided by these lamps was insufficient to balance the intensity of light reflecting from the vehicle surfaces with the brightness of the flames. To compensate for this imbalance, the light sensitivity adjustments on the Hi-8 camcorders were set to the manual position so that the apparent brightness of the vehicle surfaces did not change as the fire developed. As a result, the flames were overexposed, in some cases causing them to appear more opaque than they actually were.

APPENDIX B
INFRARED THERMOGRAPHY

Infrared thermal imaging radiometers were used to help determine fire propagation, flame, and surface temperatures during this test. These imaging systems measure thermal radiation within a definite waveband, over a variable field of view. The data obtained from these measurements can be analyzed to produce a two-dimensional map of apparent temperature called a thermogram.

Thermal imaging systems produce a spatially resolved map of surface temperatures from the radiant energy emitted in the field of view. The response time of these systems is nanoseconds, giving them the capability to acquire over 1 million discrete measurements per second. The capability of high-speed data acquisition is advantageous in that it can provide a tremendous amount of thermal data during a vehicle fire test, which can be over in only a few minutes. Thermal imaging radiometers can be used concurrently as a vision system and a measurement system. However, the thermal sensitivity, scan speed, and spatial resolution must be optimized for a particular application.

B.1 Infrared Camera Location

Eight thermal imaging systems were used in this test. Figure B1 shows the approximate locations of the infrared cameras relative to the test vehicle during this test. IR Camera 1 was an Inframetrics Model 760 long wavelength system (Inframetrics Inc, Billerica, MA). It was inside the vehicle and had a field of view that included the entire rear passenger area. IR Camera 2 was an Agima model 900 long wavelength system. It had a field of view that included the left side rear door window opening looking downward onto the rear seat backs and the rear package shelf. IR Camera 3 was an Inframetrics Model 760 long wavelength system. It had a field-of-view that included the right rear corner from the beltline to above the roof and from the B pillar to the rear of the test vehicle. IR Camera 4 was an Inframetrics Model 760BB system. It had a field-of-view that included the interior headliner looking upward through the left rear door window opening of the test vehicle. IR Camera 5 was an Inframetrics Model 740 long wavelength system. It was focused through the left rear door glass opening downward onto the rear passenger area. IR Camera 6 was an Inframetrics Model 760 long wavelength system. It had a field-of-view that included the left rear corner from the left rear tire to the left rear frame rail and from the middle of the tire up to the top of the tire. IR Camera 7 was an Inframetrics Model 760 long wavelength system. It had a field-of-view that included the left rear corner from B pillar to just past the rear of the vehicle and from the test surface to the roof of the test vehicle. IR Camera 8 was a Thermoviston Model 570. It had a field of view that included the entire rear end of the test vehicle.

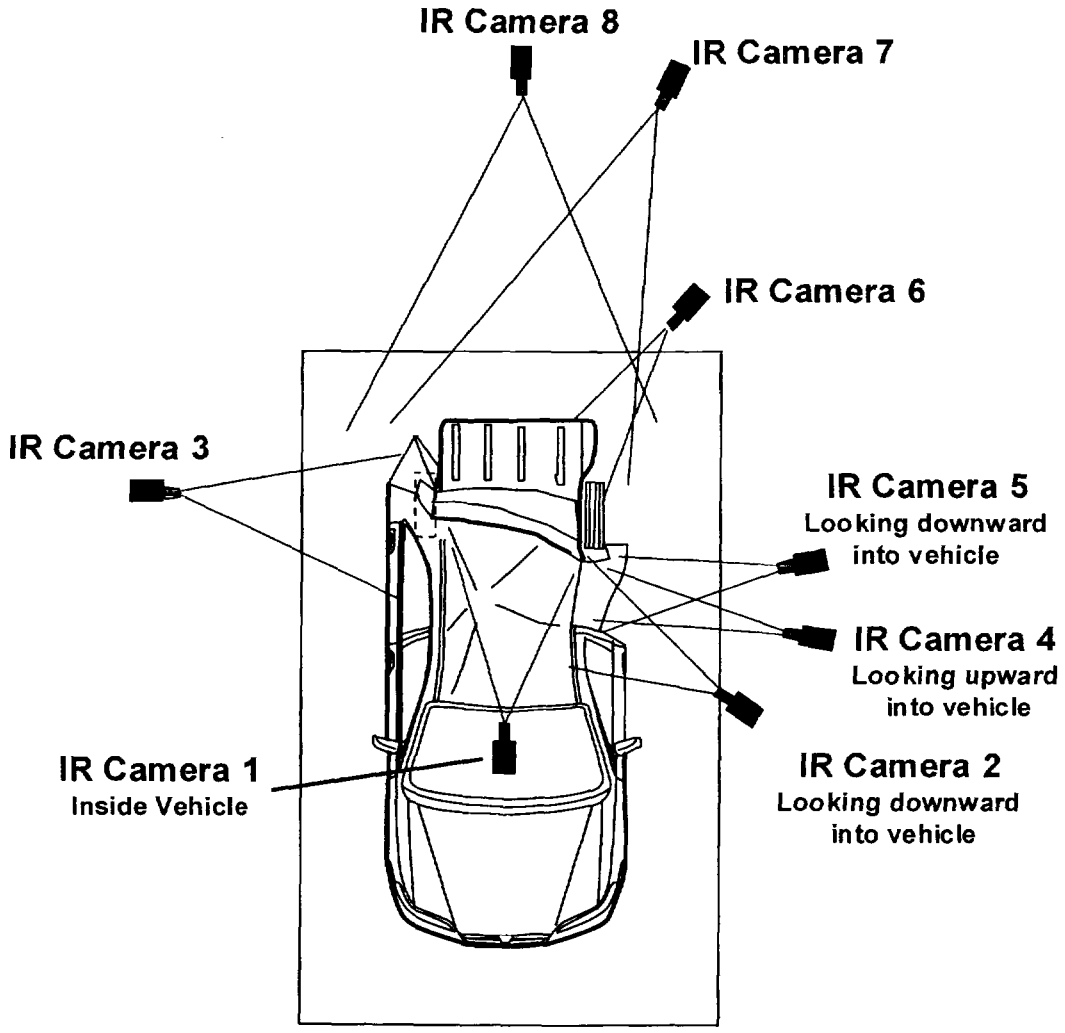

Figure B1. Fire Test F980609. Diagram showing the approximate locations of infrared cameras around the test vehicle during this test. This diagram is approximate and not drawn to scale in this diagram.

B.2 Data Analysis

Thermal imaging systems measure infrared radiation within a certain spectral band and must be calibrated to convert radiant intensity in that spectral band to temperature. Due to variations in system response, every system has to be calibrated. Calibration curves for the basic thermal imaging radiometers are measured at the factory and stored in read-only memory or in analysis software programs. Additional calibrations are needed for the optical filters. These calibrations are stored in the analysis software programs. Since thermal imaging radiometers are AC coupled devices, they measure differences in thermal radiation. To get absolute temperatures, there must be a reference to provide DC restoration. In these instruments, the reference is an internal blackbody reference source that is viewed periodically by the detector.

The general radiometric equation was used to convert radiant energy to temperature:

$$I = [E_t \times F(T_t)] + [(1 - E_t) \times F(T_b)] - [E_r \times F(T_r)] - [(1 - E_r) \times F(T_b)] \qquad \text{(B1)}$$

Where I is the difference in radiance between the target and a reference surface; E_t is the emittance of the target surface, generally unknown; E_r is the emittance of the reference surface, T_t is the temperature of the target surface; T_b is the temperature of background surfaces (i.e., ambient temperature), or other emitters such as flames reflected from the target; T_r is the temperature of the reference surface; $F(T_t)$ is the radiance from an ideal emitting surface (i.e., black body) at the temperature of the target surface (T_t); $F(T_r)$ is the radiance from an ideal emitting surface at the temperature of the reference (T_r); and $F(T_b)$ is the radiance from the background relative to the radiance value from the reference surface when $E_r = 1$. Factors other than temperature determine the emittance of an object. These factors include the type of material, the texture of the surface, the wavelength of the detector, and the view-angle. In determining temperatures from the radiant energy from an object, the operator can set the emittance of an unknown target surface to a value of between .01 and 1.0.

Radiant intensity measured by the thermal imaging system is converted to a gray-scale value. An 8 bit system provides gray scale values from 0 to 255 for the radiant energy at each pixel in the instantaneous field of view. A 12 bit system provides gray scale values from 0 to 4095. As the radiometer scans the image, each pixel is assigned a gray scale value, and the gray scale image is stored either in a computer memory or onto videotape. When stored in computer memory, a

single frame (1 thermogram) can contain up to 68,000 pixels (discrete measurements) with an assigned 8 bit or 12 bit value. Videotape provides a temporal resolution of 30 frames per second. Depending on the thermal range of the thermal imaging radiometer, a temperature value was assigned to each pixel using either the factory calibration curves accompanying each instrument, or calibration curves stored in IR analysis software.

Separation of the apparent temperatures of various surfaces on and inside a burning vehicle from the captured data is not a trivial task. The data represent a complex combination of emitted infrared energy from those surfaces as well as reflected infrared energy from the flames, and reflected infrared energy from high intensity lights used to illuminate the vehicle for visual data capture. In addition, the flames themselves were emitting infrared radiation due to their sooty content, some part of which was captured by the infrared thermal imaging systems. Also, some of the infrared radiation being emitted by the vehicle surfaces had to pass through flames containing soot from incomplete combustion of synthetic polymers or through clear (clean) flames where more complete combustion was occurring, and/or a combination of both types of flames. In all of these cases, gases in the flame absorbed some of the infrared radiation emitted by objects behind the flame.

The following steps were taken to minimize the impact of unwanted infrared radiation being captured by the thermal imaging systems.

- Anti-reflection tapes, paint, and glazes were applied to highly reflective surfaces on the test vehicle to minimize interference from reflections of the video floor and spot lights on the test vehicle.
- The thermal imaging systems were located in the shadows of the vehicle to block the video lights from shining directly into the radiometer.
- In some cases, flame filters (3.9 μm) were used in an attempt to screen out a portion of the infrared radiation from flames.

Despite these precautions, accurate surface temperatures could not be determined for areas of the vehicle blocked by intense flame. As a result, only surface temperatures determined to be reliable by the IR analysts are reported here. In some cases, specialized data analysis techniques were used to obtain reliable surface temperatures from areas in close proximity to, but not shielded by flame. Where possible, temperature data were reported from areas that lie in the shadow of the flames, which comes from highly emissive surfaces not affected by the flame radiation, and/or is deemed reliable based on the experience of the analysts. Data from nearby thermocouples were compared to IR temperature readings for a more comprehensive analysis.

During the data analysis, the videotapes were reviewed frame-by-frame to observe the burn sequence. The analyst captured images from selected frames on a video board. The image was processed to produce a digitized gray scale value for each element in the pixel matrix utilizing the camera settings automatically documented between video frames on the videotape during data acquisition. Thermograms were produced from the digitized image matrix using a commercial software package (Thermogram Pro V1.3, sold by Inframetrics, Inc., Billerica, MA). This software utilized the NIST traceable calibration tables supplied by the manufacturer with each thermal imaging system.

APPENDIX C
THERMOCOUPLE DATA

The thermocouples used in this test were type-N thermocouples fabricated by Medtherm Corporation (Huntsville, AL). Each thermocouple consisted of an ungrounded thermocouple junction (30 AWG thermocouple wire) enclosed in an Inconel 600 sheath insulated with magnesium oxide (o.d. = 0.040 in. (1 mm), length = 50 ft. (15.2 m)). A transition was made through a stress-relief bushing to a duplex thermocouple extension cable (24 AWG) with fiberglass insulation and a stainless steel over-braid (length = 1 ft. (0.28 m)). Each thermocouple wire terminated in a grounded, compensated Type-N thermocouple plug. The thermocouples were connected to the data acquisition system using Type-N thermocouple extension cables (length = 50 ft. (15.2 m)).

The data acquisition system consisted of a PC (75 MHz Pentium Processor, 16 MB RAM, an 814 MB hard disk, and a 16-bit, Model BG45-AP5CP, ACER Inc., Taiwan R. O. C.) with a 100 kHz I/O board with 16 analog input channels (DaqBoard 200A, IOTech, Inc., Cleveland, OH). Thermocouple multiplex expansion cards (DBK-19, IOTech, Inc., Cleveland, OH) were used for data acquisition from the thermocouples. The expansion cards were mounted in an electronics cabinet and hard-wired to a panel containing compensated Type-N thermocouple jacks.

To reduce electronic noise on the thermocouples, the ground leads from each thermocouple jack was connected to the electronic chassis ground of the thermocouple mutliplex extension cards. The vehicle chassis was connected to the electronic chassis ground by a large-gauge cable. The electronic chassis ground was connected to an isolated earth ground.

The data acquisition software (DASYLab, Daten System Technik GmbH, Mönchengladbach, Germany) was configured to sample each channel at a rate of 10 Hz and store the data in 10-point block averages.

Figures C1 through C4 show the approximate locations of thermocouples in the test vehicle. Plots C1 through C58 show plots of the temperature data recorded from these thermocouples during this test.

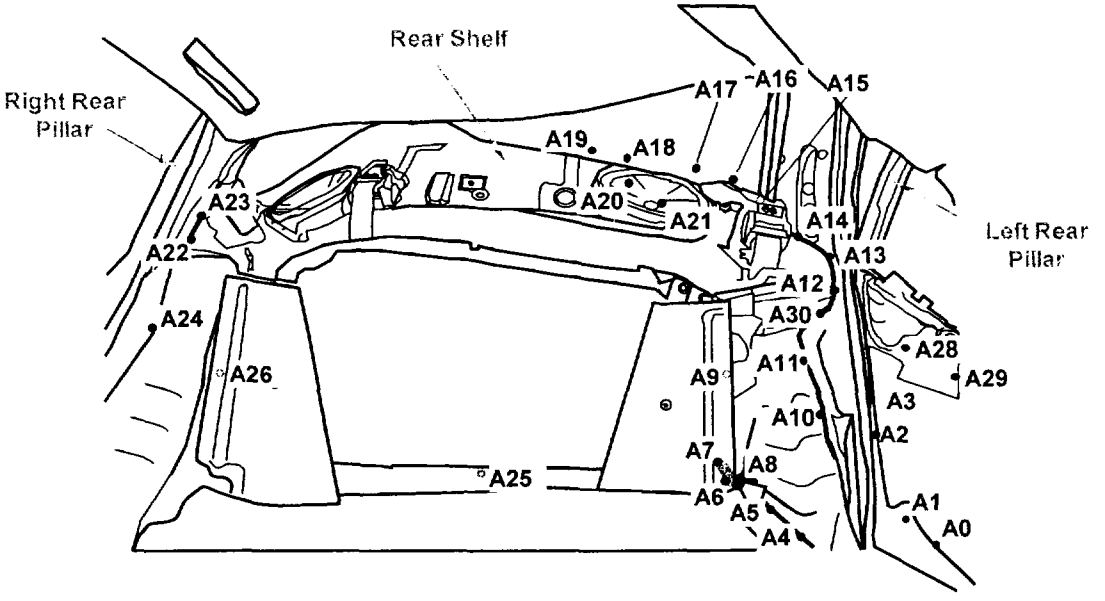

Figure C1. Fire Test F99030A. Diagram showing the approximate locations of thermocouples A0 through A30 in the test vehicle. Thermocouples A0, A1, A2, A3, A28, and A29 were located on the left rear inner door trim panel. Thermocouples A 4, A5, A6, A7, and A8 were located in a crash-induced seam opening between the left rear wheelhouse panel and the floor panel that extended from the passenger compartment rearward into the trunk. Thermocouple A9 was located behind the left rear seat back support panel above a crash-induced seam opening between the left rear wheelhouse panel and floor panel. Thermocouples A10, A11, A12, A13, A14, A15, and A30 were located in a crash-induced seam opening between the left rear wheelhouse panel and the left inner quarter panel. Thermocouples A16, A17, A18 and A19 were located along the rear edge of the rear package shelf. Thermocouples A20 and A21 were located above the speaker cone in the speaker on the left side of the rear package shelf. Thermocouples A22, A23, and A24 were located in a crash-induced seam opening between the right rear wheel house and the right inner quarter panel. Thermocouple A25 was located under the caret in a crash-induced gap between the floor panel and fuel pump assembly access cover plate in the trunk. Thermocouple A26 was located in a gap between the right rear wheelhouse and the right left rear seat back support panel. See Figure C4 for the location of Thermocouple A27. Thermocouples A28 and A29 located on the inner surface of the interior trim panel on the left rear door.

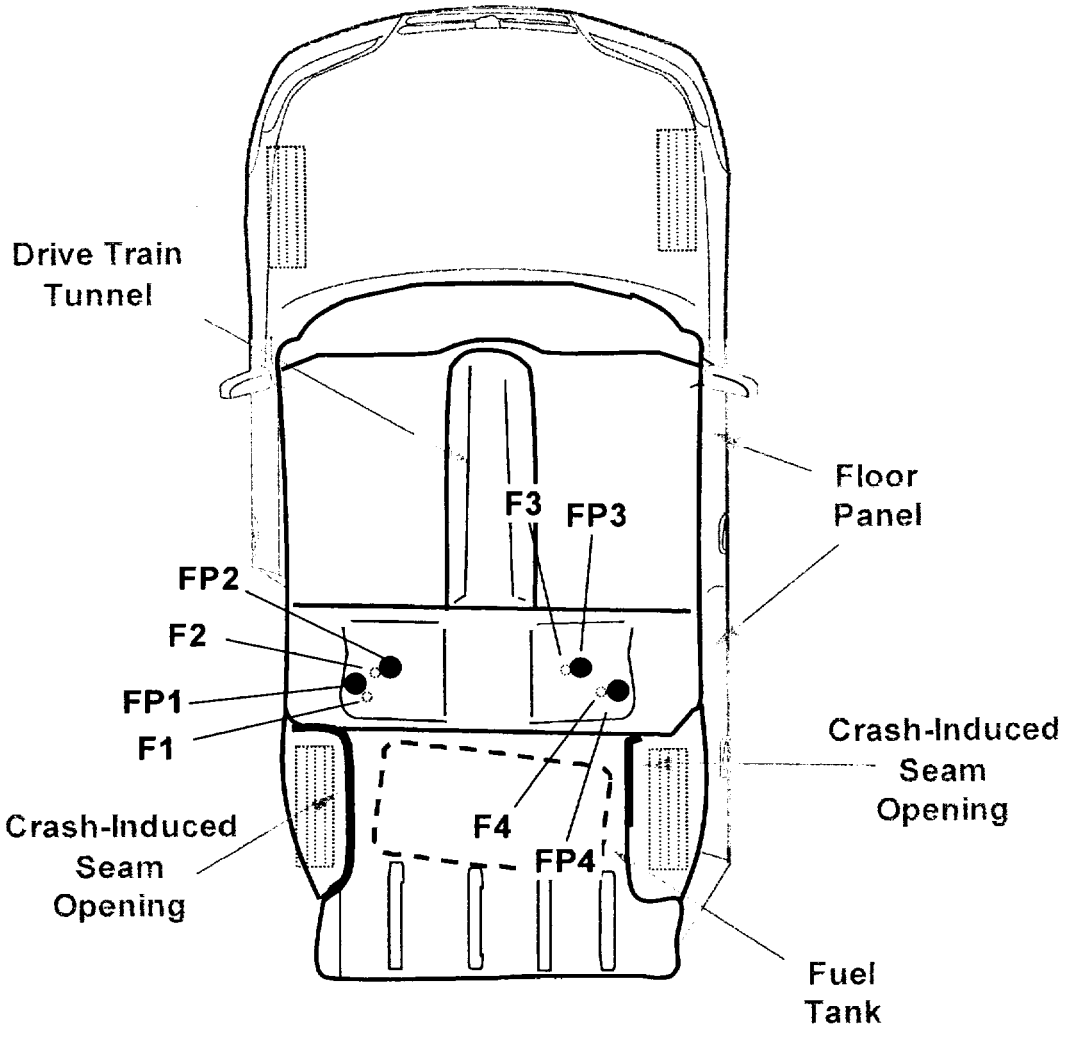

Figure C2. Fire Test F99030A. Diagram showing the approximate locations of thermocouples F1 through F4 and Thermocouples FP1 through FP4. Thermocouples F1, F2, F3, and F4 were located approximately 1 cm below the lower surface of the floor panel. Thermocouple FP1 was located on the upper surface of an electrical pass through in the floor panel under the left side of the rear seat cushion. Thermocouples FP2, FP3, and FP4 were located on the upper surfaces of drain hole plugs in the floor panel under the rear seat cushion.

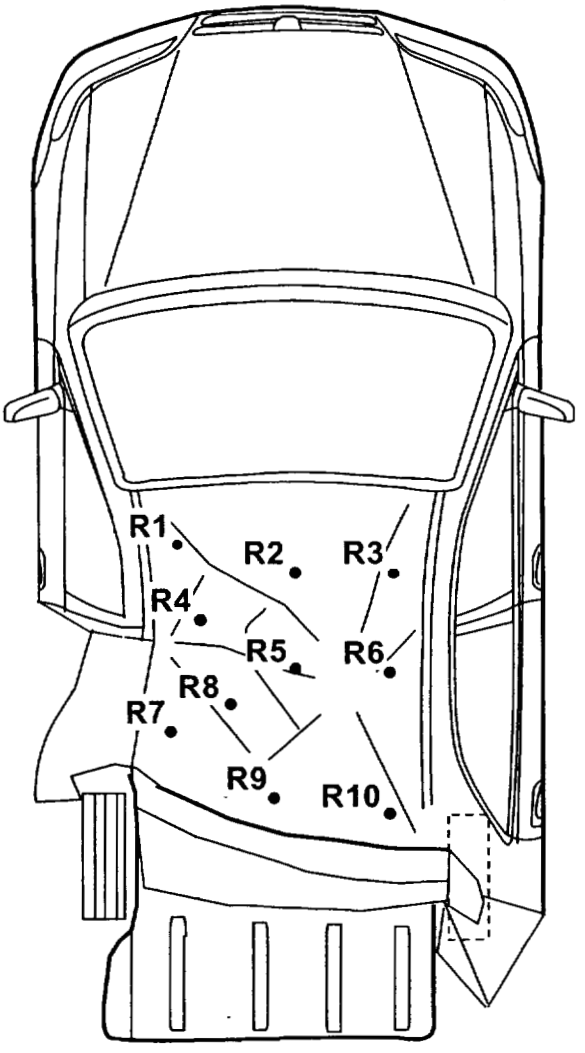

Figure C3. Fire Test F99030A. Diagram showing the approximate locations of thermocouples R1 through R10 in the test vehicle. Thermocouples R1, R2, R3, R4, R5, R6, R7, R8, R9, and R10 were located approximately 1 cm below the lower surface of the heat lining panel.

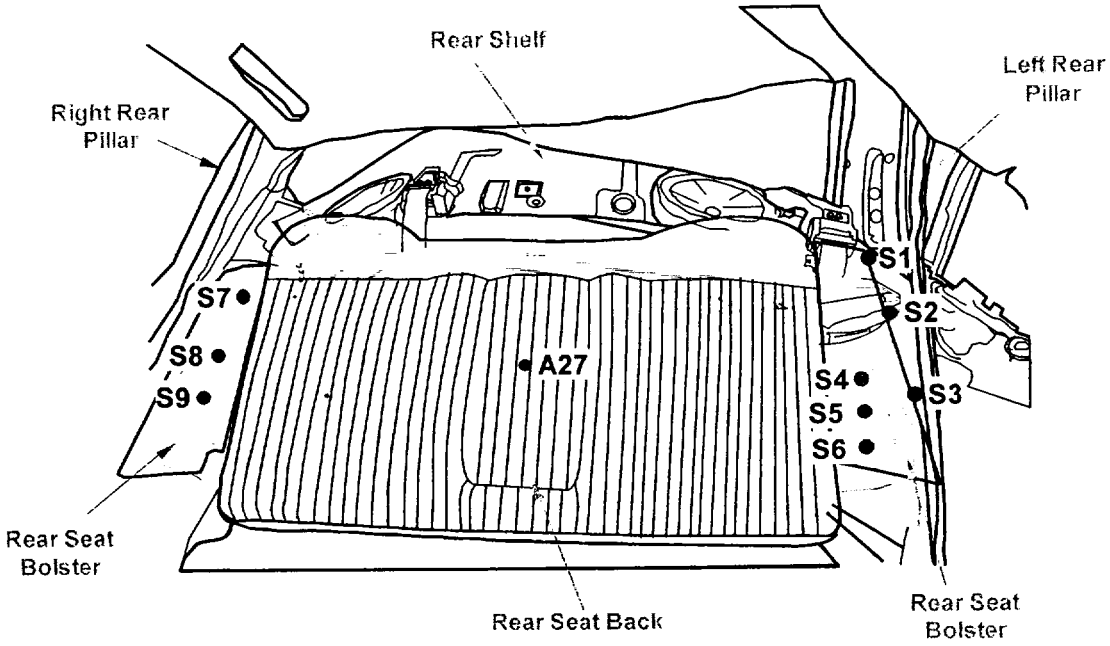

Figure C4. Fire Test F99030A. Diagram showing the approximate locations of thermocouples A 27 and S1 through S9 in the test vehicle. Thermocouple A27 was located on the rear surface of an access panel in the rear seat back. Thermocouples S1, S2, and S3 were located on the rear surface of the outer edge of the rear seat back left side panel. Thermocouples S4, S5, and S6 were located on the rear surface of the outer edge of the rear seat back left side panel. Thermocouples S7, S8, and S9 were located on the rear surface of the outer edge of the rear seat back right bolster.

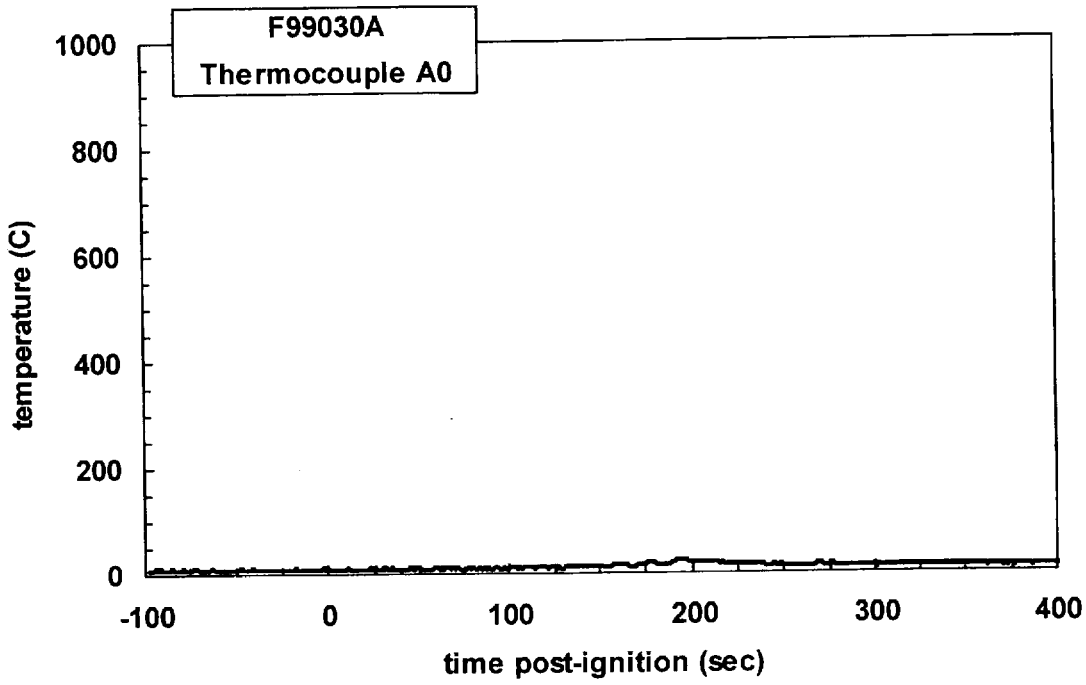

Plot C1. Fire Test F99030A. Data plot from thermocouple A0.

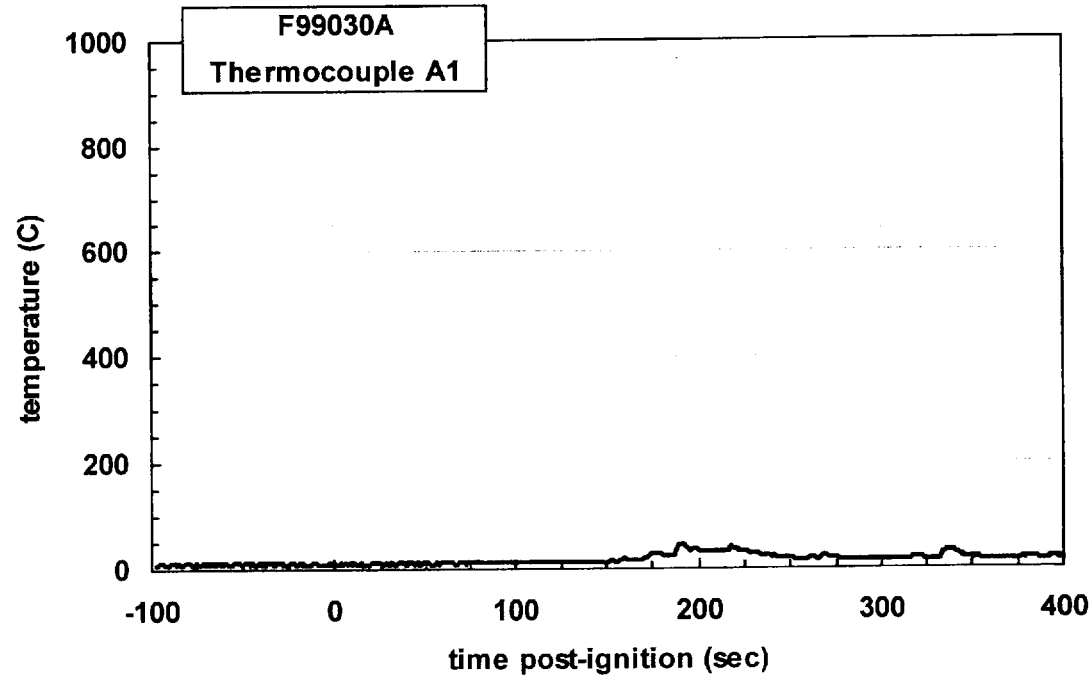

Plot C2. Fire Test F99030A. Data plot from thermocouple A1.

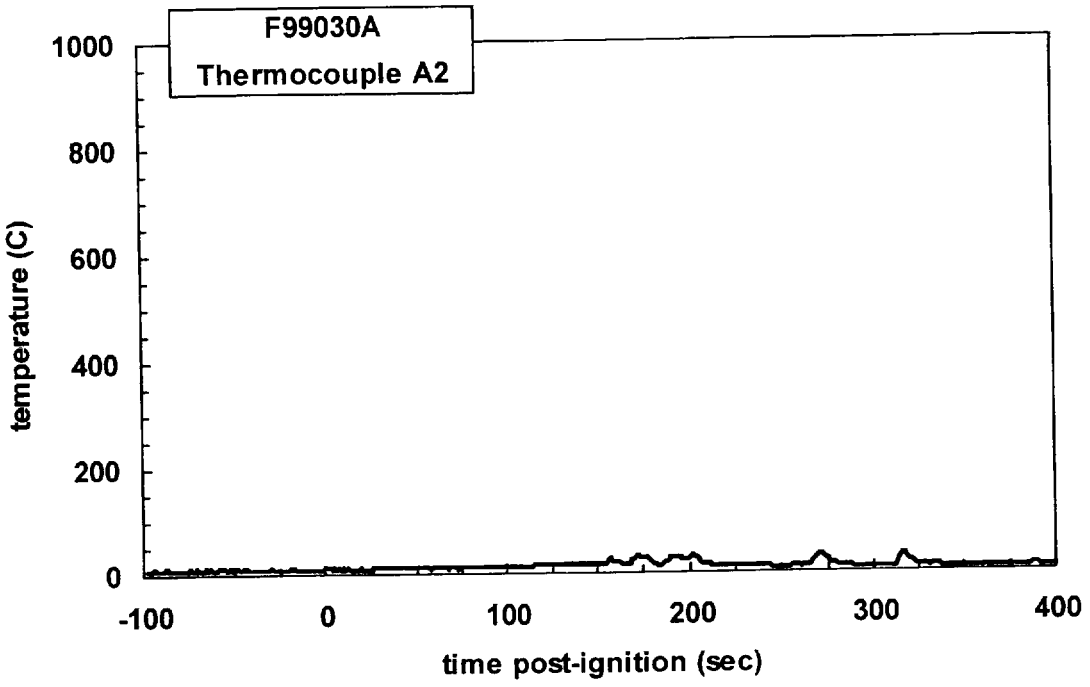

Plot C3. Fire Test F99030A. Data plot from thermocouple A2.

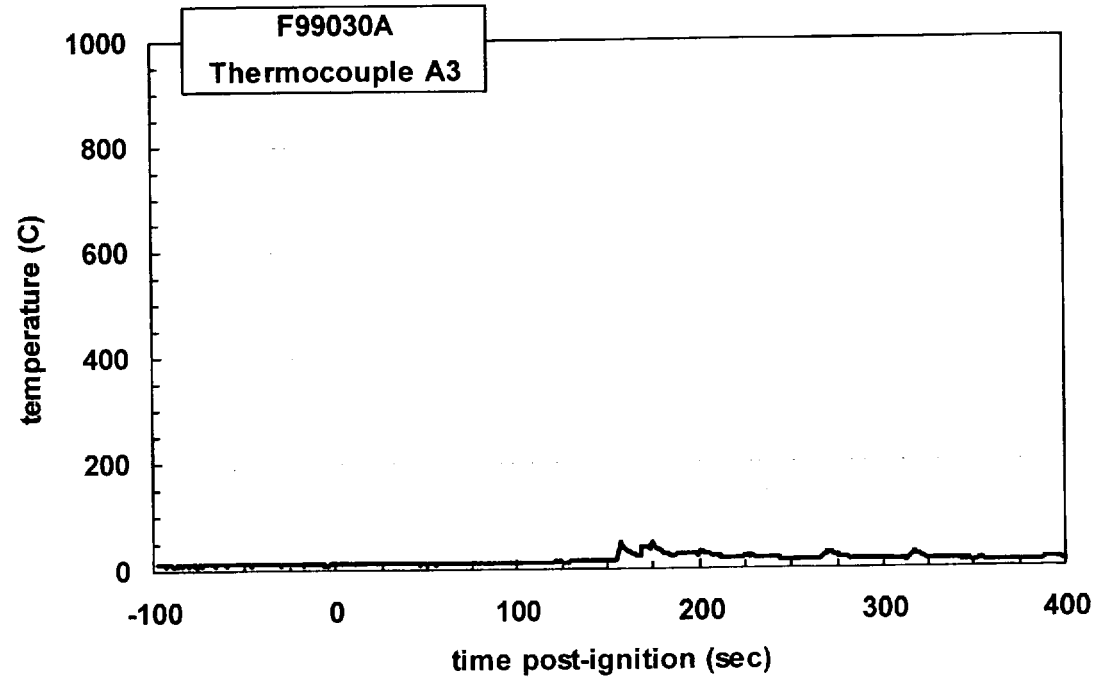

Plot C4. Fire Test F99030A. Data plot from thermocouple A3.

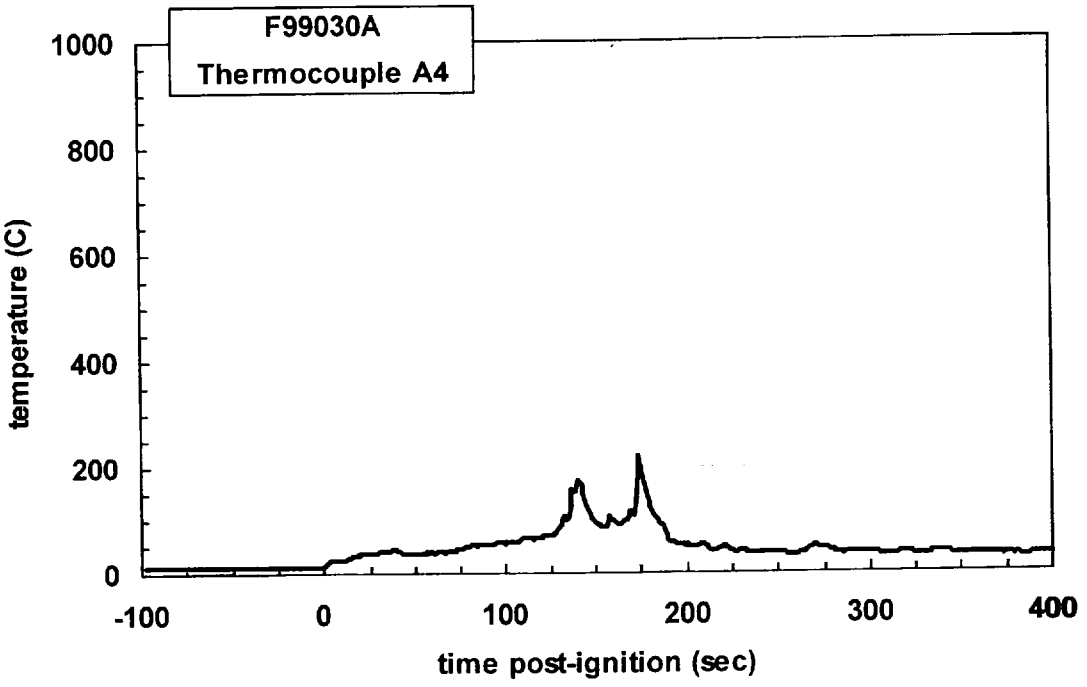

Plot C5. Fire Test F99030A. Data plot from thermocouple A4.

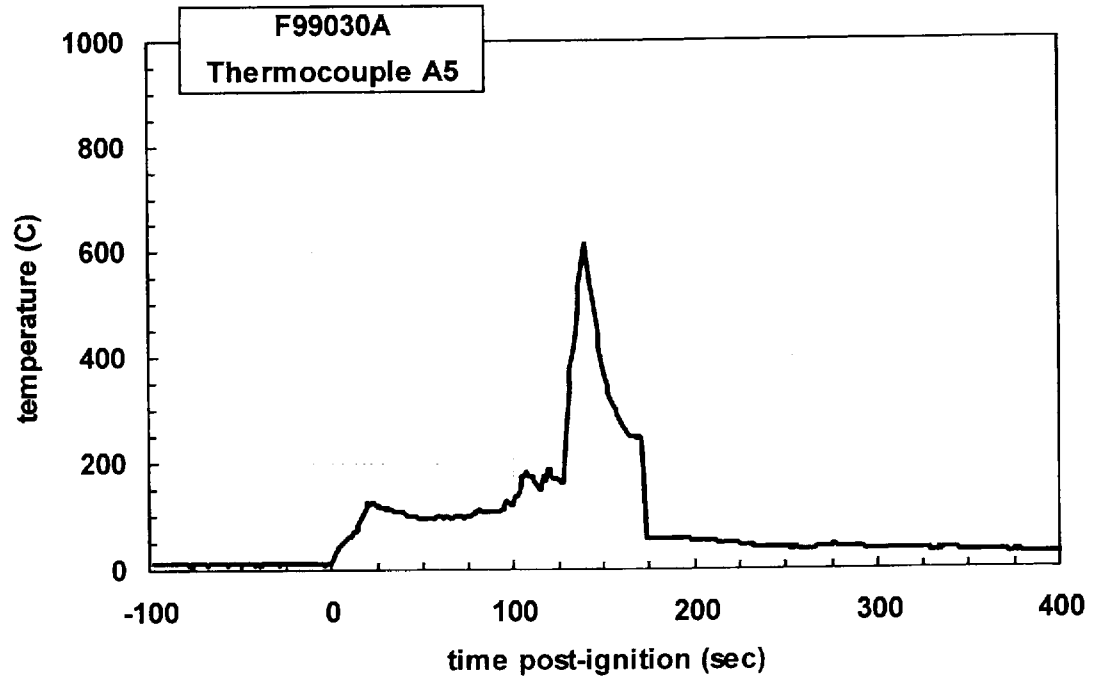

Plot C6. Fire Test F99030A. Data plot from thermocouple A5.

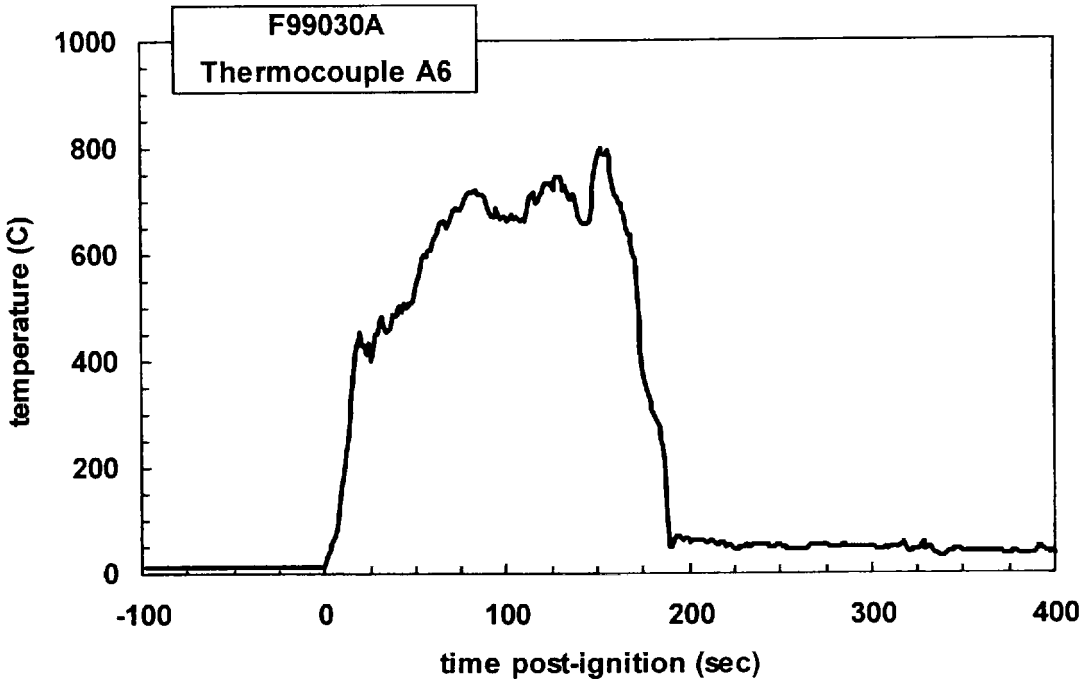

Plot C7. Fire Test F99030A. Data plot from thermocouple A6.

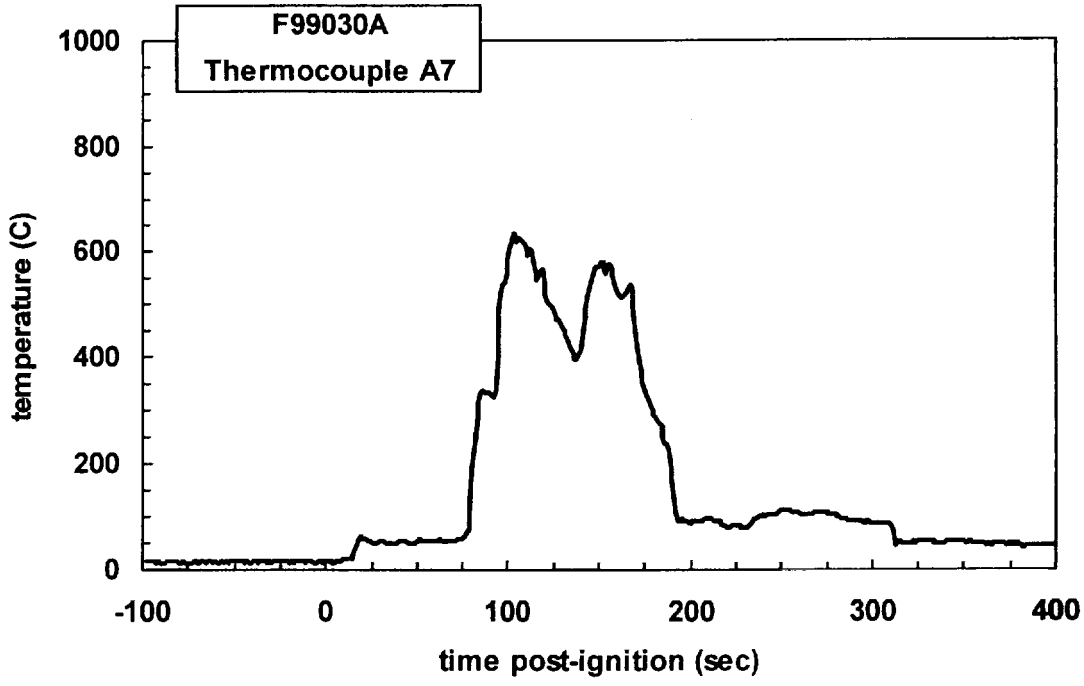

Plot C8. Fire Test F99030A. Data plot from thermocouple A7.

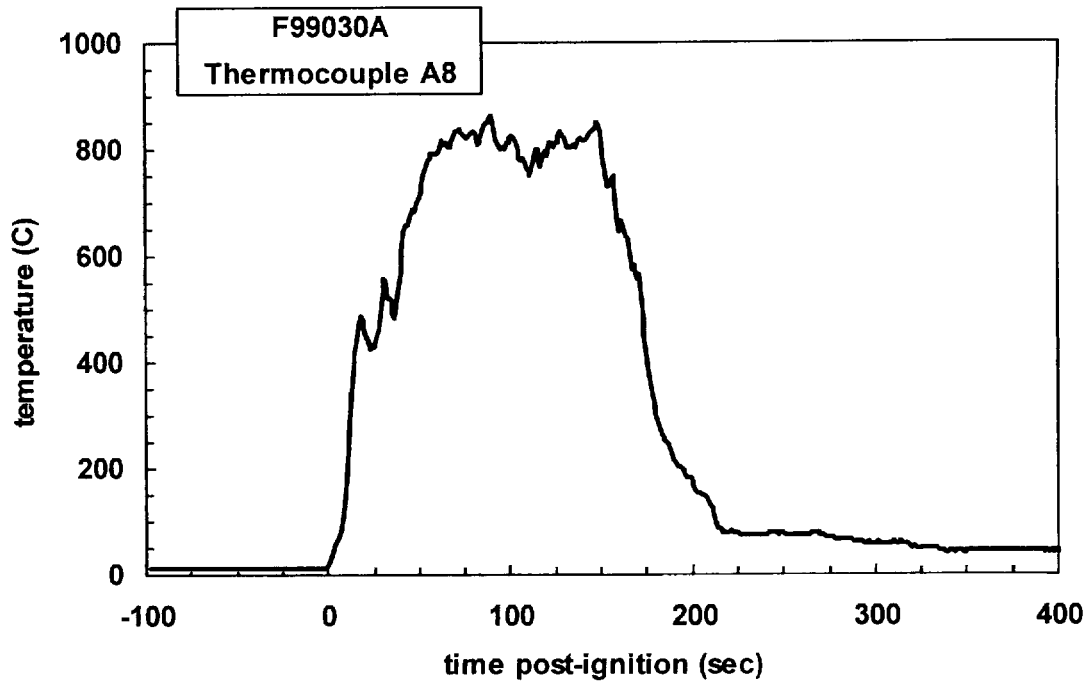

Plot C9. Fire Test F99030A. Data plot from thermocouple A8.

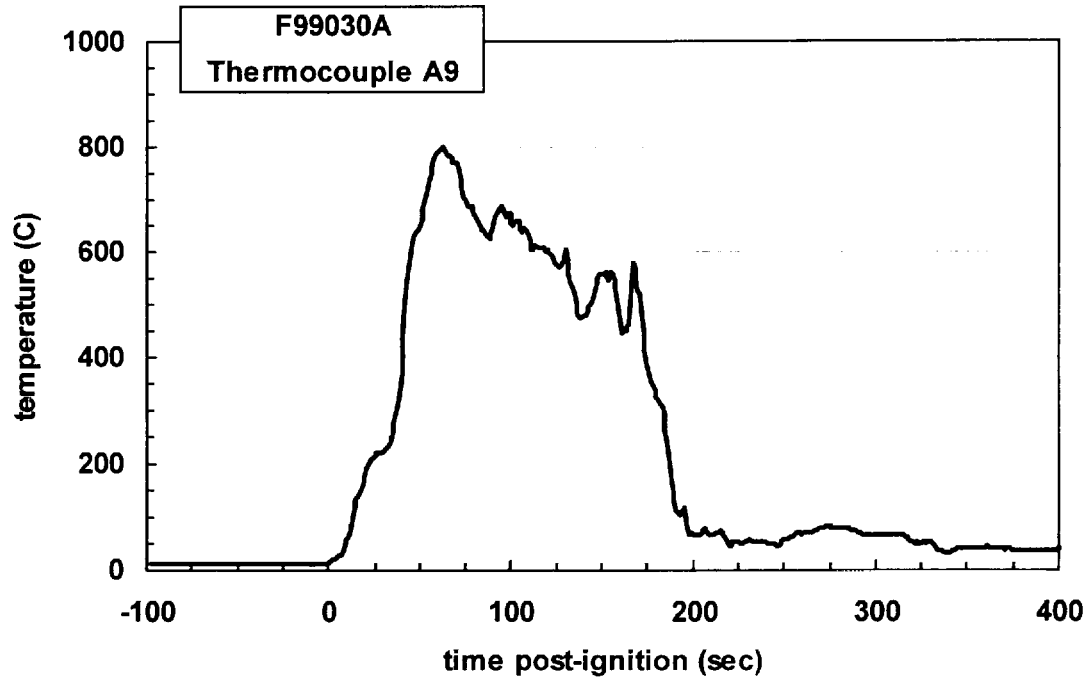

Plot C10. Fire Test F99030A. Data plot from thermocouple A9.

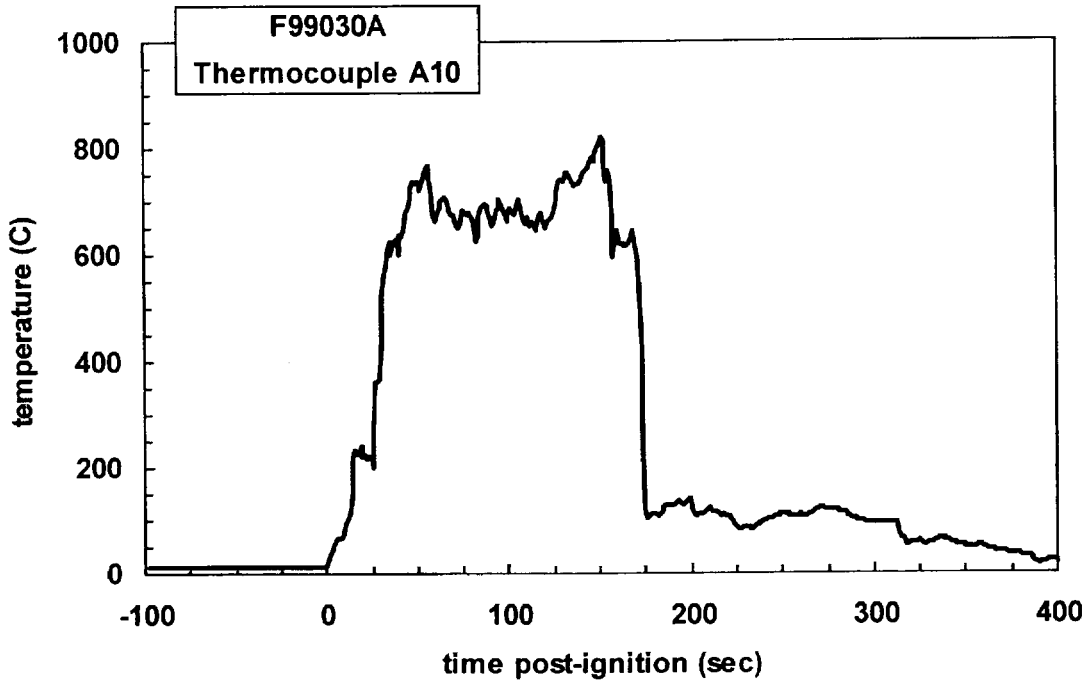

Plot C11. Fire Test F99030A. Data plot from thermocouple A10.

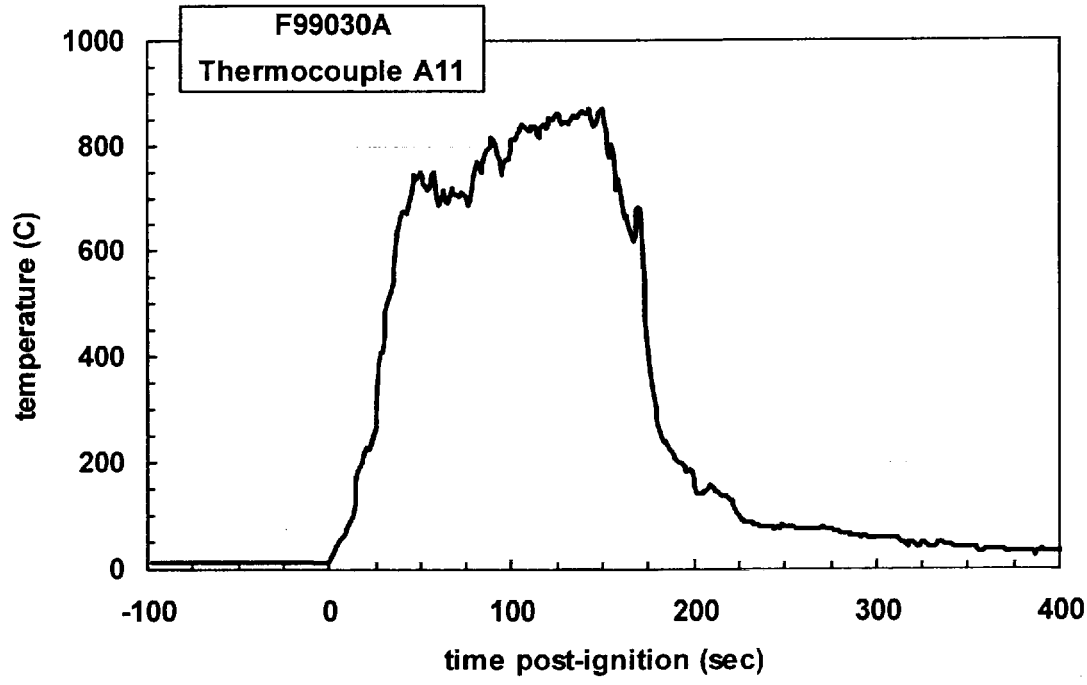

Plot C12. Fire Test F99030A. Data plot from thermocouple A11.

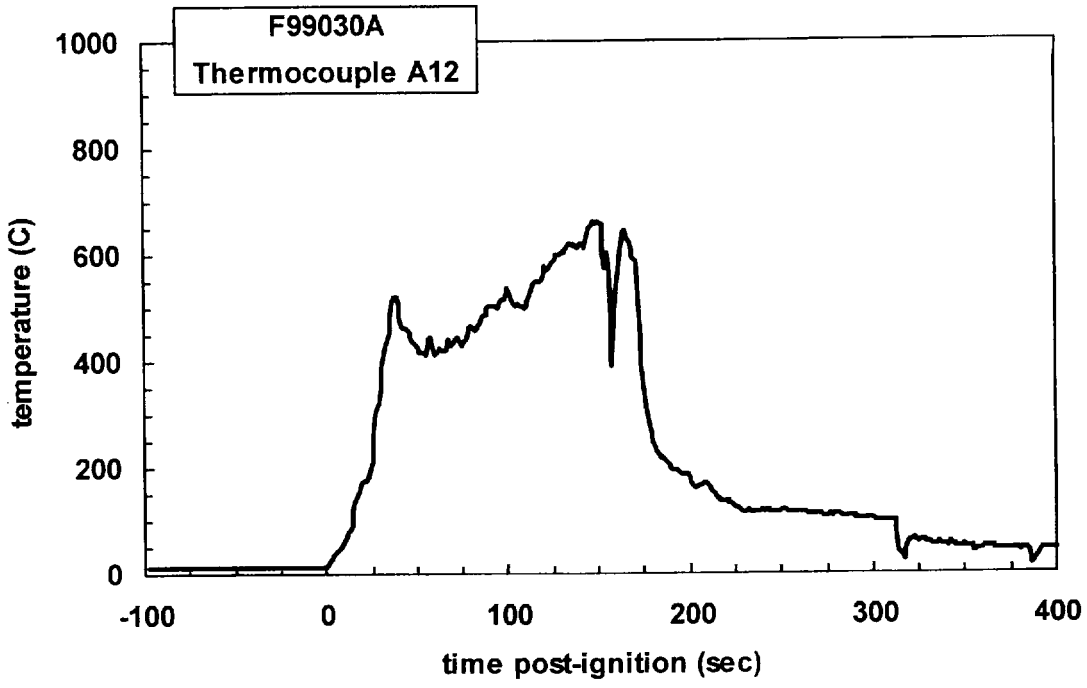

Plot C13. Fire Test F99030A. Data plot from thermocouple A12.

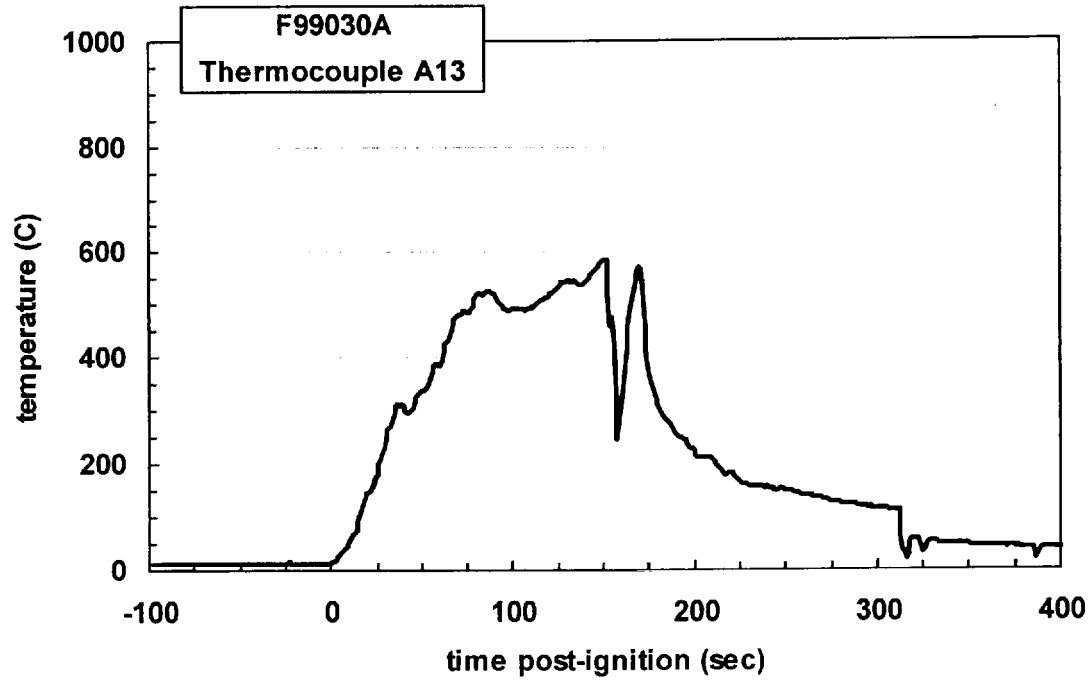

Plot C14. Fire Test F99030A. Data plot from thermocouple A13.

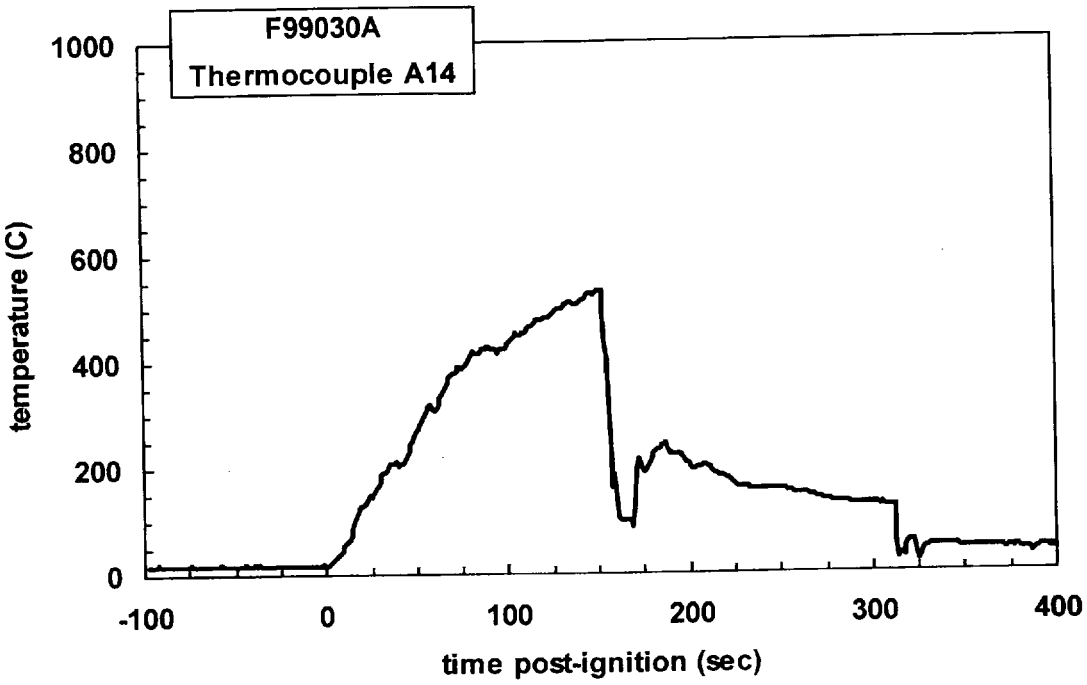

Plot C15. Fire Test F99030A. Data plot from thermocouple A14.

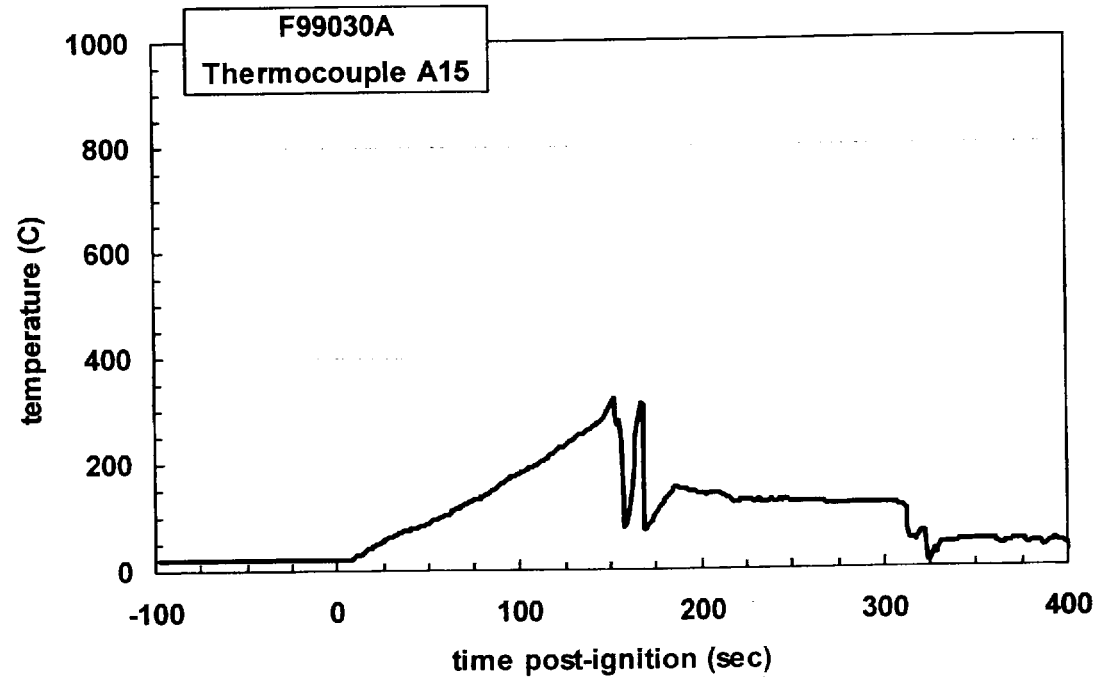

Plot C16. Fire Test F99030A. Data plot from thermocouple A15.

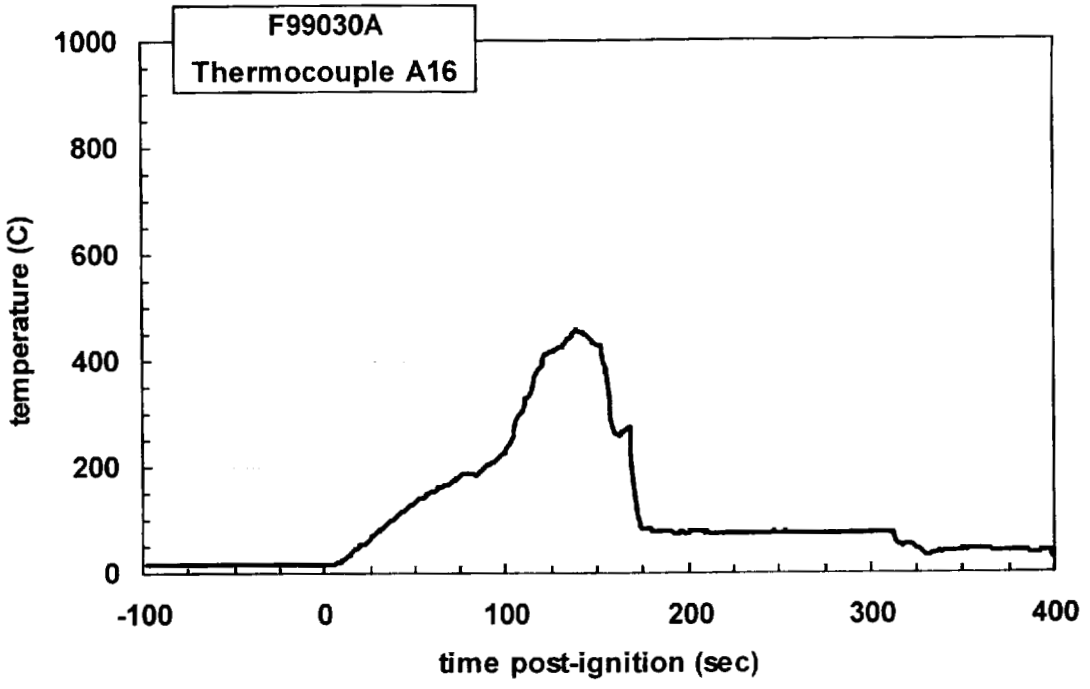

Plot C17. Fire Test F99030A. Data plot from thermocouple A16.

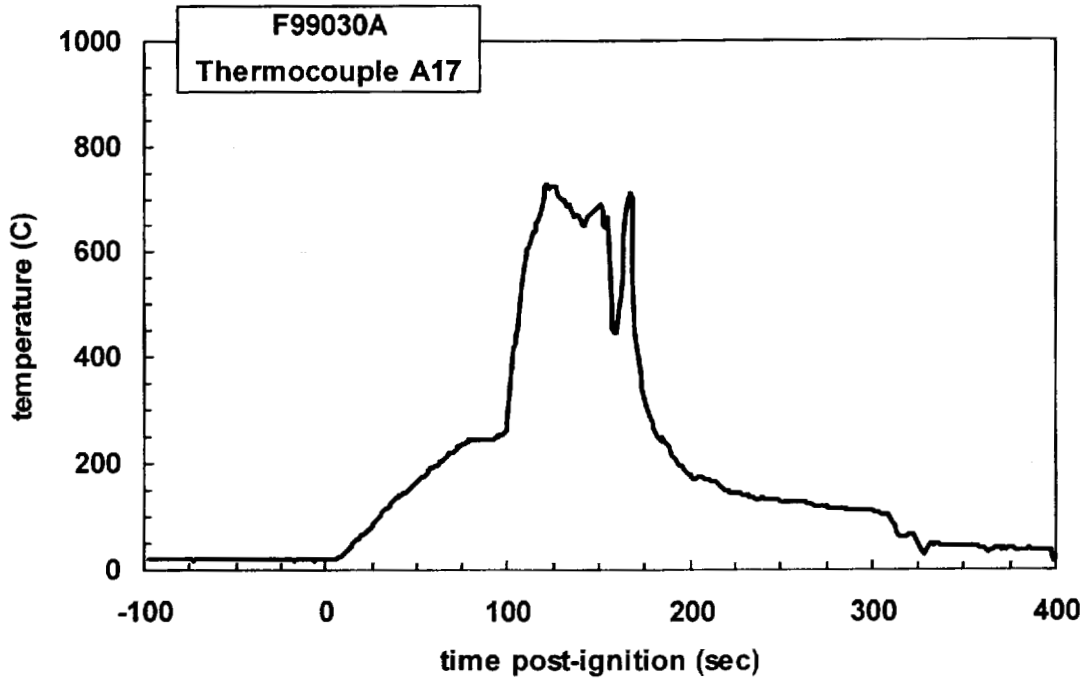

Plot C18. Fire Test F99030A. Data plot from thermocouple A17.

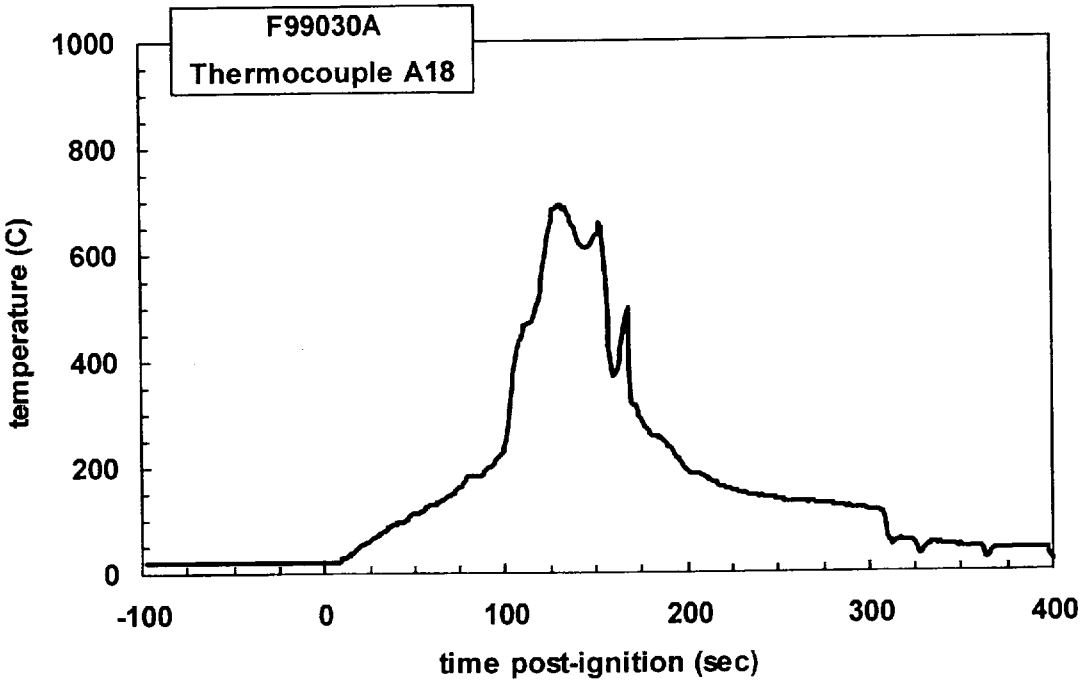

Plot C19. Fire Test F99030A. Data plot from thermocouple A18.

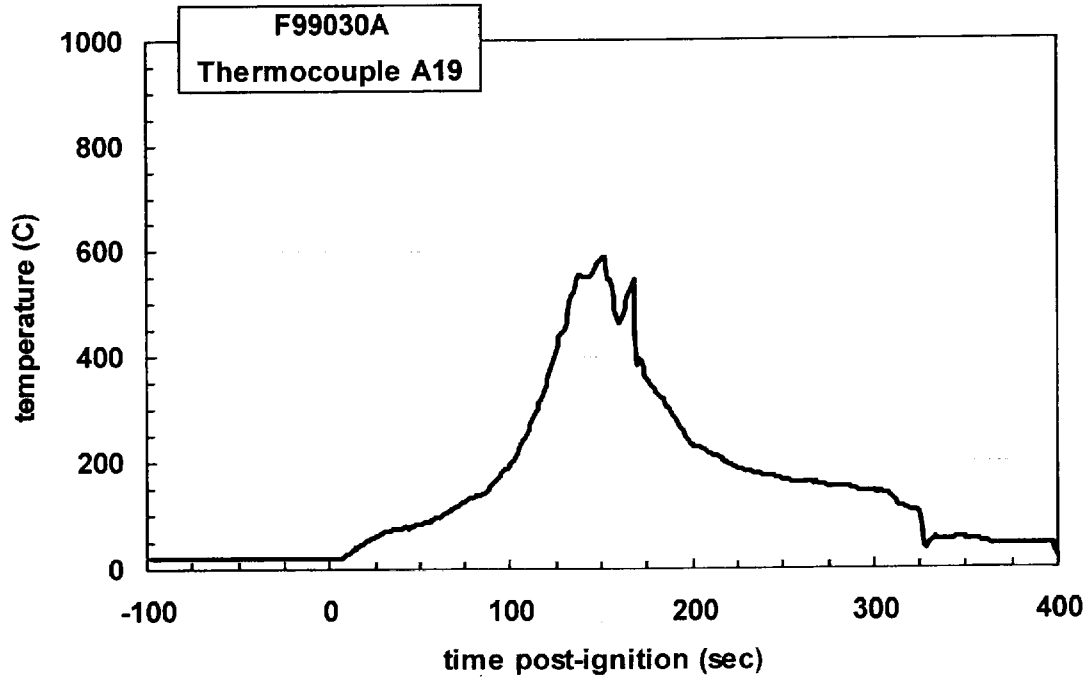

Plot C20. Fire Test F99030A. Data plot from thermocouple A19.

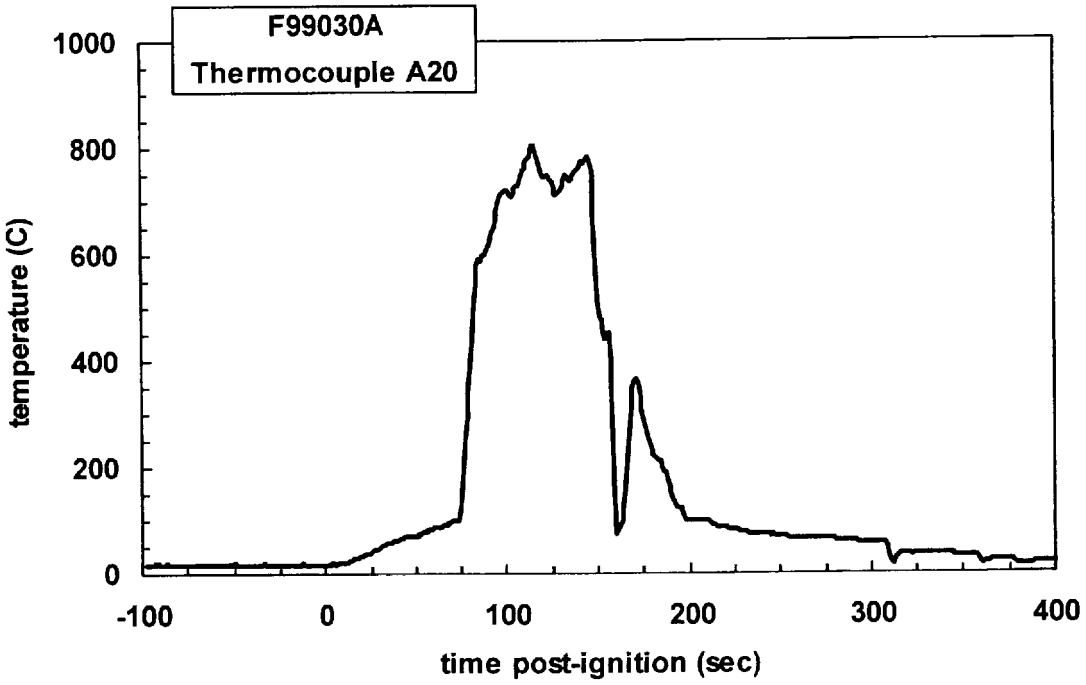

Plot C21. Fire Test F99030A. Data plot from thermocouple A20.

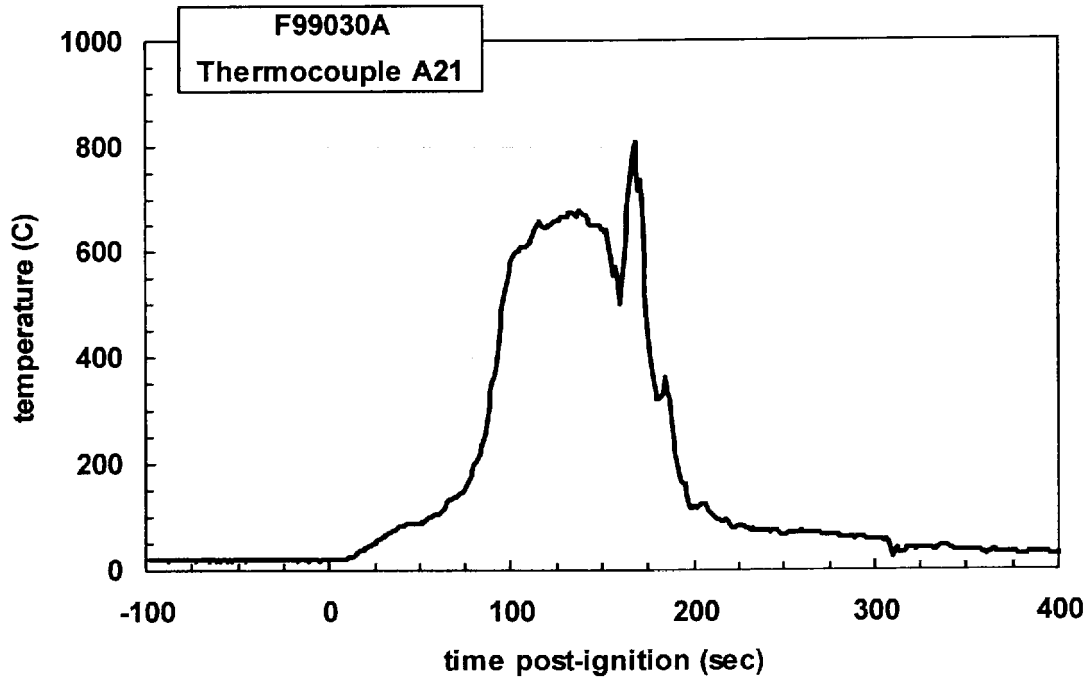

Plot C22. Fire Test F99030A. Data plot from thermocouple A21.

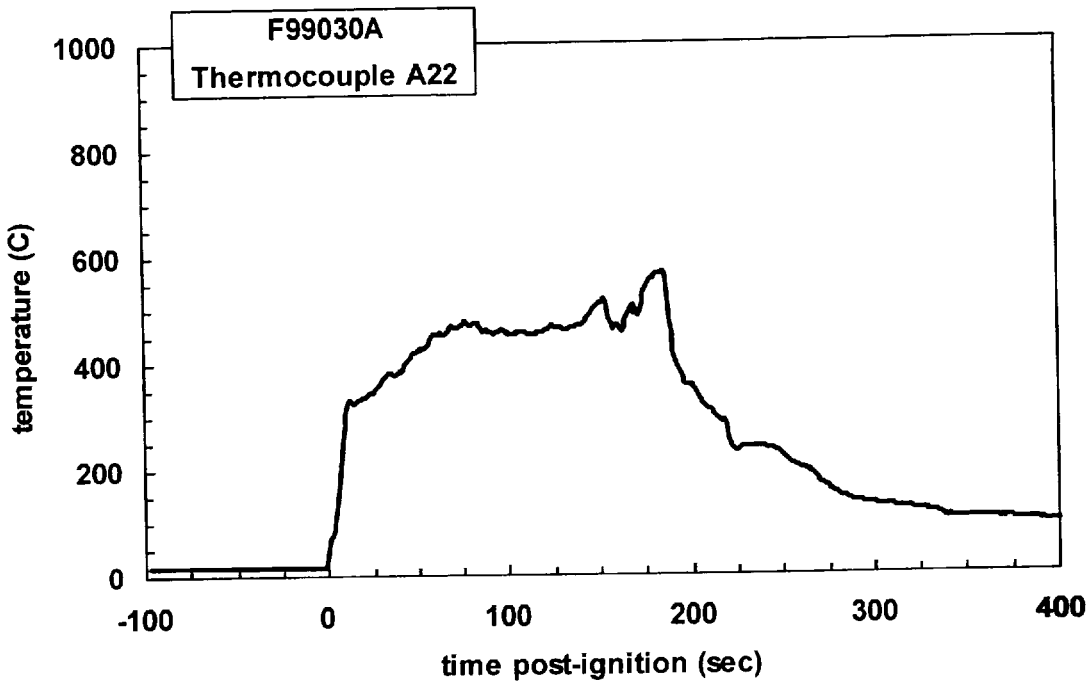

Plot C23. Fire Test F99030A. Data plot from thermocouple A22.

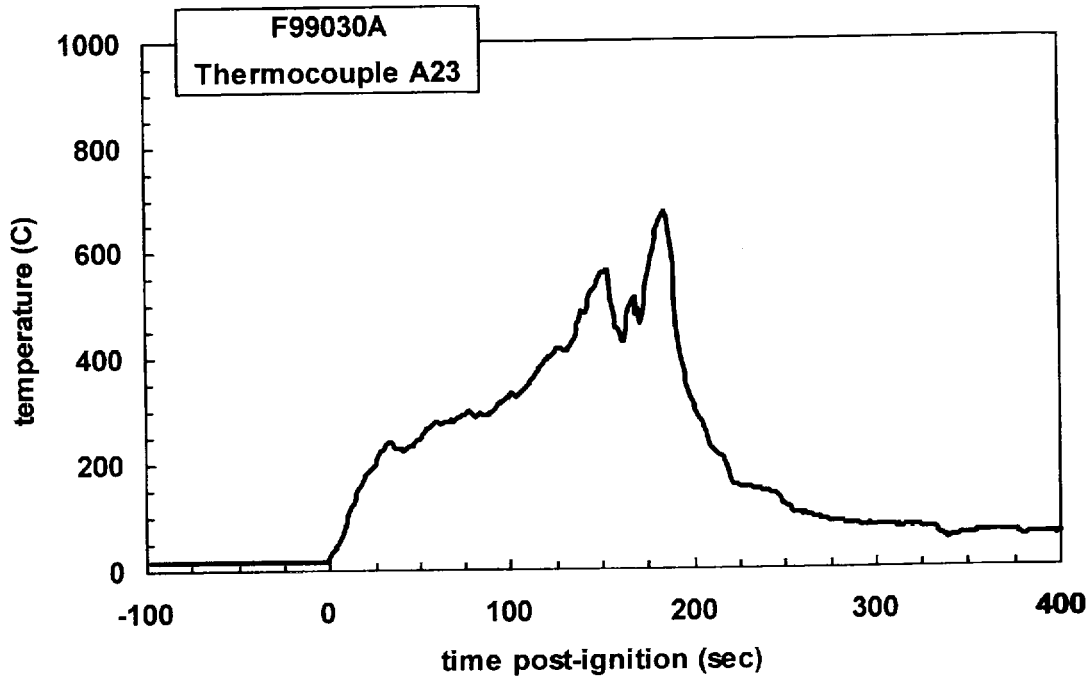

Plot C24. Fire Test F99030A. Data plot from thermocouple A23.

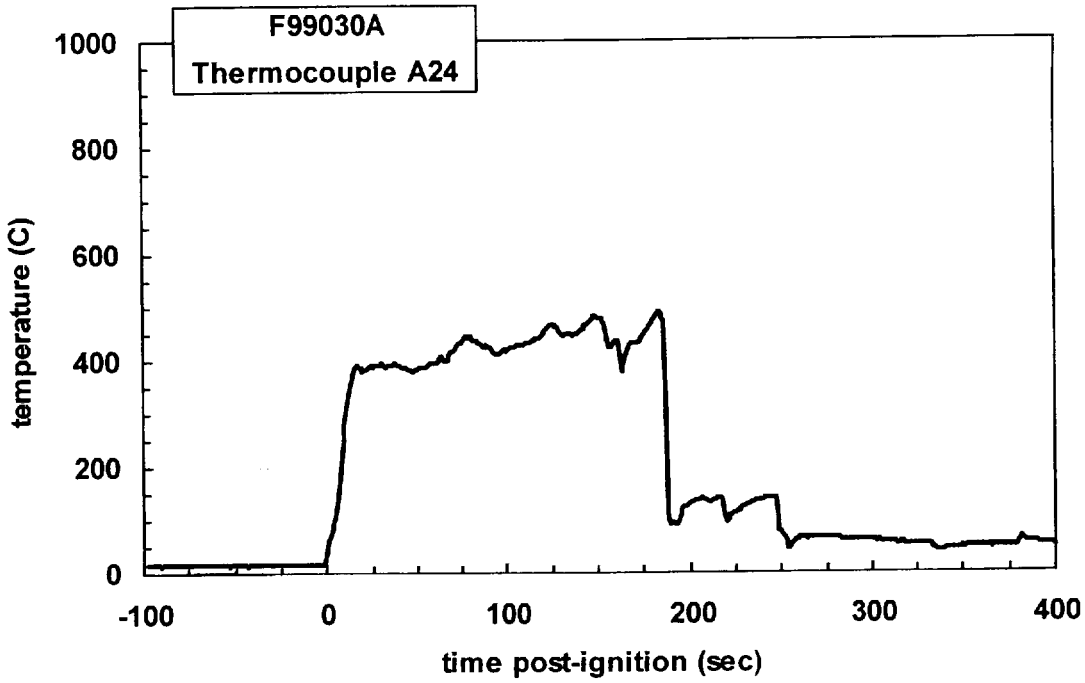

Plot C25. Fire Test F99030A. Data plot from thermocouple A24.

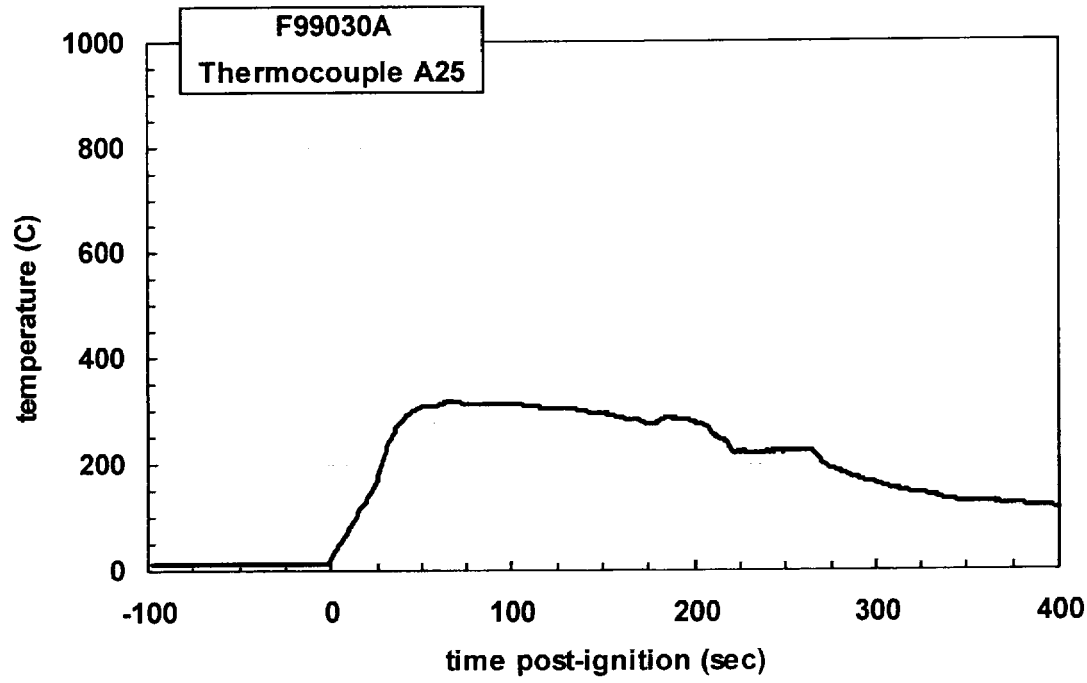

Plot C26. Fire Test F99030A. Data plot from thermocouple A25.

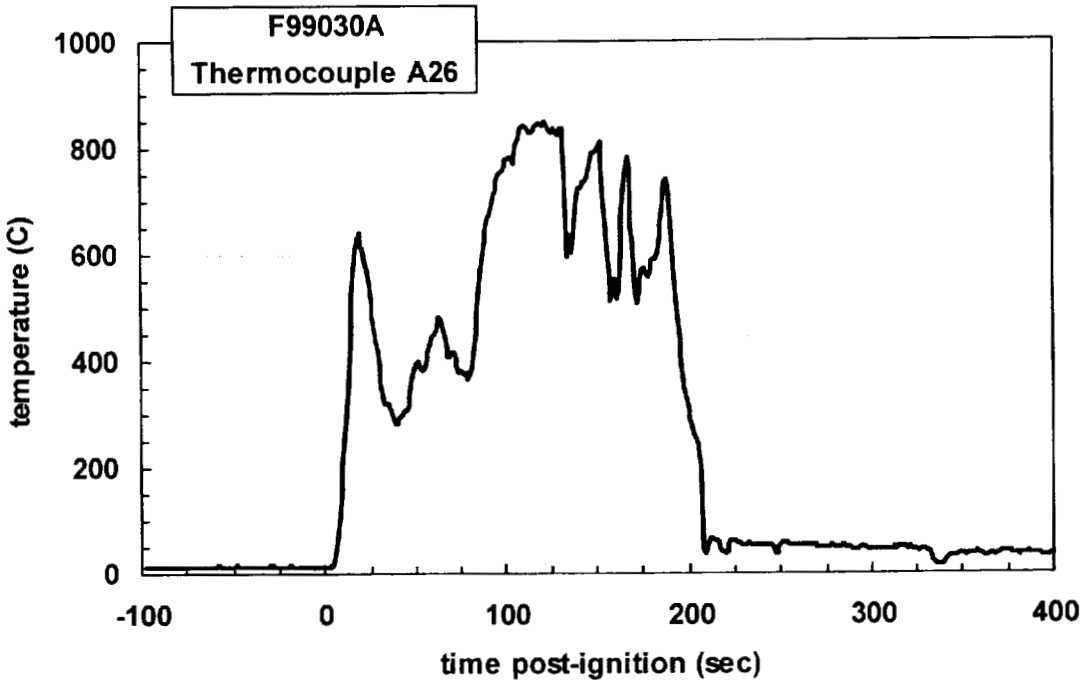

Plot C27. Fire Test F99030A. Data plot from thermocouple A26.

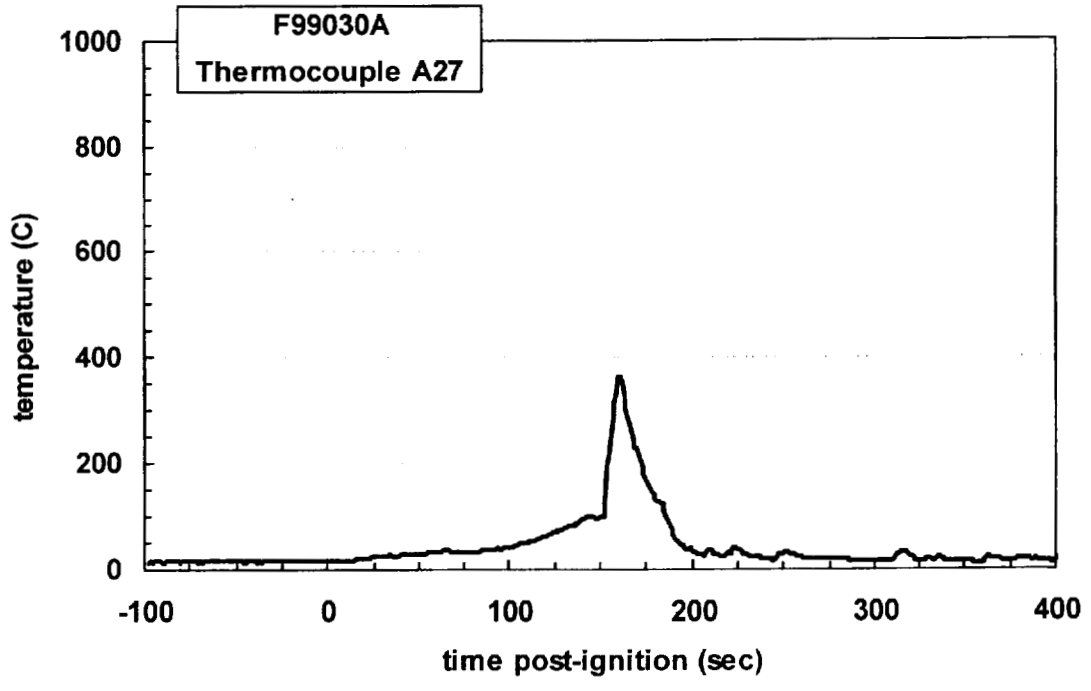

Plot C28. Fire Test F99030A. Data plot from thermocouple A27.

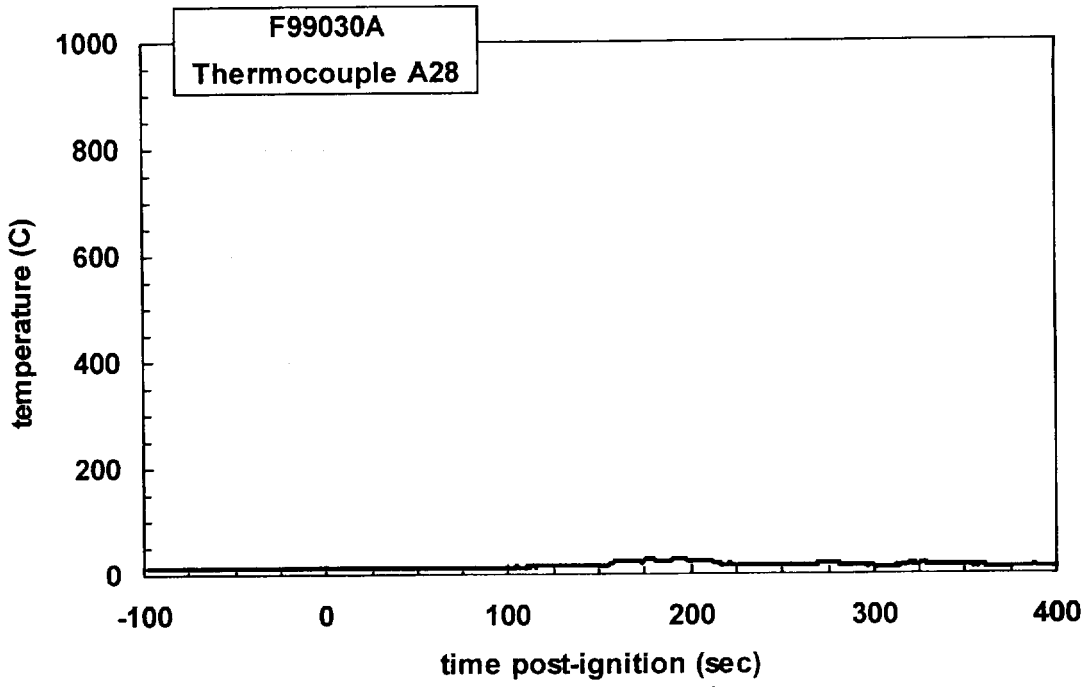

Plot C29. Fire Test F99030A. Data plot from thermocouple A28.

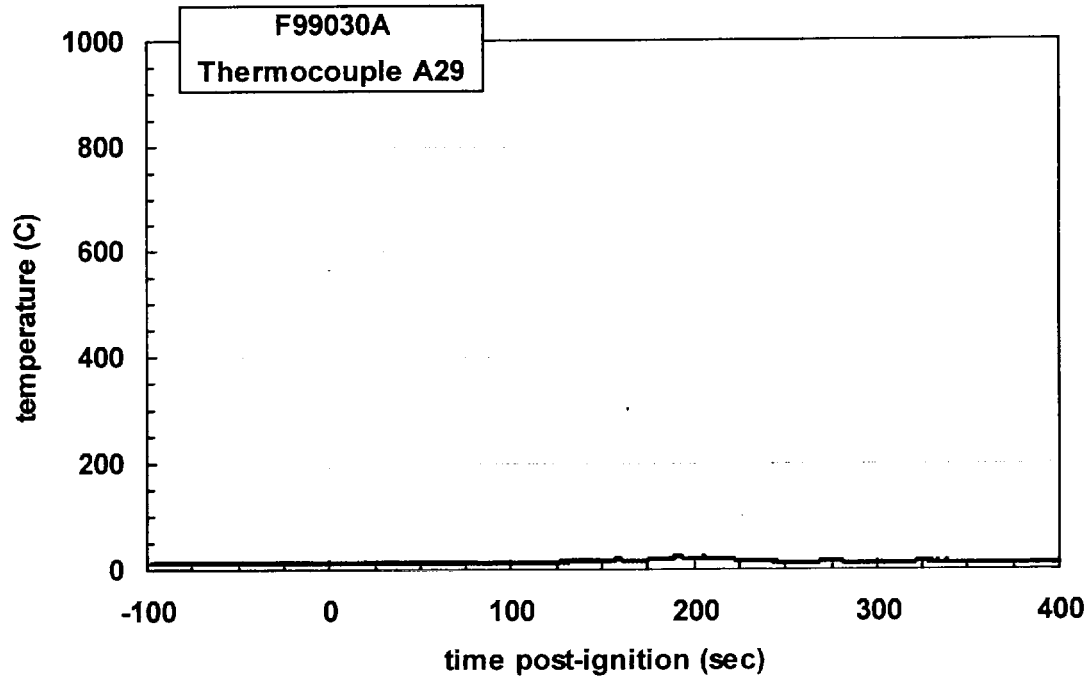

Plot C30. Fire Test F99030A. Data plot from thermocouple A29.

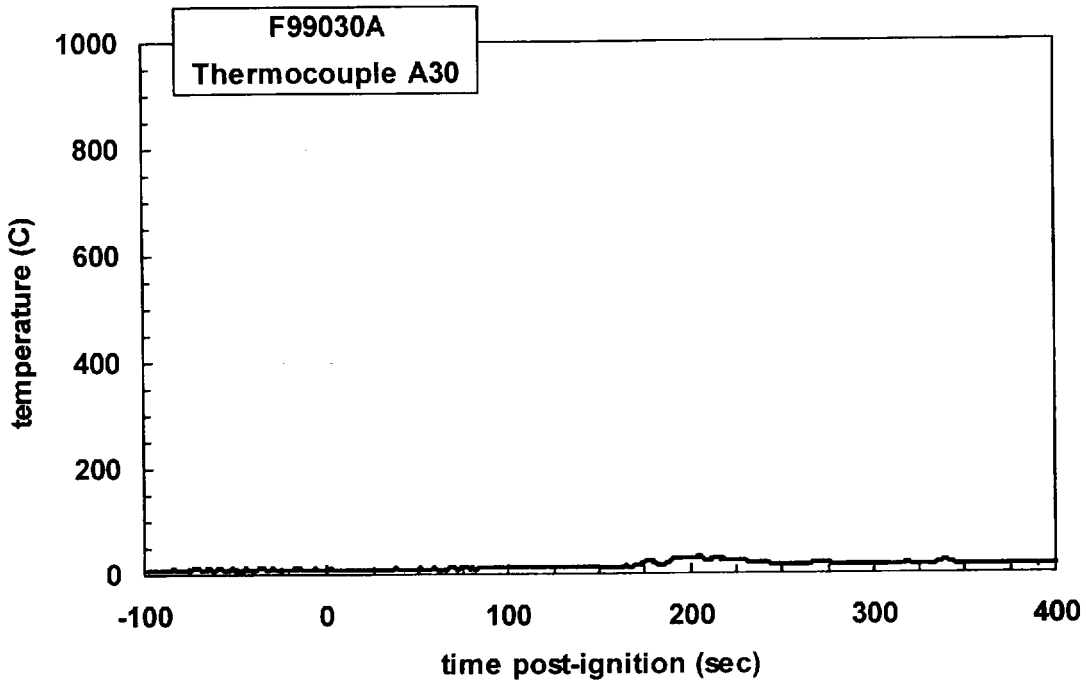

Plot C31. Fire Test F99030A. Data plot from thermocouple A30.

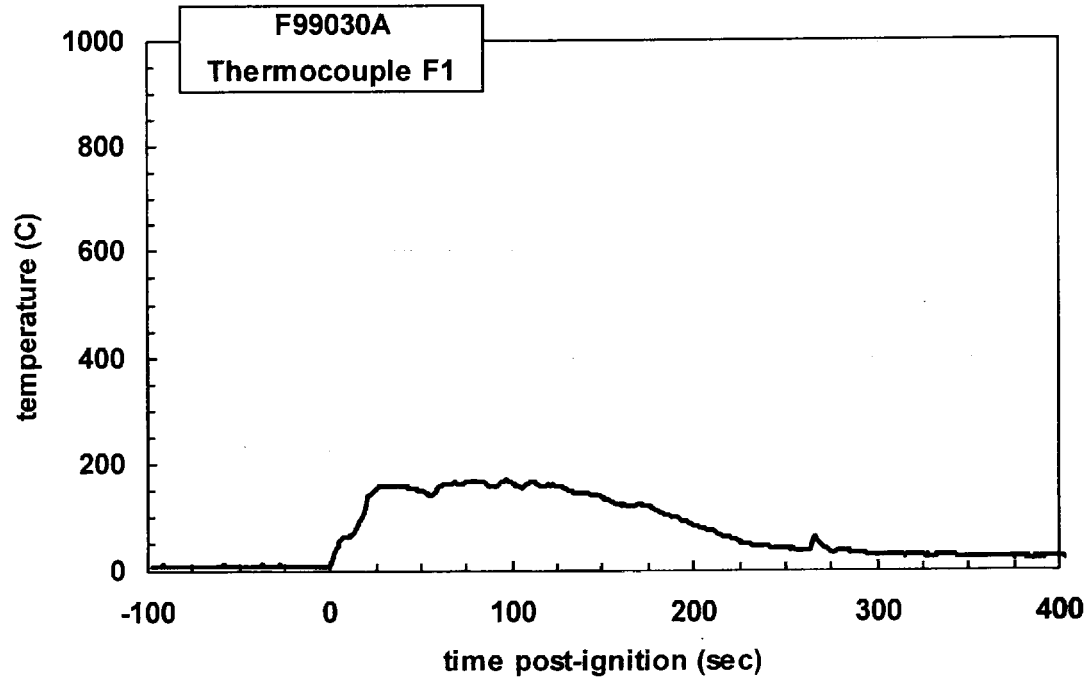

Plot C32. Fire Test F99030A. Data plot from thermocouple F1.

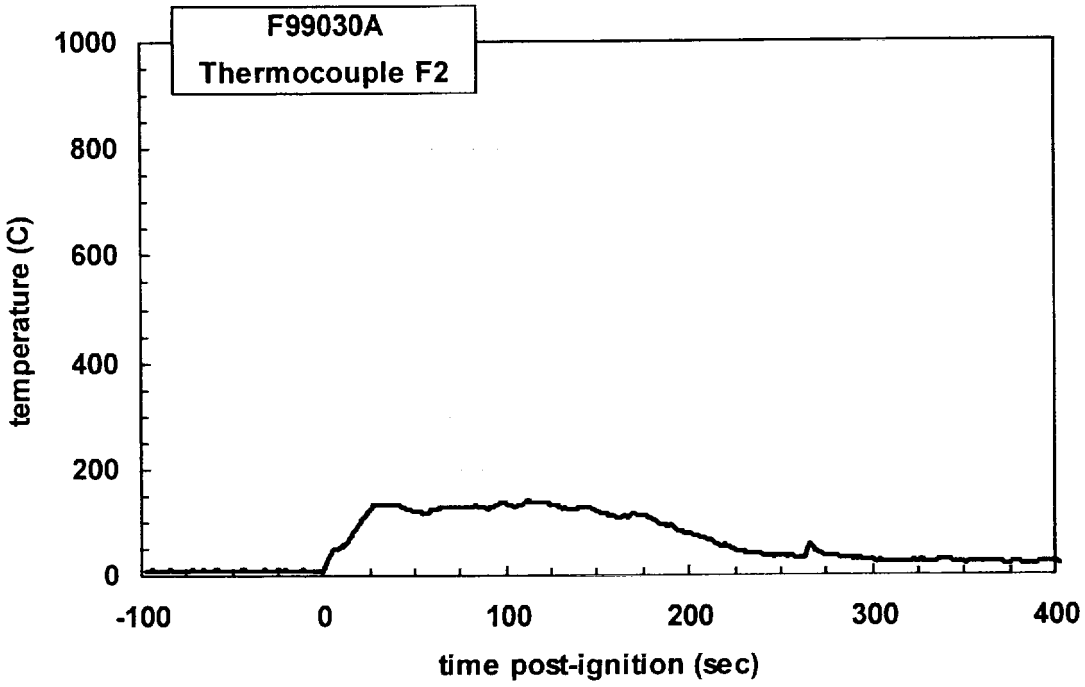

Plot C33. Fire Test F99030A. Data plot from thermocouple F2.

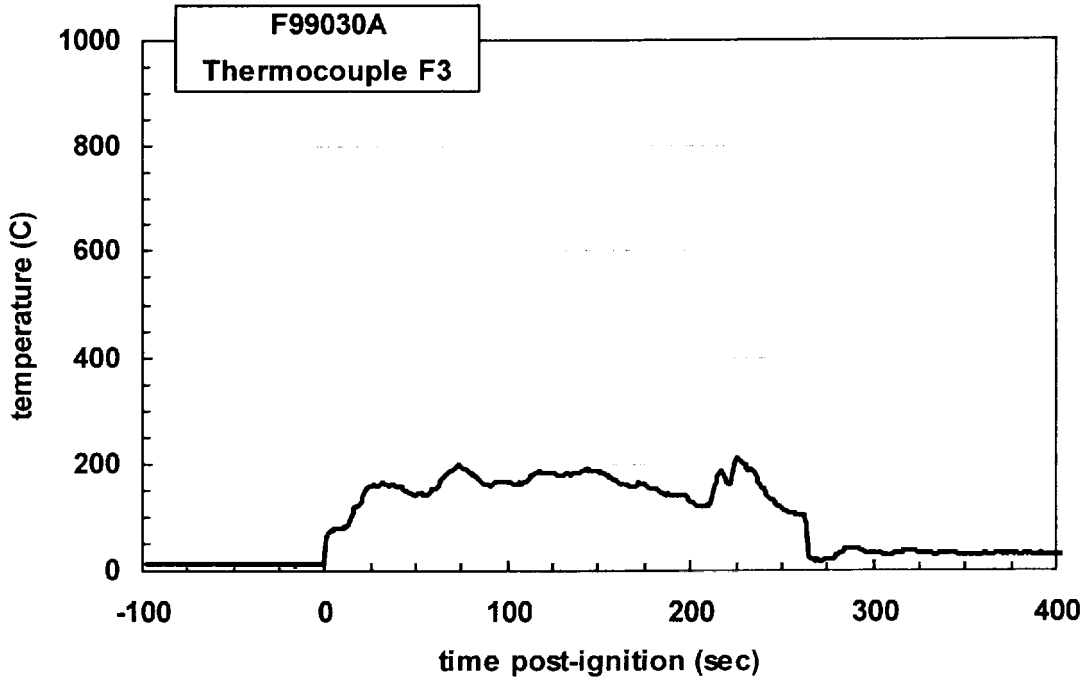

Plot C34. Fire Test F99030A. Data plot from thermocouple F3.

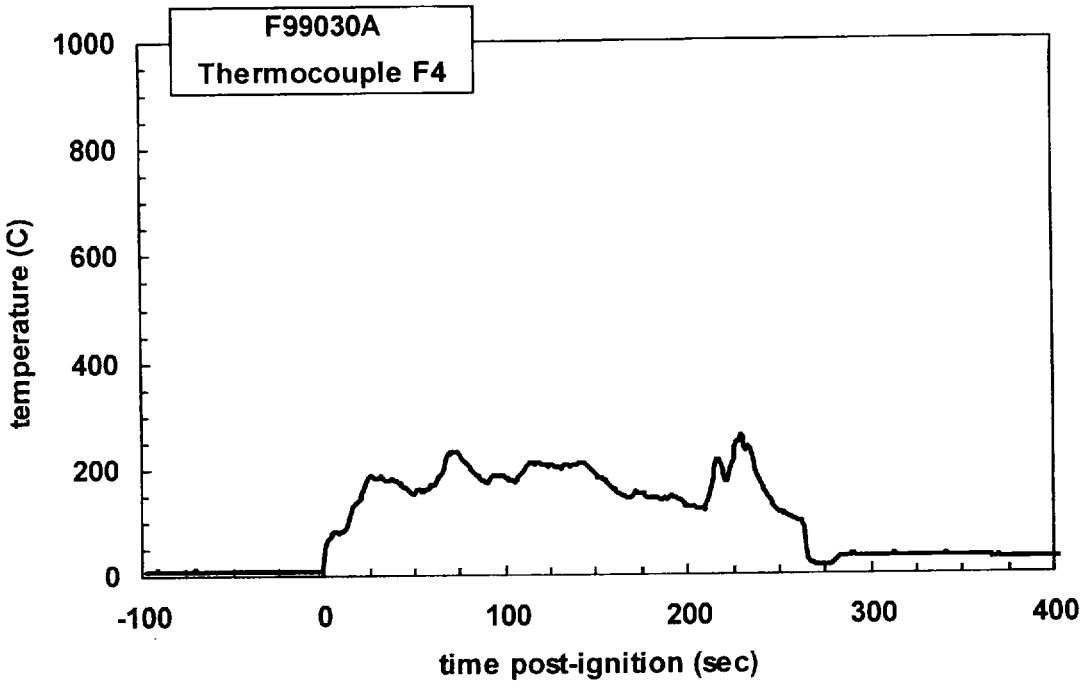

Plot C35. Fire Test F99030A. Data plot from thermocouple F4.

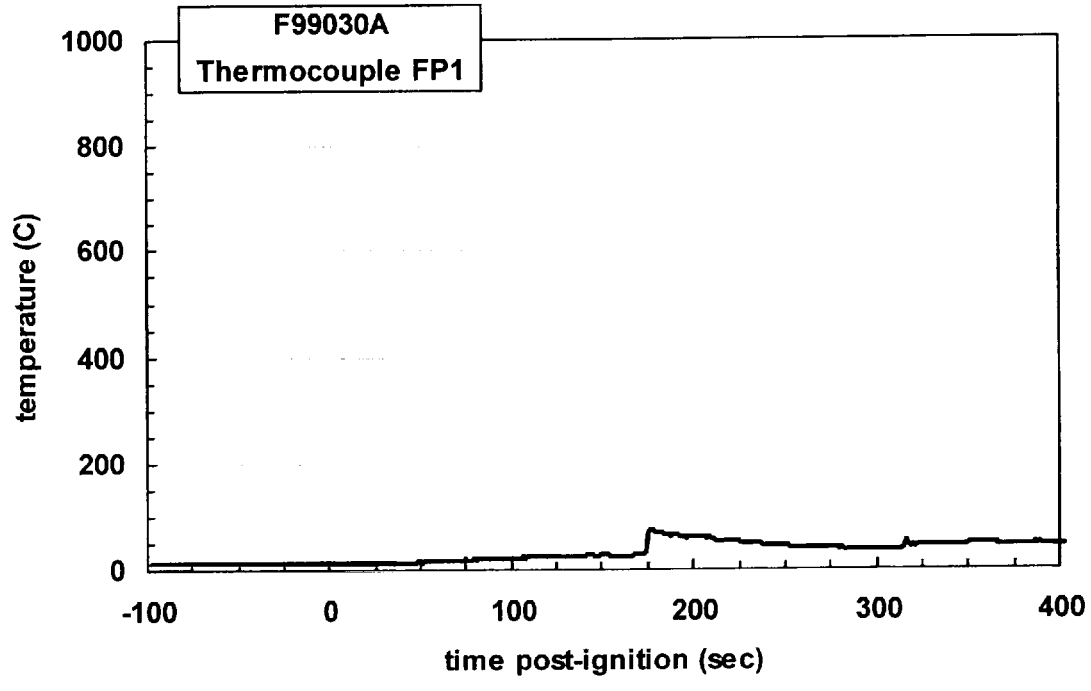

Plot C36. Fire Test F99030A. Data plot from thermocouple FP1.

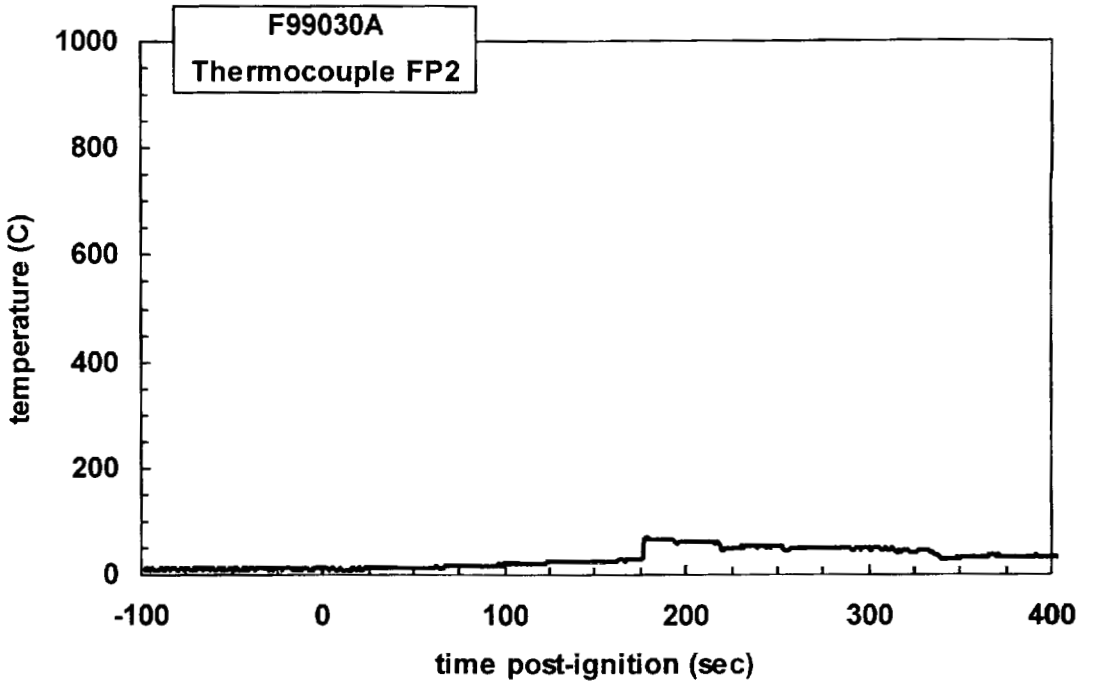

Plot C37. Fire Test F99030A. Data plot from thermocouple FP2.

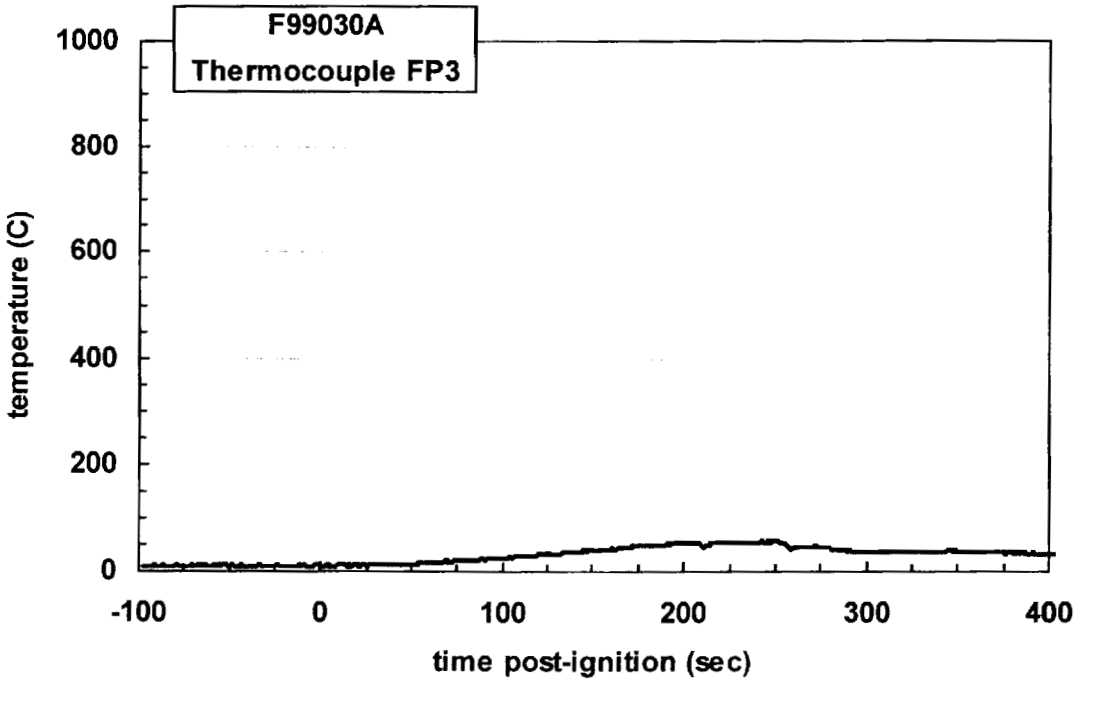

Plot C38. Fire Test F99030A. Data plot from thermocouple FP3.

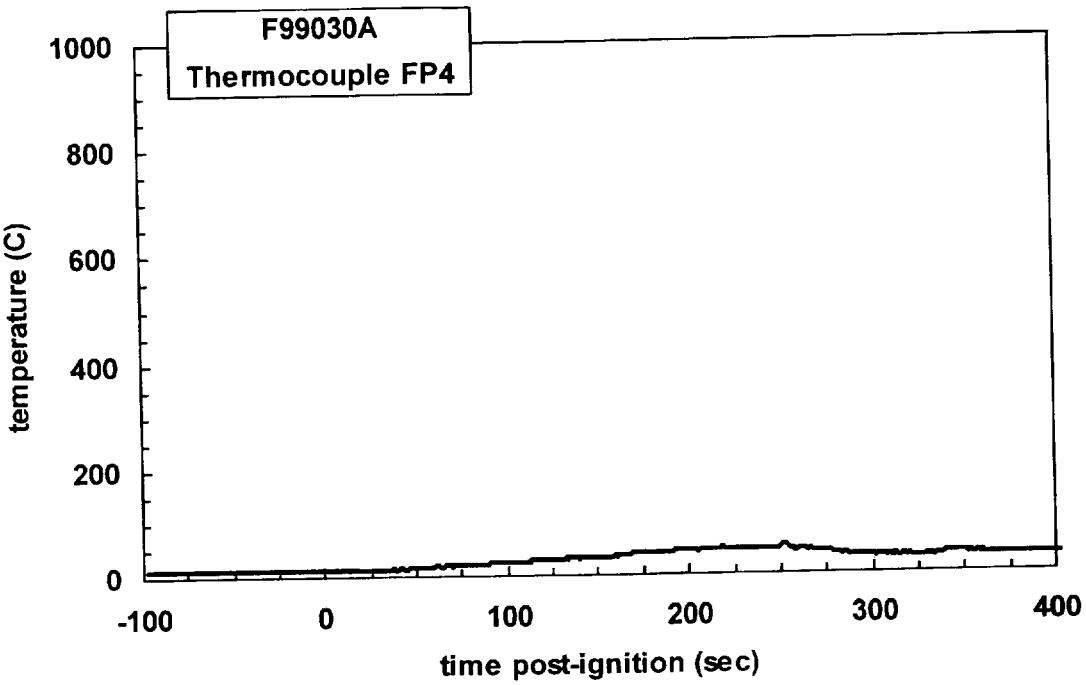

Plot C39. Fire Test F99030A. Data plot from thermocouple FP4.

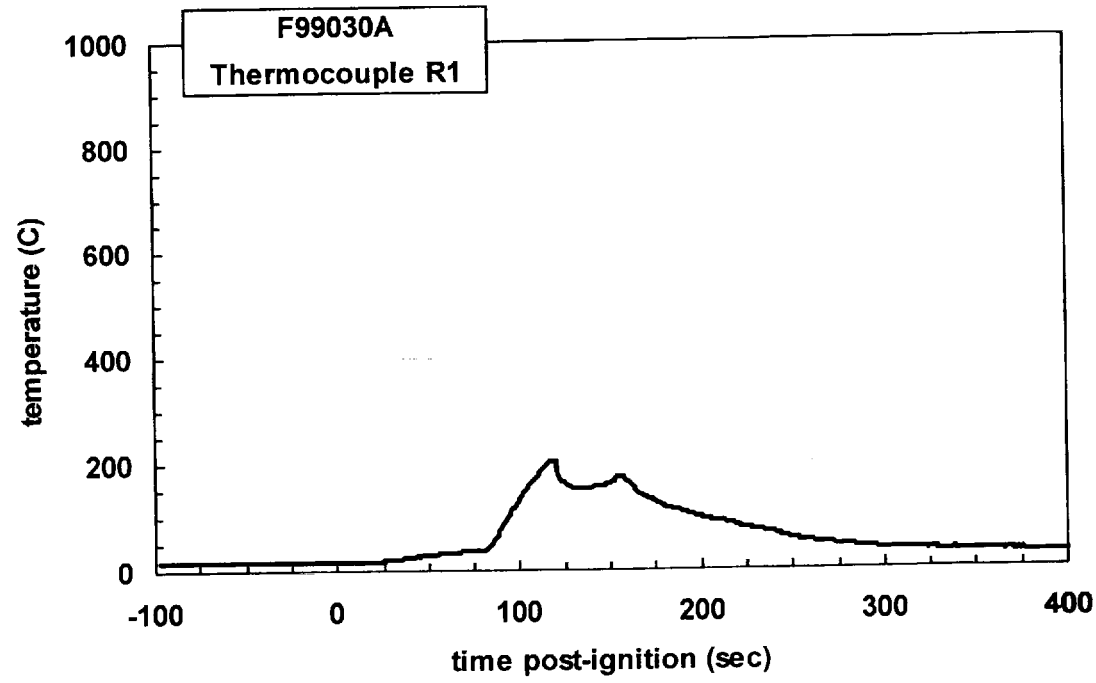

Plot C40. Fire Test F99030A. Data plot from thermocouple R1.

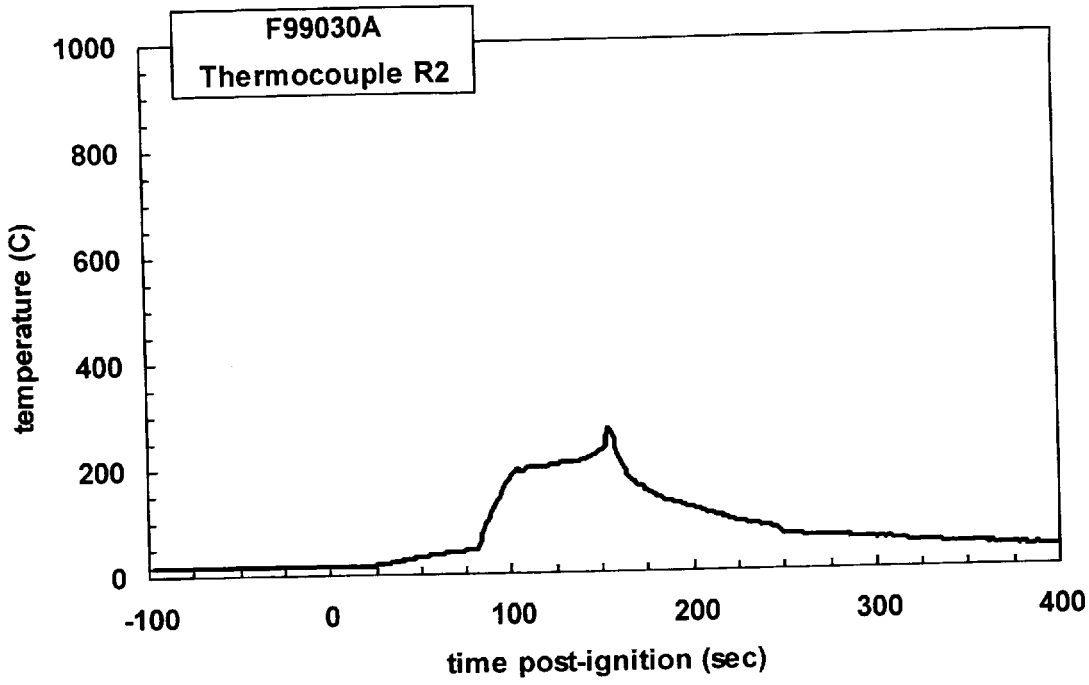

Plot C41. Fire Test F99030A. Data plot from thermocouple R2.

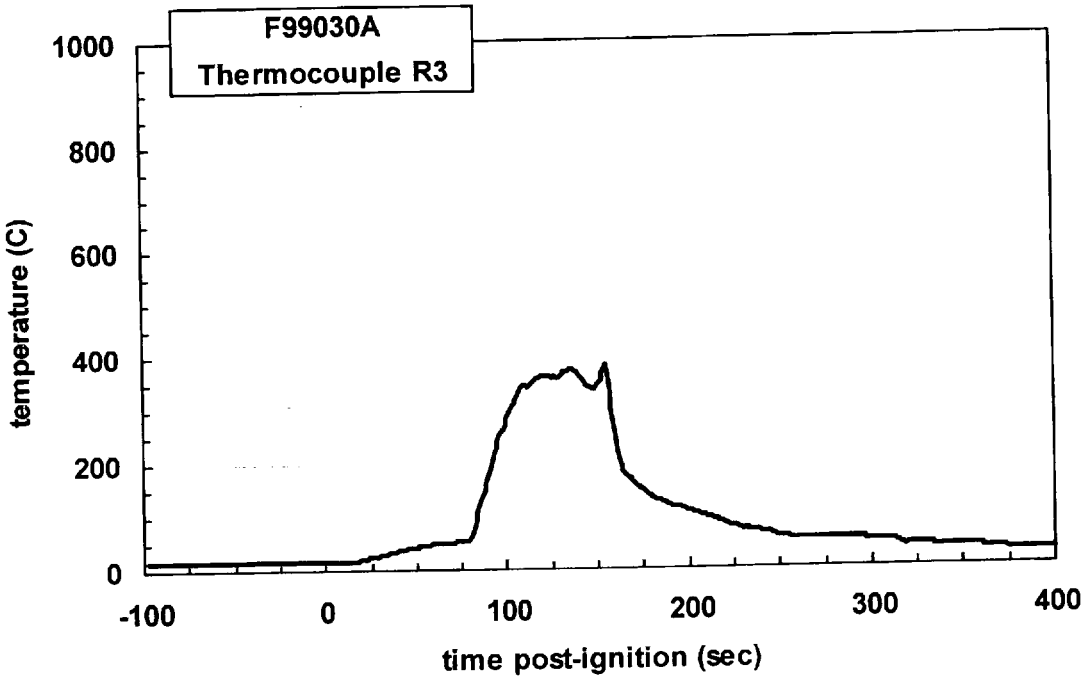

Plot C42. Fire Test F99030A. Data plot from thermocouple R3.

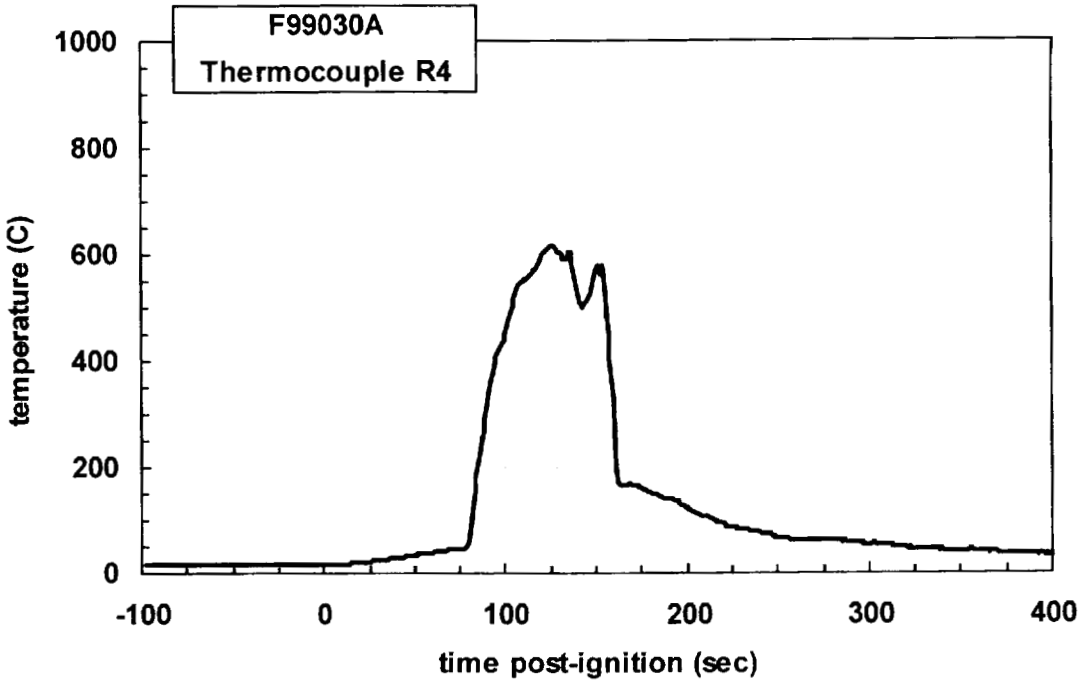

Plot C43. Fire Test F99030A. Data plot from thermocouple R4.

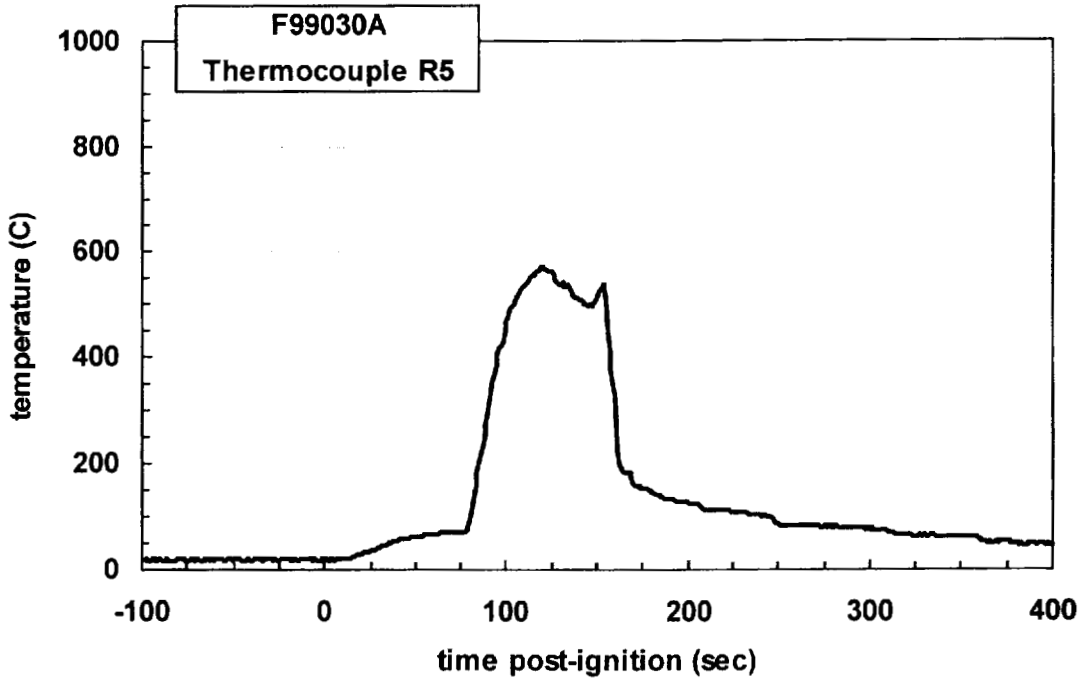

Plot C44. Fire Test F99030A. Data plot from thermocouple R5.

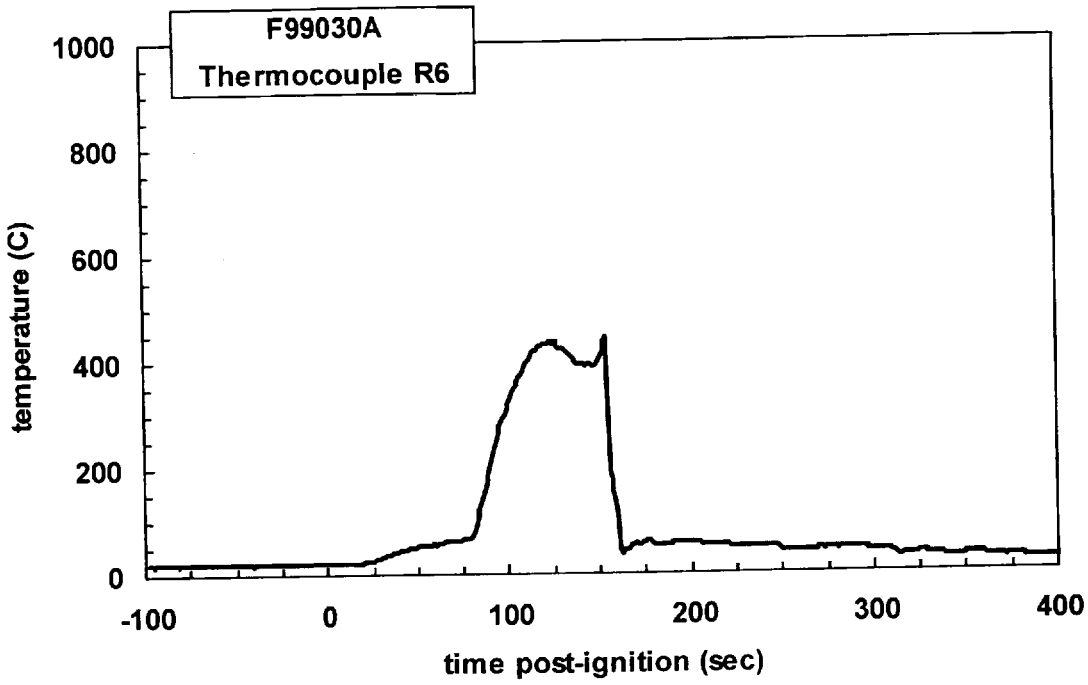

Plot C45. Fire Test F99030A. Data plot from thermocouple R6.

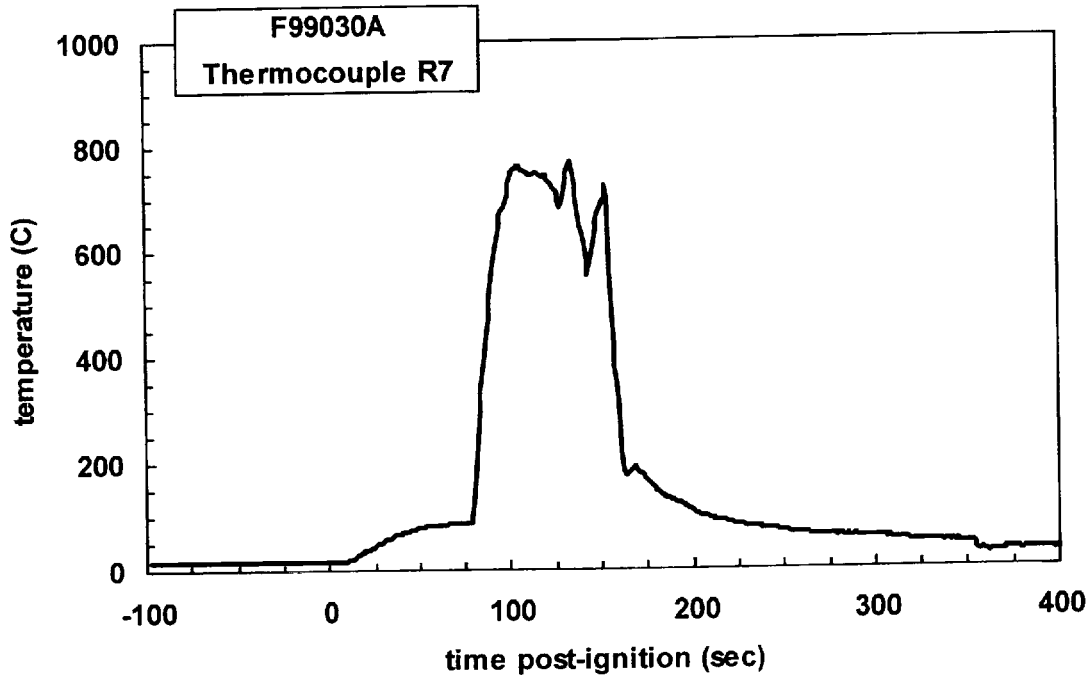

Plot C46. Fire Test F99030A. Data plot from thermocouple R7.

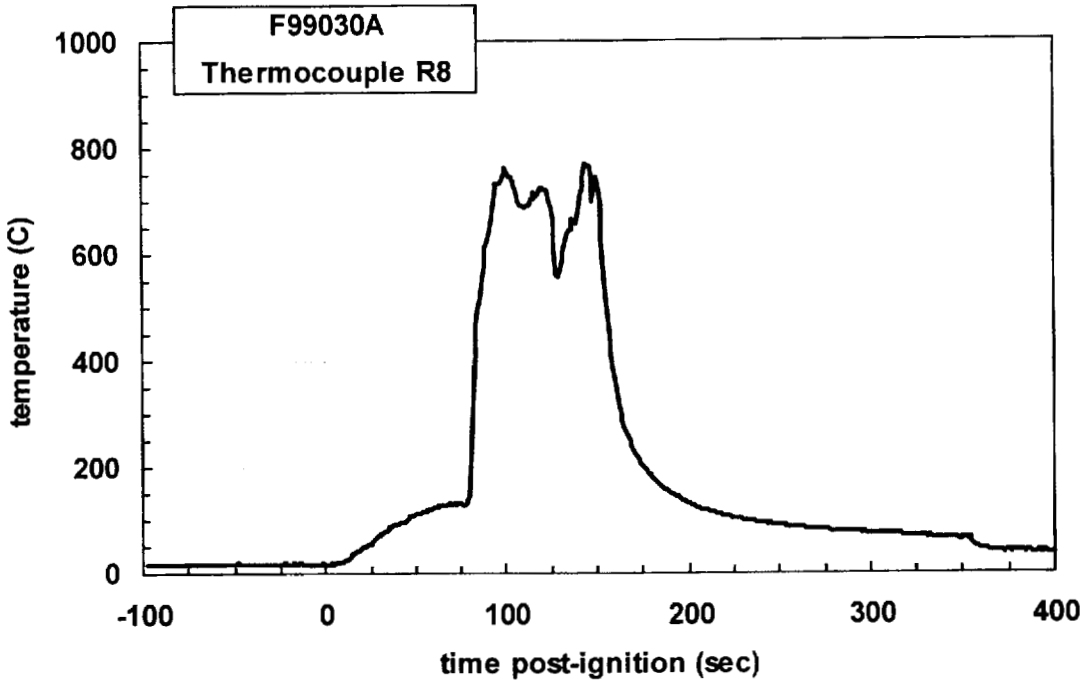

Plot C47. Fire Test F99030A. Data plot from thermocouple R8.

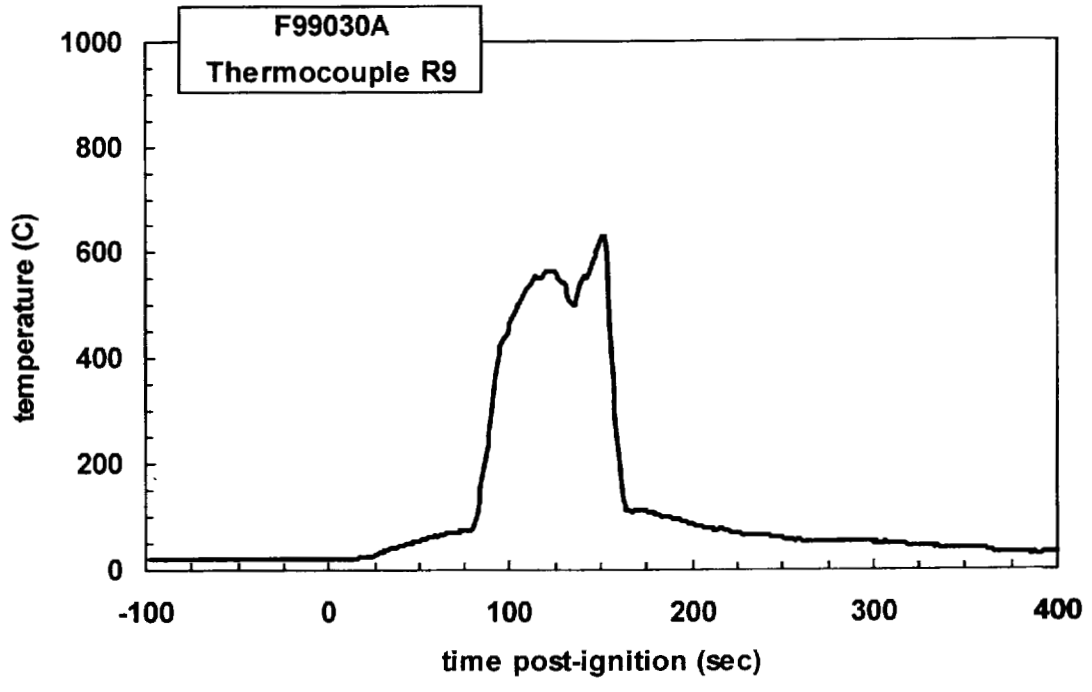

Plot C48. Fire Test F99030A. Data plot from thermocouple R9.

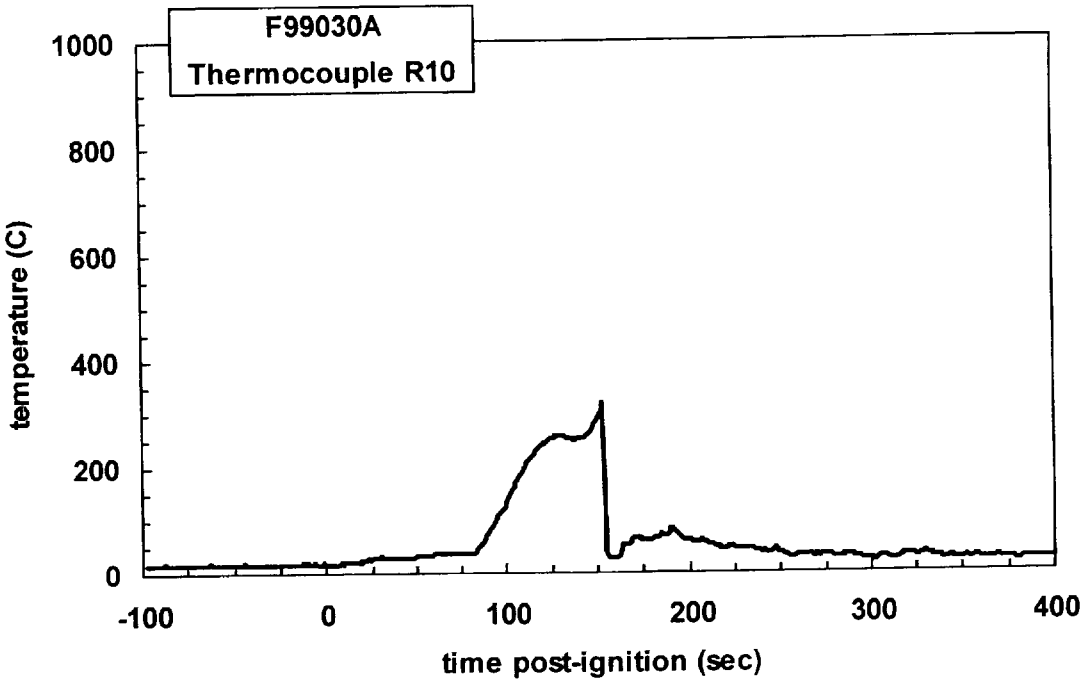

Plot C49. Fire Test F99030A. Data plot from thermocouple R10.

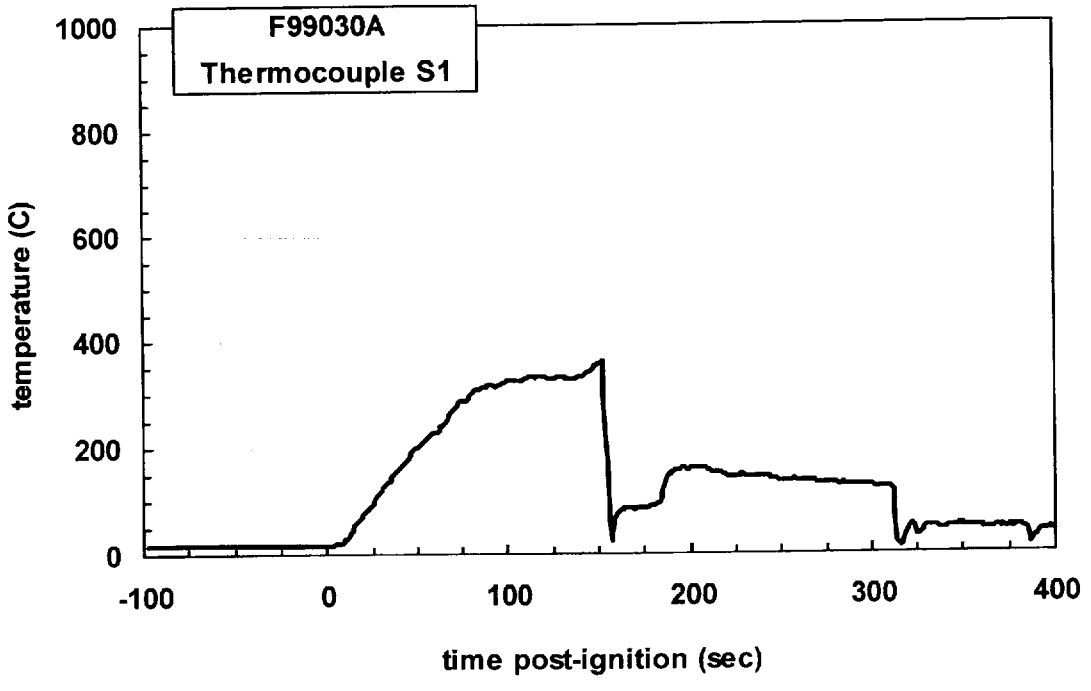

Plot C50. Fire Test F99030A. Data plot from thermocouple S1.

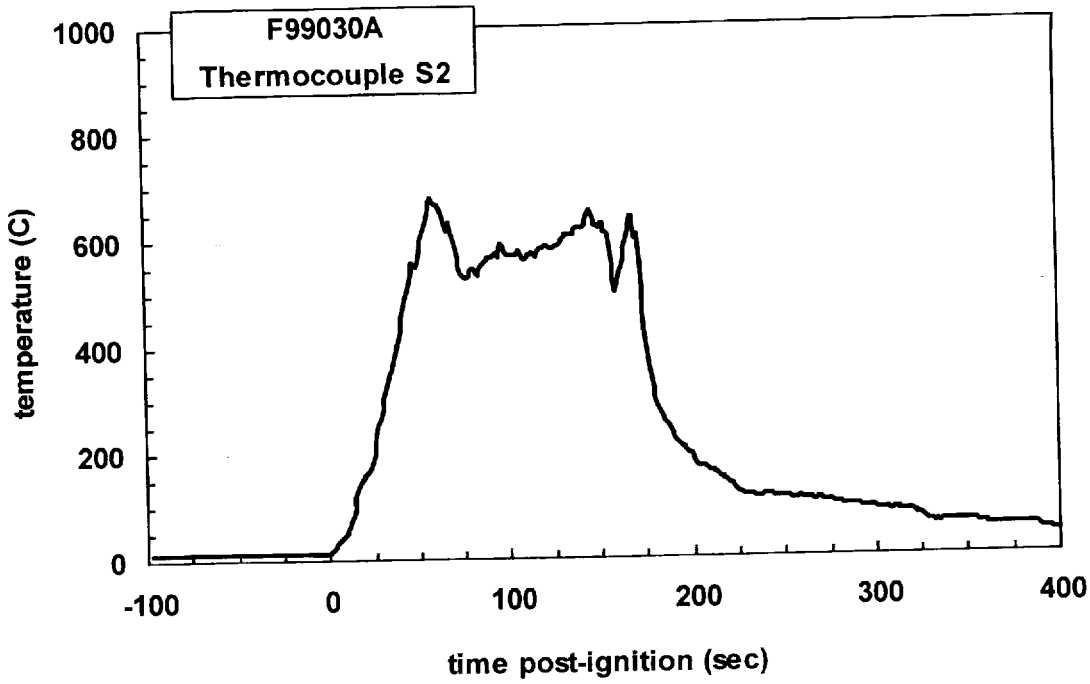

Plot C51. Fire Test F99030A. Data plot from thermocouple S2.

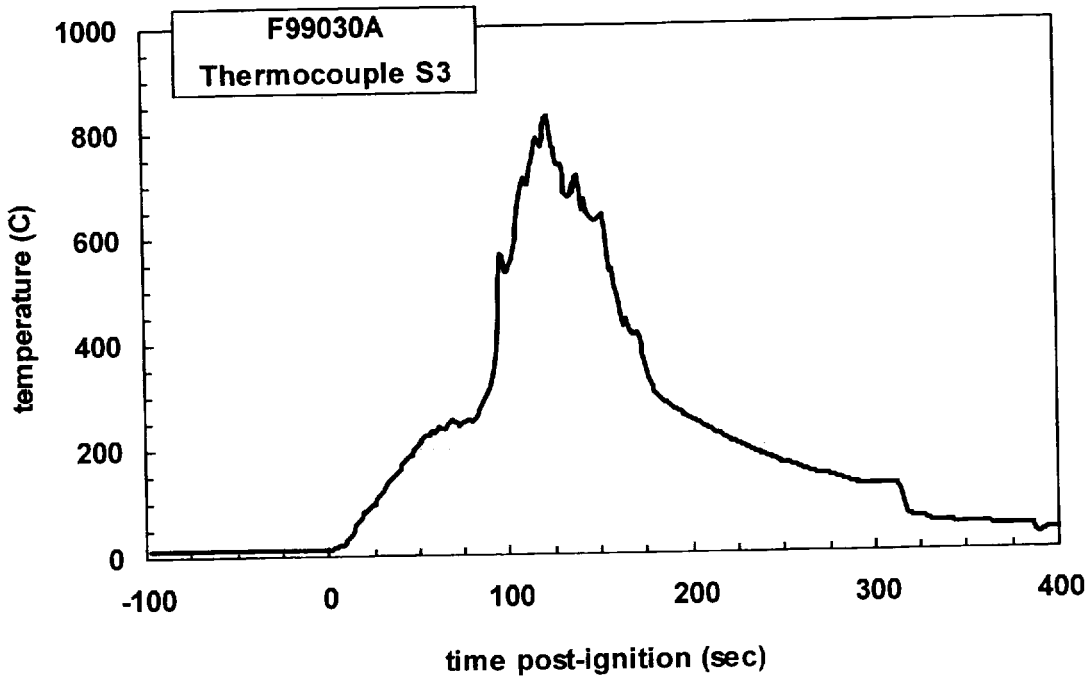

Plot C52. Fire Test F99030A. Data plot from thermocouple S3.

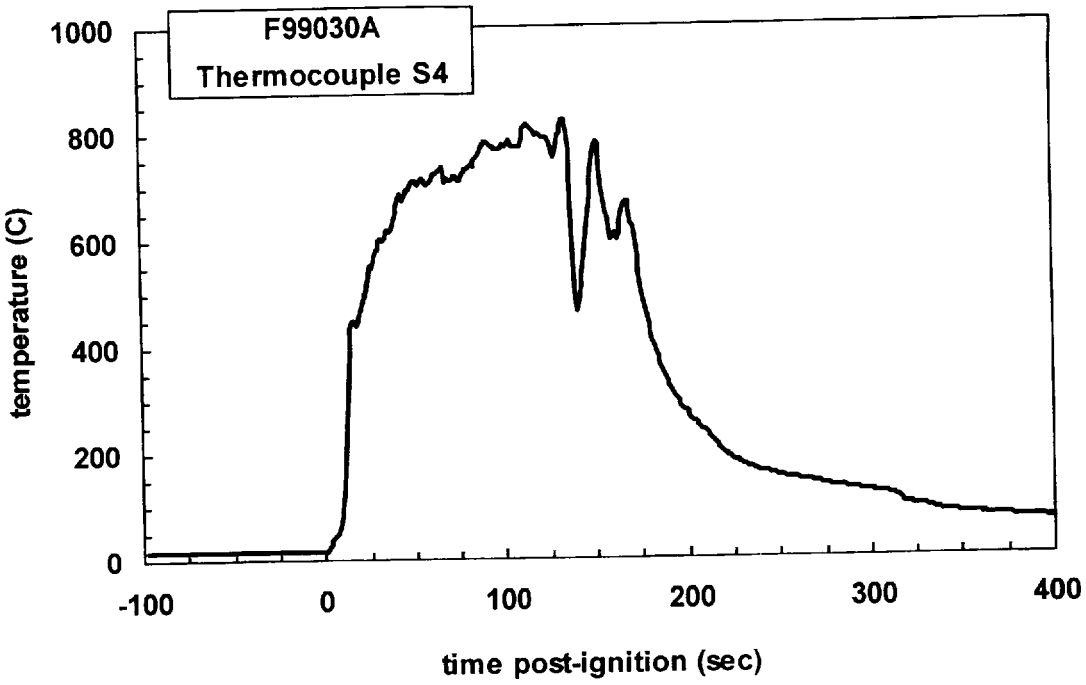

Plot C53. Fire Test F99030A. Data plot from thermocouple S4.

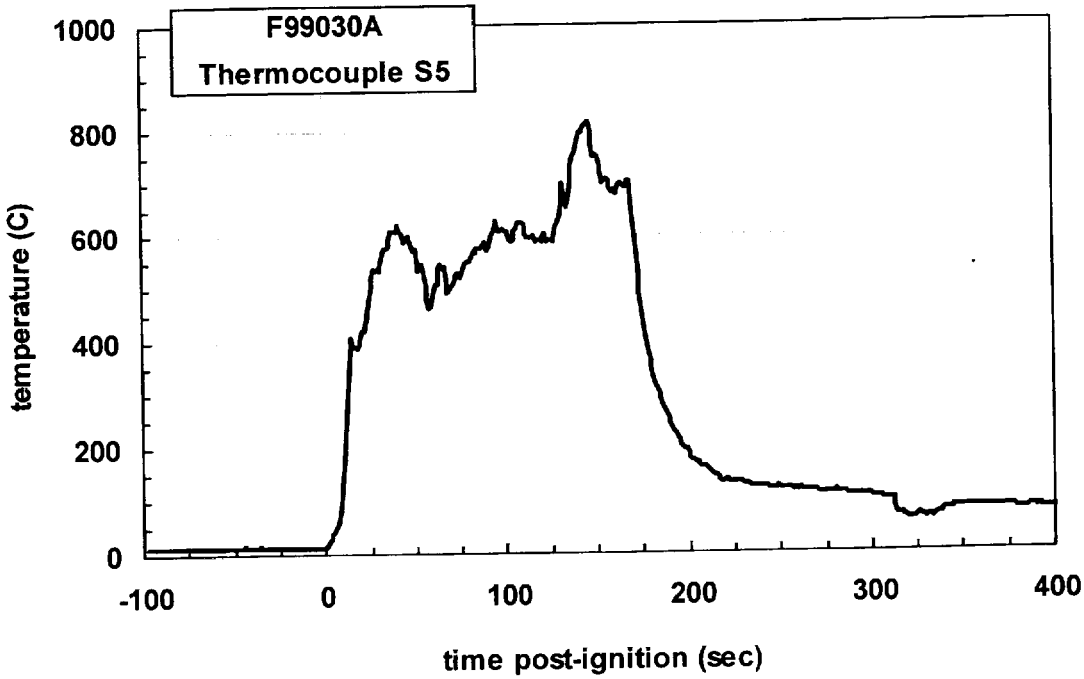

Plot C54. Fire Test F99030A. Data plot from thermocouple S5.

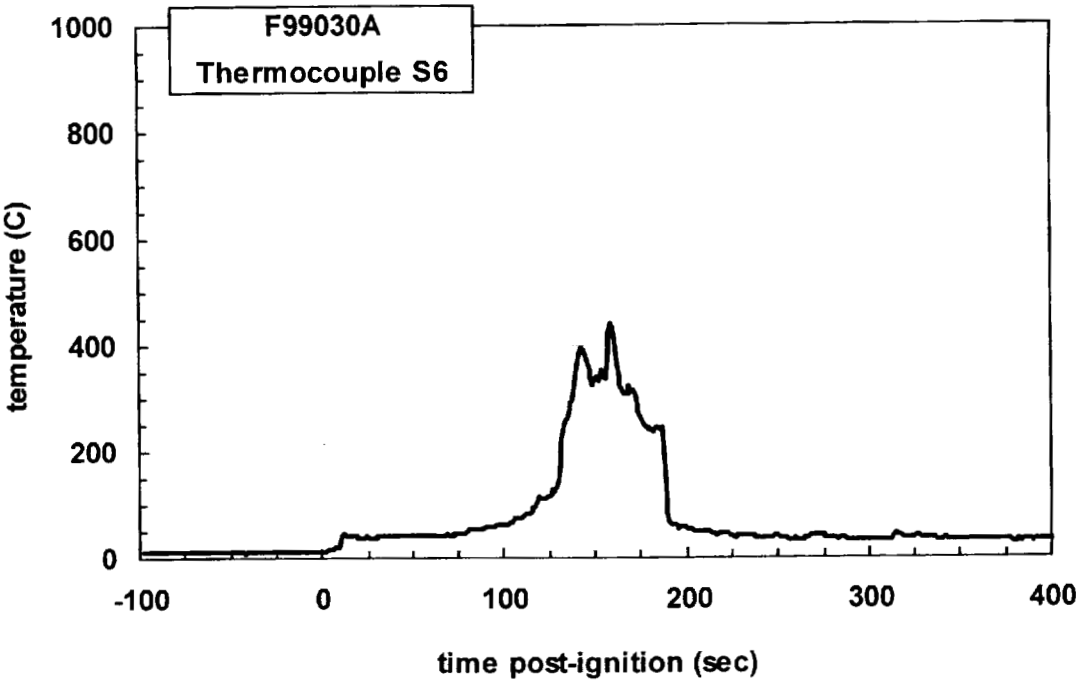

Plot C55. Fire Test F99030A. Data plot from thermocouple S6.

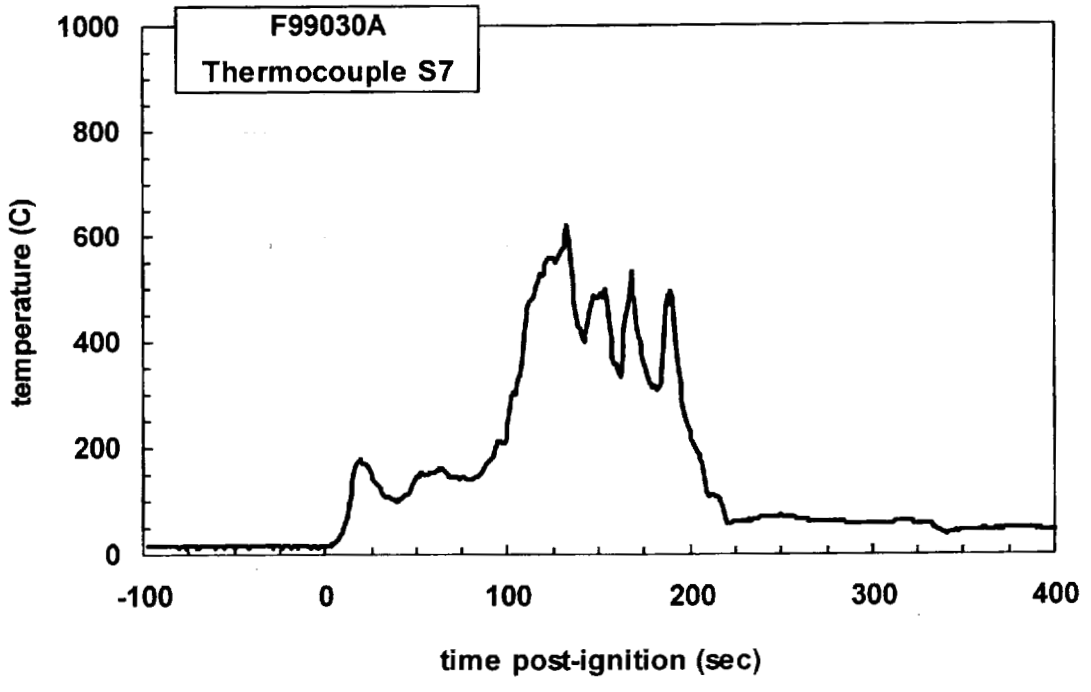

Plot C56. Fire Test F99030A. Data plot from thermocouple S7.

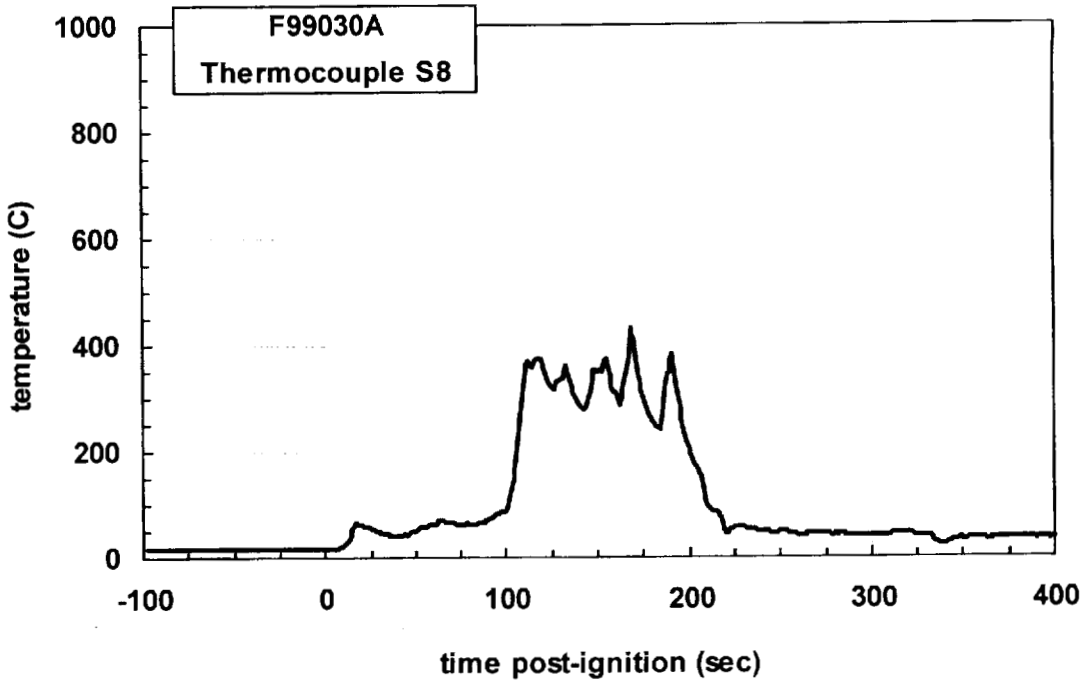

Plot C57. Fire Test F99030A. Data plot from thermocouple S8.

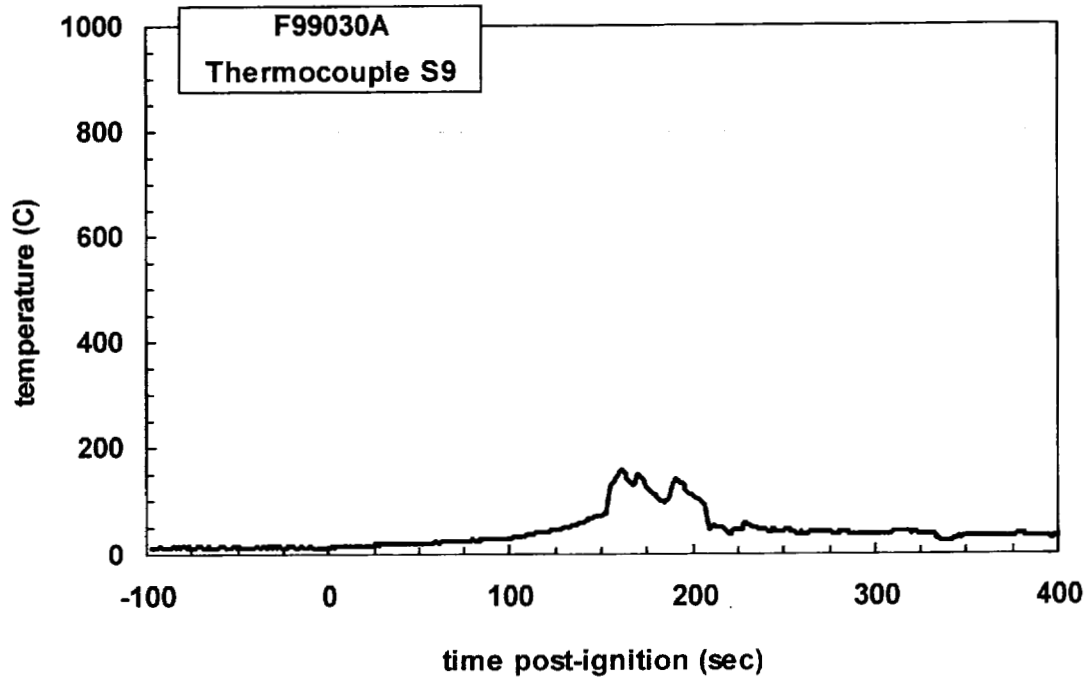

Plot C58. Fire Test F99030A. Data plot from thermocouple S9.

APPENDIX D
ASPIRATED THERMOCOUPLE DATA

One aspirated thermocouple assembly (Medtherm Corporation) was installed in the test vehicle (Fig. D1). The aspirated thermocouple assembly was fabricated from Inconel 600 tubing. Each assembly consisted of a vertical manifold (o.d. = 0.375 in. (9.5 mm), i.d. = 0.25 in. (6.4 mm), length = 16 in. (406 mm)) with six horizontal radiation shields (o.d. = 0.25 in. (6.4 mm), i.d. = 0.19 in. (4.8 mm), length = 1.00 in. (25.4 mm)). The vertical spacing between the radiation shields along the manifold was 3 in. (75 mm). Three radial holes were drilled near the tip of each radiation shield. The holes were sized to approximately balance the airflow-rates over each thermocouple. A Type-N thermocouple inserted into each radiation shield so that the thermocouple junction was positioned approximately 0.2 in. (5.1 mm) down-stream from the inlet holes.

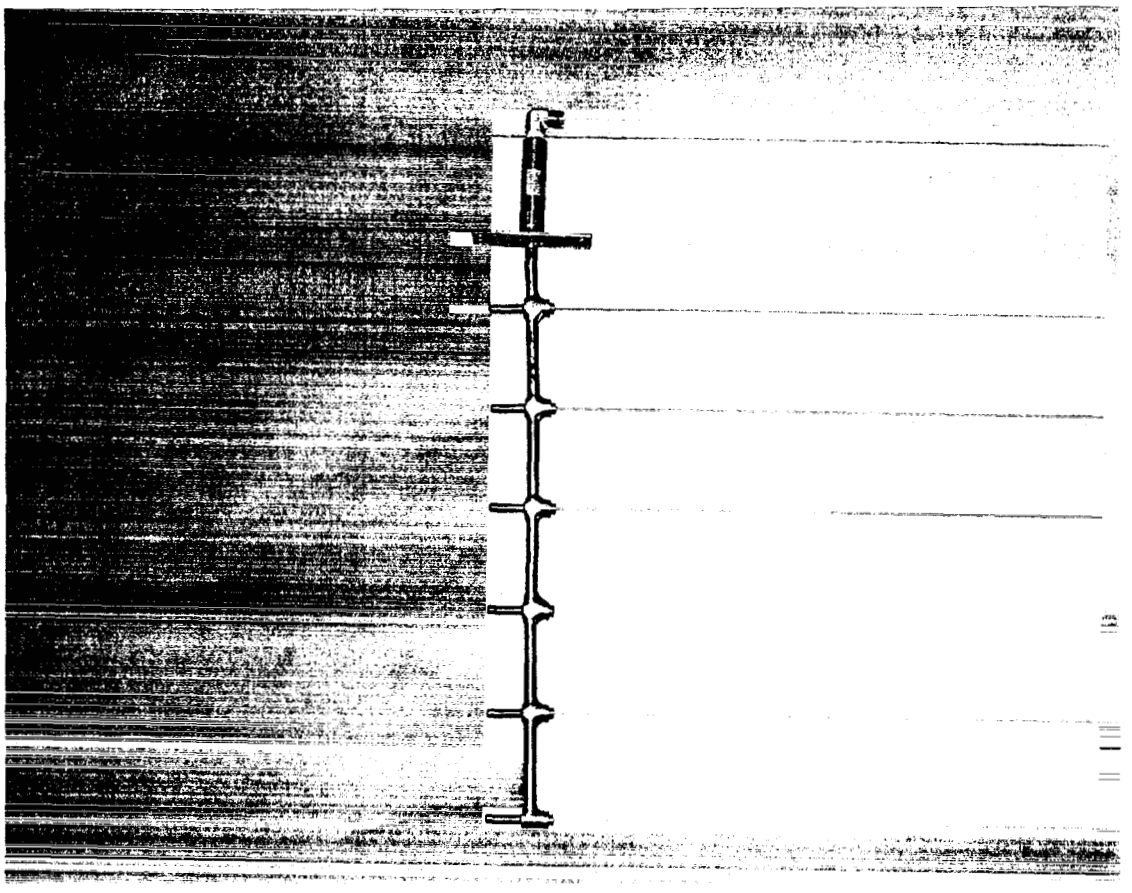

Figure D1. Fire Test F99030A. Photograph of the aspirated thermocouple assembly used in the passenger compartment of the test vehicle.

The mounting flange of the aspirated thermocouple probe assembly was attached to the roof of the vehicle. The probe extended into the passenger compartment through a hole in the roof so that all 6 thermocouples were located below the headliner. The probe was vertical and located

along the longitudinal mid-line of the vehicle approximately equidistant from the driver and passenger seat backs. The upper-most aspirated thermocouple was approximately 0.5 in. (12 mm) below the lower surface of the headliner. The manifold was connected to a rotary-vane pump with flexible copper tubing (o.d. = 0.5 in. (12 mm), length = 15 ft. (4.6 m)). The capacity of the pump was 50 L/min at atmospheric pressure.

Figures D2 and D3 show the approximate location of the aspirated thermocouple probe assembly in the test vehicle for this test. Data recorded from these aspirated thermocouples during this test is shown Plots D1 through D6. Thermocouple ASP 1-1 was at the top of the probe and ASP 1-6 was as the bottom of the probe as oriented in the test vehicle.

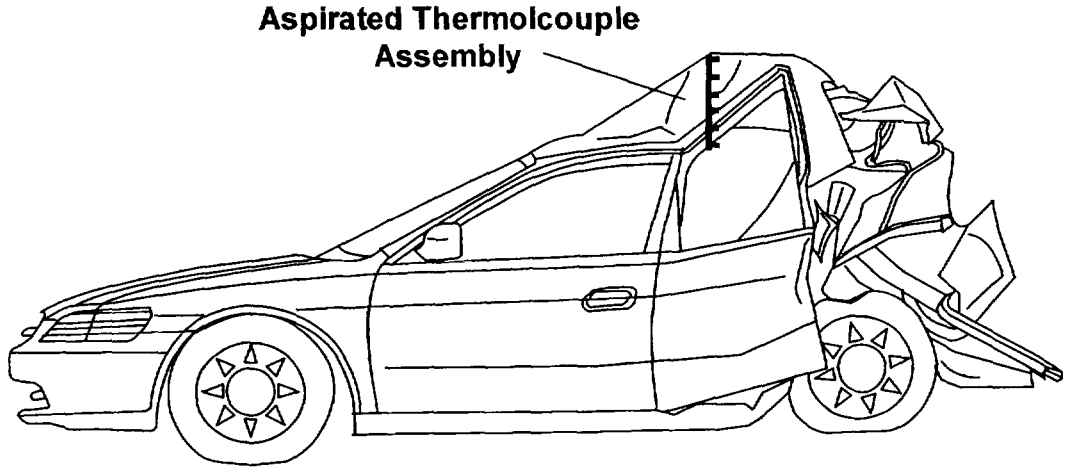

Figure D2. Fire Test F99030A. Side view of the test vehicle showing the approximate location of the aspirated thermocouple probe assembly in the passenger compartment.

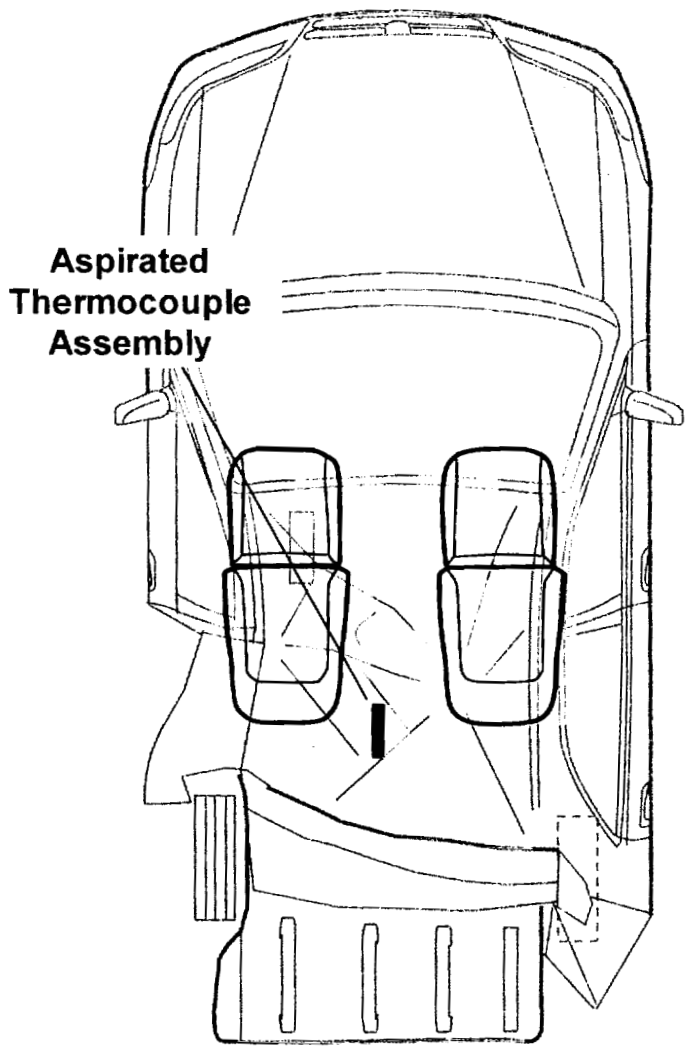

Figure D3. Fire Test F99030A. Top view of the test vehicle showing the approximate location of the aspirated thermocouple probe assembly in the passenger compartment.

REFERENCES

D1. J. S. Newman and P. A. Croce. A simple aspirated thermocouple for use in fires. *J. Fire Flamm.* **10**:326-336 (1979).

D2. N. R. Keltner and K. A. Strom. Thermal Measurement Uncertainty and Compensation. Paper in preparation.

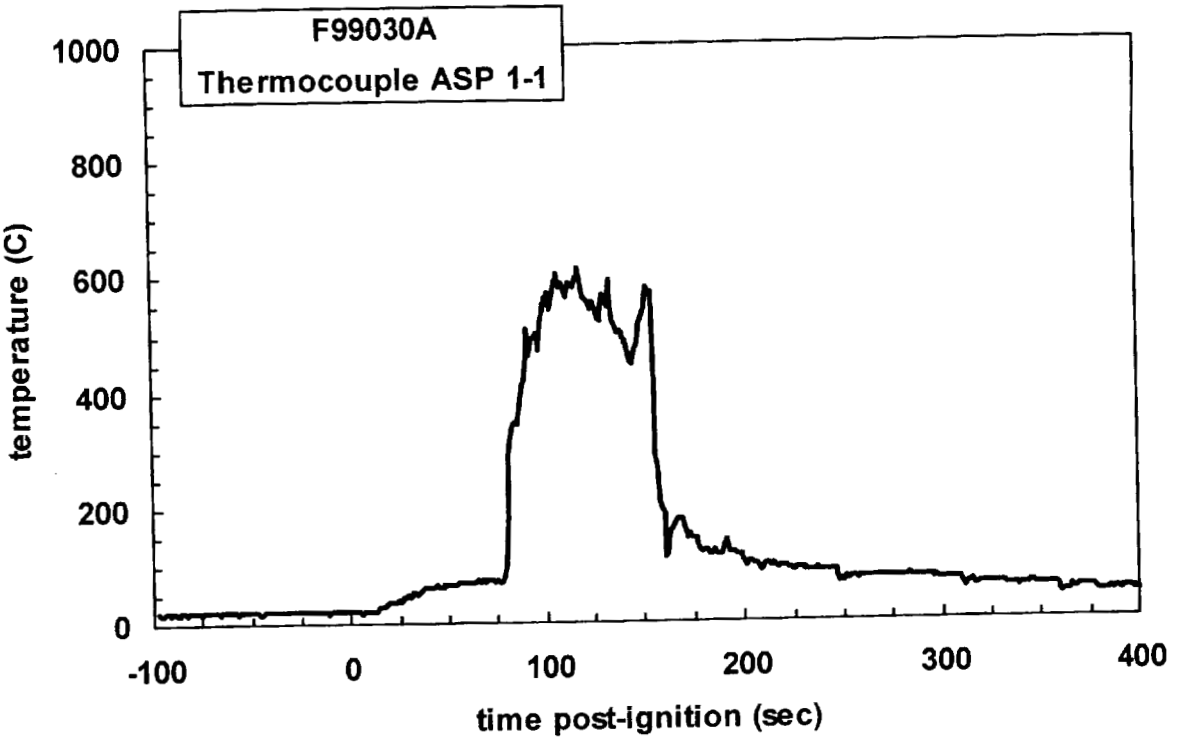

Plot D1. Fire Test F99030A. Data plot from thermocouple ASP1-1.

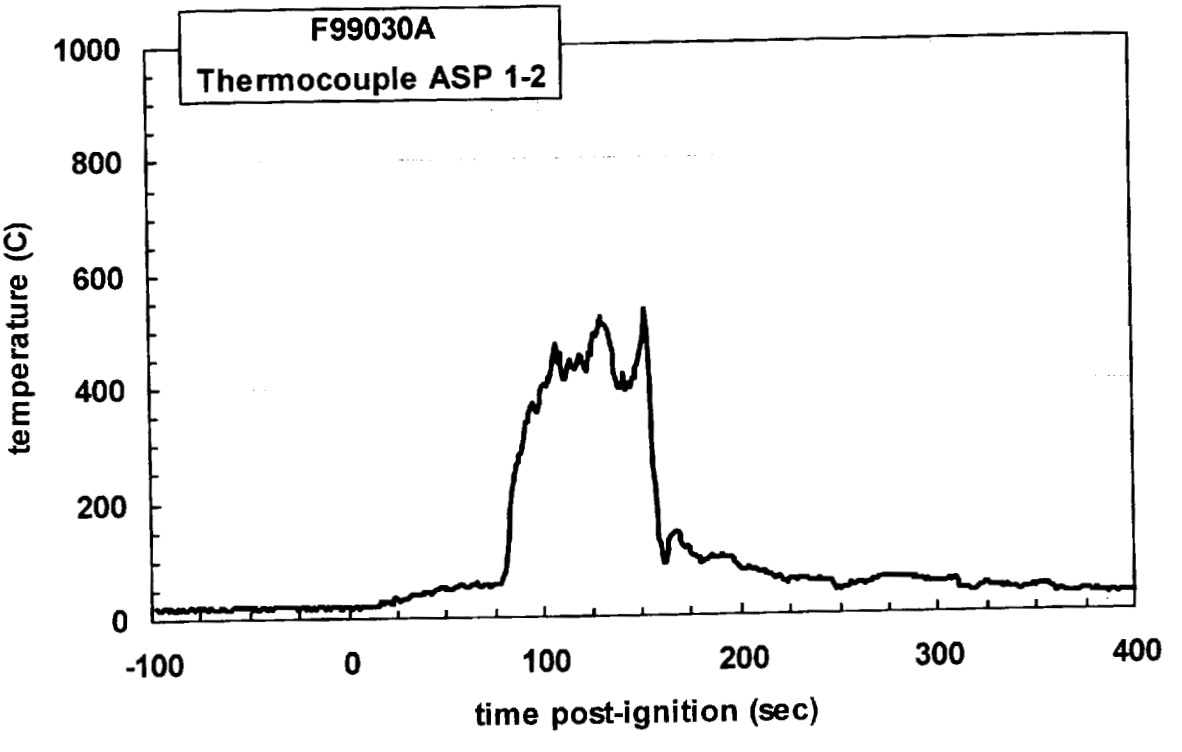

Plot D2. Fire Test F99030A. Data plot from thermocouple ASP1-2.

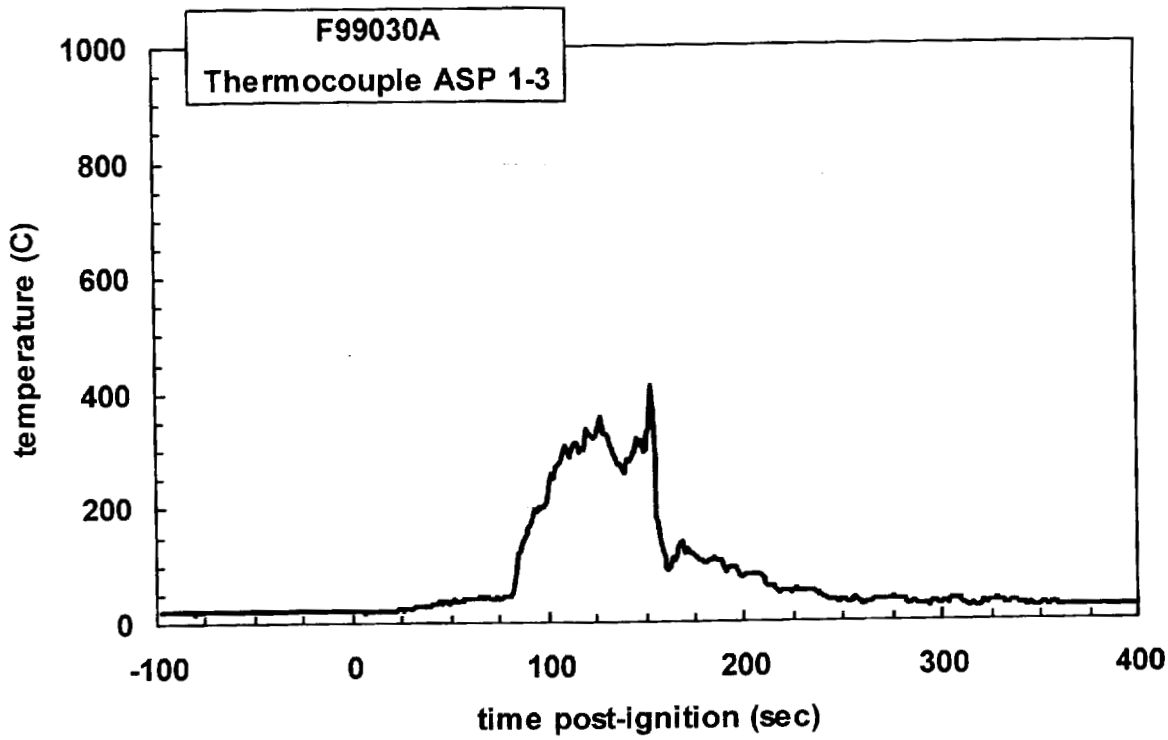

Plot D3. Fire Test F99030A. Data plot from thermocouple ASP1-3.

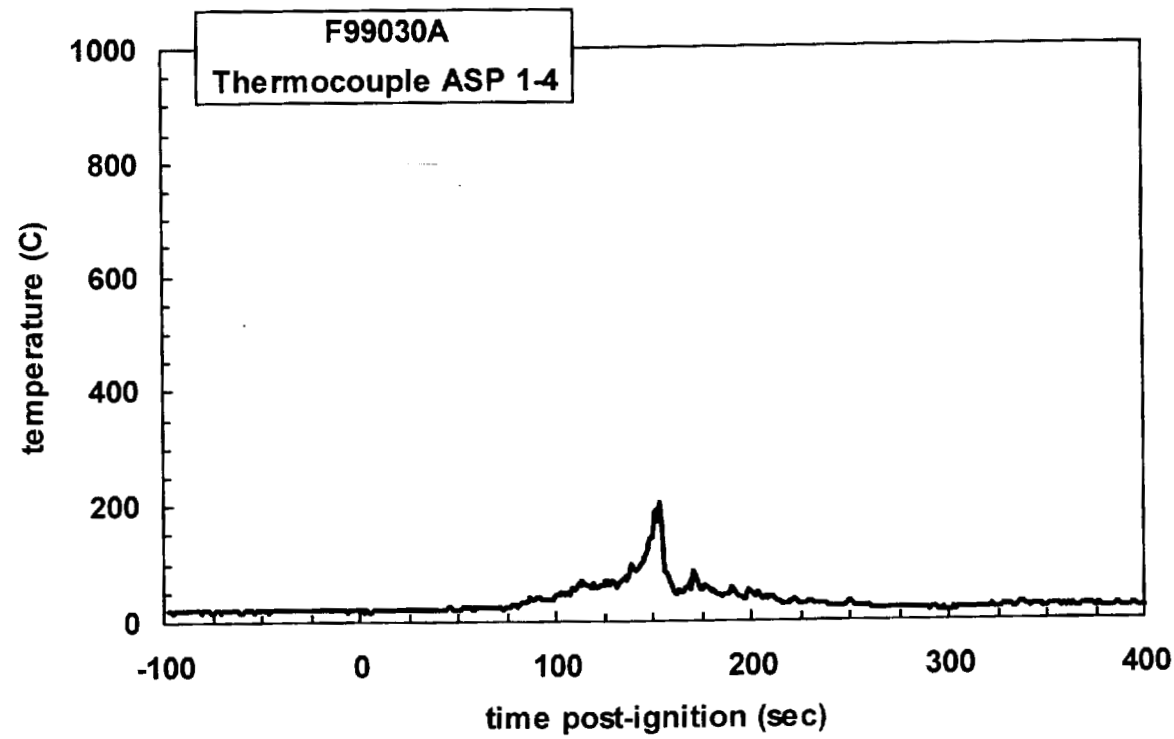

Plot D4. Fire Test F99030A. Data plot from thermocouple ASP1-4.

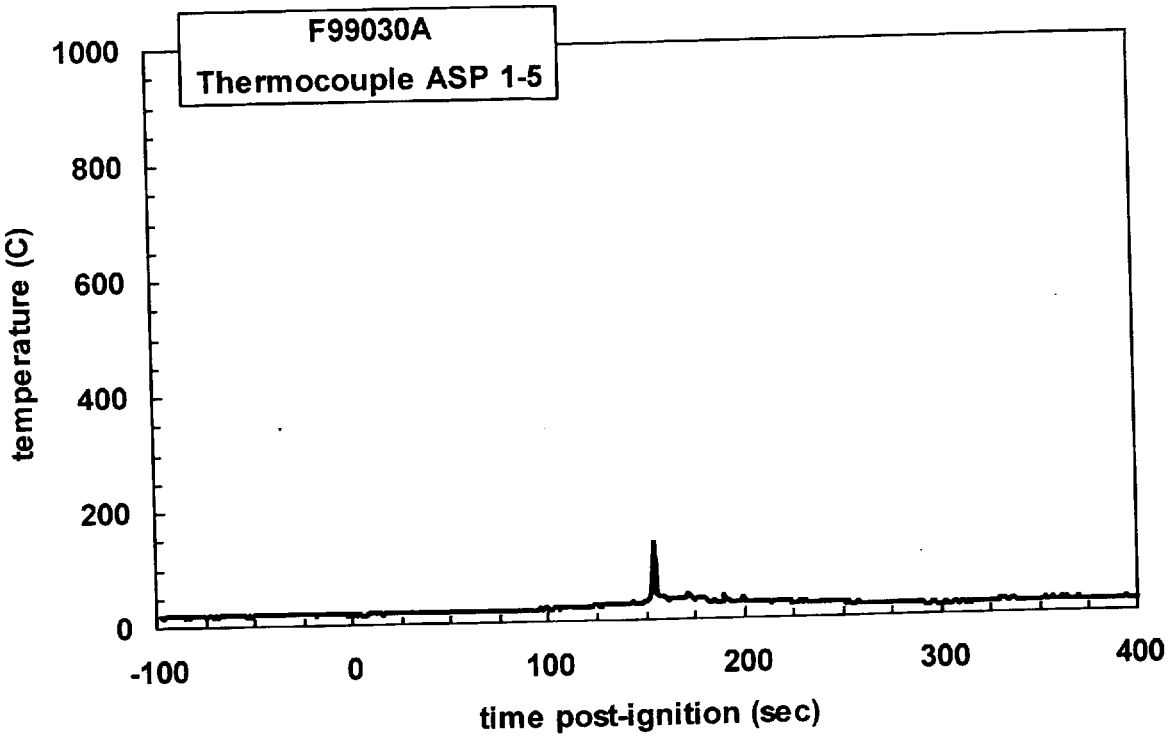

Plot D5. Fire Test F99030A. Data plot from thermocouple ASP1-5.

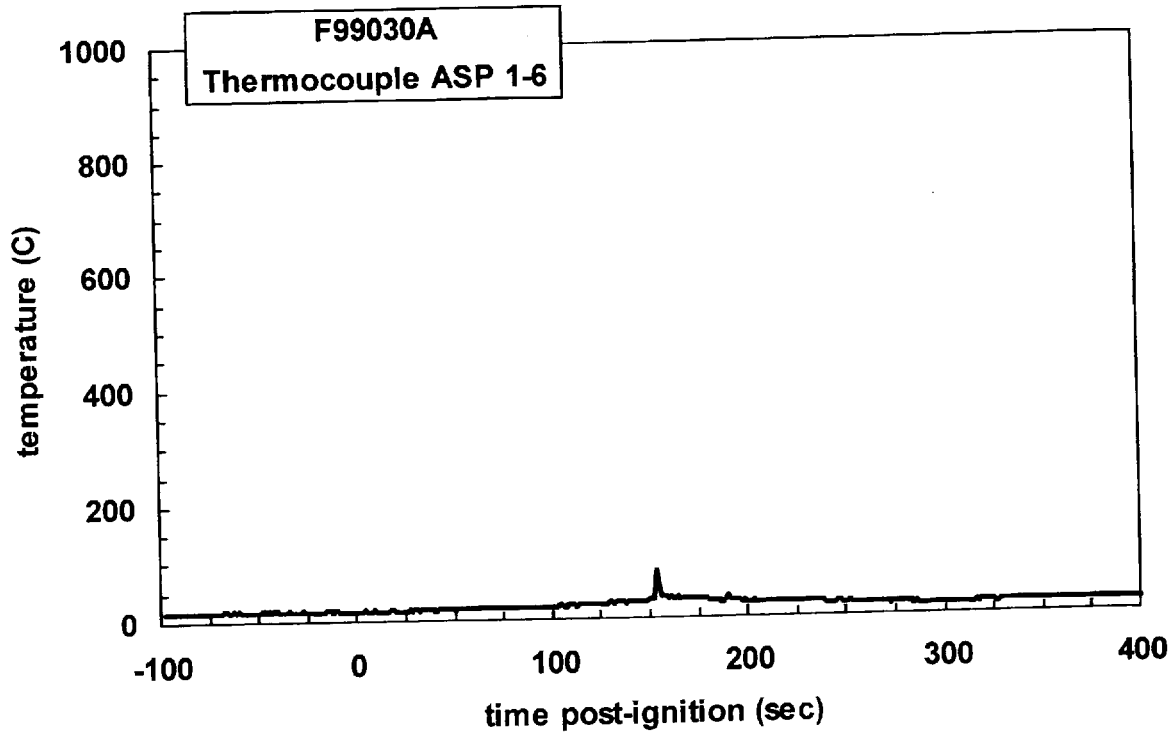

Plot D6. Fire Test F99030A. Data plot from thermocouple ASP1-6.

APPENDIX E
HEAT FLUX TRANSDUCER/RADIOMETER DATA

Heat-flux transducers (HFT) and heat flux transducer/radiometer (HFT/RAD) assemblies (64 Series, Medtherm Corporation) were used to measure convective and radiative heat transfer to selected objects in the vehicle. HFT1 and HFT2 were heat flux transducers. Each HFT contained one Schmidt-Boelter thermopile in a water-cooled copper body (diameter = 1 in. (25.4 mm), length = 1 in. (25.4 mm)). The faces of the heat flux transducers were coated with high-temperature optical black paint. Both HFTs were calibrated to 100 kW/m^2 at a reference temperature of 80°C.

HFT/RAD10 through HFT/RAD15 were heat flux transducer/radiometer assemblies. Each HFT/RAD contained two Schmidt-Boelter thermopiles in a water-cooled copper body (diameter = 1 in. (25.4 mm), length = 1 in. (25.4 mm)). The faces of the heat flux transducers were coated with high-temperature optical black paint. The radiometers had permanent sapphire windows (view-angle = 150°; optical transmittance range 0.4 to 4.2 μm). The HFTs and RADs in these assemblies were calibrated to 10 kW/m^2 at a reference temperature of 80°C.

The PC-based data system used to acquire data from the thermocouples (**APPENDIX C**) also was used to acquire data from the heat flux transducers and radiometers. The electrical signal wires from these transducers terminated in a 5-pin circular connector (165 Series, Amphenol). Each connector was plugged into a panel-mounted jack, which was hard wired to an analog-input multiplex expansion card (DBK-12, IOTech, Inc., Cleveland, OH). As with the thermocouples, the electrical shields on the signal cables were connected to the electronic chassis grounds on the analog-input expansion cards. The data acquisition software (DASYLab) was configured to sample each channel at a rate of 10 Hz and store the data in 10-point block averages.

Figure E1 shows the approximate locations of HFT1 and HFT in the test vehicle. HFT1 was mounted to the floor panel under the rear seat cushion on the left side of the test vehicle. HFT2 was mounted to the left rear wheel house panel. Both HFTs were inserted into a clearance-holes that was drilled in the sheet metal panels and were mounted on stand-offs so that the faces of the transducer was flush with the exterior surfaces of the metal panels. The transducer faces on both HFT1 and HFT2 were facing downward. Thermocouples TC/HFT1 and TC/HFT2 were located in the bodies of each heat flux transducer or heat flux transducer/radiometer assemblies HFT1 and HFT2, respectively.

Figures E2 and E3 show the approximate locations of HFT/RAD10 through HFT/RAD15 in the test vehicle. HFT/RAD10, HFT/RAD11, and HFT/RAD12 were located above the left front seat back as shown in Figures E1 and E2. HFT/RAD13, HFT/RAD14, and HFT/RAD15 were located above the right front seat back as shown in Figures E1 and E2. Threaded rods (diameter = ½ in.) was inserted through holes in the roof above each of the front seats of the test vehicle. The lower

end of each rod was secured to the seat back to stabilize the transducers during the test. HFT/RAD10 through HFT/RAD15 were mounted to one of these threaded rods. Thermocouples O10, O11, O12, O13, O14, and O15 were located in the bodies of each heat flux transducer or heat flux transducer/radiometer assemblies HFT/RAD10,HFT/RAD11, HFT/RAD12, HFT/RAD13, HFT/RAD14, and HFT/RAD15, respectively.

One of the two fluid ports on each transducer was connected to the outlet manifold of a thermostated recirculating water bath, and the other fluid port was connected to the return manifold of the water bath using copper tubing (o.d. = 0.25 in.). The water in the water bath was equilibrated to 60°C before the test. Te flow rate of water through each body was approximately 100 mL/min during this test.

Data recorded from these transducers is shown in Plots E1 through E14.

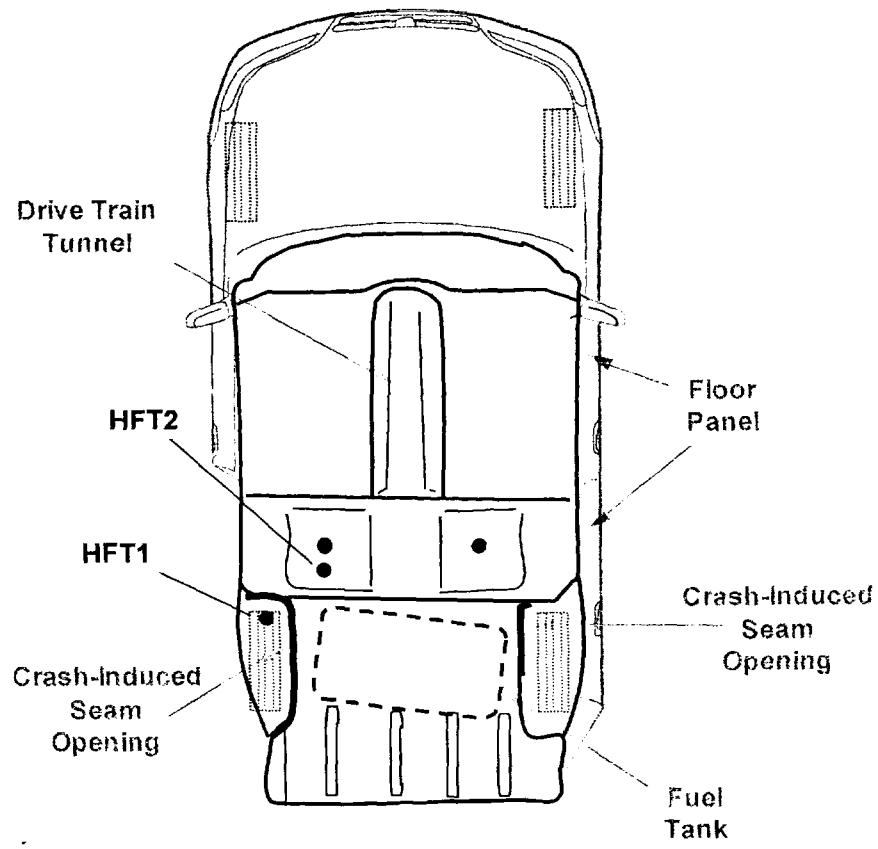

Figure E1. Fire Test F99030A. View showing the approximate locations of HFT1 and HFT2 in the test vehicle. HFT1 was mounted in the left rear wheel house panel of the test vehicle. HFT2 was mounted on the floor panel under rear passenger seat on the left side of the test vehicle.

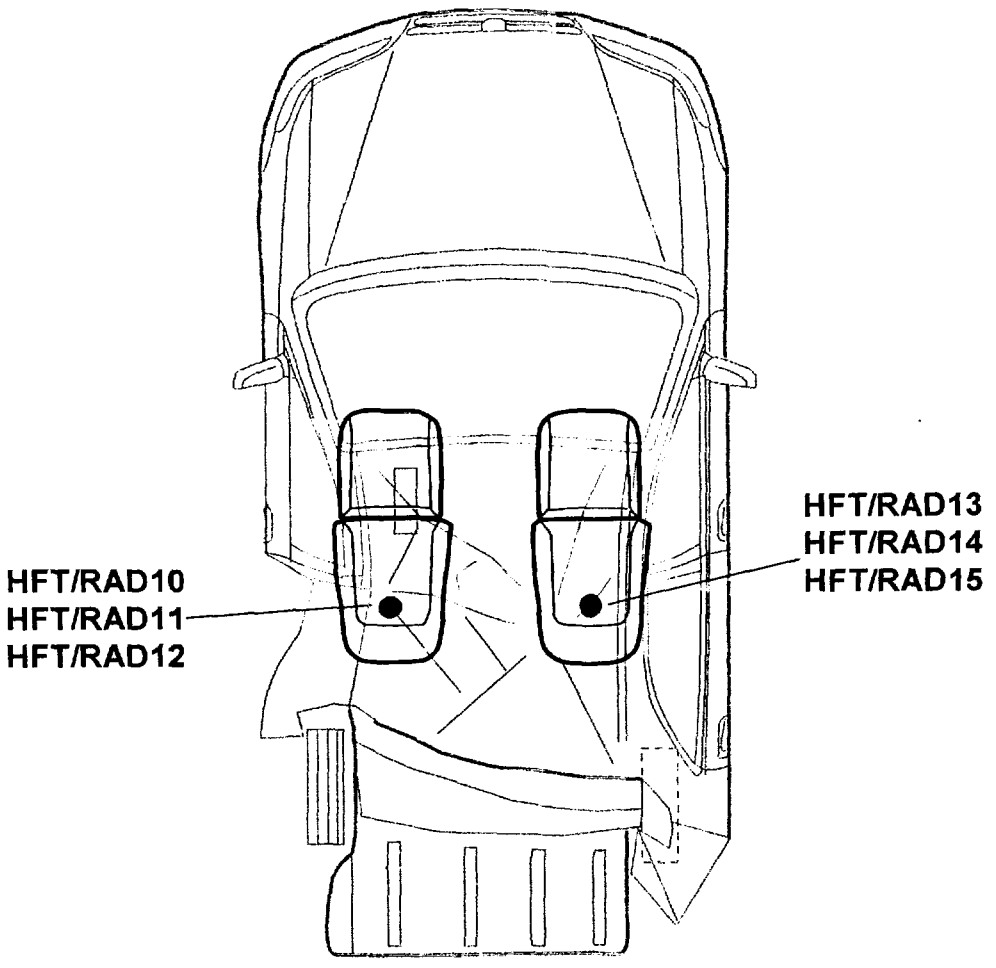

Figure E2. Fire Test F99030A. Top view of the test vehicle showing the approximate locations of heat flux transducer/radiometer (HFT/RAD) assemblies mounted in the test vehicle. HFT/RAD10 was located above the left front seat back facing the right rear corner of the test vehicle. HFT/RAD11 was located above the left front seat back facing upward. HFT/RAD12 was located above the left front seat back facing the left rear corner of the test vehicle. HFT/RAD13 was located above the right front seat back facing the right rear corner of the test vehicle. HFT/RAD14 was located above the right front seat back facing upward. HFT/RAD15 was located above the right front seat back facing the left rear corner of the test vehicle.

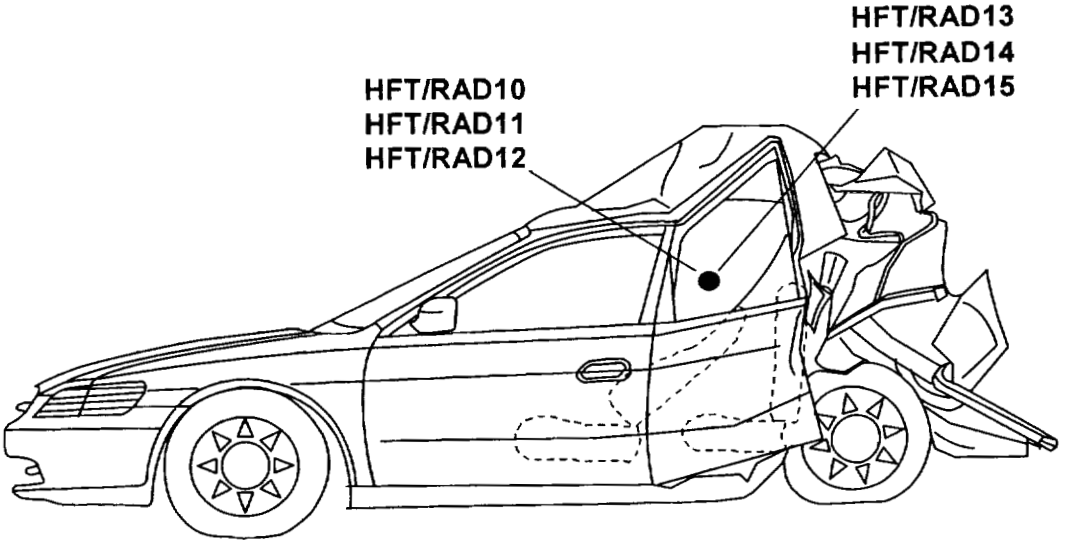

Figure E3. Fire Test F99030A. Side view of the test vehicle showing the approximate locations of heat flux transducer/radiometer (HFT/RAD) assemblies in the test vehicle. See the caption to Figure E2 for a description of the location of each transducer

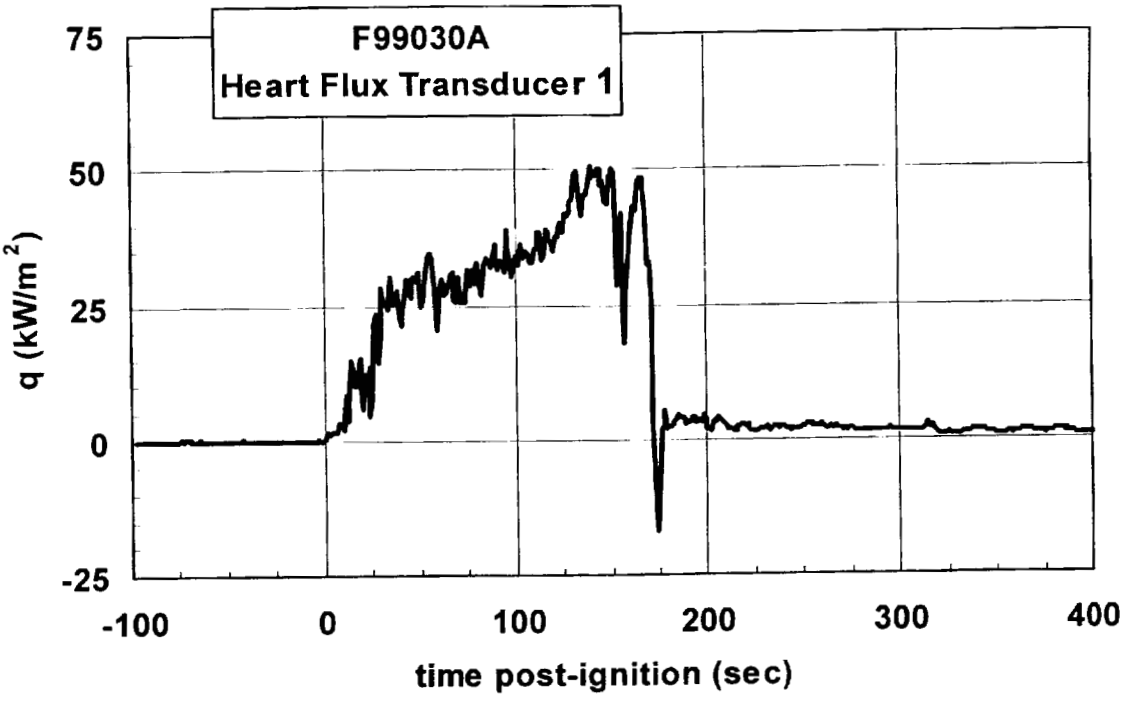

Plot E1. Fire Test F99030A. Data plot from Heat Flux Transducer 01.

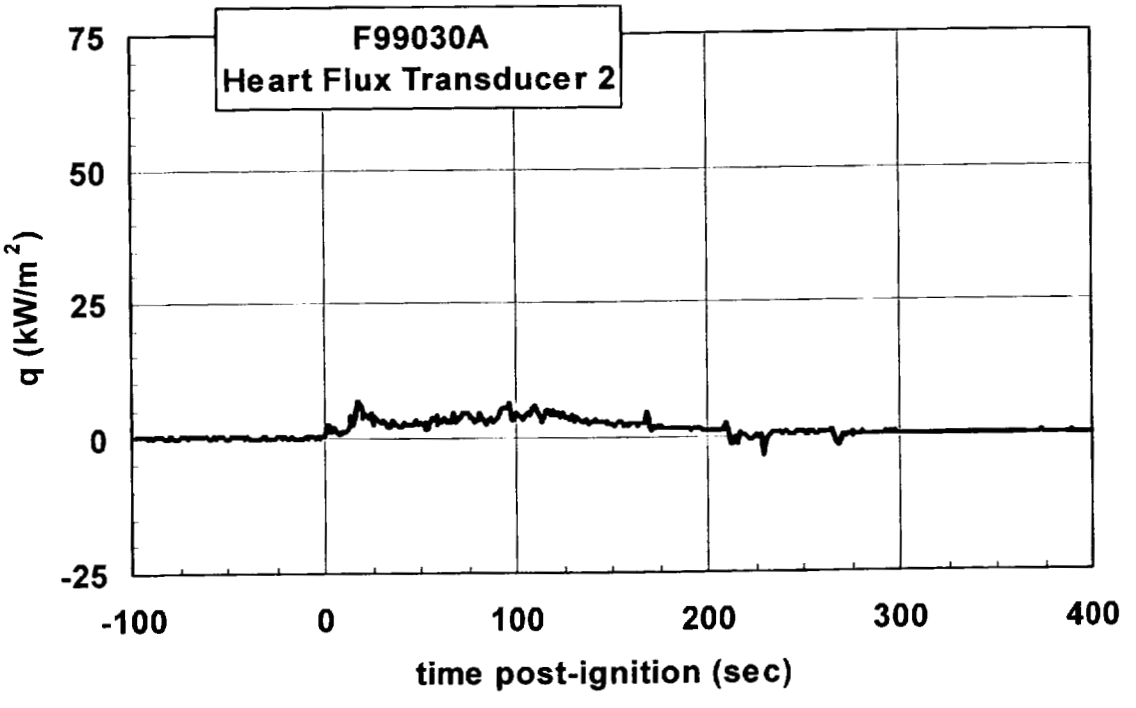

Plot E2. Fire Test F99030A. Data plot from Heat Flux Transducer 02.

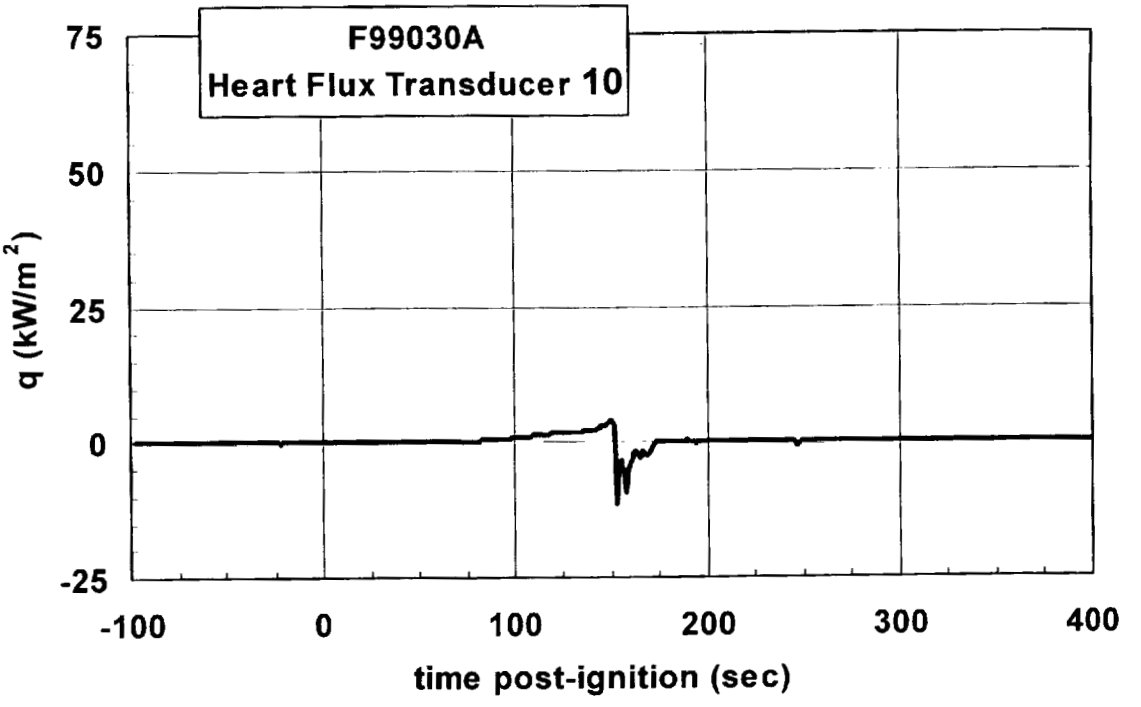

Plot E3. Fire Test F99030A. Data plot from Heat Flux Transducer 10.

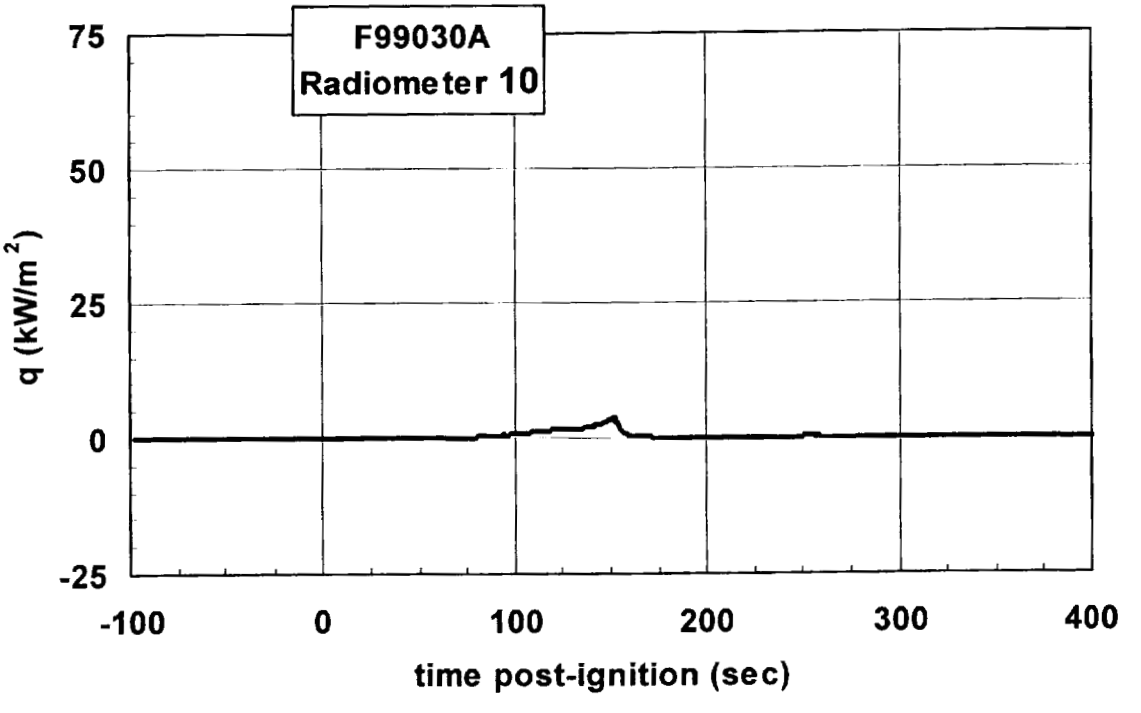

Plot E4. Fire Test F99030A. Data plot from Radiometer 10.

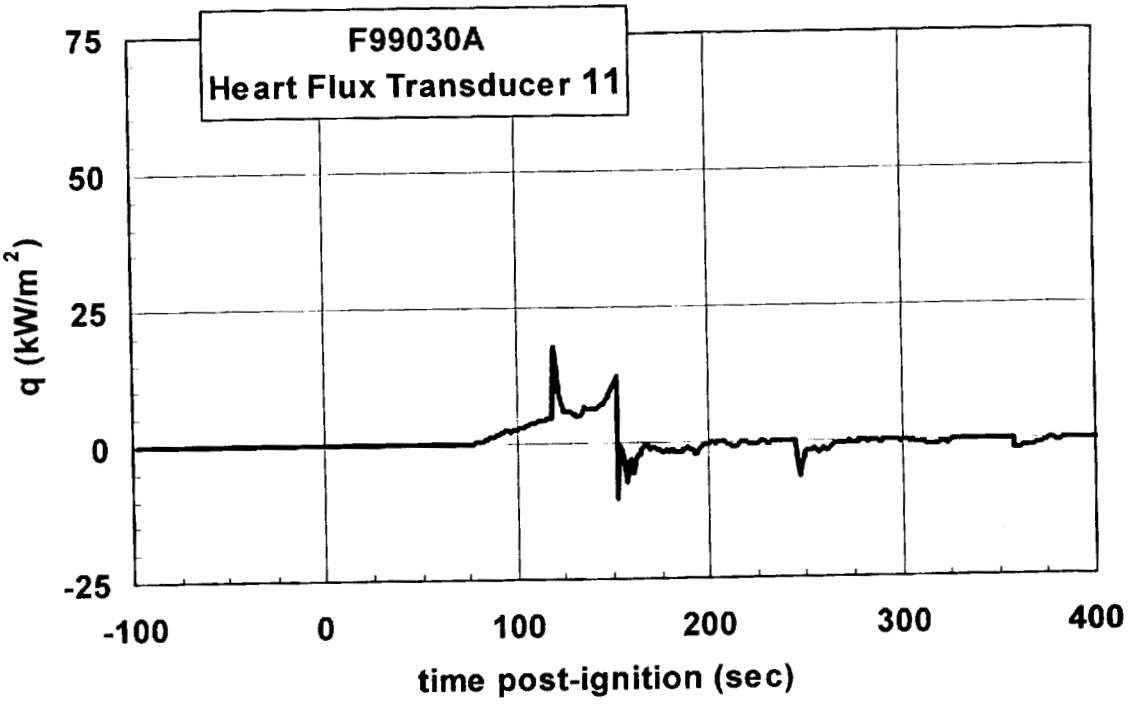

Plot E5. Fire Test F99030A. Data plot from Heat Flux Transducer 11.

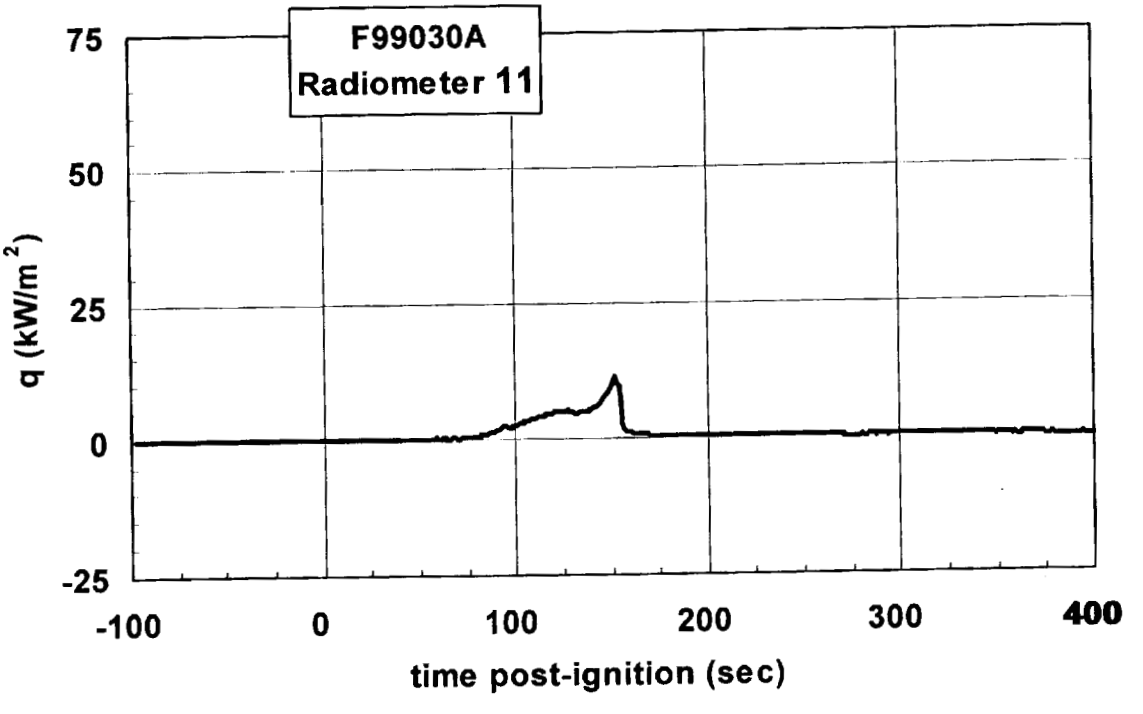

Plot E6. Fire Test F99030A. Data plot from Radiometer 11.

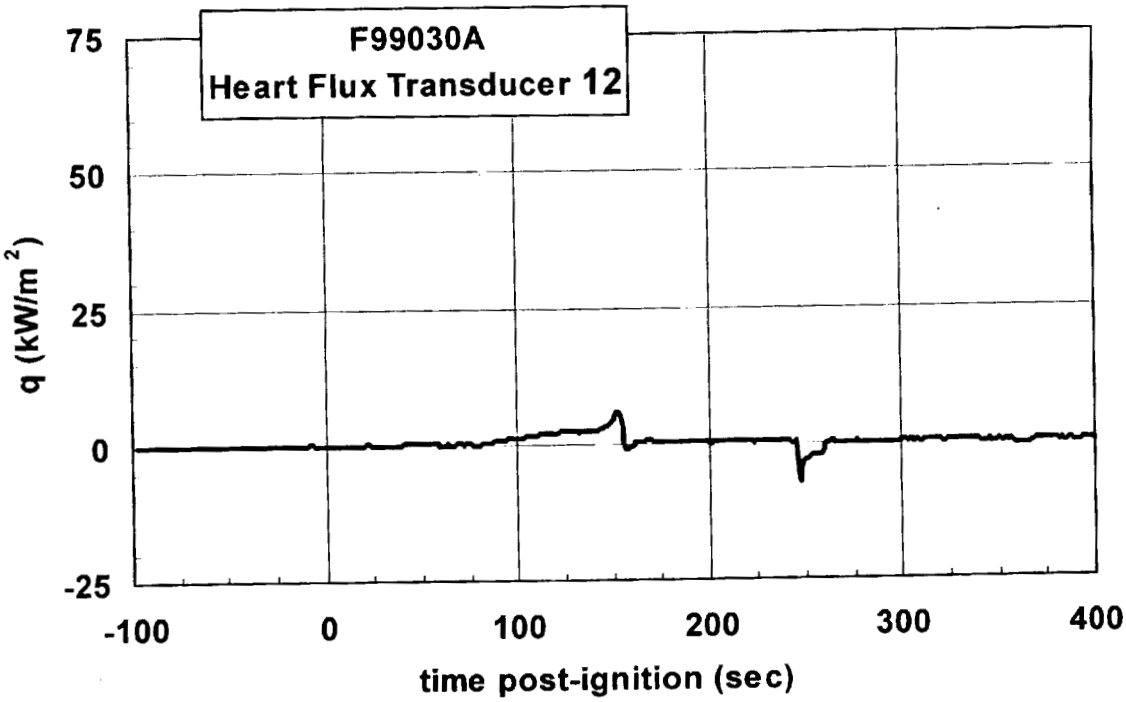

Plot E7. Fire Test F99030A. Data plot from Heat Flux Transducer 12.

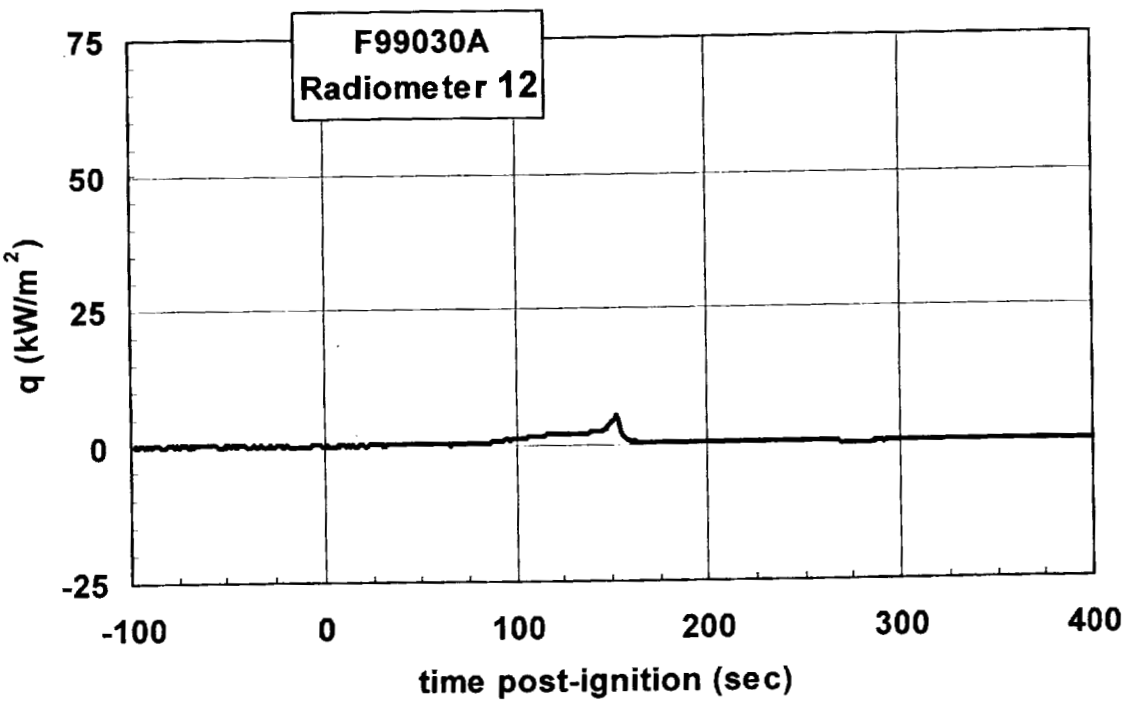

Plot E8. Fire Test F99030A. Data plot from Radiometer 12.

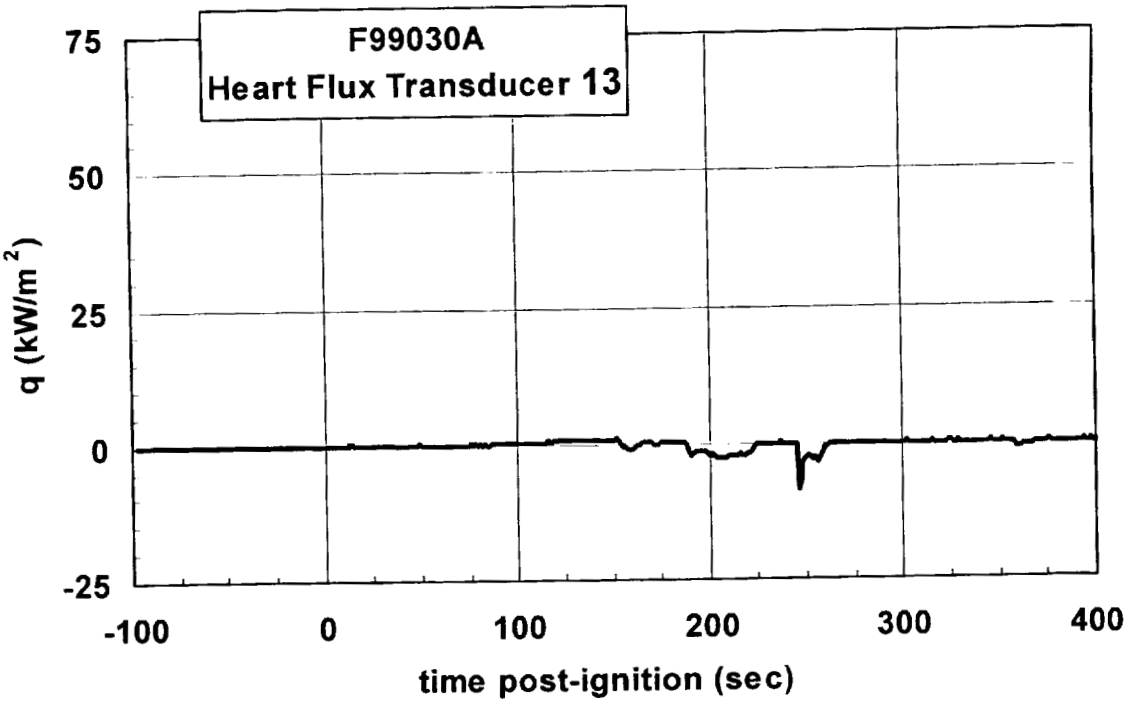

Plot E9. Fire Test F99030A. Data plot from Heat Flux Transducer 13.

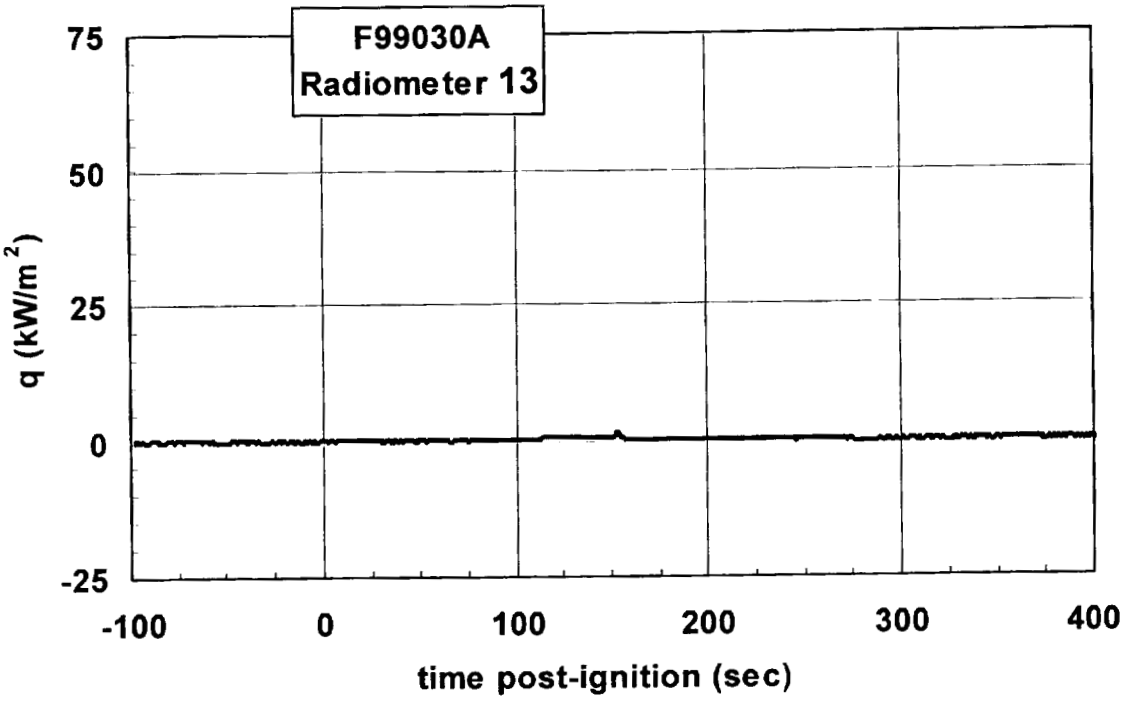

Plot E10. Fire Test F99030A. Data plot from Radiometer 13.

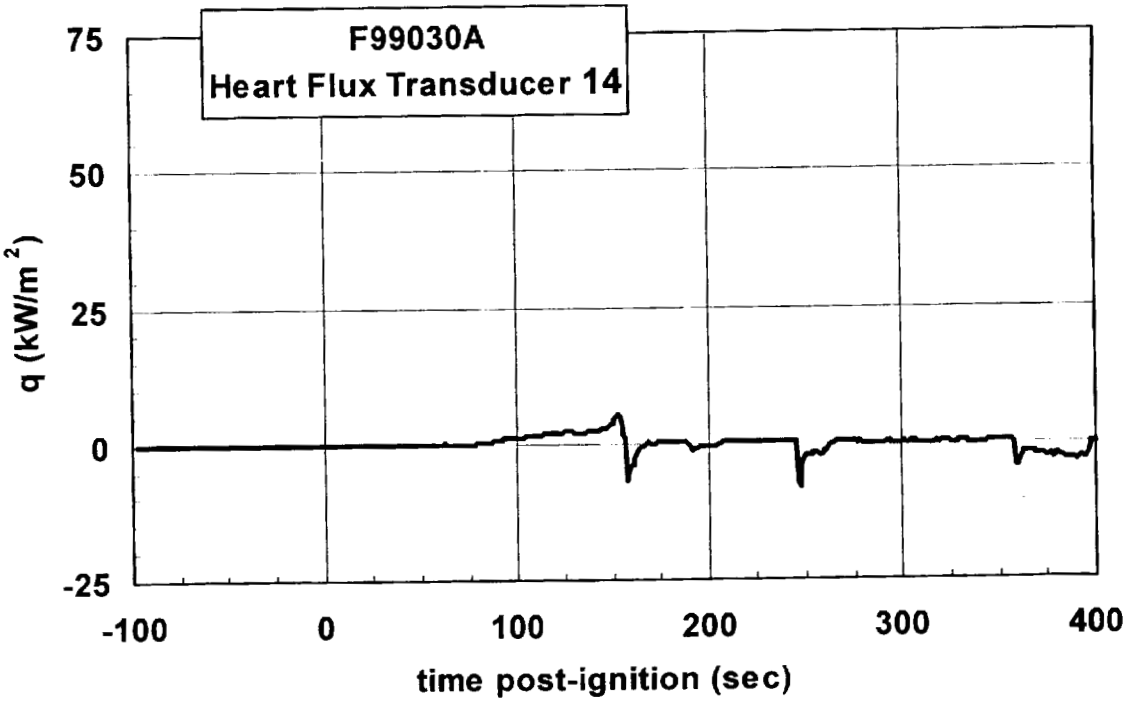

Plot E11. Fire Test F99030A. Data plot from Heat Flux Transducer 14.

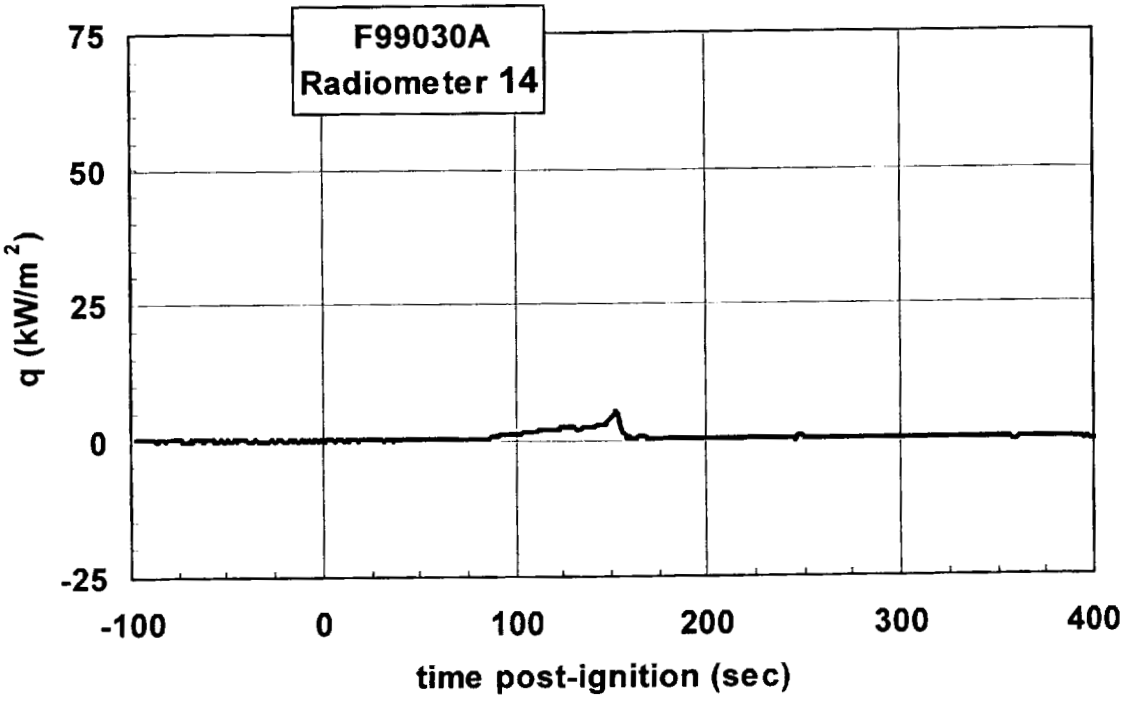

Plot E12. Fire Test F99030A. Data plot from Radiometer 14.

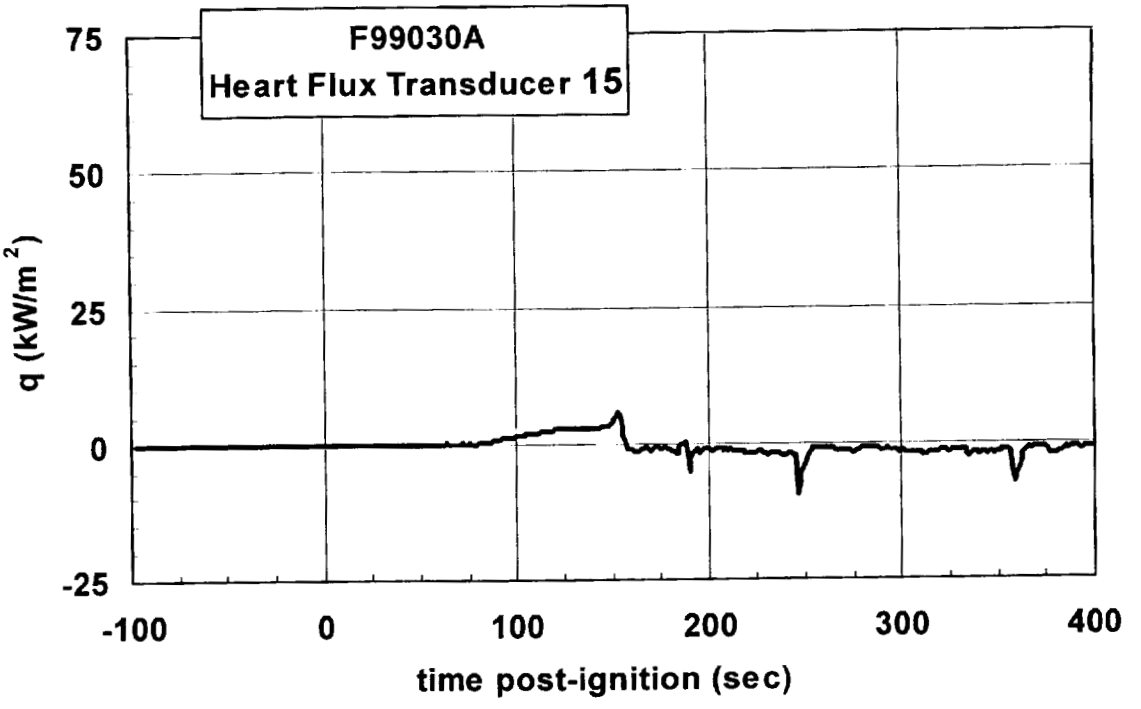

Plot E13. Fire Test F99030A. Data plot from Heat Flux Transducer 15.

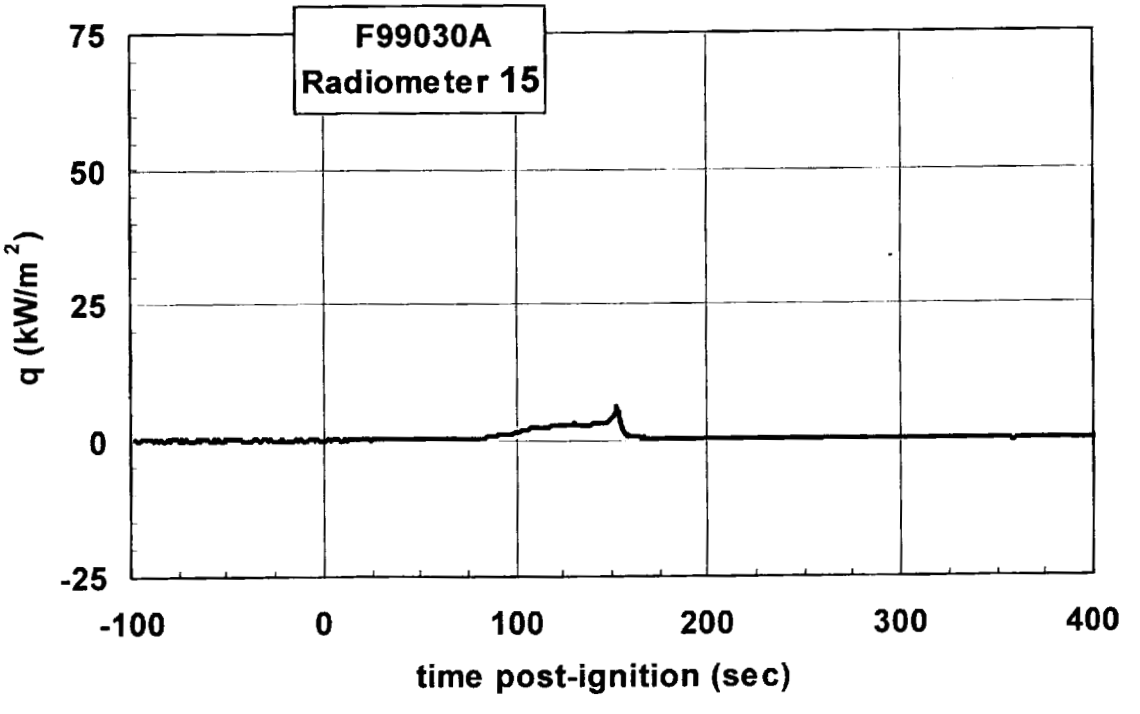

Plot E14. Fire Test F99030A. Data plot from Radiometer 15.

APPENDIX F
PRESSURE AND AIRFLOW MEASUREMENTS

Figures F1 through F3 show the approximate locations of the pressure taps and a bi-directional probe in the test vehicle.

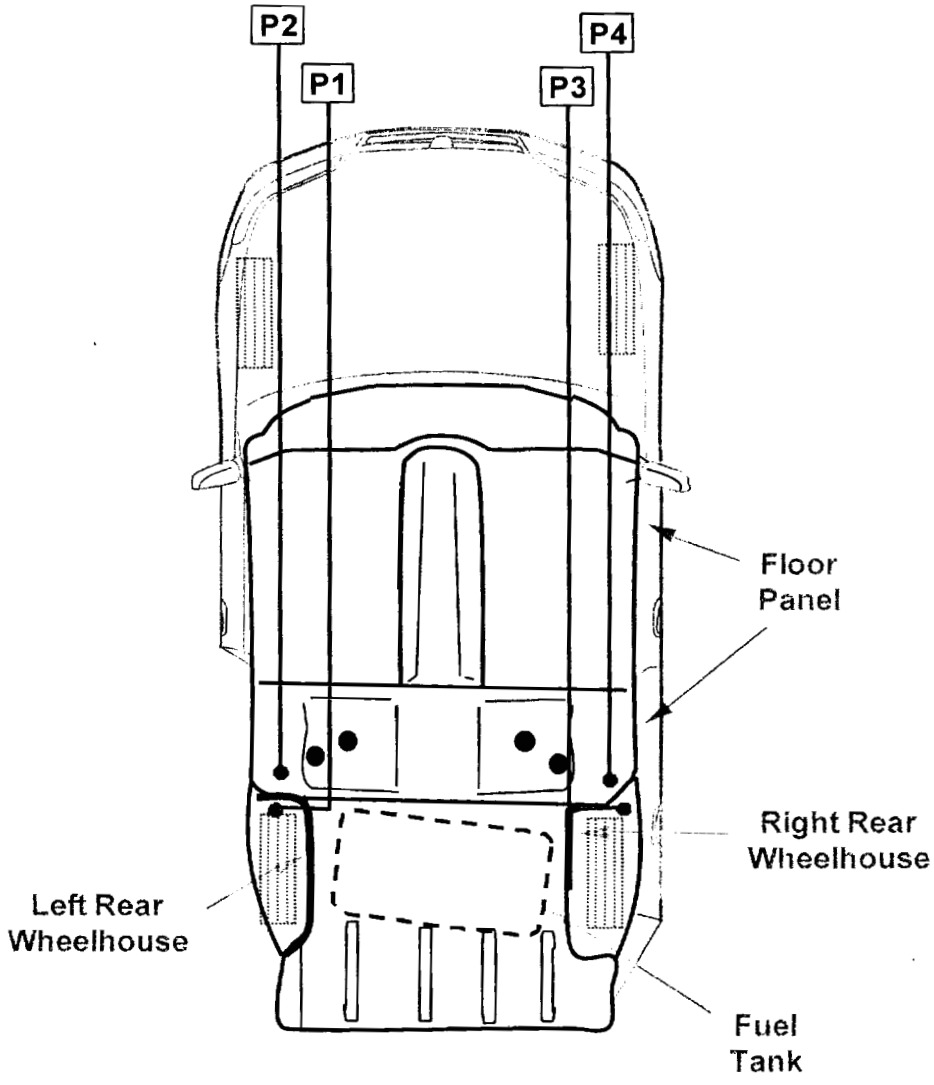

Figure F1. Fire Test F99030A. Top view showing the approximate locations of pressure taps around the rear wheelhouses of the test vehicle.

Six pressure taps were installed in the test vehicle for this test in the following locations: inside the left rear wheelhouse, just above the floor panel in the passenger compartment adjacent to the left rear wheelhouse panel, inside the right rear wheelhouse, just above the floor panel in the passenger compartment adjacent to the right rear wheelhouse panel, above the carpet in the

center of the foot area in front of the rear seat, and below the headlining panel above the rear seat.

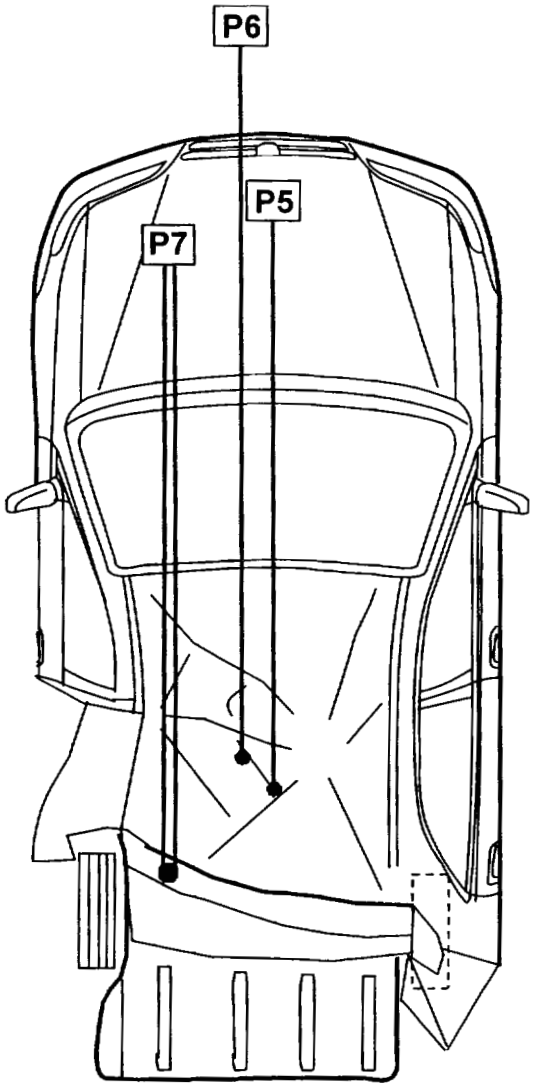

Figure F2. Fire Test F99030A. Top view showing the approximate locations of pressure taps at the roof and floor of the test vehicle, and of a bi-directional flow probe above the left side of the rear package shelf.

Each pressure tap was constructed from stainless steel tubing (o.d. = 0.250 in.). A union-T fitting with compression-type couplings (Parker) was attached to the inlet of the stainless steel tubing, with two of the three positions in the union-T fitting were left open. The other end of stainless steel tubing was connected to a pressure gauge with solvent-resistant flexible tubing (Tygon

Masterflex® 6049; i.d. = 0.250 in.; o.d. = 0.438 in.). The total length of the stainless steel and flexible tubing was approximately 10 m.

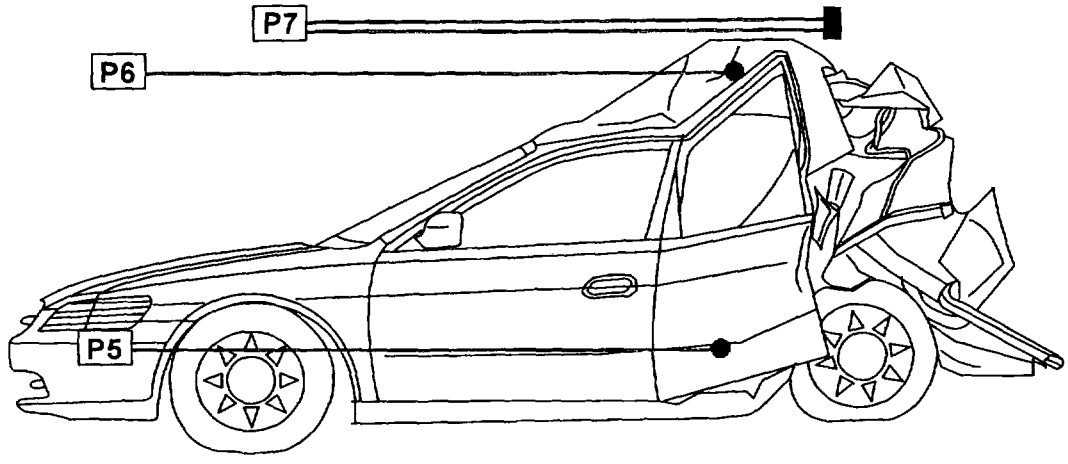

Figure F3. Fire Test F99030A. Side view showing the approximate locations of pressure taps at the roof and floor of the test vehicle, and of a bi-directional flow probe above the left side of the rear package shelf.

A bi-directional flow probe was installed in the test vehicle so that it was located just outboard of the center of the upper edge of the left quarter opening. This probe was used to determine the velocity and direction of airflow through the window opening during the test. The stainless steel tubes leading from the flow probe were connected to pressure gauges with solvent-resistant resistant flexible tubing (Tygon Masterflex® 6049; i.d. = 0.250 in.; o.d. = 0.438 in.). The total length of tubing was approximately 10 m.

The velocity of gas flow through the window opening in the driver's door was calculated from the pressure difference measured across the bi-directional probe using the following relationship:

$$V = 0.070\sqrt{T\Delta p} \qquad \text{(F1)}$$

where V is the gas velocity in m/s, T is the gas temperature in degrees Kelvin, and Δp is the pressure difference in Pascals (N/m^2) [F1 and F2].

Pressure gauges (Model C-264, Setra Systems, Acton, MA) with two pressure ranges were used for this test: - 0.5 to 0.5 (± 0.0013) in. W.C. (-124.5 to 124.5 Pascal) and -0.1 to 0.1 (± 0.0003) in. W.C. (-24.9 to 24.9 Pascal). Both gauges were accurate to 0.25% full scale. The gages were

powered with a 24 volt non-regulated power supply (Setra Systems). The high-pressure inlet of Pressure Gauge P1 was connected to the pressure tap located inside the left rear wheelhouse. The low-pressure inlet of Pressure Gauge P1 was left open to the atmosphere. The high-pressure inlet of Pressure Gauge P2 was connected to the pressure tap located just above the floor panel in the passenger compartment adjacent to the left rear wheelhouse panel. The low-pressure inlet of Pressure Gauge P2 was left open to the atmosphere. The high-pressure inlet of Pressure Gauge P3 was connected to the pressure tap located inside the right rear wheelhouse. The low-pressure inlet of Pressure Gauge P3 left open to the atmosphere. The high-pressure inlet of Pressure Gauge P4 was connected to the pressure tap located just above the floor panel in the passenger compartment adjacent to the right rear wheelhouse panel. The low-pressure inlet of Pressure Gauge P4 left open to the atmosphere. The high-pressure inlet of Pressure Gauge P5 was to the pressure tap located above the carpet in the center of the foot area in front of the rear seat. The low-pressure inlet of Pressure Gauge P5 was left open to the atmosphere. The high-pressure inlet of Pressure Gauge P6 was connected to the pressure tap located below the headlining panel above the rear seat. The low-pressure inlet of Pressure Gauge P6 was left open to the atmosphere. The low- and high-pressure inlets of pressure gauge P7 were connected to the bi-directional flow probe.

The PC-based data acquisition system described in **APPENDIX C** also was used to record the electronic signals from the pressure gauges during the test. The signal leads from the pressure gauges were plugged into panel-mounted connectors, which were hard-wired to a low-gain analog-input multiplex expansion card (DBK12, IOTech). The analog-input expansion card was interfaced to the main A/D card in the PC. The signal from each pressure gauge was sampled at a rate of 100 Hz. The analog data was stored to a data file in 100-point block-averages so that the effective sampling rate during the test was 1 Hz.

Plots of the pressures recorded with Pressure Gauges P1 through P7 are shown in Plots F1 through F7. Steam generated by the start of fire suppression and water entering the pressure taps caused the positive- and negative-going pressure deflections at about 140 seconds post-ignition.

REFERENCERS

F1. N. R. Keltner and J. L. Moya. Defining the thermal environment in fire tests. *Fire and Materials* **14**: 133-138, 1989.

F2. B. J. McCaffrey and G. A. Heskestad. Robust bi-directional low-velocity probe for flame and fire application. *Combustion and Flame* **26**: 125-127, 1976.

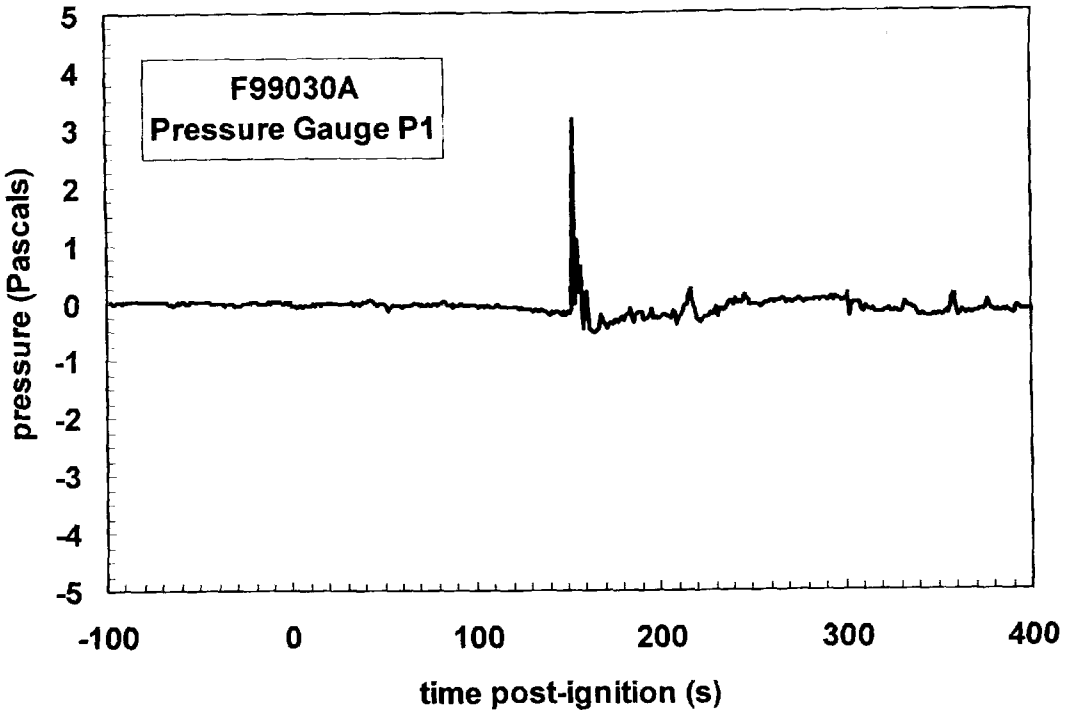

Plot F1. Fire Test F99030A. Absolute pressure at the pressure tap inside the left rear wheelhouse relative to atmospheric pressure measured with pressure gauge P1.

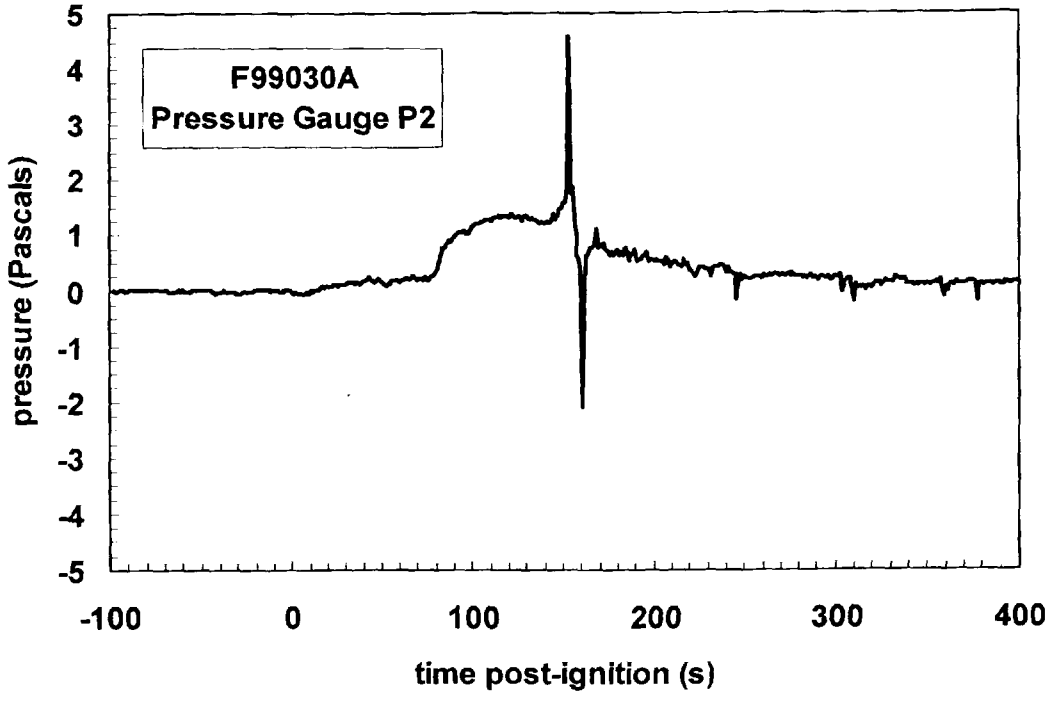

Plot F2. Fire Test F99030A. Absolute pressure above the floor panel adjacent to the left rear wheelhouse panel relative to atmospheric pressure measured with pressure gauge P2.

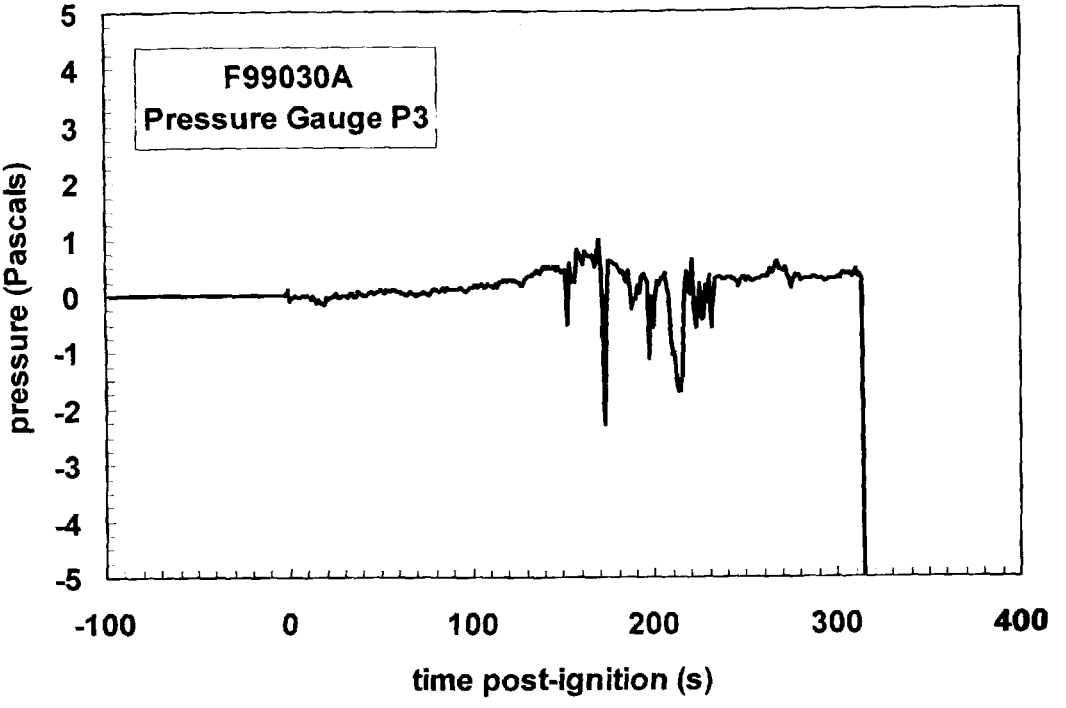

Plot F3. Fire Test F99030A. Absolute pressure at the pressure tap inside the right rear wheelhouse relative to atmospheric pressure measured with pressure gauge P3.

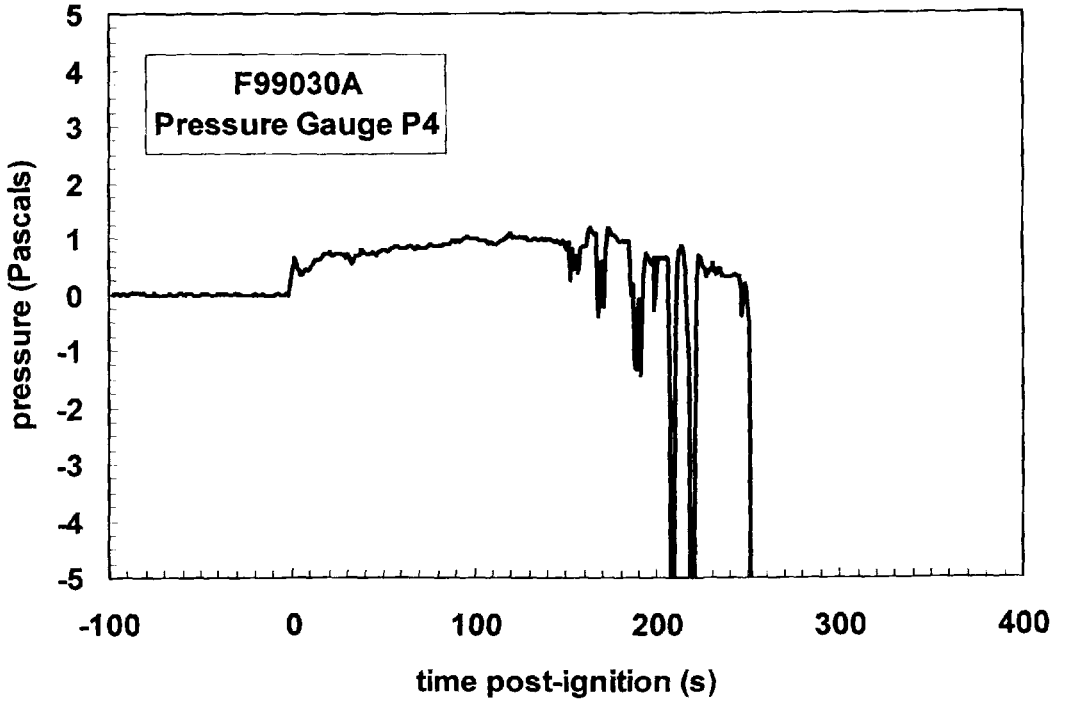

Plot F4. Fire Test F99030A. Absolute pressure above the floor panel adjacent to the right rear wheelhouse panel relative to atmospheric pressure measured with pressure gauge P4.

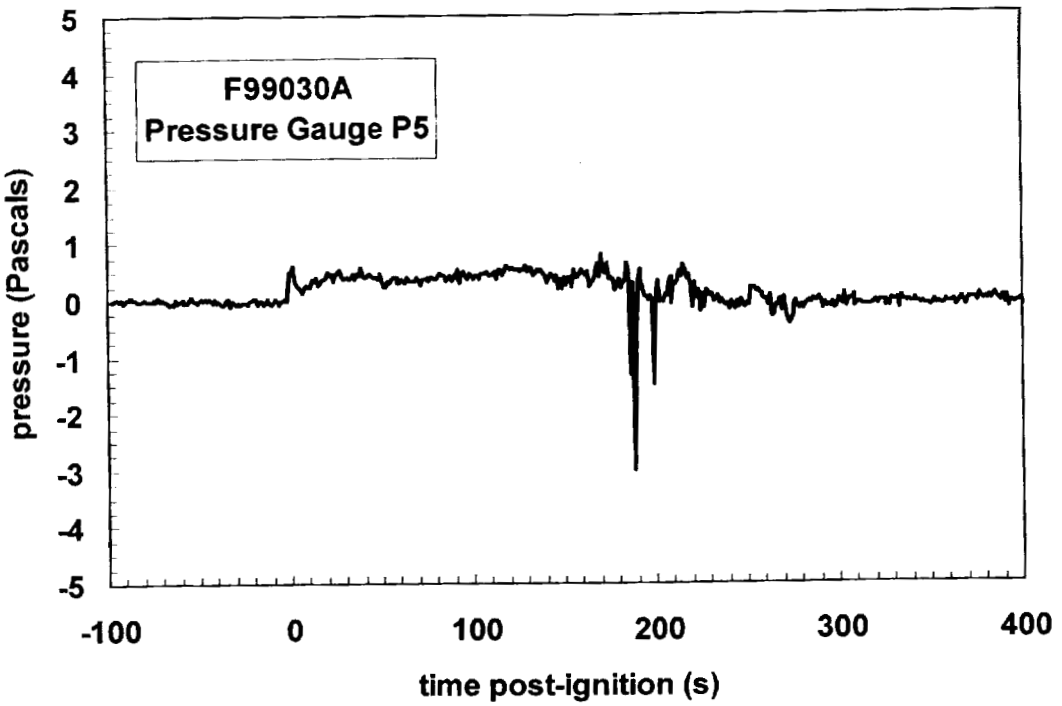

Plot F5. Fire Test F99030A. Absolute pressure above the carpet in the center of the foot area in front of the rear seat relative to atmospheric pressure measured with pressure gauge P5.

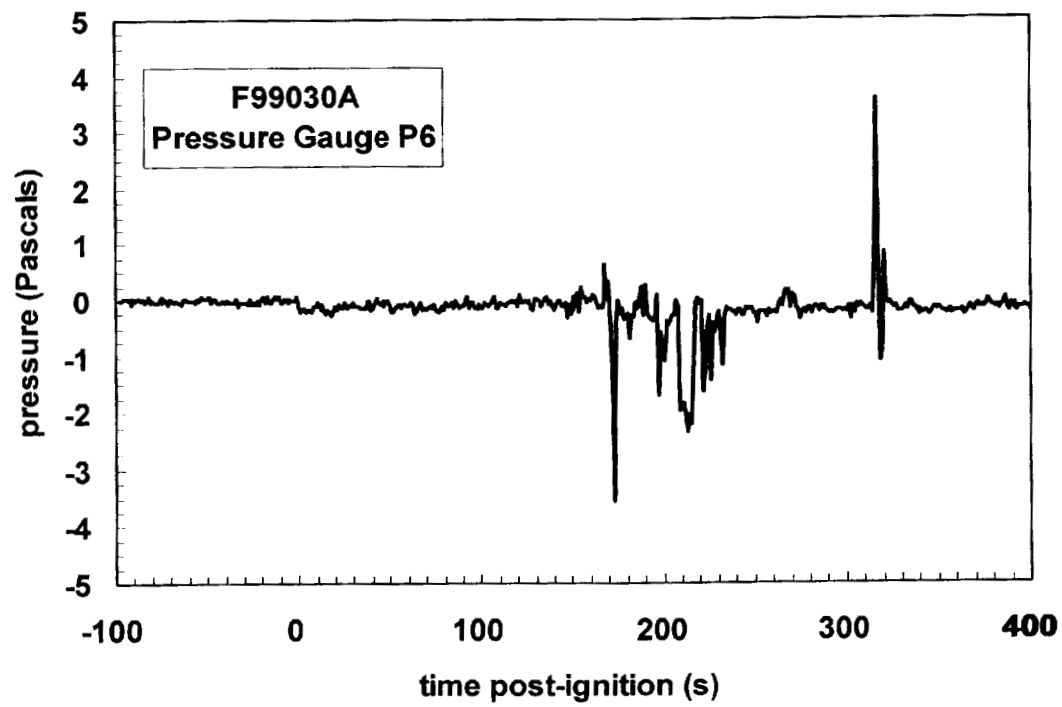

Plot F6. Fire Test F99030A. Absolute pressure below the headlining panel above the rear seat relative to atmospheric pressure measured with pressure gauge P6.

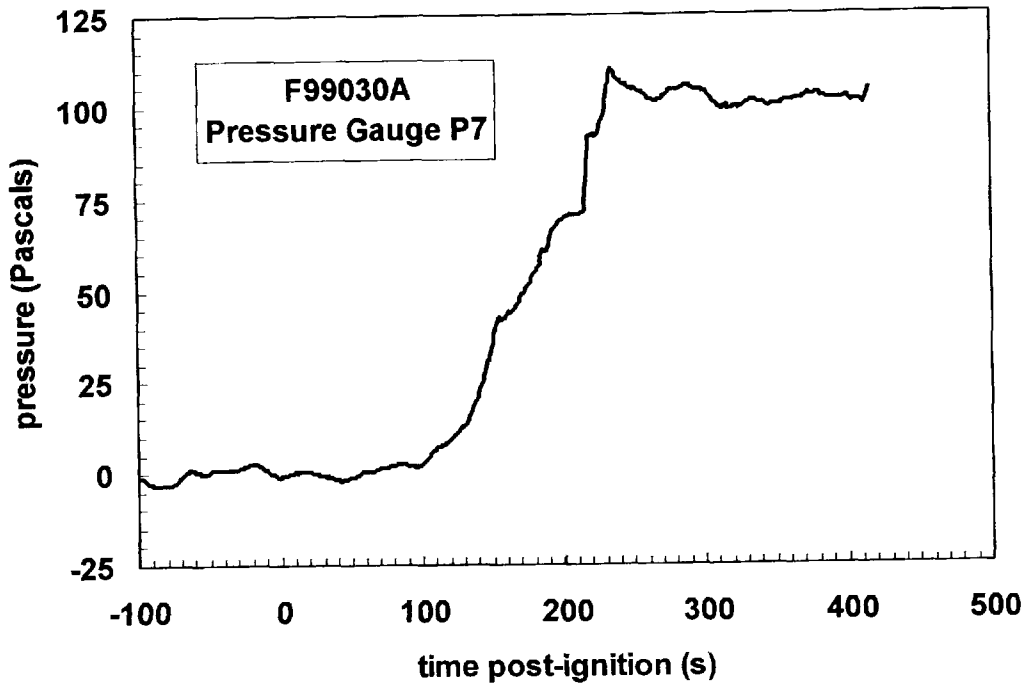

Plot F7. Fire Test F99030A. Pressure difference across the bi-directional flow probe measured with P7. Positive pressure indicated pressure was greater at the lower cup of the probe.

APPENDIX G
FIRE PRODUCTS COLLECTOR DATA

Scientific and technical personnel from Factory Mutual Research Corporation were primarily responsible for obtaining and analyzing data from the Fire Products Collector (FPC) at the Factory Mutual Test Center.

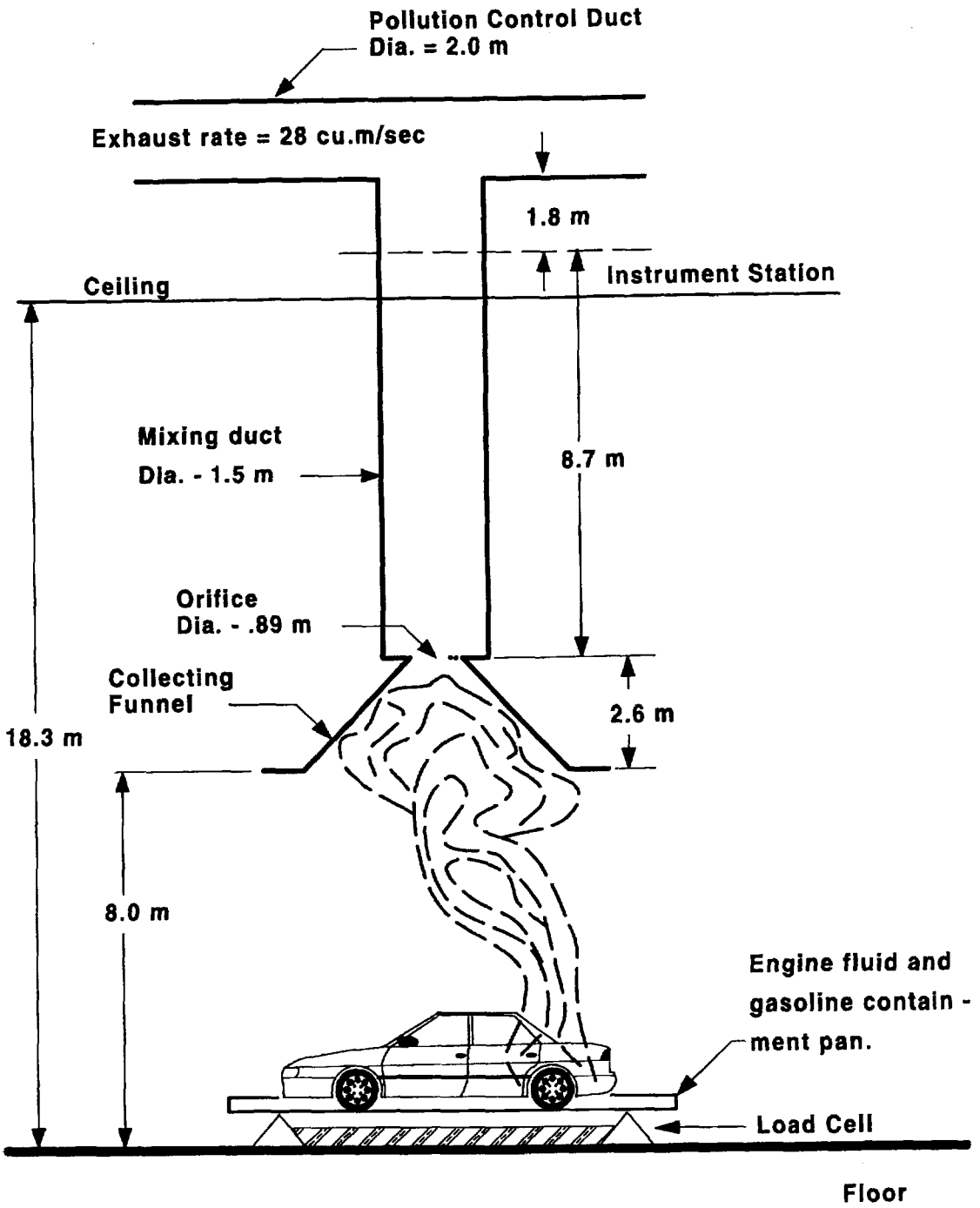

Figure G1. Fire Test F99030A. Diagram of the test vehicle under the fire products collector at the Factory Mutual Test Center.

A fire products collector was used to measure heat and combustion gases generated by the burning vehicle during this test (Fig. G1). The fire products collector consisted of a collection funnel (diameter = 6.1 m), an orifice plate (hole = 0.9 m), and a vertical stainless steel sampling duct (diameter = 1.5 m). The sampling duct was connected to the air pollution control system of the Test Center. The blower of the air pollution control system induces gas flow through the sampling duct. Air enters the sampling duct via the orifice plate. The temperature, linear velocity, optical transmission, and chemical composition of the entrained gas were measured in the center of the sampling duct 8.66 m (5.7 duct diameters) downstream from the orifice plate, ensuring a flat velocity profile at the sampling location. The data acquisition system consisted of a Hewlett Packard 2313B analog-to-digital conversion sub-system interfaced to a Hewlett Packard 1000 computer.

Gas temperature in the sampling duct was measured with two Type-K thermocouples (30 gage) with exposed bead-type junctions. The thermocouple leads were housed in stainless steel tubes (o.d. = 6.4 mm). Ambient air temperature in the facility was measured by five Type-K thermocouples attached to the external surface of the duct at 2.44, 5.49, 9.14, 12.8, and 15.9 m above the floor. These thermocouples were shielded from radiation from the fire.

The linear velocity of the gas entrained in the sampling duct was measured with a Pitot ring consisting of four Pitot tubes. A static pressure tap was mounted on the inside wall of the sampling duct. The pressure difference between the Pitot ring and the static wall tap was measured with an electronic manometer (Barocel Model 1173, CGS Scientific Corporation).

The particulate concentration in the entrained air was determined from the optical transmission across the duct measured at 0.4579 μm (blue), 0.6328 μm (red), and 1.06 μm (infrared). The optical path length across the duct was 1.524 m. Gas was withdrawn from the sampling duct through a stainless steel tube (o.d. = 3.9 mm) at a flow rate of 0.17×10^{-3} m^3/s for chemical analysis. The gas flowed through a particulate filter, a water condenser, and a drying agent before entering the analyzers. Carbon dioxide (CO_2) and carbon monoxide (CO) were measured with two dedicated non-disperse infrared analyzers (Beckman Model 864 Infrared Analyzers). Oxygen (O_2) was measured with a paramagnetic oxygen analyzer (Beckman Model 755 Paramagnetic Oxygen Analyzer). Total gaseous hydrocarbons were measured with a flame ionization analyzer (Beckman Model 400 Flame Ionization Analyzer).

The rate of product release was calculated using the following relationship:

$$\left(\frac{dR_j}{dt}\right) = f_j\left(\frac{dV}{dt}\right)\rho_j = f_j\left(\frac{dW}{dt}\right)\left(\frac{\rho_j}{\rho_g}\right) \qquad \text{(G1)}$$

where $d(R_j)/dt$ is the mass release rate of product j in kg/s; f_j is the volume fraction of product j; dV/dt is the total volume flow rate of the gas entrained in the sampling duct in m^3/s; dW/dt is the total mass flow rate of the gas entrained in the sampling duct in kg/s; ρ_j is the density of product j in g/m^3; and ρ_g is the density of the gas entrained in the concentration measurements. The rate of oxygen consumption was calculated using equation (G1), where the volume fraction of oxygen consumed was substituted for f_j.

The volume fraction of smoke particulate was calculated from the following relationship:

$$f_s = \frac{D\lambda \times 10^{-6}}{\Omega} \qquad \text{(G2)}$$

where f_s is the volume fraction of smoke, λ is the wavelength of the light source, Ω is the extinction coefficient of particulate (a value of 0.7 was used in these calculations), and D is the optical density at each of the three wavelengths at which measurements were made:

$$D = \frac{\ln\left(I_0/I\right)}{L} \qquad \text{(G3)}$$

where I_0 is the intensity of light transmitted through clean air, I is the intensity of light transmitted through air containing smoke particulate, and L is the optical pathlength, which was equal to 1.524 m. A value of 1.1×10^6 g/m^3 was used for the density of smoke particulate (ρ_j) in equation (G1).

The convective heat release rate was calculated using the following relationship:

$$\left(\frac{dE_{conv}}{dt}\right) = \left(\frac{dW}{dt}\right) \times c_p \times \left(T_g - T_a\right) \qquad \text{(G4)}$$

where $d(E_{conv})/dt$ is the convective heat release rate in kW; dW/dt is the mass flow rate of the gas entrained in the sampling duct in kg/s; c_p is the heat capacity of the gas entrained in the sampling

duct at the gas temperature in kJ/(kg×K); T_g is the temperature of the gas entrained in the sampling duct in K; and T_a is the ambient air temperature in K.

The chemical heat release rate was calculated from the release rates of carbon dioxide and carbon monoxide as follows:

$$\left(\frac{dE_{ch}}{dt}\right) = \Delta H^*_{CO_2} \times \left(\frac{dR_{CO_2}}{dt}\right) + \Delta H^*_{CO} \times \left(\frac{dR_{CO}}{dt}\right) \qquad \text{(G5)}$$

where $d(E_{ch})/dt$ is the chemical heat release rate in kW; ΔH^* is the net heat of complete combustion per unit mass of carbon dioxide or carbon monoxide released in the fire in kJ/g; and dR/dt is the mass release rate of carbon dioxide or carbon monoxide in kg/s. Values of ΔH^* for carbon dioxide and carbon monoxide were obtained from the literature [G1 and G2].

The chemical heat release rate also was calculated from the oxygen consumption rate as follows:

$$\left(\frac{dE_{ch}}{dt}\right) = \Delta H^*_O \left(\frac{dC_O}{dt}\right) \qquad \text{(G6)}$$

where $d(E_{ch})/dt$ is the chemical heat release rate in kW; ΔH^*_O is the net heat of complete combustion per unit mass of O_2 consumed in kJ/g; and $d(C_O)/dt$ is the consumption rate of oxygen in kg/s. The value for ΔH^*_O was obtained from the literature [G1 and G2].

The radiative heat release rate was the difference between the chemical heat release rate and the convective heat release rate:

$$\left(\frac{dE_{rad}}{dt}\right) = \left(\frac{dE_{ch}}{dt}\right) - \left(\frac{dE_{conv}}{dt}\right) \qquad \text{(G7)}$$

where $d(E_{rad})/dt$ is the radiative heat release rate; and $d(E_{ch})/dt$ is the average chemical heat release rate calculated using equations (G5) and (G6).

The vehicle was placed in a rectangular steel pan (length = 25 ft., width = 15 ft., height = 4 in.) to prevent spilled and leaking automotive fluids from spreading in the test facility. This fluid containment pan was fabricated from two sheets of carbon steel. Angle-braces were welded to

the under-side of the pan to keep it from flexing under the weight of the vehicle. The corners of the support frame rested on load cells. Mass loss was determined from data acquired from the load cells during the test.

The fluid containment pan was lined with a layer of fiberglass-reinforced cement construction board (DuraRock, USG Corporation). A thin layer of sand was used to level the concrete board so that the grade of the surface measured from the center to the edges along the major and minor axes was no greater than 1%. The joints between boards were sealed with latex caulking.

Mass loss from the burning vehicle and any burning fluids retained by the containment pan was measured with a load cell weigh-module system. The fluid containment pan was supported by an I-beam frame a load cell weight-module (KIS Series, BLH Electronics, Inc.) at each corner. These weight-modules contain cylindrical, double cantilever strain gauge transducers that are not generally affected by changes in mass distribution. The weight-module system was calibrated before this test by placing a series of standard weights on the fluid containment pan.

Data from the fire-products collector and load cell weight-module system are shown in Plots G1 through G5. The analyzer for measuring carbon monoxide in the fire plume malfunctioned during this test. The carbon monoxide release rate data in Plot G3 are invalid.

REFERENCES

G1. G. Heskestad. A Fire Products Collector for Calorimetry into the MW Range, Technical Report J.I. OC2E1.RA. Factory Mutual Research Corporation, Norwood, MA. June, 1981.

G2. Archibald Tewarson. "Generation of Heat and Chemical Compounds in Fires" Section 3/Chapter 4, SFPE Handbook of Fire Protection Engineering, 2nd Edition, 1995, pp. 3:53-124.

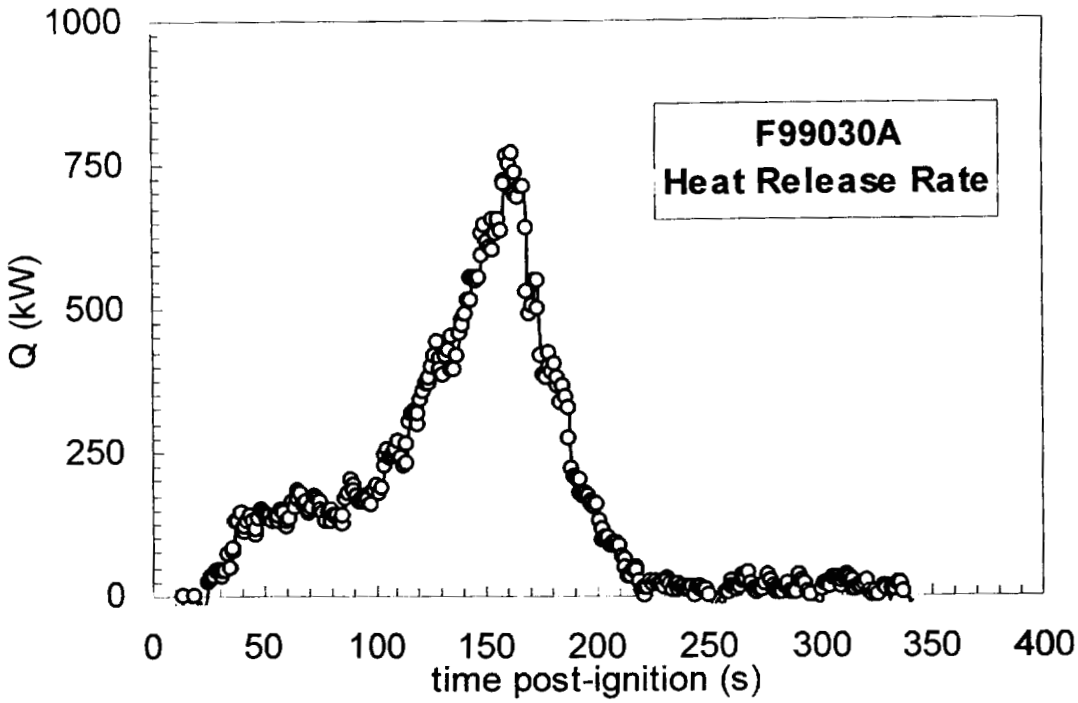

Plot G1. Fire Test F99030A. Heat release rate measured using the Fire Products Collector.

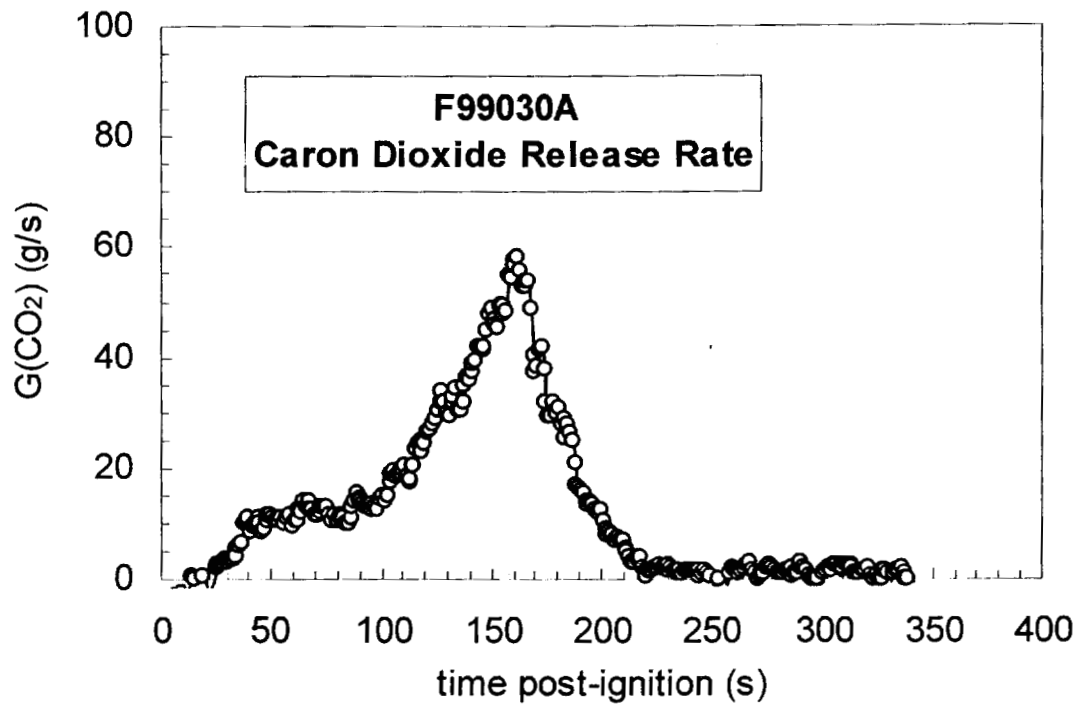

Plot G2. Fire Test F99030A. Carbon dioxide release rate measured using the Fire Products Collector.

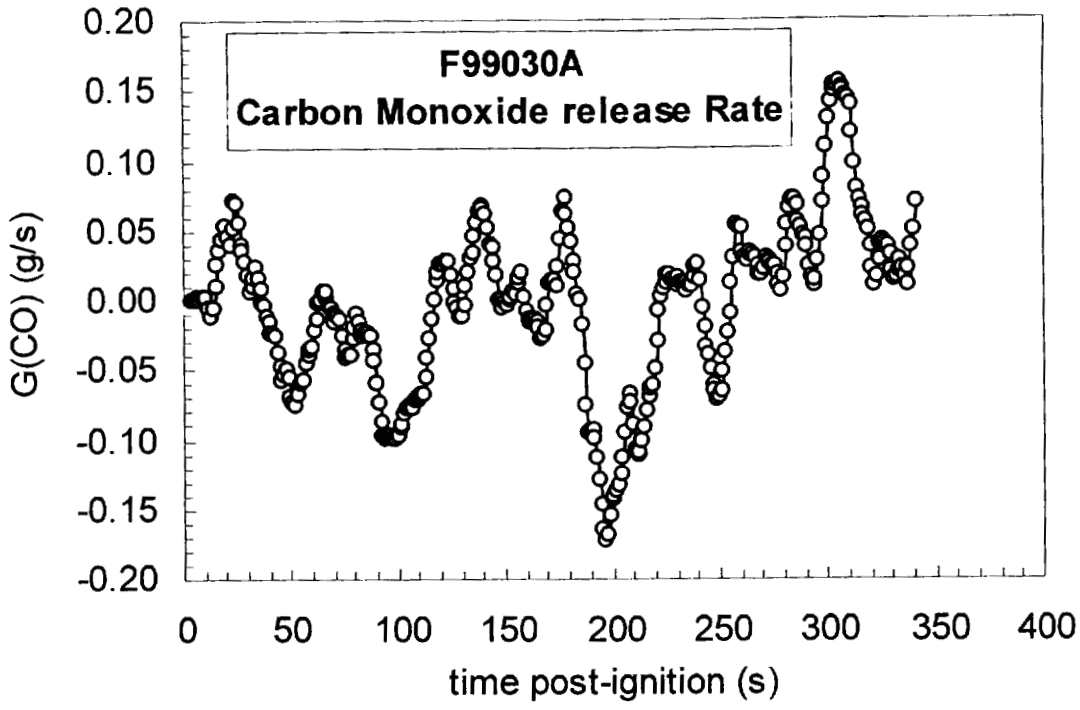

Plot G3. Fire Test F99030A. Carbon monoxide release rate measured using the Fire Products Collector.

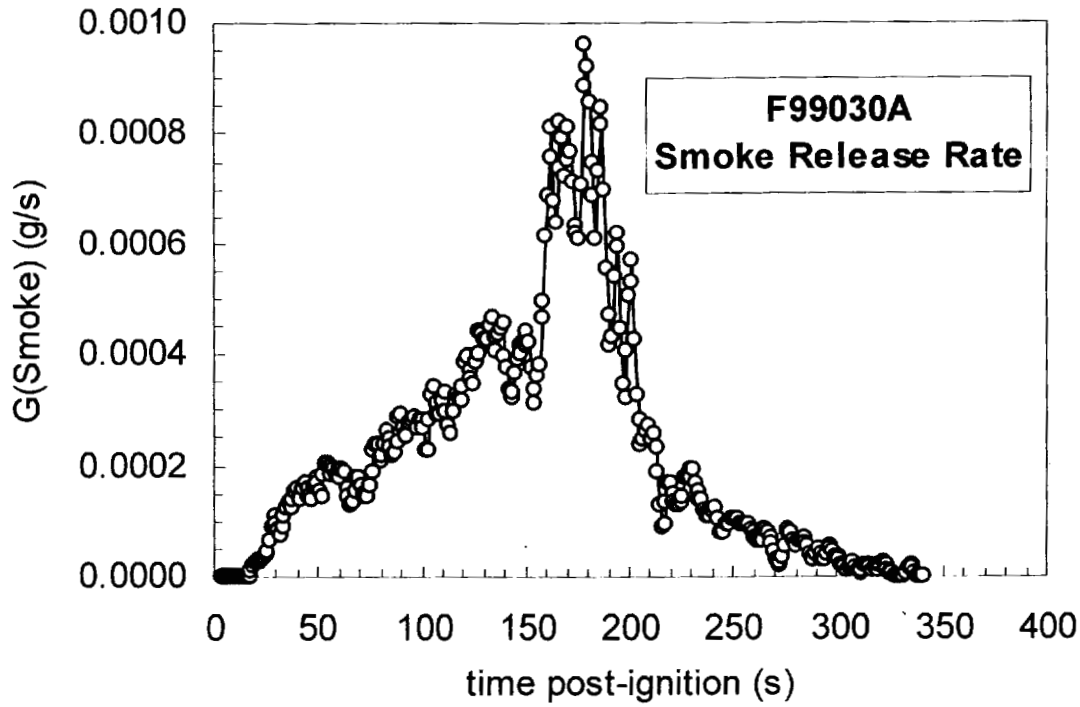

Plot G4. Fire Test F99030A. Smoke release rate measured using the Fire Products Collector.

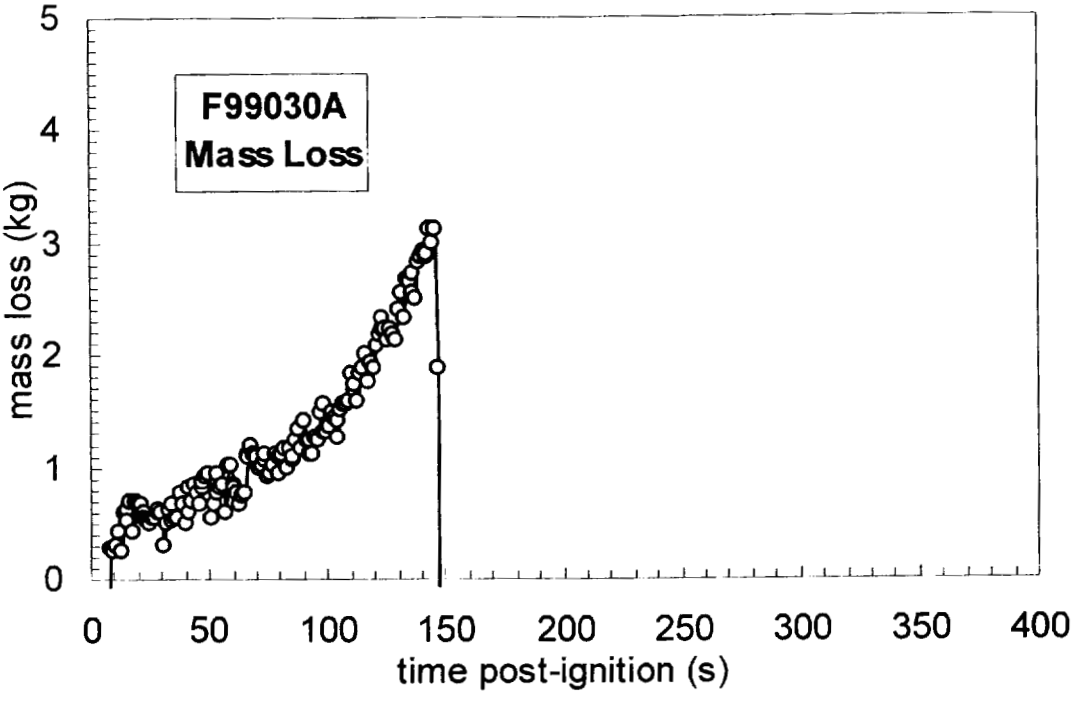

Plot G5. Fire Test F99030A. Mass Loss from the test vehicle during the fire test. The mass data was not valid after 147 seconds post-ignition because test personnel stepped onto the fluid containment pan to move video equipment.

APPENDIX H
PASSENGER COMPARTMENT COMBUSTION GAS DATA
FOURIER TRANSFORM INFRARED SPECTROSCOPY

The sampling-line for FTIR analysis consisted of a stainless-steel tube (o.d. = 0.250 in. (6.4 mm), i.d. = 0.125 in. (3.2 mm), l = 20 ft (6.1 m)) inserted through the roof between the front seats along the longitudinal midline of the test vehicle (Fig.'s H1 and H2). The inlet of the sample-tube extended approximately 10 in. below the headlining. The tube was not heated. The outlet of the sample tube was connected to a heated Teflon® transfer-line (o.d. = 0.250 in. (6.4 mm), i.d. = 0.125 in. (3.2 mm), l = 75 ft. (23 m)), which was connected to the gas cell of the FTIR spectrometer. The transfer-line was heated to 105°C during the test to prevent condensation of water and water-soluble gases (*e.g.*, HCl, HCN, NO, and NO_2). An in-line stainless steel filter holder containing a quartz fiber filter (o.d. = 47 mm) was placed between the sample-tube and the transfer-line to prevent smoke particles from contaminating analytical instrumentation.

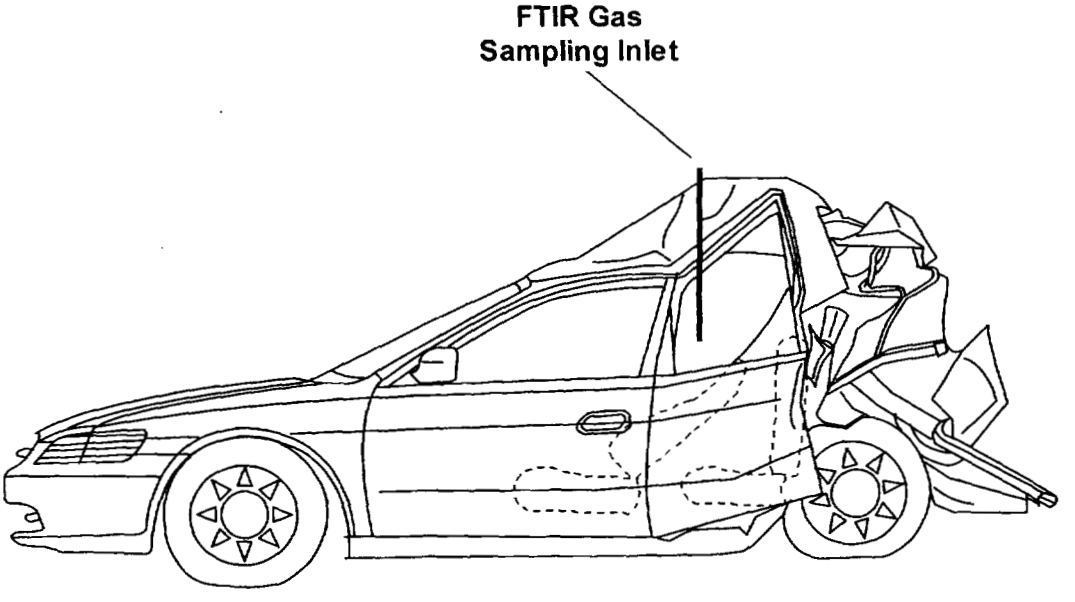

Figure H1. Fire Test F99030A. Side-view of the test vehicle show the approximate location of the FTIR gas sampling inlet in the passenger compartment.

The FTIR spectrometer was a Model I-1000 Series FTIR Spectrometer (MIDAC Corporation, Riverside, California), with a KBr beam-splitter; a liquid nitrogen-cooled Mercury-Cadmium-Telluride detector; and gold-surfaced aluminum optics. This instrument was fitted with a stainless steel, multiple-reflectance gas cell (path length = 10 m) with zinc selenide windows. The gas cell was heated to 105°C. The optical bench was filled with clean, dry argon and hermetically sealed. The usable spectral range of this instrument was approximately 7400-700 cm^{-1}. Pressure in the gas cell during the fire tests was measured with a Baratron pressure gauge (MKS Instruments, Burlington, MA). The spectrometer was operated at a spectral resolution of 0.5 cm^{-1}.

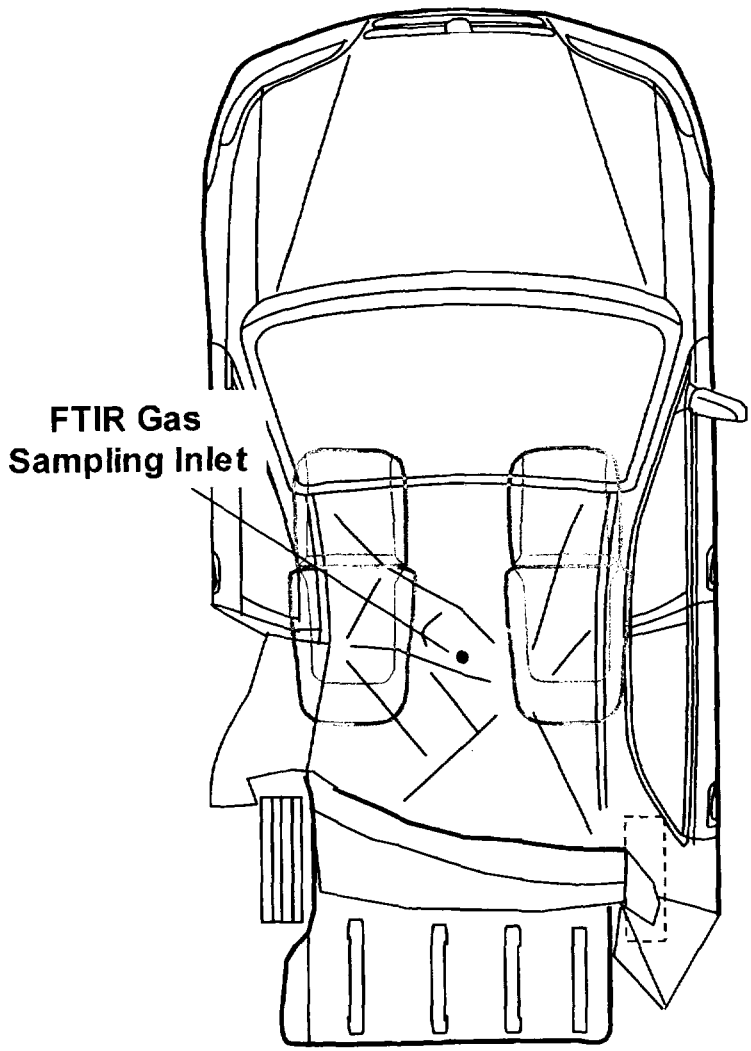

Figure H2. Fire Test F99030A. Top view of the test vehicle showing the approximate location of the FTIR gas sampling inlet in the passenger compartment.

The sampling line and gas cell were equilibrated to 105°C for at least 60 minutes before sample acquisition. A reference spectrum was acquired while the gas cell was evacuated. During the fire tests, the gas cell was purged continuously with air withdrawn from the passenger compartment at a flow rate of 7 L/min. Single-scan absorbance spectra were acquired and stored to disk at intervals of 10 s. After the test, the stored spectra were analyzed using the quantitative analysis software provided by the instrument manufacturer (AutoQuant, MIDAC). This software uses a Classical Least Squares algorithm to determine gas concentrations. The method developed for analysis of combustion gases was calibrated with gas standards (Scott Specialty

Gases, Inc., Troy, MI). The standards were either NIST-traceable or produced by a gravimetric blending process.

The gaseous combustion products measured by FTIR in the passenger compartment during this test included carbon dioxide, carbon monoxide, methane, ethylene, acetylene, hydrogen cyanide, nitric oxide, and hydrogen chloride (Plots H1 through H8). Except for carbon dioxide, which has a background concentration in air of approximately 0.05%, and hydrogen chloride, the concentrations of all of these gases were less than their respective lower limits of detection before ignition. The background concentration of carbon dioxide in air is approximately 0.04%. Noise in the Infrared spectra acquired before ignition resulted in an apparent hydrogen chloride concentration of < 1 ppm.

Carbon dioxide, carbon monoxide, methane, ethylene, and acetylene started to accumulate in the passenger compartment between 50 and 75 seconds post-ignition (Plots H1 through H5). The concentration of carbon dioxide in the passenger compartment of the test vehicle increased until approximately 170 seconds post-ignition (Plots H2). The concentrations of carbon monoxide, methane, ethylene, and acetylene increased until approximately 190 seconds post-ignition (Plots H1, H3, H4, and H5).

The Infrared spectra acquired during this test also contained a broad absorbance band between 2800 and 3200 cm^{-1}, indicating the presence of a mixture of aliphatic hydrocarbons in the air samples from the passenger compartment. The intensity of this absorbance band generally followed the same time-course as that of methane (Plot H3), ethylene (Plot H4), and acetylene (Plot H5). This broad band appeared to contain absorbances from ethane, propane, and butane. However, all of the gaseous species contributing to this absorbance band in this region of the infrared spectrum spectrum could not be identified or accurately quantified.

Hydrogen cyanide (Plot H7) and nitric oxide (Plot H8) started to accumulate in the passenger compartment between 125 and 150 seconds post-ignition. The concentrations of hydrogen cyanide and nitric oxide in the passenger compartment of the test vehicle increased until approximately 190 seconds post-ignition (Plots H7 and H8).

Hydrogen chloride (HCl) was not detected in the passenger compartment of the test vehicle during this test (Plot H6).

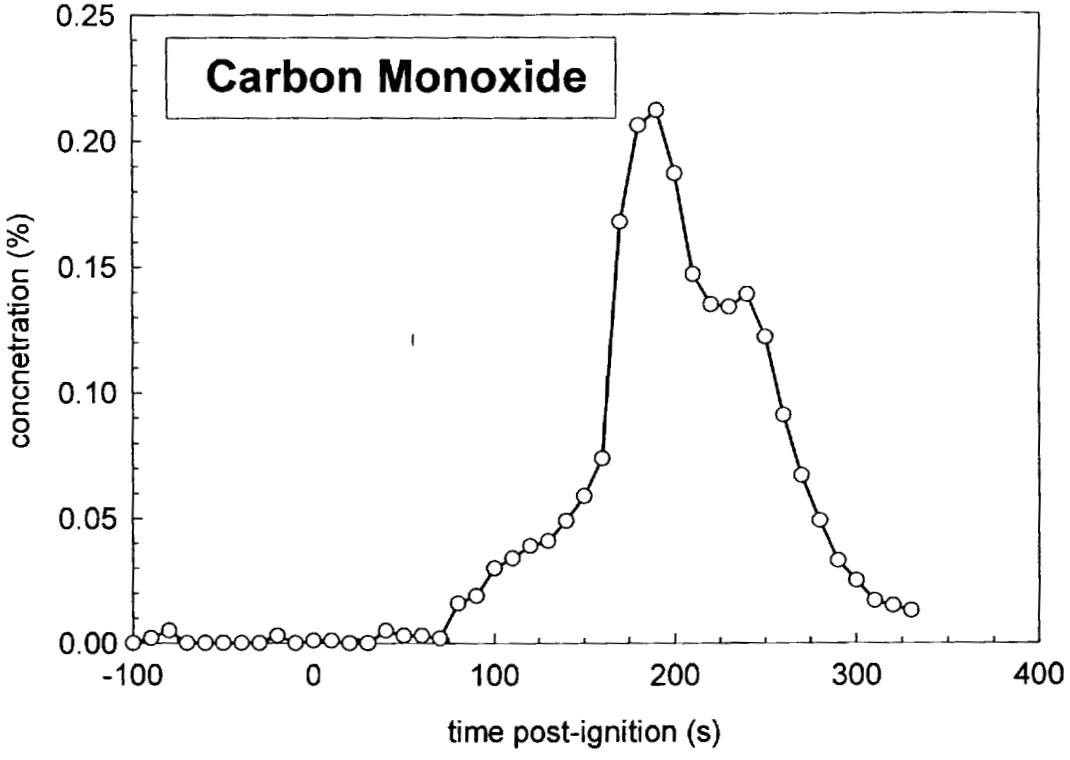

Plot H1. Fire Test F99030A. Concentration of carbon monoxide (CO) in the passenger compartment determined by FTIR analysis.

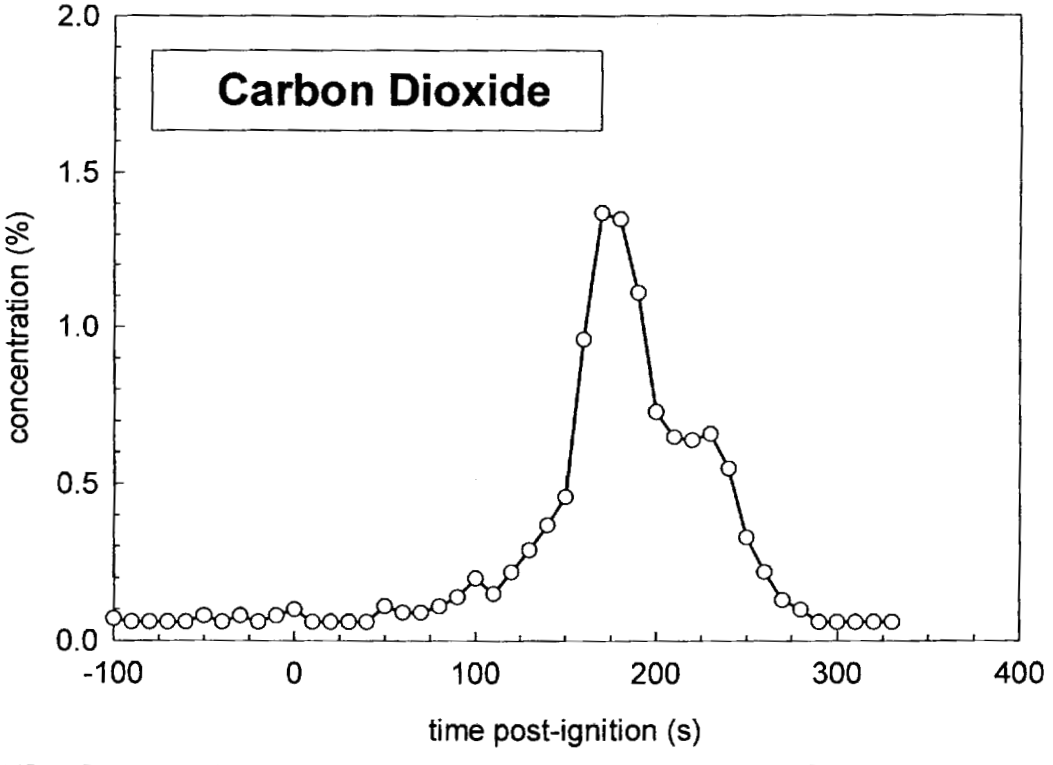

Plot H2. Fire Test F99030A. Concentration of carbon dioxide (CO_2) in the passenger compartment determined by FTIR analysis.

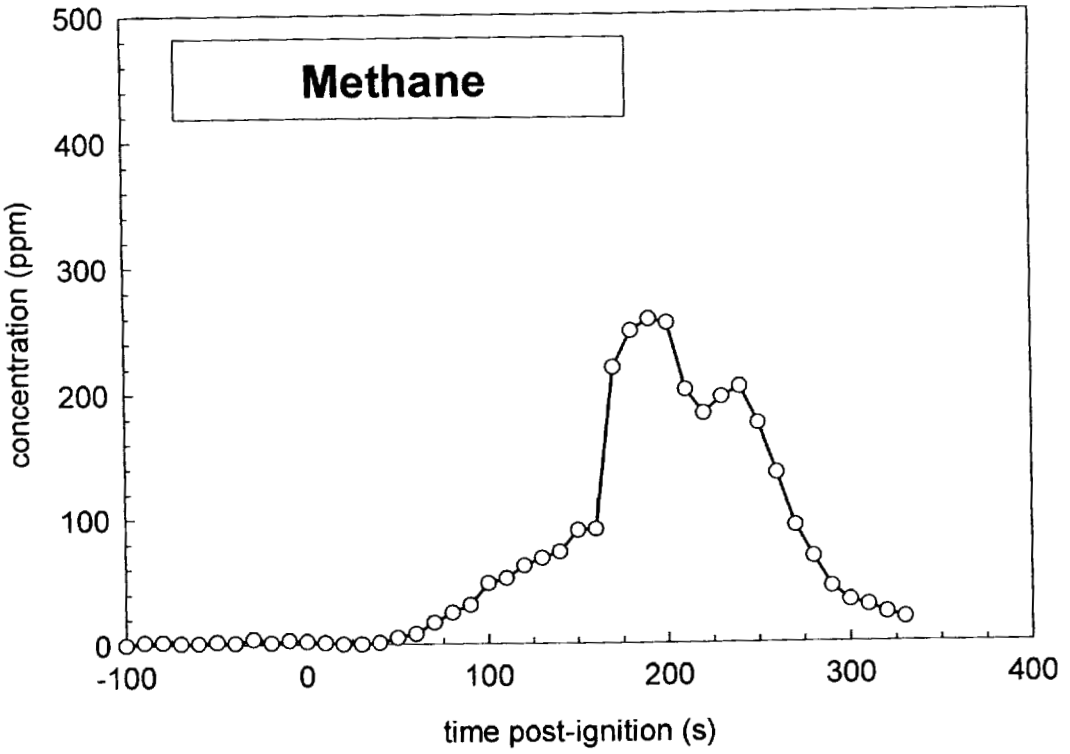

Plot H3. Fire Test F99030A. Concentration of methane (CH_4) in the passenger compartment determined by FTIR analysis.

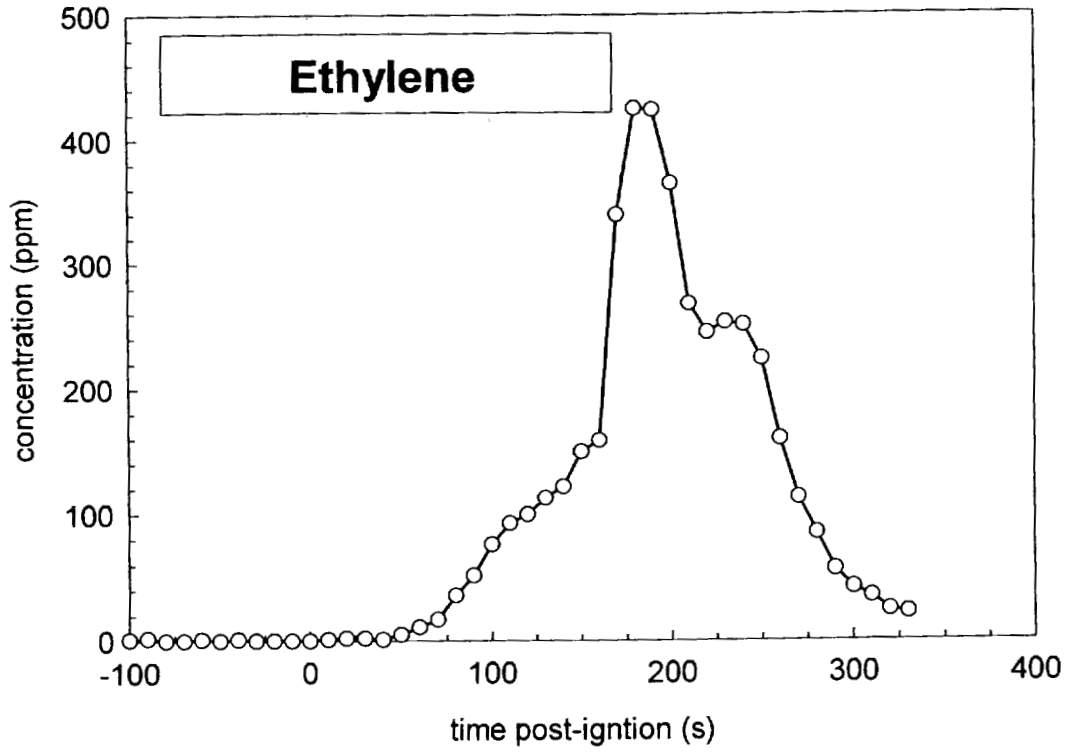

Plot H4. Fire Test F99030A. Concentration of ethylene (C_2H_4) in the passenger compartment determined by FTIR analysis.

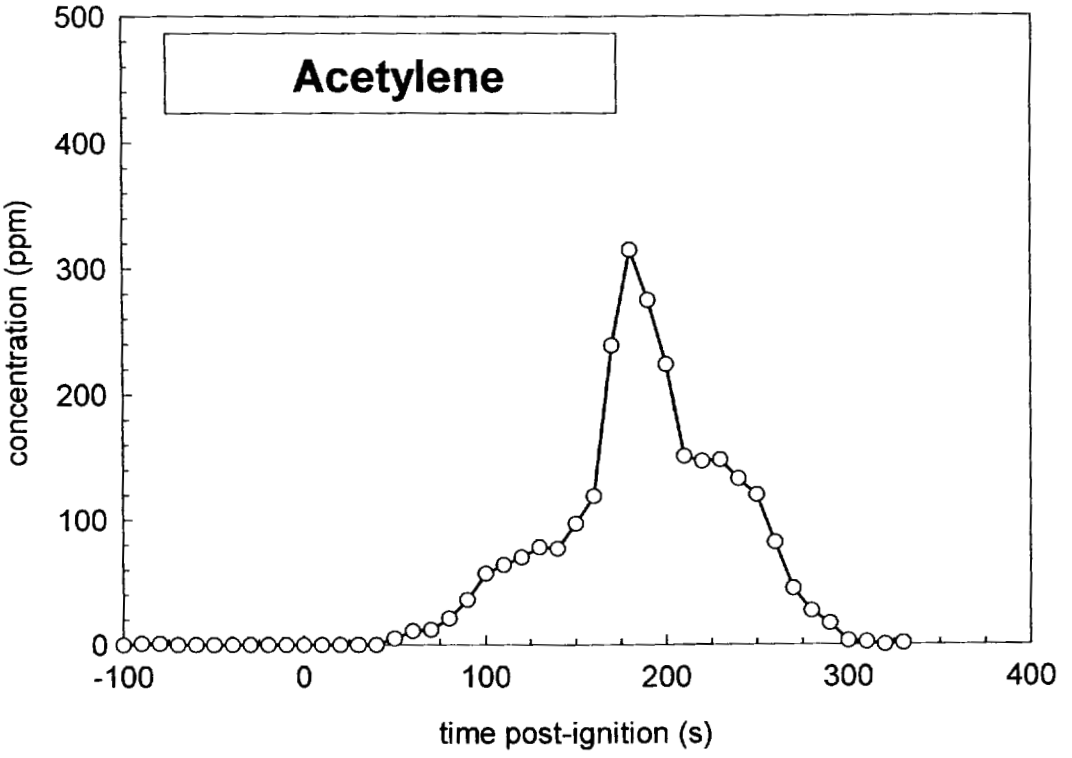

Plot H5. Fire Test F99030A. Concentration of acetylene (C_2H_2) in the passenger compartment determined by FTIR analysis.

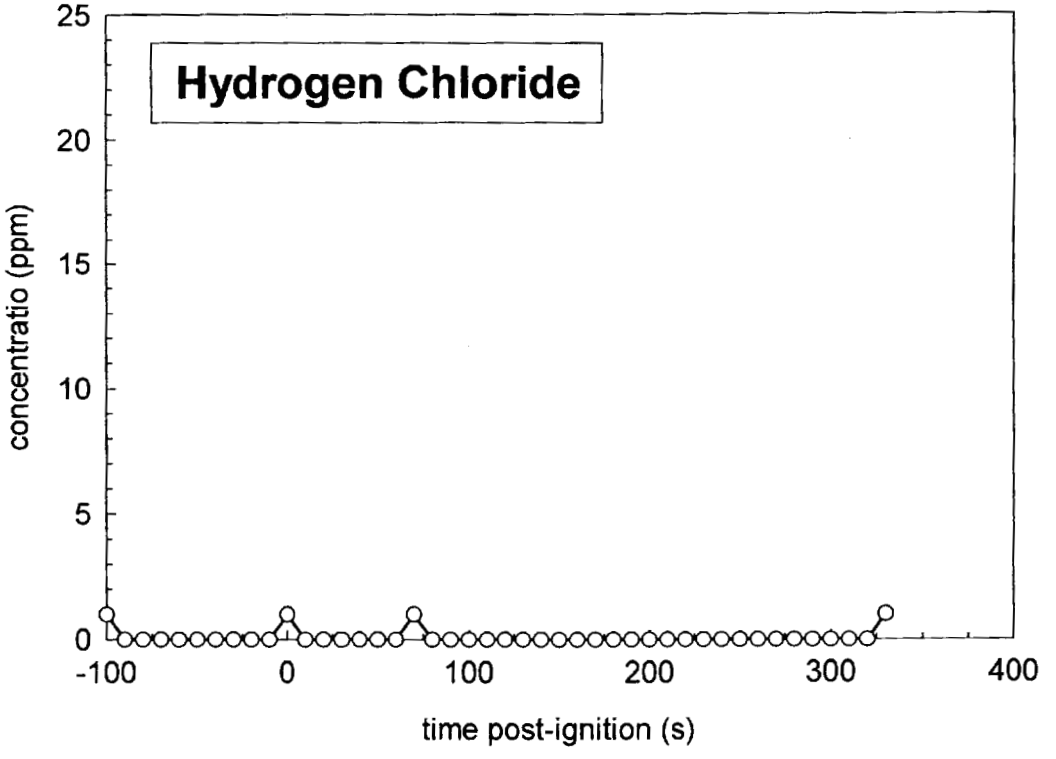

Plot H6. Fire Test F99030A. Concentration of hydrogen chloride (HCl) in the passenger compartment determined by FTIR analysis.

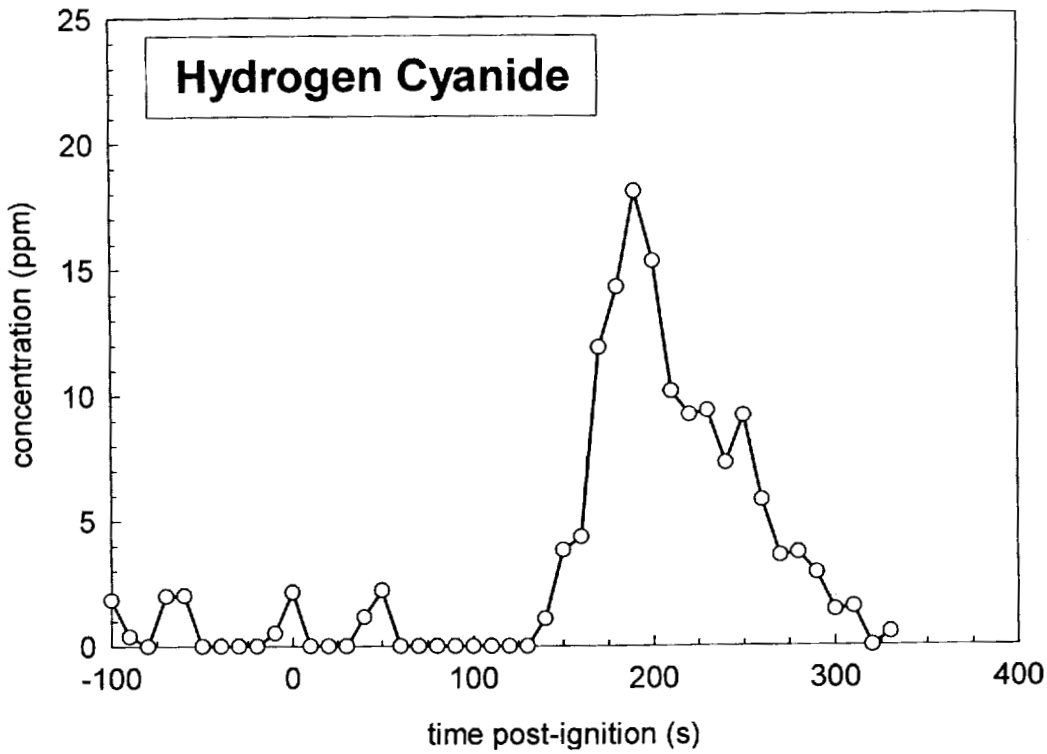

Plot H7. Fire Test F99030A. Concentration of hydrogen cyanide (HCN) in the passenger compartment determined by FTIR analysis.

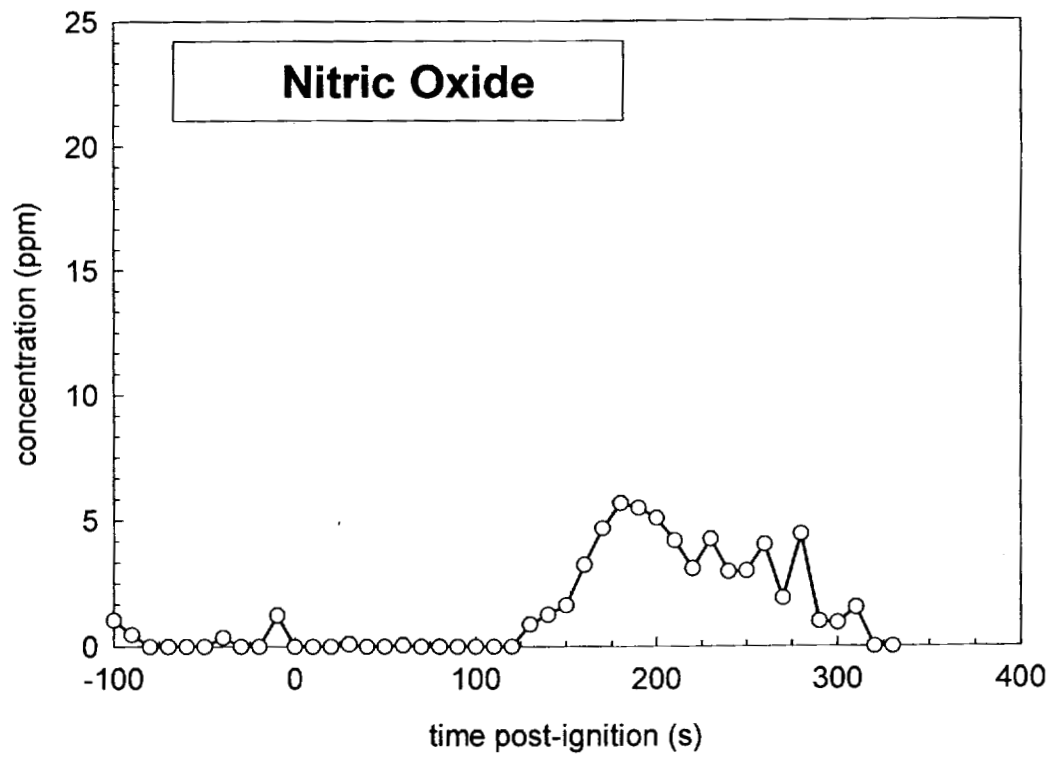

Plot H8. Fire Test F99030A. Concentration of nitric oxide (NO) in the passenger compartment determined by FTIR analysis.

APPENDIX I
PASSENGER COMPARTMENT COMBUSTION GAS DATA
GAS CHROMATOGRAPHY/MASS SPECTROSCOPY GAS ANALYSIS

The sampling-line for GC/MS samples consisted of a stainless-steel tube (o.d. = 0.250 in. (6.4 mm), i.d. = 0.125 in. (3.2 mm), l = 20 ft (6.1 m)) inserted through the roof between the front seats along the longitudinal midline of the test vehicle (Fig.'s I1 and I2). The inlet of the sample-tube extended approximately 10 in. below the headlining. The outlet of the sample tube was connected to sampling manifold by a length of stainless steel sampling tube (o.d. = ¼ in., length = 25 ft.). The sampling manifold contained five sample cartridges in parallel. Airflow was directed sequentially through the sample cartridges a solenoid-actuated gas-switching manifold. The airflow rate through the cartridges during sampling was adjusted 250 cm^3/min with a rotometer. None of the components of the GC/MS sampling line were heated.

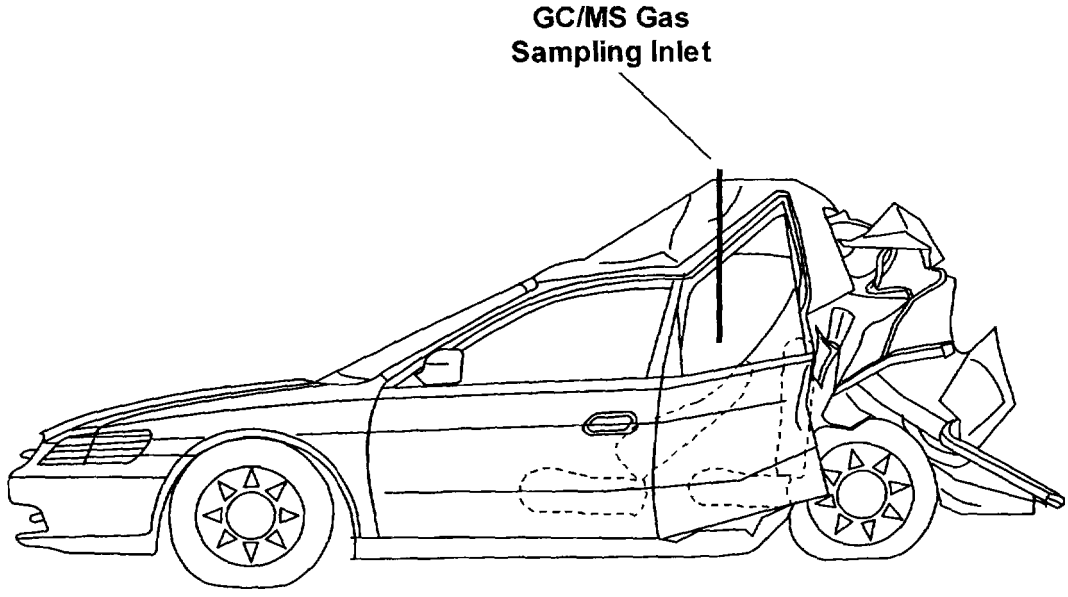

Figure I1. Fire Test F99030A. Side-view of the test vehicle show the approximate locations of the GC/MS gas sampling inlets in the passenger compartment.

Each cartridge was a glass-lined stainless steel tube (i.d. = 4 mm; length = 10 cm; Scientific Instrument Services, Inc, Ringoes, NJ) packed with 25 mg of Carbotrap™ C Graphitized Carbon Black (Supelco, Inc.; Bellefonte, PA) in series with 15 mg of Carbotrap™ Graphitized Carbon Black (Supelco).

After the test, the sample cartridges were analyzed by thermal desorption/gas chromatography/mass spectrometry. Deuterated standards dissolved in deuterated methanol were added to each sorbent cartridge to monitor sample recovery. A modified purge-and-trap concentrator was used for thermal desorption (Model 600 Purge-and-Trap Concentrator, CDS Analytical, Oxford, PA). The gas chromatograph was a Model 5890 Series II Plus Gas Chromatograph (Hewlet Packard, Palo Alto, CA). The mass spectrometer was a Hewlet Packard

Model 5989B Mass Spectrometer (Hewlett Packard). The thermal desorption unit was interfaced directly to the split/splitless injector of the gas chromatograph through a cryo-focusing unit. The injector was operated in the split mode with a split of approximately 10 mL/min. The chromatographic column was a fused silica capillary column coated with 100% methyl silicone (HP-1 ; length = 30 m; i.d. = 0.25 mm; film thickness = 0.25 μm).

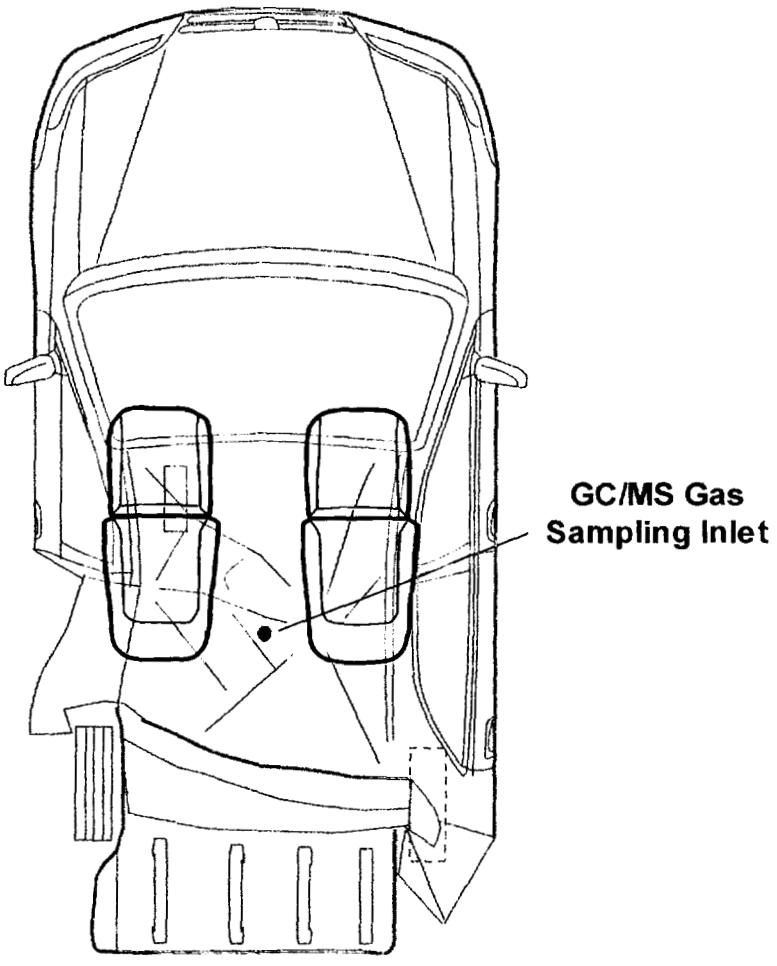

Figure I2. Fire Test F99030A. Top view of the test vehicle showing the approximate locations of the GC/MS gas sampling inlet in the passenger compartment.

The sample was desorbed at 320°C for 10 min, and cryofocused onto the head of the chromatographic column -80°C. The temperature of the analytical column was maintained at 0°C while the sample was desorbed and cryo-focused. To start the chromatographic analysis, the

cryo-focusing unit was heated bullistically to a temperature of 320°C. The column temperature was programmed from 0 to 325°C at a rate of 5°C/min. Mass spectra were obtained by scanning from m/z 40 to 600 at a rate of 1.2 scan/s.

Plots I1 through I6 show the mass chromatograms of the blank and samples acquired during this test. The sampling intervals in the figure captions were corrected for the time-delay for airflow through the sample-line, which was estimated to have been approximately 25 seconds.

Table I1 lists 54 components tentatively identified from analysis of the mass chromatograms of these samples. The components are listed in order of chromatographic retention time. Identifications were based on the results of a spectral search a commercial mass spectral library (Wiley 275K Mass Spectral Library). The relative abundance of each compound is the ratio of the peak area of the peak in question to the average of the peak areas of the deuterated n-alkanes added as internal standards are listed.

Blanks 1 and 2 contained aliphatic hydrocarbons in the range of C7 – C8 and in the range of C13 through C16. This contamination may have been kerosene vapor. A kerosene heater, used to heat area around test vehicle, was filled with kerosene before this test and a small amount of kerosene was spilled on the outside of the heater.

Samples 2, 3, and 4 contained aliphatic and aromatic hydrocarbons from gasoline vapor. Aromatic compounds such as indene, 1-methyl-1H-indene, naphthalene, 2-methylnaphthalene, and 3-methylnaphthalene in these samples were produced by incomplete combustion of the gasoline pumped below the test vehicle and other materials burning during this test. The presence of 2,4-dimethyl-1-heptene in these samples indicates that materials containing the polymer poly(propylene) were undergoing thermal decomposition when these samples were acquired. Samples 2, 3, and 4 contained small amounts of the contaminant aliphatic hydrocarbons in the blank samples.

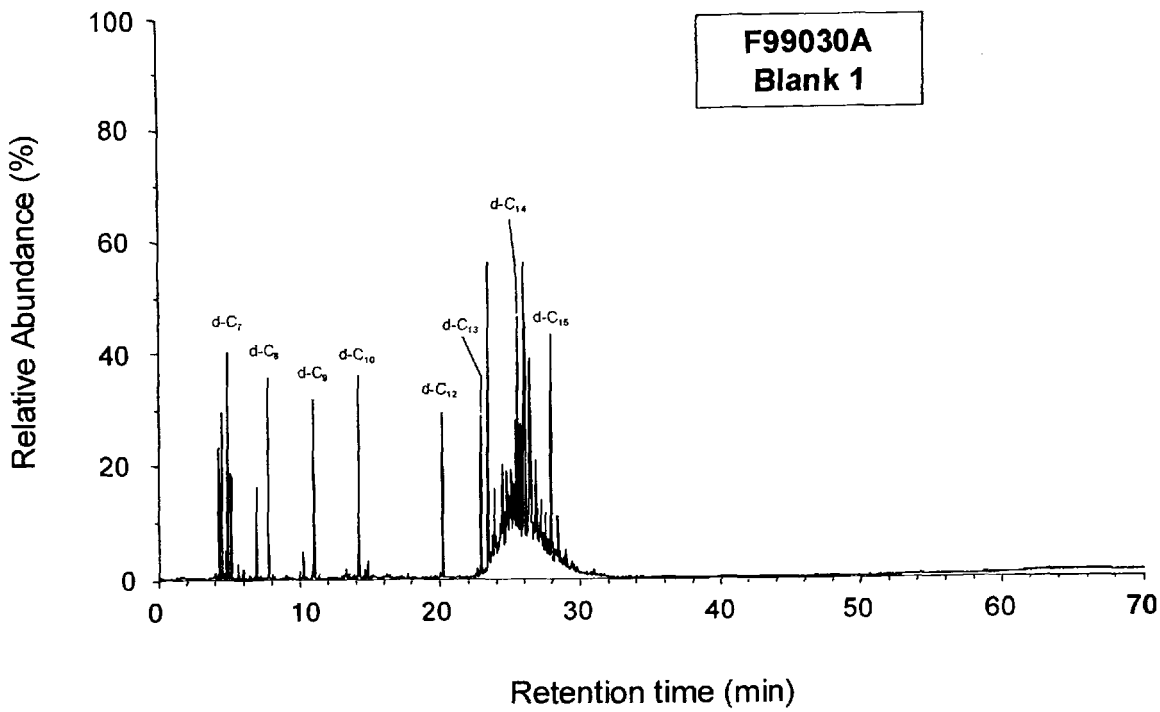

Plot I1. Fire Test F99030A. Mass chromatogram from GC/MS analysis of Blank 1 acquired for a period of 5 minutes before the test.

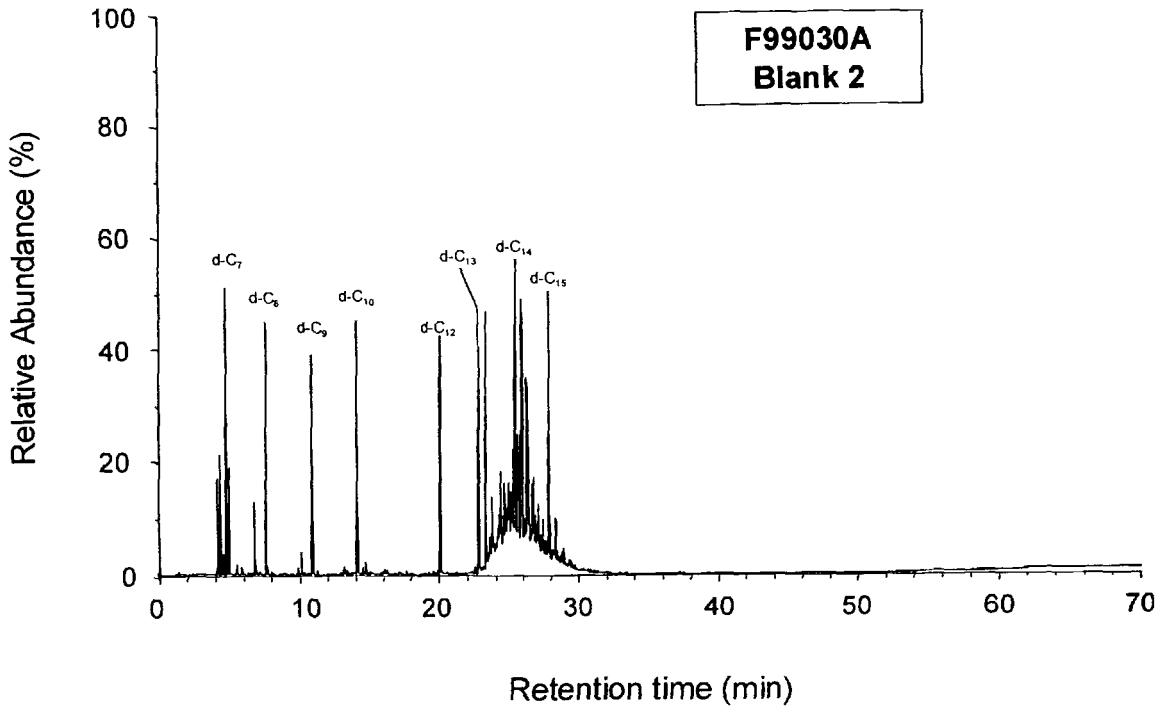

Plot I2. Fire Test F99030A. Mass chromatogram from GC/MS analysis of Blank 2 acquired for a period of 5 minutes before the test.

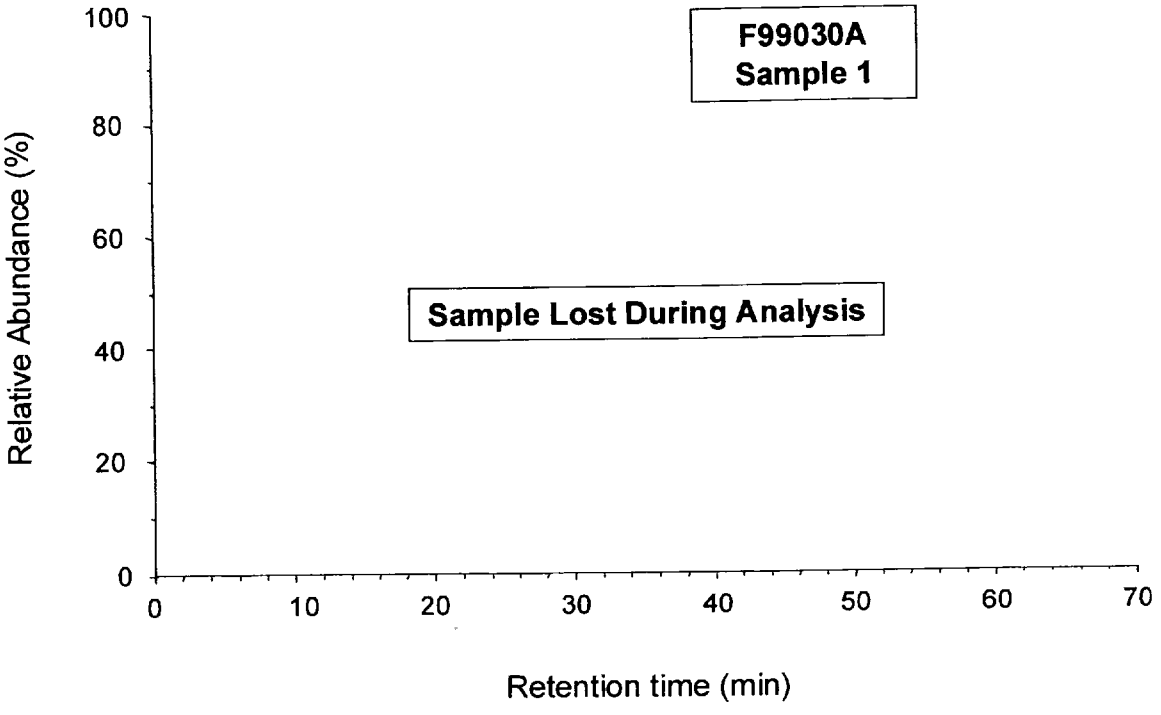

Plot I3. Fire Test F99030A. Mass Chromatogram of Sample 1 acquired from -30 to +15 seconds post-ignition.

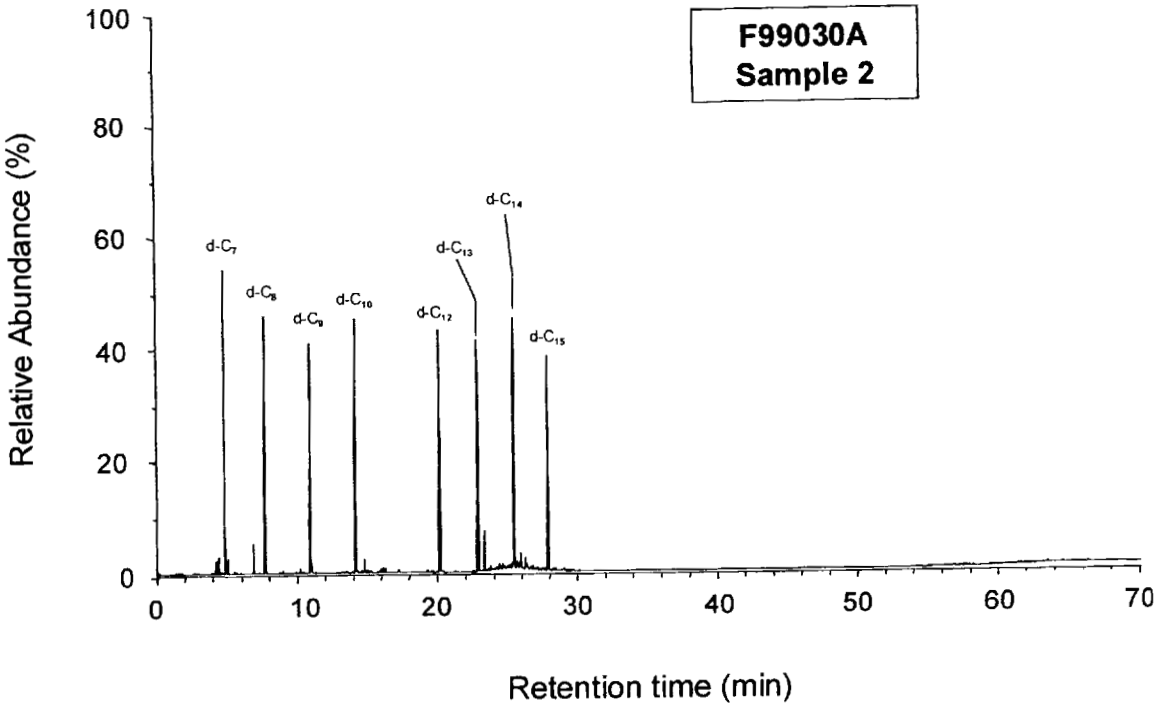

Plot I4. Fire Test F99030A. Mass Chromatogram of Sample 2 acquired from +15 to +48 seconds post-ignition.

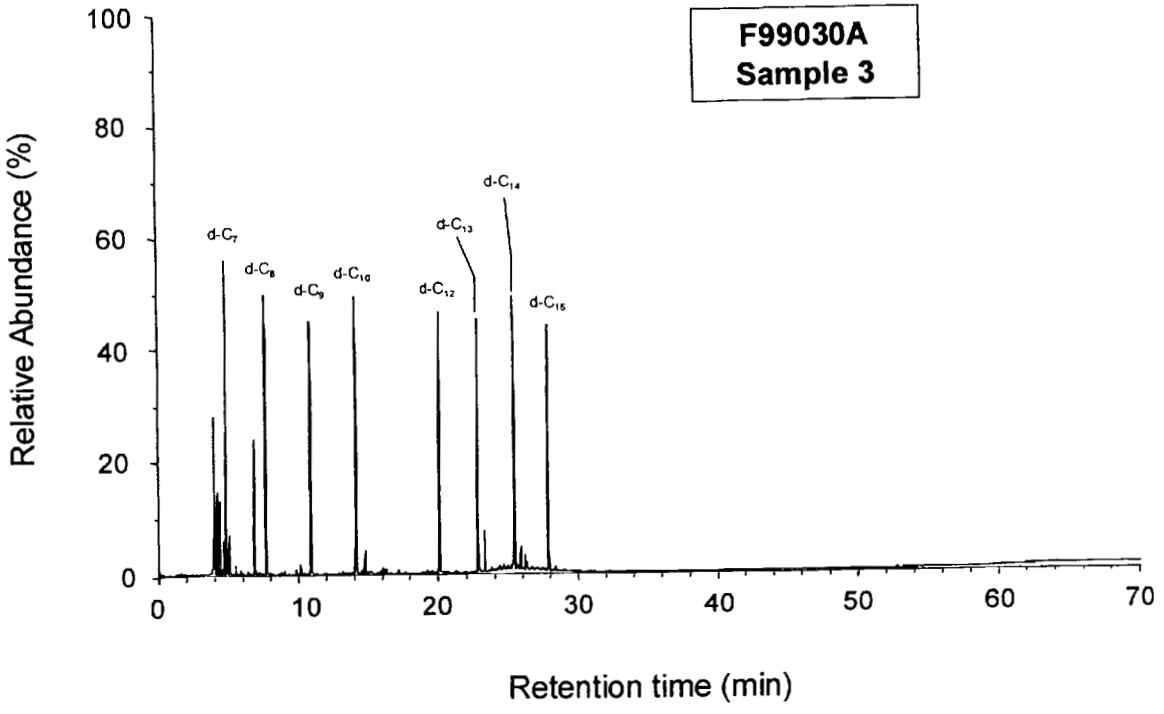

Plot I5. Fire Test F99030A. Mass Chromatogram of Sample 3 acquired from +48 to +92 seconds post-ignition.

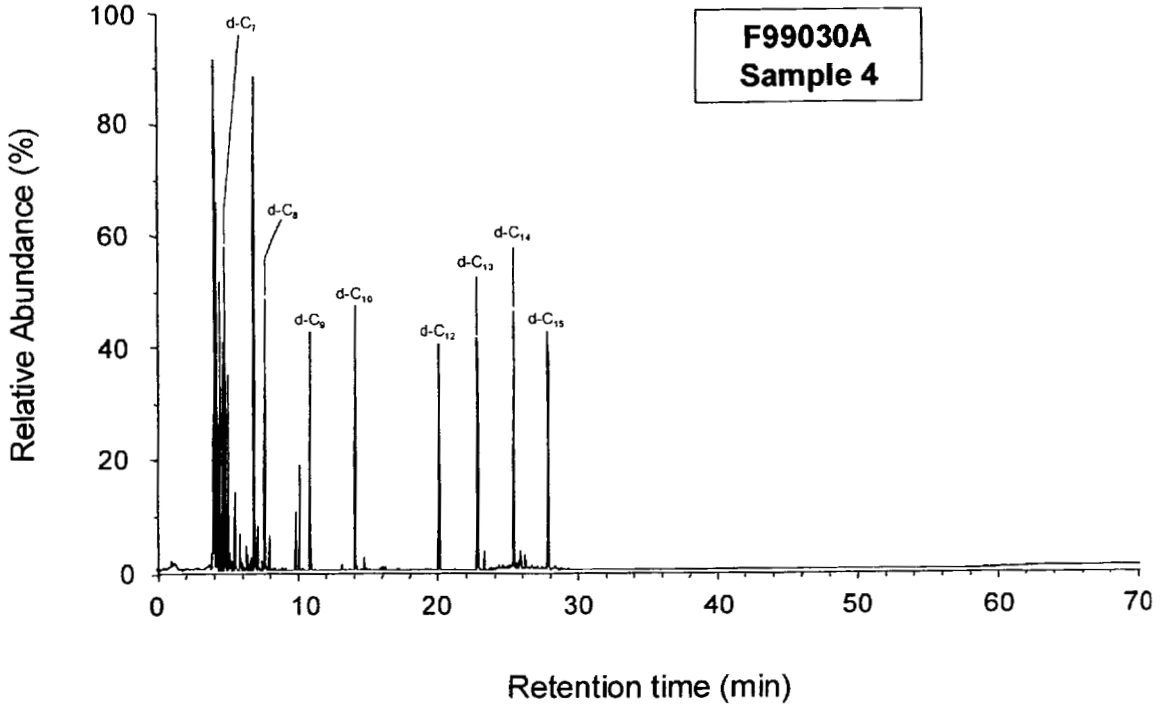

Plot I6. Fire Test F99030A. Mass Chromatogram of Sample 4 acquired from +92 to +127 seconds post-ignition.

Table I1
GC/MS Peak Identification

t_R	Compound	Relative Abundance[1]					
		Blank 1	Blank 2	Sample 1	Sample 2	Sample 3	Sample 4
4.12	benzene	0.00	0.00	n/a	0.00	0.58	2.58
4.30	2-methylhexane	0.45	0.27	n/a	0.04	0.15	0.74
4.51	3-methylhexane	0.45	0.26	n/a	0.03	0.12	0.57
4.64	1,3-dimethylcyclopentane	0.01	0.01	n/a	0.00	0.01	0.10
4.71	1,2-dimethylcyclopentane	0.01	0.00	n/a	0.00	0.00	0.05
4.76	C_8 - Alkane	0.07	0.04	n/a	0.01	0.06	0.40
4.92	d_{16}-n-heptane (d-C_7)	0.96	0.88	n/a	0.92	0.89	0.86
5.15	n-heptane	0.34	0.19	n/a	0.03	0.07	0.40
5.63	methylcyclohexane	0.04	0.02	n/a	0.00	0.01	0.13
5.98	2-methylheptane	0.01	0.01	n/a	0.00	0.01	0.06
6.02	3-methylheptane	0.01	0.01	n/a	0.00	0.00	0.03
6.44	C_8 - Alkane	0.01	0.00	n/a	0.00	0.01	0.05
6.59	C_8 - Alkane	0.01	0.00	n/a	0.00	0.00	0.03
6.83	C_8 - Alkane	0.00	0.00	n/a	0.00	0.00	0.04
6.95	methylbenzene	0.25	0.14	n/a	0.06	0.25	1.96
7.24	C_8 - Alkane	0.00	0.01	n/a	0.00	0.01	0.10

Table I1, continued
GC/MS Peak Identification

t_R	Compound	Relative Abundance[1]					
		Blank 1	Blank 2	Sample 1	Sample 2	Sample 3	Sample 4
7.77	d_{18}-n-octane (d-C_8)	0.84	0.79	n/a	0.82	0.84	0.81
8.09	n-octane	0.01	0.01	n/a	0.00	0.00	0.07
9.97	ethylbenzene	0.03	0.02	n/a	0.00	0.01	0.14
10.23	1,4-dimethylbenzene 1,3-diemthylbenzene	0.11	0.06	n/a	0.01	0.03	0.30
11.00	d_{20} -n-nonane (d-C9)	0.97	0.94	n/a	0.94	0.96	1.06
13.27	C_3 - benzene	0.02	0.04	n/a	0.01	0.01	0.02
13.49	C_3 - benzene	0.02	0.01	n/a	0.00	0.00	0.00
14.22	d_{22}-n-decane (d-C10)	0.93	0.94	n/a	0.98	0.98	0.93
14.27	C_3 - benzene	0.03	0.94	n/a	0.00	0.00	0.00
14.61	n-decane	0.03	0.02	n/a	0.01	0.01	0.00
15.18	C_3 - benzene	0.01	0.01	n/a	0.00	0.00	0.00
16.15	C_3 - benzene	0.01	0.01	n/a	0.01	0.01	0.01
16.34	C_3 - benzene	0.01	0.01	n/a	0.01	0.01	0.01
17.71	n-undecane	0.01	0.01	n/a	0.00	0.00	0.00
19.97	naphthalene	0.03	0.01	n/a	0.00	0.00	0.00
20.19	d26-n-dodecane (d-C12)	0.90	1.04	n/a	1.06	1.05	1.04

Table I1, continued
GC/MS Peak Identification

t_R	Compound	Relative Abundance[1]					
		Blank 1	Blank 2	Sample 1	Sample 2	Sample 3	Sample 4
22.92	d28-n-tridecane (d-C13)	0.97	1.11	n/a	1.11	1.10	1.11
23.40	n-tridecane	2.15	1.29	n/a	0.11	0.10	0.05
23.74	C_{14} - alkane	0.14	0.09	n/a	0.00	0.00	0.00
23.85	C_{14} - alkane	0.28	0.16	n/a	0.01	0.01	0.00
24.44	alkylated cyclhexane	0.26	0.17	n/a	0.01	0.02	0.00
24.71	C_{14} - alkane	0.27	0.17	n/a	0.02	0.01	0.01
25.06	C_{14} - alkane	0.27	0.16	n/a	0.02	0.02	0.01
25.22	C_{15} - alkane	0.19	0.12	n/a	0.01	0.01	0.01
25.45	C_{15} - alkane	0.44	0.26	n/a	0.00	0.00	0.00
25.51	d30-n-tetradecane (d-C14)	1.03	1.07	n/a	1.09	1.08	1.09
25.67	C_6 - benzene / C_2 - naphthalene	0.45	0.31	n/a	0.02	0.02	0.01
25.98	n-tetradecane / C_2 - naphthalene	2.75	1.71	n/a	0.09	0.10	0.08
26.31	C2 - naphthalene	0.93	0.62	n/a	0.03	0.03	0.03
26.40	C2 - naphthalene	0.37	0.24	n/a	0.01	0.01	0.00
26.82	C2 - naphthalene	0.28	0.18	n/a	0.01	0.00	0.00
27.15	C2 - naphthalene	0.19	0.13	n/a	0.01	0.01	0.00

Table I1, continued
GC/MS Peak Identification

t_R	Compound	Relative Abundance[1]					
		Blank 1	Blank 2	Sample 1	Sample 2	Sample 3	Sample 4
27.53	C_{16} - alkane	0.27	0.17	n/a	0.00	0.00	0.00
27.93	d32-n-pentadecane (d-C15)	1.41	1.24	n/a	1.06	1.09	1.10
28.40	n-pentradecane / C_3 - naphthalene	0.28	0.17	n/a	0.01	0.02	0.00

[1] The abundance values shown in this table are the ratio of the peak area of the compound of interest to the average peak area of the deuterated n-alkanes (internal standards) in each sample.

APPENDIX J
PASSENGER COMPARTMENT
AIRBORNE PARTICULATE ANALYSIS

Five samples of airborne particulate were samples from the passenger compartment during this test. The approximate locations of the inlets particulate samplers are shown in Figures J1 and J2.

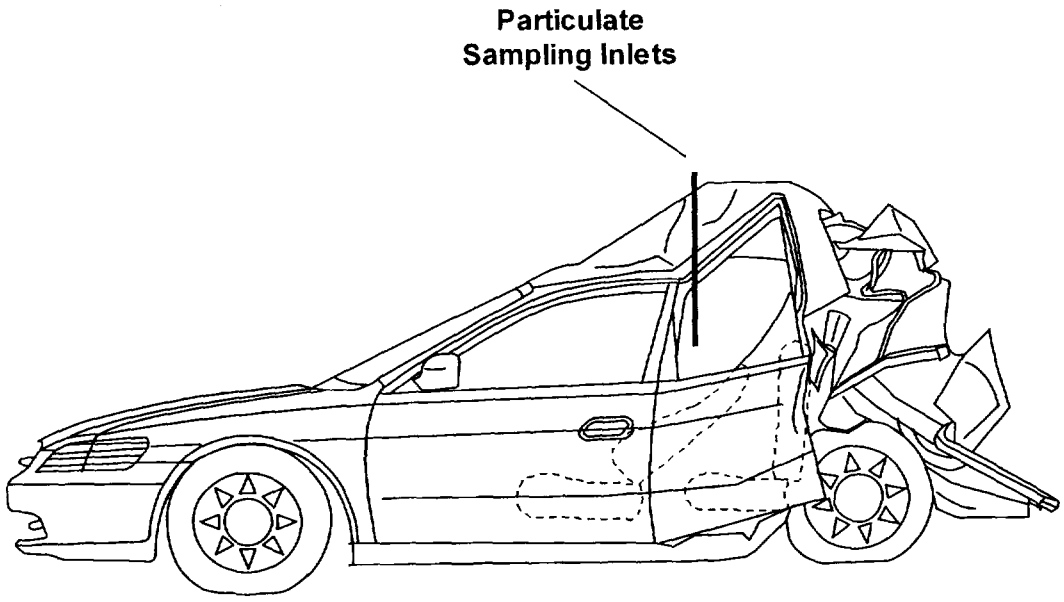

Figure J1. Fire Test F99030A. Side-view of the test vehicle showing the approximate locations of the particulate sampling inlets in the passenger compartment.

Each particulate sampling apparatus consisted of an in-line stainless steel filter holder (filter diameter = 47 mm, Gelman Scientific). The inlet of each filter holder was fitted with a straight length of stainless steel tubing (o.d. = ¼ in., o.d. = $^{5}/_{16}$ in., length = 12 in.) using a compression fitting (¼ in., Swagelok). The inlet tube was inserted through the roof of the test vehicle so that it extended below the headlining approximately 10 in.. The outlet of each filer holder was connected to a vacuum manifold using flexible copper tubing (o.d. = $^{5}/_{16}$ in., length = 25 ft.). The vacuum manifold was connected to a pumping system configured to maintain constant flow through the filter holder as the pressure drop across the filter increased due to particulate loading. Qartz-fiber filters were used to collect particulate from the passenger compartment. The filters were placed in an electric furnace at 650°C in air overnight and pre-weighed. The pumping system was adjusted to maintain a volume flow rate of 30 L/min. through a single filter holder. This produced a linear velocity of approximately 29 cm/sec. of airflow perpendicular the face of the filter.

Two blanks were collected for 10 minutes before the test. Samples were collected during the test. In-line solenoid valves fitted to each port of the vacuum manifold and were actuated

manually during the test to direct flow through the filter holders sequentially. The time intervals for sample acquisition were the same as those for acquiring GC/MS samples.

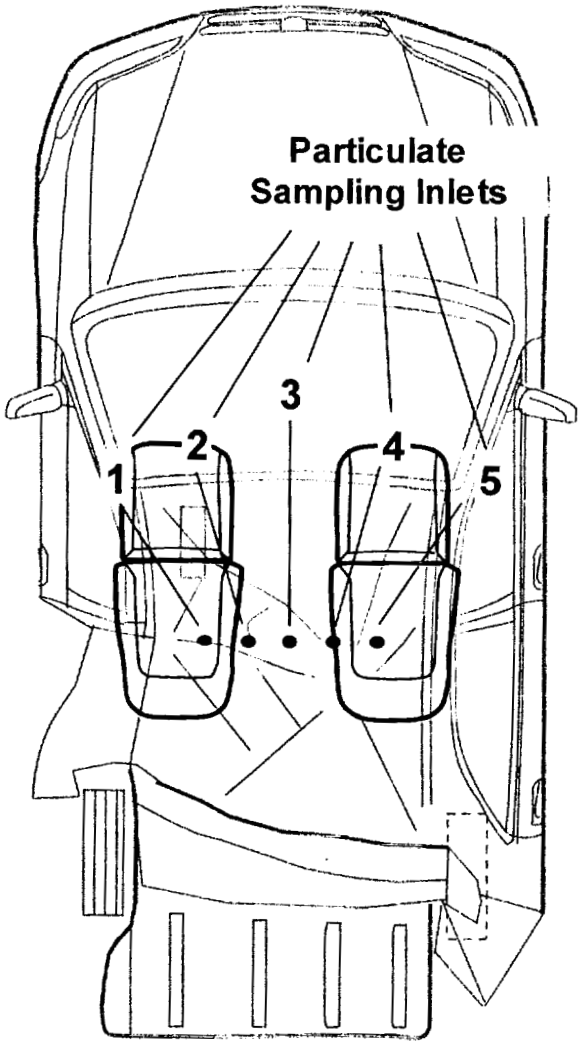

Figure J2. Fire Test F99030A. Top-view of the test vehicle showing the approximate locations of the particulate sampling inlets in the passenger compartment.

After the test, the filters placed in a dissector cabinet overnight to remove water absorbed by the filter media and particulate. The weight of each filter was recorded only after constant weight was achieved. The average concentrations of airborne particulate during each sample interval were determined from the mass of particulate collected, the volume flow rate, and the elapsed time.

A quarter was cut from each filter, weighted, and extracted for quantitative ion chromatographic analysis. The extracting solution was the mobile phase buffer. The chromatography column was

an IC-Pak A HC column (Waters, Milford, MA). The mobile phase was a sodium borate/gluconate buffer at a flow rate of 1.8 mL/min [J1]. The chromatographic system consisted of a Model 616 Pump, a Model 717 Autosampler, and a Model 431 Conductivity Detector (Waters). The following anions were measured in the ion chromatographic analysis: fluoride (F^-), bicarbonate (HCO_3^-), chloride (Cl^-), nitrite (NO_2^-), bromide (Br^-), hypochlorite ($HClO_3^-$), nitrate (NO_3^-), phosphate (HPO_4^-), sulfate (SO_4^-), and oxalate ($C_2O_4^-$).

Table JI shows the concentration of airborne particulate in the passenger compartment during this test.

Table J1
Average Airborne Particulate Concentration

Sample	Sampling Interval (sec.)	Sampling Time (sec.)	Airborne Concentration (mg/m^3)
Blank	n/a	300	4
Sample 1	-45 to 0	45	48
Sample 2	0 to +33	33	80
Sample 3	+33 to +77	44	31
Sample 4	+77 to +112	35	161
Sample 5	+112 to +142	30	432

Table J2 shows the results of the average anion concentration in the airborne particulate. The results shown in Table J2 were corrected for bicarbonate, nitrate, phosphate, sulfate, and oxalate detected in the blanks. Samples 3, 4, and 5 contained chloride. All samples contained phosphate.

Table J2

Average Anion Concentration in the Airborne Particulate

Sample	Anion Concentration in Airborne Particulate (μg/mg)[1]									
	F^-	HCO_3^-	Cl^-	NO_2^-	Br^-	$HClO_3^-$	NO_3^-	HPO_4^-	SO_4^-	$C_2O_4^-$
Sample 1	n/d[1]	n/d	n/d	n/d	n/d	n/d	n/d	9	n/d	n/d
Sample 2	n/d	n/d	n/d	n/d	n/d	n/d	n/d	33	n/d	n/d
Sample 3	n/d	n/d	31	n/d	n/d	n/d	n/d	23	n/d	n/d
Sample 4	n/d	n/d	56	n/d	n/d	n/d	n/d	7	n/d	n/d
Sample 5	n/d	n/d	65	n/d	n/d	n/d	n/d	21	n/d	n/d

[1] n/d = not detected

REFERENCES FOR APPENDIX J

J1. Method A-102, Waters Innovative Methods for Ion Analysis, Manual Number 22340, Waters Corporation, Milford, MA.